Photoluminescent carbogenic nanoparticles for potential healthcare applications

by

Spyridon Gavalas

A thesis submitted in partial fulfilment for the requirements for the degree of Doctor of Philosophy at the University of Central Lancashire

April 2024

RESEARCH STUDENT DECLARATION FORM

Type of Award   **Doctor of Philosophy**

School   **School of Pharmacy and Biomedical Sciences**

1.   Concurrent registration for two or more academic awards

I declare that while registered as a candidate for the research degree, I have not been a registered candidate or enrolled student for another award of the University or other academic or professional institution

2.   Material submitted for another award

I declare that no material contained in the thesis has been used in any other submission for an academic award and is solely my own work.

3.   Collaboration

Where a candidate's research programme is part of a collaborative project, the thesis must indicate in addition clearly the candidate's individual contribution and the extent of the collaboration. Please state below:

N.A.

4.   Use of a Proof-reader

No proof-reading service was used in the compilation of this thesis.

Signature of Candidate

Print name: Spyridon Gavalas

Abstract

Carbon dots (C-dots) are zero-dimensional fluorescent nanomaterials typically measuring below 10 nm. They have gained attention for their unique structure and properties, including cost-effective fabrication, easy chemical functionalization, high photoluminescence, tunable optical properties, resistance to photobleaching, thermal stability, and biocompatibility. Their growing use in biomedical applications is driven by their impressive potential as highly responsive optical sensors, monitoring probes, antimicrobial agents, and trackable carriers for drug delivery. This thesis explores two distinct methods for modifying the structure, and therefore their properties, of C-dots, each based on different precursor materials: one involves electrochemical surface functionalization, while the other employs an oxidizing agent to modify structural properties. The study examines how these approaches uniquely impact the optical and structural properties of each C-dot system, as well as their potential applications in the biomedical field.

Firstly, a novel electrochemical mechanism is presented, that significantly transforms the structural and optical features of C-dots that were synthesized via pyrolysis of citric acid and ethanolamine at 300°C. This method uses electrogenerated hypochlorite for electrochemical etching, which causes intense oxidation and breaks carbon-carbon bonds on the nanoparticle surface. As a result, the particle size is progressively reduced while the quantum yield increases dramatically, reaching an enhancement of up to 640%. This research is the first to provide concrete evidence of this highly efficient reshaping mechanism in C-dots, enabling precise control over particle size and photoluminescence emission properties.

Secondly, this chapter investigates the structural, optical, and biological properties of C-dots (CU100D) synthesized via pyrolytic treatment of citric acid and urea at 230°C, particularly after oxidation treatment with NaClO. This treatment reduced the particle size from 4.3 nm to 2.9 nm, enhancing the surface area-to-volume ratio and altering the physicochemical properties, while FTIR analysis showed improved dispersibility. Optical properties underwent notable transformations, as NaClO treatment decreased UV

intensity and increased transparency, while boosting the quantum yield by up to 350%, addressing the common challenge of low quantum yield compared to commercial graphene quantum dots. The irreversible destruction of the 2-(2'-hydroxyphenyl) benzothiazole (HTTP) fluorophore, a byproduct formed during synthesis, upon interaction with NaClO, suggests potential for novel functionalities beyond fluorescence imaging. This cost-effective and scalable method yielded nanoparticles with high cell viability and strong antifungal activity, demonstrating their excellent performance for biomedical applications.

Finally, the citric acid-urea-derived C-dots, following NaClO treatment, were compared to commercially available surface-modified graphene quantum dots functionalized with amine groups and imidazole. This comparison underscored the CU100D nanoparticles' cost efficiency, superior optical properties—such as a markedly higher quantum yield—and enhanced cell viability, showcasing their benefits over functionalized graphene quantum dots.

In conclusion, this thesis presents simple, green, cost and time-efficient, and scalable strategies for generating multifunctional C-dots with improved optical properties and versatile chemical compositions. Both approaches allowed the fine-tuning of the structural characteristics, and thereby the optical properties of C-dots, with significant quantum yield improvements. Treatment with NaClO enhances the C-dots' optical properties, biocompatibility, and biological activity. Overall, these findings highlight the potential of C-dots as a promising, cost-effective alternative to conventional fluorescent materials in various applications.

Table of Contents

Acknowledgements

I am profoundly grateful to my primary supervisor, Dr. Antonios Kelarakis, for his unwavering support, guidance, and the invaluable time he dedicated to bringing this project to fruition. His unwavering availability to address my inquiries and our frequent research meetings have not only honed my scientific abilities but also fostered my personal development, instilling in me a greater sense of maturity and humanity. For his boundless assistance and patience, I extend my deepest gratitude.

I want to express my sincere appreciation to my secondary supervisor, Dr. Marta Krysmann, for her invaluable assistance in the laboratory and the exceptional support she provided throughout this academic journey. I deeply value the meaningful discussions and small talks we've shared, which have been influential in shaping my PhD experience.

My time at UCLan has been enriched by the kindness and support of many individuals. Dr. Claire Mellor and Dr. Mark Holden provided invaluable assistance and guidance in the cell culture laboratory and physical characterisation, respectively. The expertise and support of lab technicians Tamar Garcia, Sameera Mahmood, Dr. Peter Bentley, Kane Fox, Elinor Clayton, and Beth Milnes have been indispensable. Additionally, I am grateful for the camaraderie and technical discussions with research team members Dr. Ruqiya Al-Jaafar, Dr. Ella Gibbons, Dr. Joanna Stachowska, Mohammed Suleman Beg, and Yang Chen.

I am deeply grateful to the Doctoral Training Alliance for their support throughout my PhD journey. Their funding of my project provided the essential resources needed for my research endeavours, enabling me to pursue my academic passions and make meaningful contributions to my field. Moreover, I extend my heartfelt appreciation for the invaluable social support provided through the numerous events and networking opportunities organized over the years. These events not only fostered interdisciplinary collaboration but also created a supportive and inclusive community where I could exchange ideas, gain new perspectives, and forge lifelong connections.

I am profoundly grateful to my family and friends, whose unwavering support and encouragement served as the bedrock of my PhD journey. Their belief in my abilities and unwavering sacrifices made this achievement possible. To my family, for their boundless love, understanding, and unwavering faith in my pursuits, I owe immeasurable gratitude. To my friends, for their laughter, companionship, and endless encouragement, I am deeply thankful. Each of you played a vital role in my success, offering solace during challenging times and joining me in celebrating moments of triumph. This thesis stands as a testament to your unwavering presence and steadfast support.

Thank you for all being an integral part of this remarkable journey with me.

List of figures

List of tables

List of abbreviations

AFM	**Atomic force microscopy**
AIE	**Aggregation-induced emission**
AIQ	**Aggregation-induced quenching**
BPEI	**Branched polyethyleneimine with Mw ~ 800 (g/mol)**
CA	**Citric acid**
C-dots	**Carbon dots**
CF	**Carbon fiber**
CLSM	**Confocal laser scanning microscope**
CNTs	**Carbon nanotubes**
CQDs	**Carbon quantum dots**
CU-dots	**Carbon dots prepared from citric acid/urea mixture**
CVD	**Chemical vapor deposition**
DEF	**Diethylformamide**
DIEA	**N-ethyldiisopropyleamine**
DLS	**Dynamic light scattering**
DMAC	**Dimethylacetamide**
DMEM	**Dulbecco's modified eagle medium**
DMF	**N,N-dimethylformamide**
DMSO	**Dimethyl sulfoxide**
DOX	**Doxorubicin**
DPP	**Diketopyrrolopyrrole**
E. coli	***Escherichia coli***
EA	**Ethanolamine**
EDA	**Ethylenediamine**
EDTA	**Ethylenediaminetetraacetic acid**
EPR	**Enhanced permeability and retention**
FBS	**Fetal bovine serum**
FL	**Fluorescence lifetime**
FTIR	**Fourier transform infrared spectroscopy**
GO	**Graphene oxide**

GOQDs	Graphene oxide quantum dots
GQDs	Graphene quantum dots
GQDs-Amin	Amine-functionalized Graphene quantum dots
GQDs-Chlor	Chlorine-functionalized Graphene quantum dots
GQDs-Imid	Imidazole-functionalized Graphene quantum dots
HOMO	Highest unoccupied molecular orbital
HRTEM	High-resolution transmission electron microscopy
IPCA	Imidazo-[1,2-a] pyridine-7-carboxylic acid
IRF	Instrument response factor
LED	Light emitting diode
LIS	Lisinopril
LUMO	Lowest unoccupied molecular orbital
MB	Methylene blue
MetHb	Methemoglobin
MPD	M-Phenylenediamine
MTT	3-(4,5-dimethylthiazolyl-2)-2,5-diphenyltetrazolium bromide
MWCNTs	Multi-walled carbon nanotubes
MWCO	Molecular weight cut-off
N, S-C-dots	Nitrogen and sulfur co-doped carbon dots
N-C-dots	Nitrogen-doped C-dots
N-GQDs	Nitrogen-doped graphene quantum dots
NIR	Near infra-red
OPD	O-Phenylenediamine
PAA	Poly(acrylic acid)
PAI	Photoacoustic imaging
PBS	Phosphate-buffered saline
PDT	Photodynamic therapy
PEG200	Polyethylene glycol with MW=200 (g/mol)
PEG400	Polyethylene glycol with MW=400 (g/mol)
PEG800	Polyethylene glycol with MW=800 (g/mol)
PEI	Polyethyleneimine

PL	**Photoluminescence**
PMMA	**Polymethylmethacrylate**
PPEI	**Propionylethylenimine**
PpIX	**Protoporphyrin IX**
PTT	**Photothermal therapy**
QCE	**Quantum confinement effect**
QY	**Quantum yield**
RhB	**Rhodamine B**
ROS	**Reactive oxygen species**
S. aureus	***Staphylococcus aureus***
SEM	**Scanning electron microscopy**
SLN	**Sentinel lymph nodes**
SQDs	**Semiconductor quantum dots**
STEM	**Scanning-transmission electron microscopy**
SWCNTs	**Single-wall carbon nanotubes**
TEM	**Transmission electron microscopy**
TPP	**Triphenylporphyrin**
UV-Vis	**Ultraviolet-visible spectroscopy**
Van	**Vancomycin**
XRD	**X-ray powder diffraction**
ζ-potential	**Zeta potential**
λ_{em}	**Emission wavelength**
λ_{ex}	**Excitation wavelength**
τ	**Lifetime component**
τ_{avg}	**Average fluorescence lifetime**

Chapter 1:   Introduction

1.1. Overview of nanomaterials

Nanotechnology focuses on the creation, synthesis, characterization, and application of innovative nanomaterials, which are materials exhibiting at least one dimension that measures 1-100 nanometers [1]. The past decade has witnessed significant attention directed toward nanomaterials owing to their extensive utilization across various domains including electronics, sensors, catalysis, photonics, microfluidic lateral flow devices, pharmaceutics, and medical diagnostics [2]. The ability to engineer nanomaterials with specific shapes, sizes, and structures is achievable by selecting appropriate synthesis methods and adjusting manufacturing parameters.

Nanomaterials are classified based on their dimensional attributes—zero-dimensional (0D), one-dimensional (1D), two-dimensional (2D), and three-dimensional (3D)—wherein 0D nanomaterials encompass all dimensions at the nanoscale, while 1D, 2D, or 3D materials exhibit one, two, or three dimensions at the macroscale, respectively. This classification system is closely tied to electron movement within nanoscopic materials. In 0D nanomaterials, electrons are confined within dimensionless spaces, while in 1D materials, electrons are able to move along a single axis measuring less than 100 nm. In 2D and 3D nanomaterials, electron movement extends across the x,y-axes and x,y,z-axes, respectively. However, the spotlight largely rests on zero-dimensional nanoparticles, which are categorized as organic, inorganic, or hybrid, contingent upon their inherent components. Inorganic nanoparticles are constructed from diverse inorganic constituents, organic nanoparticles are composed of basic polymeric building blocks, such as C-dots, and hybrid nanomaterials enclose engineered nanoparticles, like carbon-coated magnetic nanoparticles [3]. Notably, the nanoscopic dimensions of nanoparticles enable them to easily traverse bacterial and mammalian cells (Figure 1), rendering them highly promising for diverse biomedical applications. These applications range from functioning as fluorescent nanoprobes for imaging bacteria or cancer cells to serving as highly efficient nanocarriers with exceptional loading capacities for targeted drug delivery systems [4].
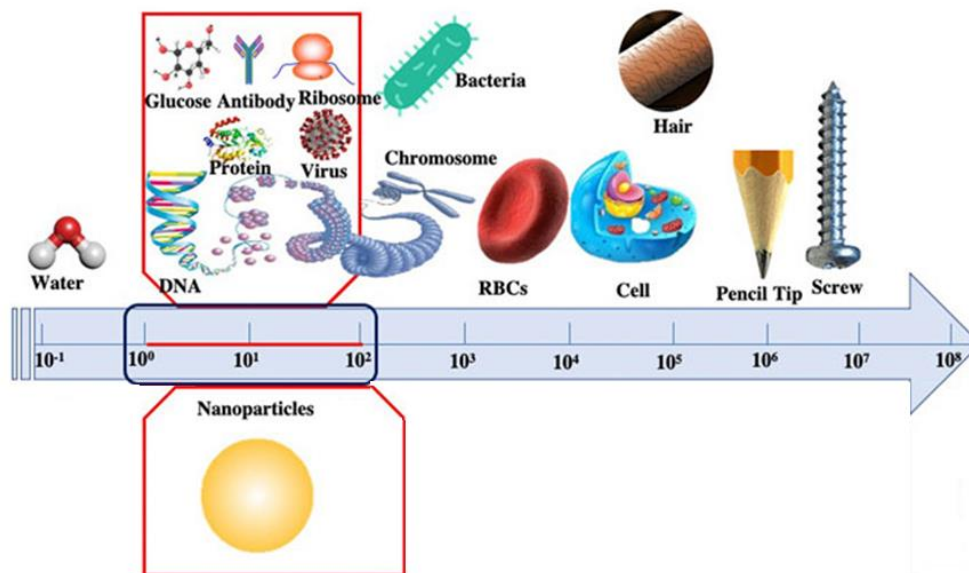
Figure 1. Comparative size scale from macroscale to nanoscale represented by different objects. [5]

1.2.   History of carbon nanomaterials

The origin of carbon nanomaterials can be traced back to 1985 (Figure 2). The discovery of fullerenes by Harold Kroto, Robert Curl, and Richard Smalley, awarded them the Nobel Prize in Chemistry in 1996 [6]. Fullerenes, such as C_{60}, C_{70}, and other cage-like structures, were the first members of the carbon nanomaterial family to captivate scientific interest. These hollow, soccer ball-shaped molecules comprising carbon atoms exhibit remarkable mechanical, electrical, and optical properties [7]. Their discovery not only introduced a new class of carbon allotropes but also spurred intense research into other carbon-based nanostructures.

The subsequent groundbreaking revelation came in 1991 with the isolation of CNTs by Sumio Iijima [8]. CNTs, cylindrical arrangements of carbon atoms resembling rolled-up graphene sheets, quickly became a focal point in nanoscience due to their exceptional strength, electrical conductivity, and thermal stability [9]. The two main types of CNTs—SWCNTs and MWCNTs—captured attention for their potential applications in nanoelectronics, nanocomposites, and various other fields. Further advancements in carbon nanomaterials unfolded with the discovery of graphene, a one-atom-thick sheet of carbon atoms arranged in a hexagonal lattice, in 2004 by Andre Geim and Konstantin Novoselov [10]. This two-dimensional material exhibited extraordinary mechanical

20

strength, high electrical conductivity, and exceptional flexibility, opening up avenues for fundamental studies and technological innovation. Graphene's emergence led to extensive research into its properties and applications, ranging from flexible electronics to energy storage and biomedical devices.

Beyond fullerenes, CNTs, and graphene, the carbon nanomaterial family expanded to include various derivatives and hybrids. C-dots, zero-dimensional carbon-based nanoparticles with intriguing photoluminescent properties, emerged as a new frontier in nanomaterials research [11]. These fluorescent nanoparticles have found applications in bioimaging, sensors, and optoelectronic devices. Moreover, the development of carbon-based nanocomposites, integrating carbon nanomaterials with polymers, metals, or ceramics, showcased synergistic properties, combining the unique characteristics of each component for enhanced performance in diverse applications.
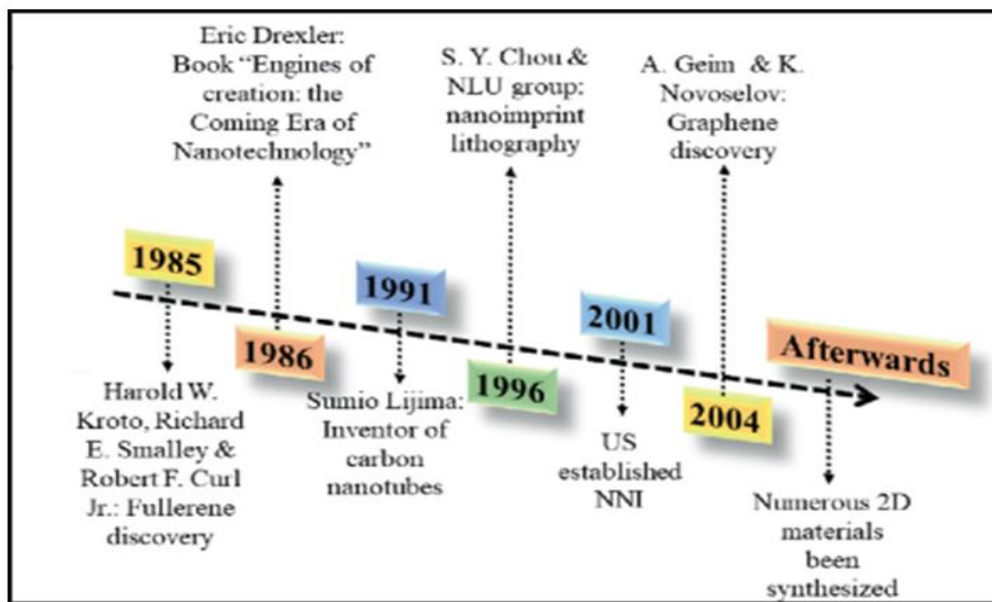
Figure 2. Schematic illustration of different structures of nanomaterials in the order of their discovery. [12]

1.3. Structure of C-dots

The composition and structure of carbon dots (C-dots) can vary significantly depending on their synthesis methods, offering a wide range of possibilities for designing different types of C-dots. Essentially, C-dots represent a diverse family of nanoscale systems, each capable of unique structural variations. The core of C-dots may exhibit crystalline or

amorphous characteristics, while the outer layer can accommodate various chemical groups, including both polar and nonpolar entities. These chemical groups may vary from small functional units to longer atomic chains. Some researchers have attempted to classify C-dots into subtypes to comprehend this diversity, although there is currently no widely accepted classification system in scientific literature. [13]. To help with this, we have proposed a classification scheme in Figure 3, which identifies the most relevant types of C-dots based on their unique core structures and shapes.

| Graphene Quantum Dots | Graphitic Carbon Dots | Amorphous Carbon Dots |
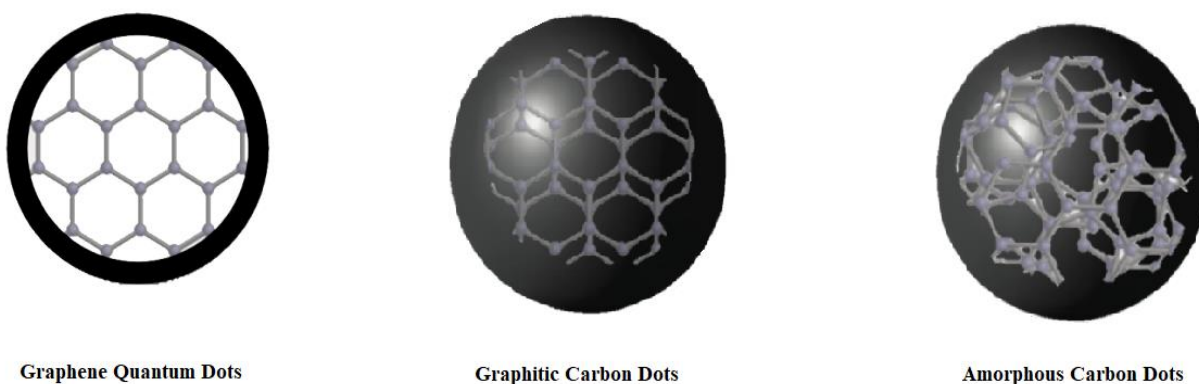
Figure 3. Characteristic C-dot structures.

Spherical-shaped graphitic C-dots are frequently encountered in the scientific literature [14], [15], [16], [17], [18], [19], [20], [21], [22], [23]. However, it's essential to acknowledge that comprehensive HRTEM studies confirming the presence of a graphitic monocrystalline structure in C-dots have only been accomplished by a limited number of studies [23], [24], [25]. Like graphite, the core of these dots consists of layers of carbon atoms arranged in a sp^2-hybridized configuration, stacked atop one another. The lateral dimensions of these layers are constrained by the overall diameter of the C-dot, typically spanning a few nanometers. The crystalline nature of the core is typically verified using various structural techniques, including HRTEM, XRD, and Raman spectroscopy. Figure 4 illustrates the visualization of the graphitic core through HRTEM measurements.
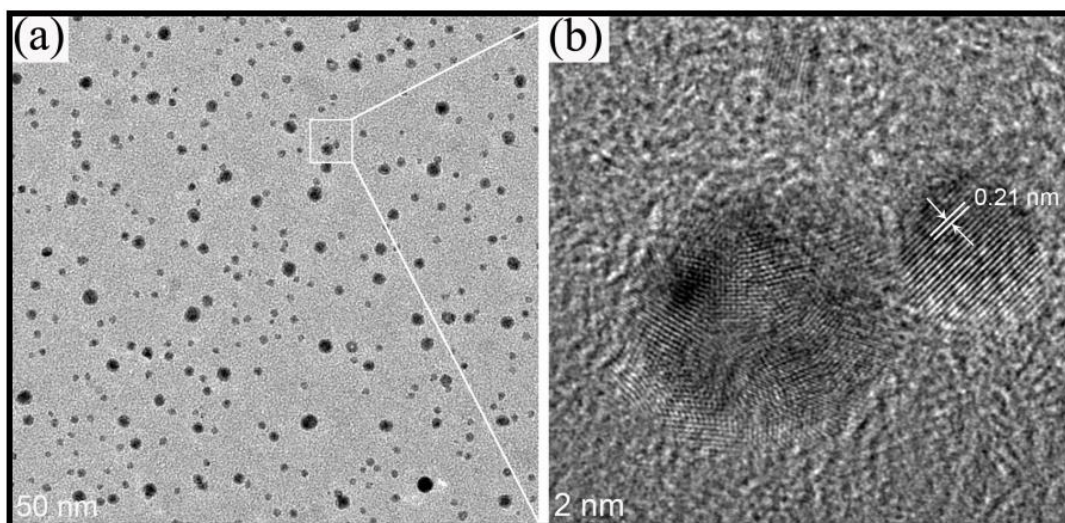
Figure 4. TEM (a) and HRTEM image (b) of C-dots with graphitic core structure; the average lattice spacing of these C-dots is 0.21 nm which is compatible with the (100) planes of graphite. [26]

In many instances, the utilization of HRTEM is commonly coupled with AFM. This combination of techniques proves essential for acquiring a comprehensive understanding of both the crystalline core structure and the three-dimensional morphology of C-dots. Moreover, it facilitates the differentiation between graphitic C-dots and graphene quantum dots (GQDs) [27], [28], [29]. It's important to emphasize that GQDs exhibit a distinct morphology; they take the form of small, layered disks composed of 1–3 layers of graphene stacked on top of each other, in contrast to the spherical nature of C-dots. While GQDs often share optical characteristics similar to those of spherical C-dots, our fundamental comprehension of GQDs remains an ongoing challenge. The scientific community continues to debate the extent to which GQDs should be considered as a truly distinct system separate from C-dots.

Moreover, in addition to the crystalline varieties, there exists a substantial body of evidence supporting the existence of amorphous C-dots [30], [31], [32], [33], [34], [35], [36]. These amorphous C-dots represent a distinct category characterized by a blend of sp^2 and sp^3 hybridized carbon atoms in variable proportions within their core. Notably, unlike their crystalline counterparts, amorphous C-dots lack long-range periodicity in their core structure. However, despite this structural distinction, they appear to share several noteworthy features with crystalline C-dots, such as their strong fluorescence properties. Within the realm of amorphous C-dots, a novel core structure has emerged in recent

studies, particularly in those C-dots synthesized through bottom-up approaches. This alternative core structure involves the aggregation of small molecules that typically form during the carbonization process of common precursors like citric acid (CA) (widely used in C-dot synthesis) [37], [38]. These aggregated molecules maintain a quasi-spherical shape due to relatively weak interactions, such as π-π stacking, hydrogen bonds, and Van der Waals forces.

1.4. Synthesis methods

In recent years, the preparation of carbon-based nanomaterials has been an active area of research, with numerous synthetic methods being developed. The methods can be broadly classified into two main approaches: top-down and bottom-up strategies.

In the top-down approach, larger carbon-based materials such as graphene sheets or CNTs are reduced in size through physical or chemical methods to create smaller nanomaterials like GQDs or nanotubes with smaller diameters. This method relies on the use of existing carbon precursors and involves breaking them down into smaller pieces, hence the name "top-down." The main advantage of the top-down approach is the ability to control the size and shape of the final nanomaterials. However, this method can also result in defects and damage to the carbon-based precursors, which can affect their properties.

On the other hand, the bottom-up approach involves the formation of carbon nanomaterials from smaller organic or inorganic molecules through chemical reactions. This method involves the formation of chemical bonds to build up the carbon-based materials from smaller building blocks, hence the name "bottom-up." The main advantage of the bottom-up approach is the ability to precisely control the chemical composition and properties of the final nanomaterials. However, this method can also be more challenging in terms of scalability and reproducibility.

Several studies have investigated the synthesis of carbon nanomaterials using both top-down and bottom-up approaches. For instance, one study reported the synthesis of GQDs using a top-down approach by using GO as a precursor and reducing it through a hydrothermal method [39]. Another study reported the synthesis of CNTs using a bottom-up approach by using a catalytic CVD method with acetylene as a carbon source.

In summary, the choice of the synthesis method depends on the desired properties of the final carbon nanomaterials and the availability of starting materials. Both top-down and bottom-up approaches have advantages and limitations, and researchers continue to investigate new methods to improve the synthesis and properties of carbon nanomaterials.

1.4.1. Top-down approaches

1.4.1.1.   Laser ablation

Laser ablation represents a method for the efficient fabrication of nanostructures through the utilization of laser irradiation, resulting in minimal by-product generation. In this process, a high-intensity laser beam is employed to penetrate the surface of a material and selectively remove a specific amount of it. The extent of material removal depends on factors such as the material's refractive index and the wavelength of the laser beam. When the laser interacts with the material's surface, it generates a strong electric field, leading to the expulsion of surface electrons. These expelled electrons subsequently undergo collisions, transferring energy to the atoms within the bulk material. As a consequence, the material's surface experiences heating, leading to vaporization. The vaporized particles can then either condense into particles without undergoing chemical reactions or aggregate into clusters. These condensed particles or clusters are subsequently collected and deposited in a collector equipped with a filtration system [40].

Following its discovery, this method has undergone extensive investigation for the fabrication of nanoscale materials. Suda's group utilized the laser ablation technique with an ArF laser beam assisted by inductively coupled plasma to create a thin film composed of carbon nanoparticles, 10 nm in size and with a clustered spherical shape [41]. This pioneering study on carbon nanoparticles spurred extensive research into employing laser ablation for the synthesis of C-dots. Li et al. employed a laser rapid passivation technique (Nd: YAG pulsed laser, 30Hz) to create GQDs, with an average size of 20 nm) out of a carbon suspension (consisting of 50 nm nanoparticles) with visible, stable, and adjustable PL performance [42]. They demonstrated that laser irradiation-induced passivation plays a significant role in the origin of PL, as illustrated in Figure 5a. Sun et al. were among the early investigators to explore C-dot synthesis through laser ablation,

using graphite powder as their carbon source (Figure 5b) [43]. Initially, they produced a heterogeneous blend of carbon nanoparticles without PL properties, indicating that the carbon core consisted of sp^3 hybridized carbon atoms. Subsequently, they passivated the nanoparticles with PEG and poly (propionylethylene-imine-co-ethyleneimine) to transform them into photoluminescent C-dots. Similarly, Hu et al. introduced a simple method for producing fluorescent carbon nanoparticles through laser ablation of suspensions containing graphite powders in organic solvents (diamine hydrate, diethanolamine, and PEG200N) (Figure 5c) [44]. The resulting GQDs' surface properties could be altered by selecting appropriate solvents, thereby enabling tunable PL emission by modifying their surface functional groups. Kang proposed a swift preparation method for synthesizing GQDs from MWCNTs via laser exfoliation, resulting in GQDs with excellent optoelectronic properties and a high PL QY of 12% (Figure 5d) [45].
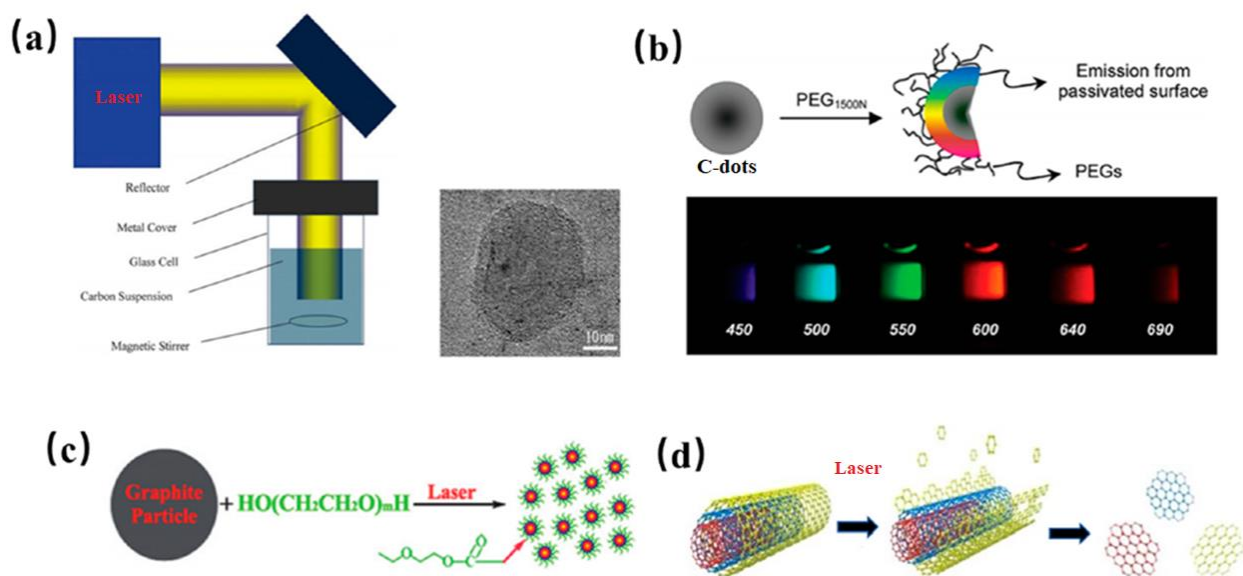
Figure 5. Schematic representations of (a) laser-induced passivation of carbon particles for GQD synthesis [42], (b) the production of GQDs via graphite laser ablation [43], (c) laser irradiation of a carbon powder suspension in PEG200N, [44] and (d) Schematic illustration of possible mechanism pulsed laser exfoliation of MWCNTs to GQDs [45].

1.4.1.2.   Chemical exfoliation

Chemical exfoliation provides an efficient and straightforward approach for the large-scale production of high-quality C-dots without the need for complex equipment. This method

involves subjecting precursor carbon materials such as CFs, GO, or CNTs to the action of potent acids or oxidizing agents.

In 2007, Liu's group pioneered the creation of luminescent GQDs of varying sizes using HNO_3 at relatively high temperatures, starting from candle soot [46]. Furthermore, Peng and his team produced GQDs (1-4nm) through chemical exfoliation of CFs using a combination of H_2SO_4 and HNO_3 [47]. These GQDs exhibited distinct yellow, green, and blue PL emissions at different synthesis temperatures (80, 100 and 120 °C, respectively), highlighting the successful generation of GQDs through the chemical cleavage of CFs. Additionally, Zhao et al. employed asphaltene, H_2SO_4 and HNO_3 under reflux at 100 °C, to create GQDs that had an average size of 2.5 nm and exhibited excitation-dependent PL (Figure 6a) [48]. Moreover, Gunjal et al. employed concentrated H_2SO_4 to cleave green tea leaf residue, resulting in the synthesis of N-GQDs with a QY of 2.5% [49]. In another approach, Sun et al. introduced an acid-based method for the preparation of fluorinated GQDs using carbon derived from fluorinated GO and a low volume of H_2SO_4/HNO_3 (Figure 6b) [50]. Additionally, Soni et al. synthesized graphitic N, S-C-dots (4-10 nm) with bright, excitation independent green PL emission through triflic acid cleavage of palm shell powder [51]. Desai et al. used H_2SO_4 and H_3PO_4 as oxidizing agents to prepare CQDs from muskmelon fruit (Figure 6c) [52]. The FL properties of CQDs were tuned by controlling the experimental conditions that allow them to emit different colors: blue, green, and yellow, with different λ_{em}= 432, 515, and 554 nm at λ_{ex} =342, 415, and 425 nm, respectively. The sizes of blue, green, and yellow CQDs were found to be 3.5, 4.3, and 5.8 nm, respectively. In addition, their QYs were 7, 27, and 14%.
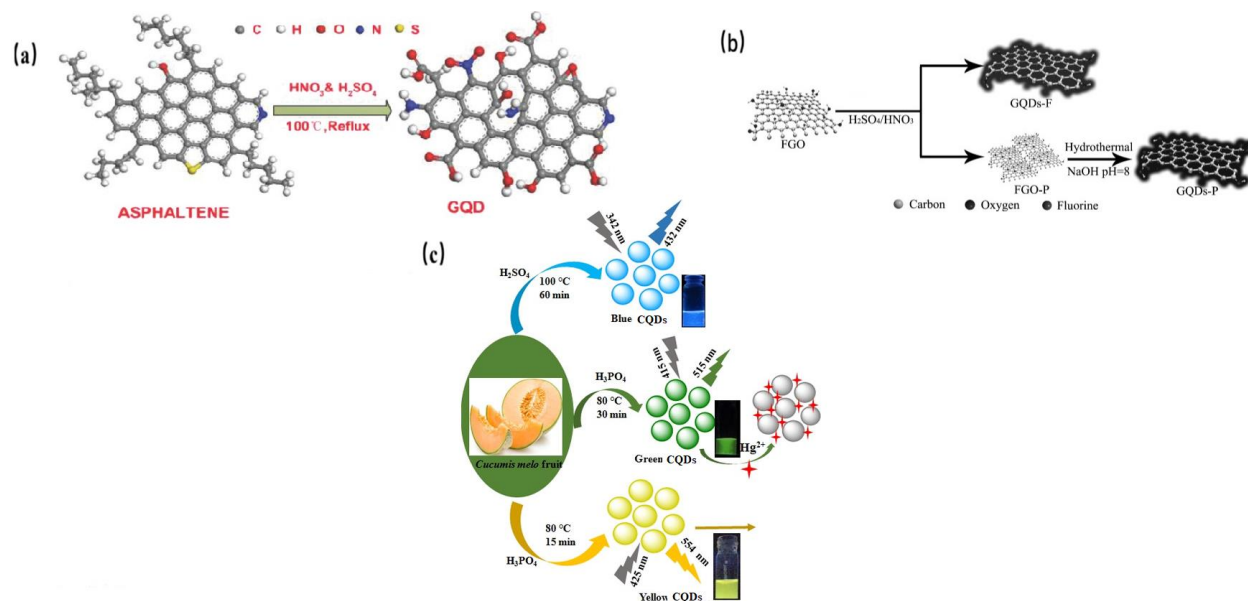
Figure 6. The process of chemical exfoliation for generating C-dots using as precursors: a) asphaltene [48], b) Fluorinated GO (FGO) [50] and c) Muskmelon fruit [52].

Indeed, aside from strong acids, various potent oxidizing agents have been employed in the production of C-dots. For instance, Kailasa et al. used H_2SO_4 as an oxidizing agent to chemically oxidize tomatoes, resulting in the creation of blue, green, and yellow, fluorescent GQDs [53]. These GQDs were subsequently utilized for detecting Fe^{3+} ions with a low detection limit of up to 0.016 μM, enabling the quantification of Fe^{3+} ions in iron supplements and biofluids. Nair et al. demonstrated that GO can be oxidized by $KMnO_4$ for 30 min and produce GQDs with a QY of 23% [54]. Moreover, Zhu et al. employed H_2O_2 as a mild oxidant to oxidize GO and produce GQDs with the assistance of $W_{18}O_{49}$ nanowires, and the size of the resulting GQDs (4-21 nm) was dependent on the concentration ratio of $W_{18}O_{49}$ and H_2O_2 [55]. Compared to acid-based oxidizing agents, the use of mild oxidants eliminates the need for further purification, making the acid-free strategy a simpler and more environmentally friendly approach, suitable for applications in bioimaging.

1.4.1.3. Electrochemical oxidation

Electrochemical oxidation stands as one of the most employed methods for crafting C-dots, offering several merits such as cost-effectiveness, high purity, substantial yield, size control, and reliable reproducibility [56]. The characteristics of C-dots, including their PL

and surface properties, are significantly influenced by two essential factors: the electrodes and the electrolyte.

Liu et al. generated C-dots through direct electrochemical oxidation of a graphite electrode in alkaline alcohols (ethanol/NaOH) at 5V for 3h, which showed an average diameter of (4 ± 0.2) nm and notable crystalline quality [57]. Interestingly, these C-dots, when initially prepared at 4°C, exhibit a colorless appearance, but their dispersion gradually changes when stored at room temperature, a phenomenon attributed to increased oxidation at higher temperatures. In another approach, Hou et al. synthesized C-dots by subjecting sodium citrate and urea to electrochemical oxidation for 1h at 5V using two platinum sheets as electrodes (1.5×2 cm^2). These resultant C-dots possessed commendable photostability under different pH values, boasting a QY of 11.4% and sizes ranging from 1.0 to 3.5 nm [58]. Ahirwar et al. devised a method to fabricate both GQDs and GOQDs using a combination of CA and NaOH as an electrolyte (Figure 7a) [59]. GQDs were synthesized through a reaction involving CA and NaOH, while four distinct types of GOQDs with adjustable oxygen-containing groups were prepared by varying the concentration of alkali while keeping CA concentration constant. The general process included inducing defects in graphite rods at elevated temperatures, followed by the intercalation of OH$^-$ ions, oxygen generation, and exfoliation. The average size of the resulting GQDs and GOQDs was found to be in the range of 2–3 nm, exhibiting blue to green emission when excited with 365 nm UV-light. Subsequently, Huang et al. generated GQDs (3-8 nm) from graphene paper using ammonia solution as a weak electrolyte to disintegrate the graphene sheets and introduce nitrogen doping into their structure [60]. The reaction yield for GQD production in a weak electrolyte was approximately 28% higher compared to that in a strong electrolyte, mainly due to enhanced cleavage efficiency. However, the rigorous electrochemical reaction in the NaOH electrolyte led to rapid consumption of the anode within 30 minutes, resulting in only a small proportion of graphene being converted to GQDs (Figure 7b).
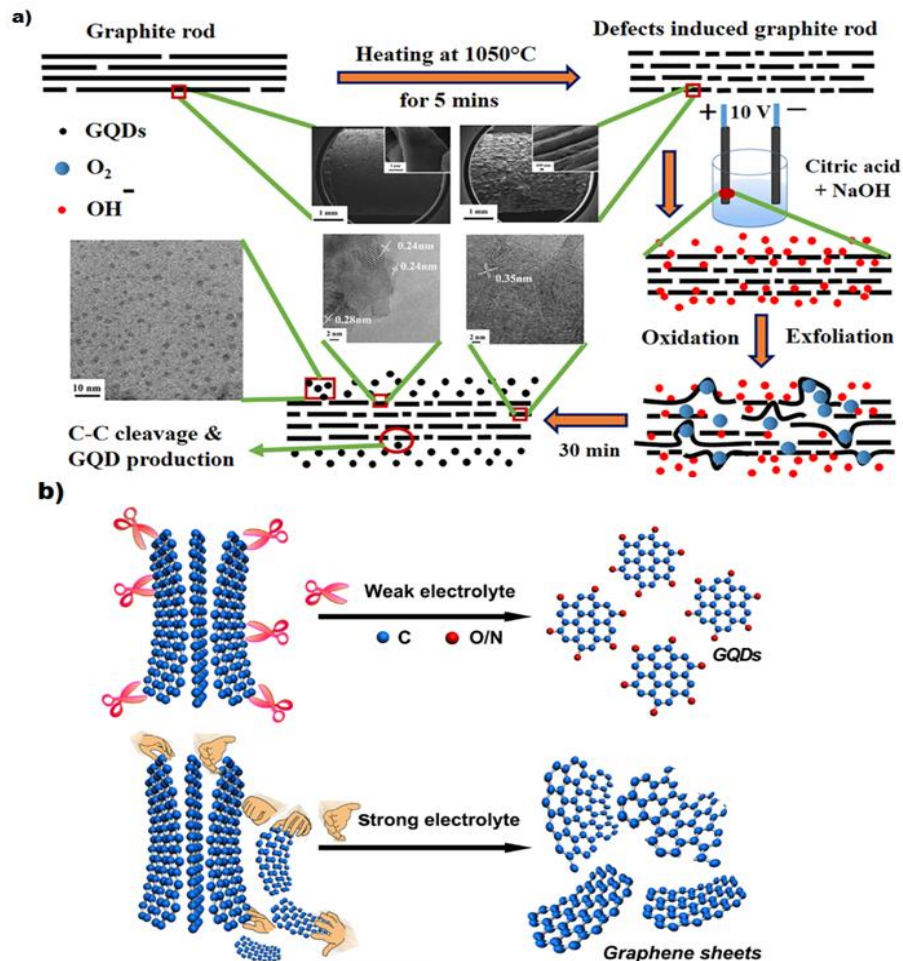
Figure 7. a) Electrochemical exfoliation of graphite rods that involves the intercalation of OH⁻ ions, the generation of O_2, and exfoliation, ultimately leading to the creation of GQDs [59]. b) A schematic illustration of GQDs production in both strong and weak electrolyte solutions [60].

Joffrion et al. synthesized GQDs (2-4 nm) exhibiting excitation-independent emission characteristics from a graphite rod within a glucose-water solution using a green electrochemical method [61]. This process entailed the decomposition of water and glucose for surface passivation. The λ_{em} of the GQDs experienced a redshift with increasing glucose concentration and longer processing times while their QY was found to be around 17.5 %. Furthermore, He et al. employed coke as an electrode in a one-pot electrochemical process to produce GQDs with a size ranging from 3 nm to 4.6 nm [62]. By adjusting the water content (40%) in the electrolyte (methanol) and the current density (30-240 mA/cm^2), they obtained GQDs with emissions ranging from green to orange. Subsequently, blue-emitting GQDs were derived by reducing the green GQDs using

NaBH$_4$. The QYs for the blue, green, yellow, and orange GQDs were measured at 19.3%, 8.5%, 7.9%, and 9.2%, respectively.

1.4.1.4.   *Ultrasonication*

Ultrasonic treatment stands out as an innovative method for synthesizing various nanostructures, like C-dots. This technique harnesses high-energy ultrasonic sound waves to break down substantial carbon sources into smaller components. In a liquid environment, these ultrasonic waves generate both high- and low-pressure regions, leading to the formation of tiny vacuum bubbles. These bubbles are uniformly dispersed and subjected to rapid liquid jet collisions, exerting potent hydrodynamic shear forces that overcome bonding forces and result in deagglomeration [63]. Consequently, these ultrasonic waves can reduce macroscopic carbon sources into nanoscale materials, contributing to C-dot formation. Moreover, the energy from ultrasonic waves aids in thoroughly mixing chemical constituents, facilitating their polymerization and carbonization, further promoting C-dot formation.

Zhuo et al. were pioneers in utilizing ultrasonic exfoliation of graphene to prepare 3 to 5 nm GQDs which exhibited an excitation-independent PL behavior and a QY of 3.4 % [64]. Since this groundbreaking work, numerous researchers have adopted ultrasonic-assisted techniques to synthesize GQDs from various carbon sources, including graphite, MWCNTs, GO, and CF, using both aqueous and organic solvents. For instance, Song et al. successfully produced GQDs by subjecting an aqueous dispersion of graphite and potassium sodium tartrate to ultrasonic treatment (Figure 8a) [65]. These GQDs had diameters ranging from 1 to 5 nm and emitted blue luminescence at 400 nm under λ_{ex}=310 nm. Dang et al. achieved a significant milestone by scaling up the production of C-dots by subjecting oligomer-polyamide resin to ultrasonic waves, resulting in 3 nm C-dots exhibiting an impressive QY of 28.3% [66]. Intriguingly, researchers have extended the ultrasonic approach to create heteroatom doped GQDs. For example, Huang et al. synthesized chlorine doped GQDs through direct ultrasonic exfoliation of a chlorinated CF precursor (Figure 8b) [67]. The GQDs had a size of 3-10 nm and showed excitation-dependent behavior. Zhang et al. developed 5-7 nm N-C-dots and prepared BiOBr/N-C-

dot nanocomposites, which showed enhanced visible-light photoactivity and photostability, via a facile ultrasonic treatment [68].
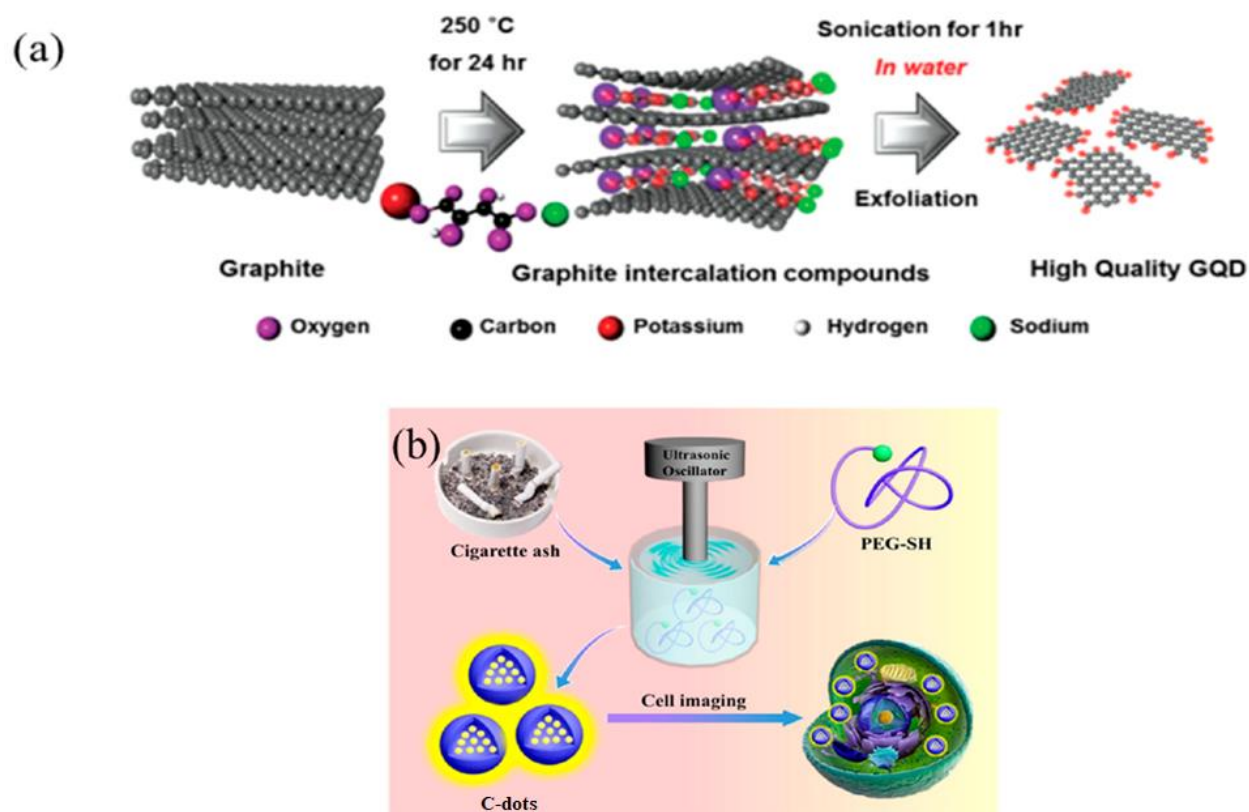
Figure 8. (a) Schematic illustration of the preparation of GQDs using graphite and potassium sodium tartrate as precursors [65]. (b) The process of fabricating PEG-functionalized GQDs through ultrasonic-assisted treatment [67].

1.4.2. Bottom-up approaches

1.4.2.1. *Chemical Vapor Deposition*

CVD is a well-established technique, which has gained widespread use in recent years for the fabrication of C-dots. This approach allows for precise control over the size of the resultant materials by manipulating various parameters, including the carbon source, growth time, hydrogen (H_2) flow rate, and substrate temperature.

A study by Fan et al. introduced the application of the CVD method for C-dot synthesis, utilizing CH_4 as the carbon source, as depicted in Figure 9a [69]. The process involved initial cleaning of oxidation groups on a copper foil surface using alcohol and HCl.

Subsequently, hydrogen residues were removed by continuous argon (Ar) supply. CH_4 was then introduced into the furnace at a flow rate of 2 mL/min for a brief duration of 3 seconds in an Ar environment. The resulting C-dots exhibited a size distribution in the range of 5–15 nm, indicating their successful preparation. In a recent approach, Ding et al. used hexagonal boron nitride as a substrate for GQDs, eliminating the need for a metal catalyst [70]. The number of GQDs was modulated by adjusting the ratio of Ar to CH_4 and H_2 gases, demonstrating thickness-dependent PL emissions in the visible region. Interestingly, carbon sources such as chitosan were employed to produce N-GQDs through a CVD method on a copper foil [71]. The obtained N-GQDs, characterized by an average diameter of 12 nm and a thickness of 3 nm via DLS analysis and AFM height profiling (Figure 9b), exhibited intense PL emission in the visible region. In 2016, single-crystalline GQDs were synthesized on a silicon wafer, featuring an average thickness of 1.2 nm and an average diameter of 7.5 nm [72].
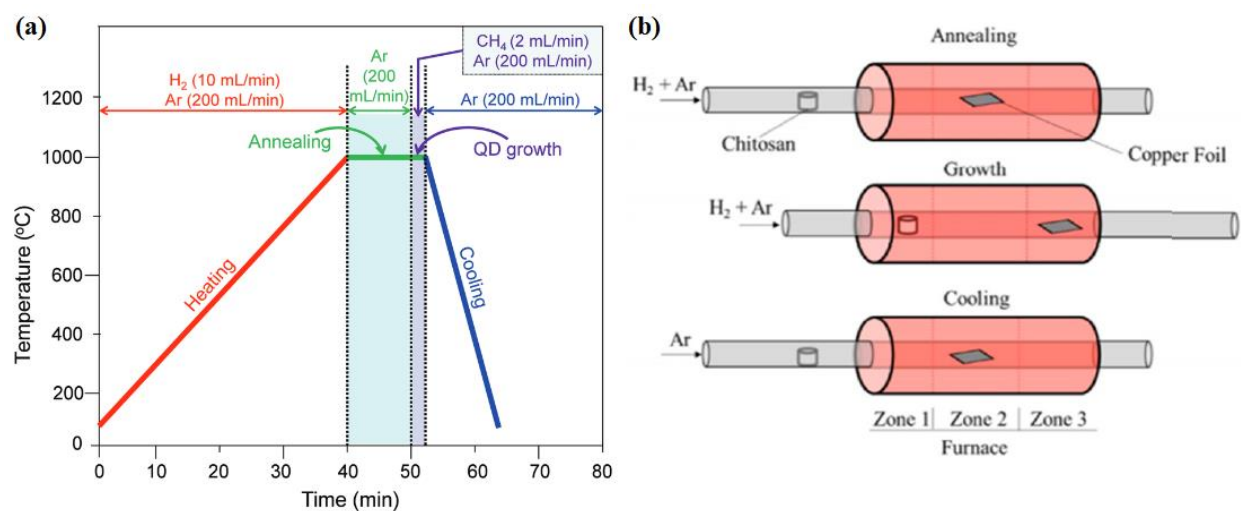
Figure 9. (a) CVD process for C-dot growth using CH4 as a precursor in an Ar environment [69], (b) Synthesis of N-GQDs through a CVD procedure using chitosan as the precursor [71].

1.4.2.2. Pyrolysis

In the process of pyrolysis, organic chemical compounds undergo dehydration and carbonization at extremely high temperatures to yield C-dots. This thermal decomposition method offers several advantages, including the ability to produce C-dots on a large scale, cost-effectiveness, and a fast and straightforward synthesis process [73], [74]. However, it's important to note that the resulting C-dots may exhibit non-uniform sizes

[73]. C-dots have been prepared through pyrolysis of various small organic compounds, including but not limited to CA [75] and glucose [76].

Zhao et al. synthesized GQDs using L-glutamic acid as a precursor, which was heated to 210 °C with a heating mantle, via a solvent-free pyrolysis method [77]. These GQDs exhibited a high QY of 54.5% (λ_{ex}=360 nm) and displayed blue, green, and red emissions when excited with ultraviolet, blue, and green light, respectively. In detail, when the GQDs were excited at 360 nm, they showed a strong FL peak at 440 nm. In addition, the fluorescence emission spectra showed an excitation-dependent manner. The emission peak of GQDs shifted from 415 nm to 580 nm, when the λ_{ex} changed from 320 nm to 540 nm. In a separate study, Kalita et al. produced GQDs with varying sizes (2-6.5 nm) using rice grains as a precursor through one-pot pyrolysis at 200 °C different heating durations (3 - 10 minutes) [78]. The synthetic procedure involved the breakdown of starch into glucose oligomers due to heat, followed by the carbonization of glucose oligomers at high temperatures, and growth of conjugated domains during pyrolysis. Interestingly, the emission of these GQDs exhibited a red shift with increasing particle size from 2 nm to 6.5 nm, attributed to QCE. However, their QY decreased from 24% to 16% with larger particle sizes.

CA is a commonly used and cost-effective precursor in the bottom-up approach for C-dot synthesis [79], [80], [81]. Li et al. developed N-doped C-dots with a high QY of 69% using CA and EDA in water through a one-pot pyrolysis process (120 °C for 48h) [82]. The synthesis process involved the dehydration and amide formation reaction between carboxyl groups of CA and amino groups of EDA, resulting in the production of a fluorescent molecule (IPCA). This IPCA compound was extracted from the synthesized N-C-dots, using ethyl acetate and rotary evaporation, and characterized by UV-vis and PL spectroscopy. By varying the reaction time (24, 48, and 72 hours), they achieved QYs of 71.1%, 65.5%, and 64.8%, with 48 hours being sufficient for N-C-dot formation, while 24 hours resulted in the production of N-CQDs with a QY higher than that at 48 hours but lower than that of IPCA (81.5%). The proposed formation mechanism involved dehydration, amide formation, pyrolysis, and polymerization, leading to the creation of N-doped aromatic domains via carbonization. In another green one-pot pyrolysis approach,

C-dots were synthesized using CA and glycine for 1 h at 180°C in air atmosphere, without the use of solvents [83]. Varying the molar ratio of CA to glycine at 28% and 54% resulted in C-dots with blue and green emissions and QYs of 84 % and 63 %, respectively. Their size decreased from 4.1 nm to 3.5 nm as the molar ratio of CA increased. The blue emission was attributed to surface states of the particles, while the green emission was linked to a higher degree of amidation and sp^3 hybridization graphitic domains. Furthermore, excitation-dependent C-dots, with an average size of 3.6 nm, were synthesized through pyrolysis of uric acid at 225 °C for about 30 min under the air atmosphere, yielding particles with a QY of 52 % [84]. These C-dots served as a promising fluorescence probe for detecting Ag^+ ions by quenching particle emission. Lastly, C-dots were prepared by Wei et al. via the thermal treatment of gynostemma without the use of any additional reagents [85]. These C-dots were soluble in water, had a diameter of 2.5 nm, exhibited blue emission after being excited by a 365 nm UV lamp (λ_{em}= 420 nm) and had a QY of 5.7 %. Notably, their emission was excitation-dependent, with increasing λ_{ex} resulting in a red shift in emission.

1.4.2.3. *Hydrothermal and solvothermal*

1.4.2.3.1. Hydrothermal method

Hydrothermal carbonization is a widely employed, environmentally friendly, and cost-effective method for crafting C-dots from various organic sources such as organic acids, saccharides, fruit juices, and discarded fruit peels [86], [87], [88]. Typically, this process involves sealing mixtures in an aqueous solution in a Teflon container, immersing it in an oven, and subjecting it to high pressure and temperature conditions [89], [90], [91], [92], [93], [94], [95].

In addition to traditional precursors, researchers have explored the use of waste biomass as carbon sources. For example, Krysmann et al. employed an environmental approach to create 2-5 nm, excitation-dependent C-dots through an acid oxidation method using unprocessed biomass as the carbon source [96]. Their method involved thoroughly mixing fresh grass with water and heating the mixture to 300°C over a period of 4 hours. Subsequently, the resulting carbon material was dispersed in water and subjected to

reflux with a 3M HNO$_3$ solution for an additional 48 hours. Mehta et al. developed a plant-based hydrothermal method (120 °C for 180 min in ethanol) to synthesize water-soluble fluorescent CQDs derived from Saccharum officinarum juice [97]. These CQDs, with an average size of approximately 3 nm and a QY of 5.6 %, were employed for the selective and sensitive detection of Cu^{2+} (Figure 6a). Similarly, Lu et al. suggested a hydrothermal approach to produce CQDs using pomelo peel in a Teflon-lined autoclave, that was heated at 200 °C for 3 h. The CQDs had an average particle size of 4 nm, exhibited a QY of 6.9% and were employed for the sensitive detection of Hg^{2+} in lake water samples [98]. Sahu et al. synthesized CQDs using a one-step hydrothermal method. They mixed orange juice with ethanol, and then the mixture was transferred into a Teflon-lined stainless-steel autoclave and heated at 120 °C for 150 min. The diameter of CQDs ranged from 1.5 to 4.5 nm, while they demonstrated tunable PL properties (QY of 26 %) and excellent biocompatibility (Figure 6b) [99]. Additionally, Huang et al. employed strawberry juice to generate N-doped CQDs through a cost-effective and environmentally friendly solvothermal method (in a Teflon-lined autoclave at 180 °C for 12 h) [100]. These CQDs, with a nitrogen content of 6.9 %, exhibited a maximum emission at 427 nm with a QY of 6.3 % and were utilized for the selective and sensitive detection of Hg^{2+} (Figure 6c). Liu et al. suggested a straightforward and low-cost synthesis route for CQDs by heating bamboo leaves in a Teflon-lined autoclave at 200 °C/6h, which exhibited a remarkably high PL QY of 7.1% [101]. These CQDs, averaging a size of 3.6 nm, were functionalized with branched-PEI for the sensitive and selective detection of Cu^{2+} in river water (Figure 6d). Li et al. successfully produced C-dots, using grape skin through a hydrothermal treatment in a Teflon-lined autoclave at 190 °C for 3 hours, that had an average size of 4 nm, exhibited green emission (λ_{em}=522 nm at λ_{ex}=430 nm), excitation-dependent properties, and a high QY of 8.7% [102]. The C-dots were also sensitive to the detection of picric acid. Moreover, Atchudan et al. employed kiwi peels and aqueous ammonia as the precursors for biowaste-derived C-dots (heating in a Teflon-lined stainless-steel autoclave at 200 °C for 24 h) [103]. The 5 nm C-dots were hydrophilic, featured surface functionalities such as -OH, -CN, and -COOH, and displayed a QY of 18% and excitation-dependent emission, making them suitable for cell imaging applications. Coffee beans and grounds, known as valuable carbon sources, have also been utilized for the

production of C-dots [104]. Zhang et al. developed C-dots from coffee beans using water as a solvent by heating in a Teflon-lined autoclave at 180 °C for 12 h [105]. They had a diameter of 4.6 nm, exhibited excitation-dependent emission, and possessed a QY of 9.8%. Their high sensitivity to Fe^{3+} ions made them a potential candidate for use as Fe^{3+} indicators.
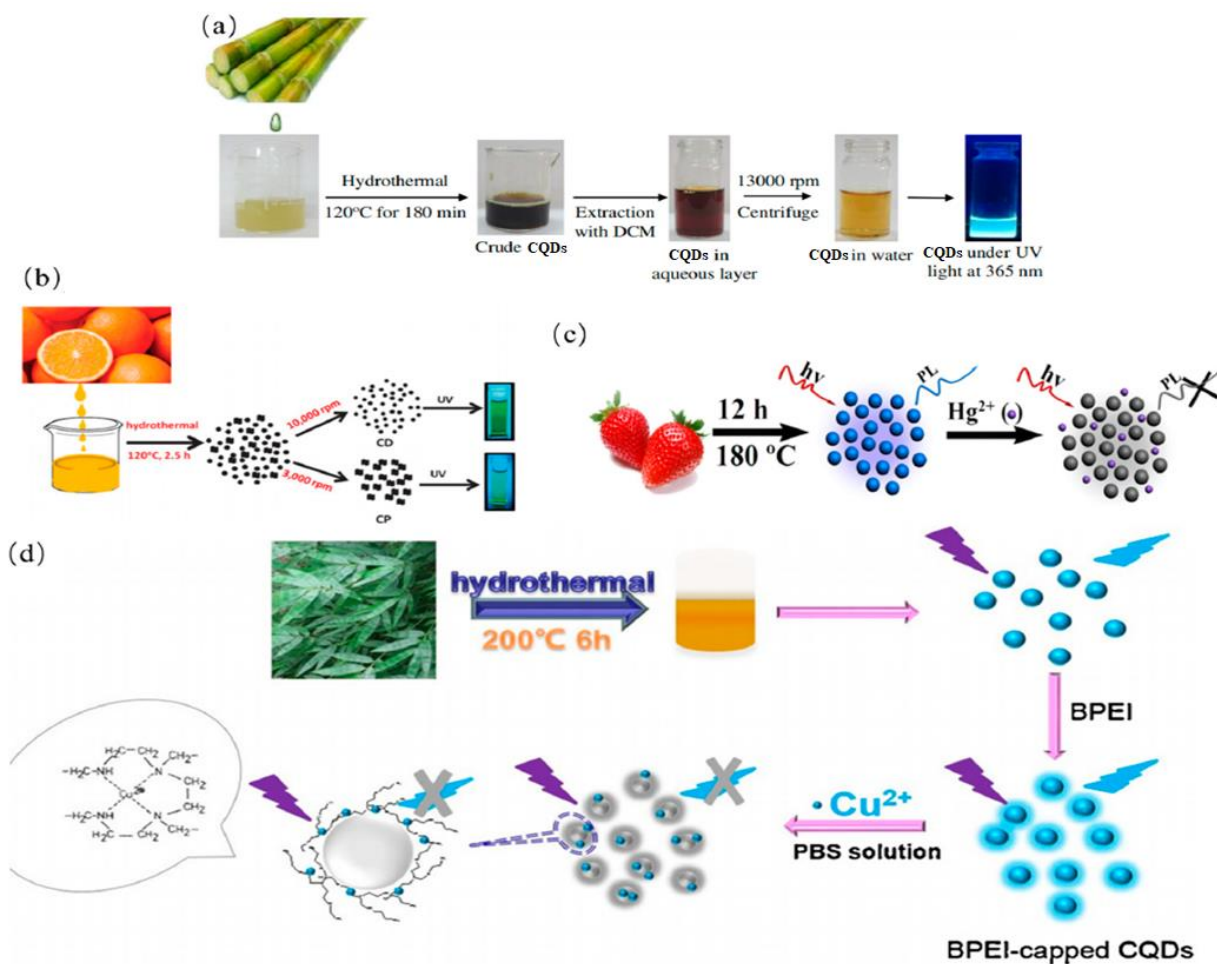
Figure 10. Schematic diagram of (a) Preparation process and application of the fluorescence C-dots from saccharum officinarum juice [97] (b) Preparation of soluble C-dots from orange juice [99] (c) Preparation of C-dots from strawberry juice [100] (d) Preparation of C-dots from bamboo leaves and functionalization with branched-PEI for the detection of Cu^{2+} [101].

CA stands out as one of the most widely used carbon sources in C-dot synthesis. Guo et al. synthesized N-CQDs using CA as a precursor, diethylenetriamine as a nitrogen source, and water as a solvent through a hydrothermal method (heating in a Teflon-lined autoclave at 180 °C for 10 h) [106]. The resulting particles had an average size of 3 nm,

featured a high QY of 85 %, and displayed excellent stability and photostability. Li et al. undertook the synthesis of C-dots from CA and PEI within a hydrothermal reactor at 110 °C for 2 hours [107]. Upon completion of the reaction, the carbon dot dispersion was purified by the addition of methanol, followed by centrifugation at 15,000 rpm for 10 minutes, resulting in uniform C-dots with a size of around 4.5 nm.

Moreover, tunable-color C-dots were produced using OPD as a precursor and KCl as a catalyst without the use of solvents [108]. The particles formed through the polymerization of OPD and subsequent carbonization, resulting in conjugated sp^2 domains whose size and nitrogen doping extent could be controlled by adjusting temperature and reaction time. They exhibited a QY of 56%, and their λ_{em} could be tailored by manipulating the size of the sp^2 conjugated domains and the degree of nitrogen doping. Qu et al. conducted the synthesis of C-dots using dopamine through a hydrothermal approach [109]. In this process, they heated a mixture of dopamine and water at a temperature of 180 °C for 6 hours. Following the reaction, centrifugation at 10,000 rpm for 10 minutes was employed to eliminate larger particles and obtain uniform C-dots with an average size of approximately 3.8 nm. Pan et al. introduced an environmentally friendly method for producing blue emissive (λ_{em}= 430 nm at λ_{ex}= 320 nm), 10 nm CQDs, using a hydrothermal process at 200 °C, in which the epoxy functional groups present on the surface of GO sheets undergo complete transformation into CQDs [110]. Chen et al. synthesized C-dots through hydrothermal treatment of lignin in the presence of H_2O_2 at 180 °C for 40 minutes [111]. Upon completing the reaction, they filtered the reaction mixture using a 0.22 μm membrane filter and subsequently conducted dialysis using a 3500 Da dialysis membrane for 2 days, yielding C-dots ranging in size from 2 to 10 nm. Halder et al. used a simple hydrothermal technique for generating GQDs by incorporating H_2O_2 (180 °C for 2 h), which accelerates the exfoliation of GO sheets, effectively acting as scissors during the hydrothermal process [112]. The GQDs had an average size of 5 nm and a PL QY of 4.6 %.

1.4.2.3.2. Solvothermal method

In addition to hydrothermal methods, solvothermal approaches for C-dot synthesis offer advantages such as cost-effectiveness and the use of basic equipment [113]. Unlike

hydrothermal processes, where water solutions are employed, solvents, either singly or in combination, are used in sealed Teflon containers within steel autoclaves [114], [115], [116]. The solvent and carbon source mixtures undergo reactions at elevated temperatures and pressures.

Shin et al. employed mild oxidation with oxone, a non-acidic mild oxidant, to chemically oxidize natural carbon sources (graphite, MWCNTs, CFs, and charcoal), resulting in GQDs with average sizes from 2nm to 8 nm, QYs of 5-8 % and blue PL (λ_{em}= 430 nm upon excitation with UV light at 365nm) (Figure 11a) [117]. Tian's group fabricated blue, fluorescent GQDs through solvothermal exfoliation of graphite aided by mild H_2O_2 in DMF (Figure 11b) [118]. These GQDs exhibited a high QY of 15% and demonstrated PL stability across various pH conditions. Qian et al. suggested a straightforward solvothermal approach to produce N-doped C-dots from a mixture of CCl_4 and diamines (2-ethylenediamine, 1,3-propanediamine, and 1,4-bu-tanediamine) at 200 °C [119]. Following dialysis, the purified C-dots (with sizes ranging from 6 to 15 nm) exhibited higher QYs (up to 36%) than many other C-dots, while showing great promise in selective and sensitive determination of pH, Ag^+, and Fe^{3+} in aqueous solutions. Sun et al. utilized a solvothermal method (at 160 °C for 8 h in a Teflon-lined stainless-steel autoclave) to synthesize full-color emitting C-dots using CA and urea with constant mass ratio (1:2) but adjusting concentrations in the reaction solvent (DMF) (Figure 11c) [120]. The resulting C-dots had sizes between 3.9 nm and 5 nm and QYs 33-48 %.
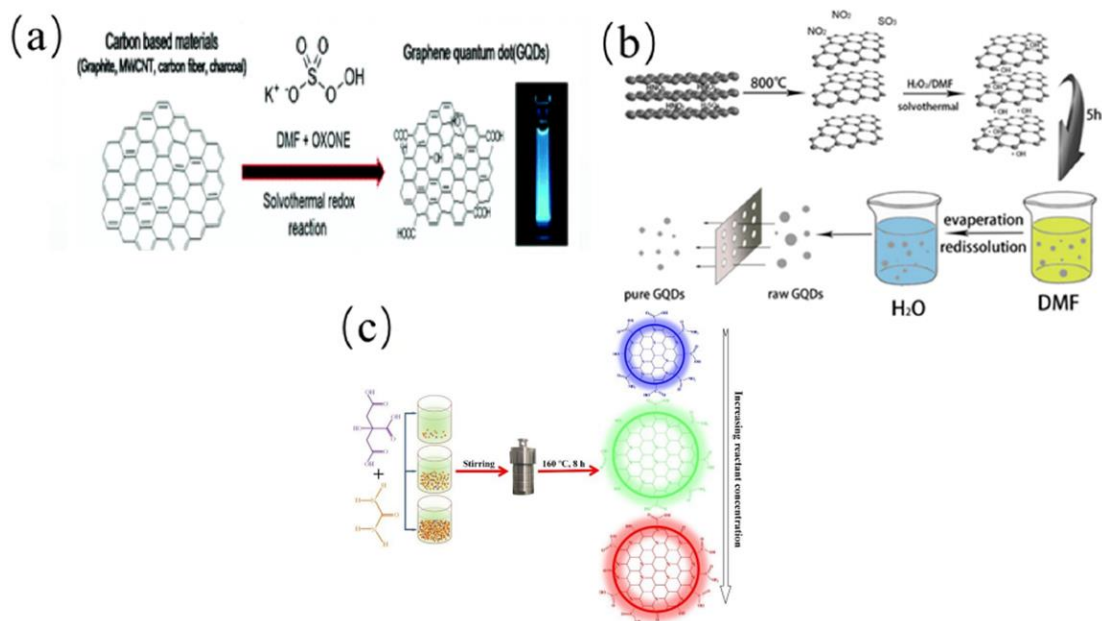
Figure 11. Several synthetic procedures for C-dots using solvothermal methods: (a) The solvothermal exfoliation of various carbon-based precursors (graphite, MWCNTs, CFs, and charcoal), via mild oxidation, to produce fluorescent C-dots [117], (b) Synthesis of C-dots from graphite in DMF [118], (c) Synthetic process responsible for generating full-color emitting C-dots in DMF [120].

Shen et al. synthesized three different types of C-dots utilizing trisodium citrate dihydrate and urea in three distinct solvents: DEF, DMAC, and DMF through a one-pot solvothermal reaction (heating at 160 °C for 4h) [121]. This approach yielded C-dots with adjustable solid-state emission colors, ranging from green to yellow-green and yellow, each exhibiting high QYs of 17.6%, 18.7%, and 21.6% in DMF, DMAC, and DMF, respectively. The synthesis mechanism suggested their formation via a chemical reaction between the reactants and the crystallization of excess trisodium citrate around the newly formed C-dots. Miao et al. synthesized C-dots with a wide range of emission colors, from blue to red (430 nm to 630 nm), by using CA and urea in DMF through a solvothermal reaction [122]. The degree of redshift in emission was controlled by manipulating the graphitization degree and the presence of surface states, primarily -COOH groups. These factors were determined by adjusting the molar ratio of CA to urea (ranging from 0.1 to 1) and varying the reaction temperature (140–200°C). These C-dots demonstrated excitation-dependent emission and possessed QYs of 52.6%, 35.1%, and 12.9% for the blue, green, and red emissions, respectively. Zhao et al. reported a series of C-dots using 1,2,4,5-

tetraaminobenzene as a precursor and nitrogen source in five different solvents, including water, ethanol, isopropanol, methanol, n-butanol, and DMF, employing a one-pot solvothermal method (in a Teflon stainless-steel autoclave at 170 °C for 5.5 h) [123]. The emission characteristics of these C-dots were related to the solvent used during the synthesis process. The ones prepared in organic solvents exhibited higher emission intensities compared to those in water. The variation in solvent properties, such as polarity, solubility, protic or aprotic nature, and boiling point, contributed to differences in carbonization, growth of conjugated domains, dehydration, core formation, and aggregation, ultimately resulting in variations in their emission properties. The λ_{em} of these C-dots ranged from 527 to 605 nm, with QYs spanning from 10% to 47.6%. The emission mechanism was further explored by comparing red and yellow emissive C-dots (543 nm and 605 nm) prepared in n-butanol and ethanol, respectively. The observed redshift in emission was attributed to factors like particle size increase and the presence of surface states. In a separate study, Zhang's group synthesized a series of C-dots using OPD as a precursor in $CHCl_3$ via a one-pot solvothermal method which included heating at 160 °C for 10h [124]. The resulting C-dots had a range of emission colors, including blue, green, yellow-green, orange, and red, through column chromatography separation of the product mixture. Among these, the green-emitting ones exhibited the highest QY of 88.9%, primarily due to their high content of C-O and C-O-C groups. The redshift in emission, spanning from 435 nm to 595 nm, could be attributed to variations in conjugation length and the extent of heteroatom doping (Figure 12). Zhu et al. achieved the preparation of green (λ_{em}= 515 nm at λ_{ex}=370 nm) GQDs with an average size of 5.3 nm and a PL QY of 11% using DMF as the solvent in a solvothermal process [125]. PEG-200 in NaOH served as precursors for the solvothermal synthesis of C-dots at 160 °C for 24 hours, as demonstrated by Mitra et al. [126]. These C-dots had sizes ranging from 1 nm to 5 nm and exhibited a QY of 2 %.
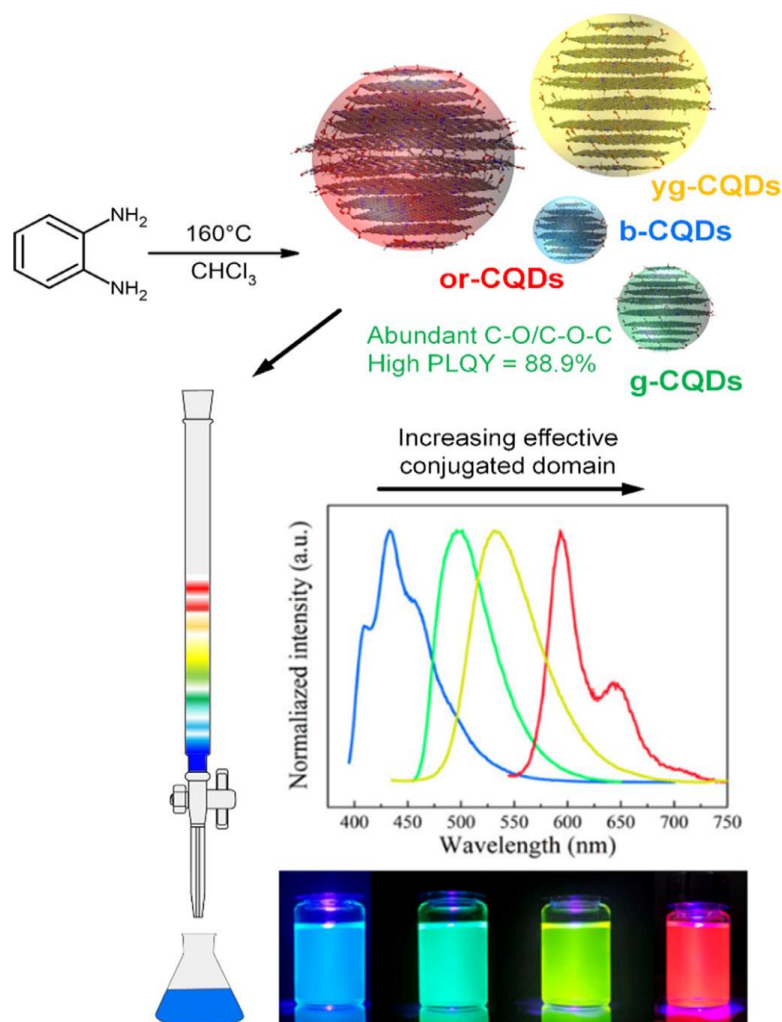
Figure 12. The synthesis and separation of C-dots with different emission colors followed by their normalized PL emission spectra and images of the C-dots in solution under 395 nm UV-light [124].

1.4.2.4. *Microwave-assisted method*

Microwave-assisted methods offer several advantages, including speed, cost-effectiveness, and reduced side product formation, making them widely employed in the synthesis of C-dots [127].

Li et al. reported the synthesis of green, fluorescent GQDs through a microwave-assisted procedure using GO sheets in acidic conditions (3.2 M HNO_3 and 0.9 M H_2SO_4) for 3h (Figure 13a) [128]. This process led to the formation of single-layer GQDs with an average diameter of 4.5 nm and a QY of 11.7 %. Wang et al. introduced a straightforward one-pot microwave-assisted method to produce water-soluble C-dots derived from protein-rich eggshell membranes and NaOH placed in a domestic microwave oven for 5 minutes

(Figure 13b) [129]. The resulting C-dots exhibited a QY of approximately 14%. They also demonstrated the ability to simultaneously detect Cu^{2+} and glutathione.

In another study, Kumawat et al. synthesized C-dots using Mangifera indica (mango) leaves through a straightforward microwave-assisted hydrothermal process (900W for 5 minutes) (Figure 13c) [130]. These C-dots had a size between 2 nm and 8 nm, exhibited excitation-independent fluorescence emission in the NIR region (between 650 and 750 nm), and had favorable biocompatibility and high photostability. Pires et al. introduced a two-step microwave-assisted method for producing C-dots from raw cashew gum (Figure 13d) [131]. These resulting C-dots had an average size of 9 nm displayed a QY of 8.7 % and low cytotoxicity, making them valuable for live-cell imaging. Moreover, Ren et al. prepared N-doped GQDs using sodium citrate and triethanolamine as raw materials, with a diameter of 5.6 nm through microwave-assisted heating, which exhibited blue (λ_{em}= 442 nm at λ_{ex}=340 nm) fluorescence with a QY of 8% (Figure 13e) [132].
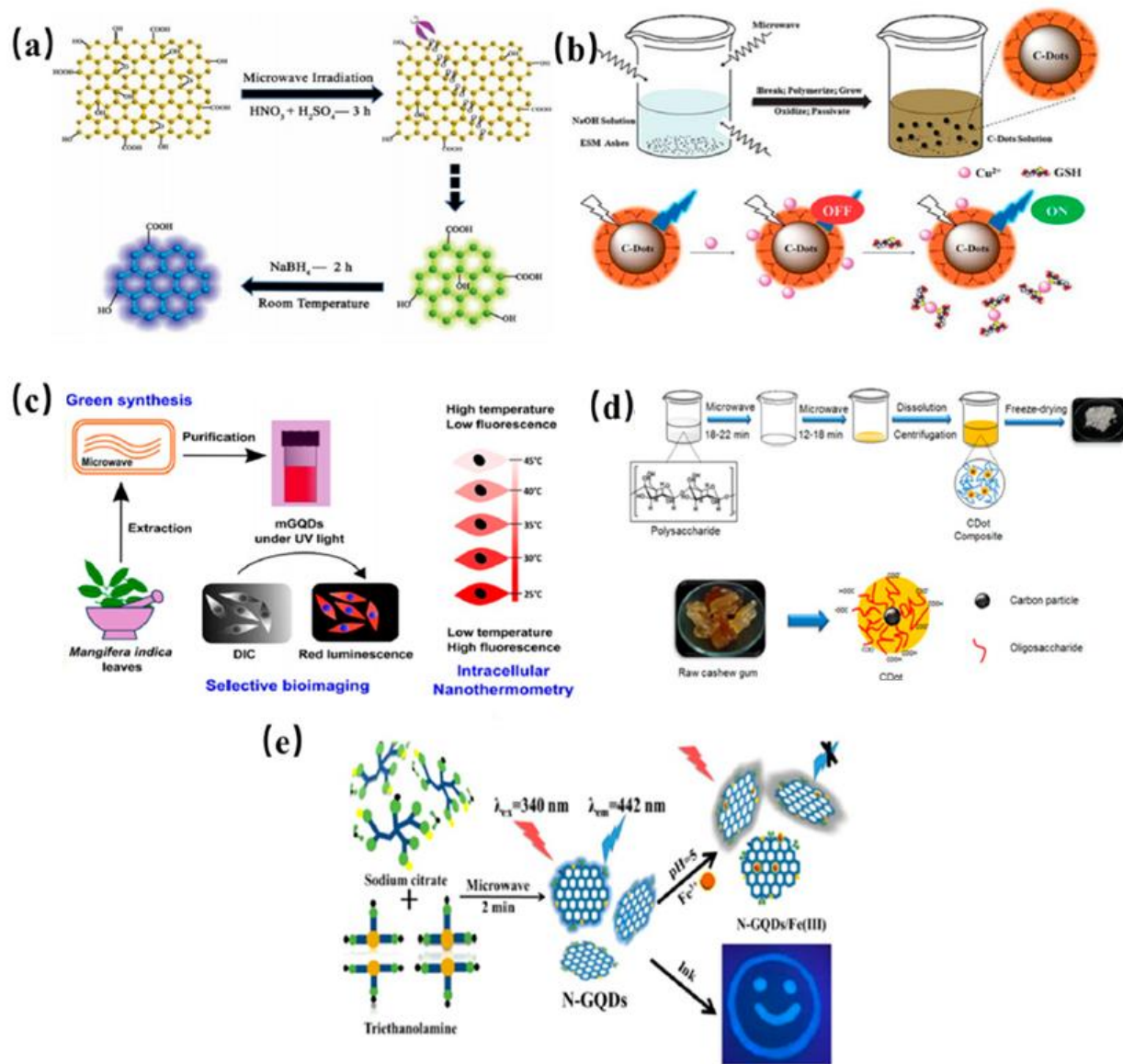
Figure 13. (a) Preparation route for GQDs under acidic conditions [128], (b) Preparation of C-dots derived from protein rich eggshell membranes in NaOH [129], (c) Preparation of C-dots using mango leaves [130], (d) Preparation of C-dot composites from raw cashew gum [131], (e) Synthesis of fluorescent N-GQDs from triethanolamine and sodium citrate [132].

Zhang et al. utilized a microwave-assisted approach to synthesize GQDs using aspartic acid and NH_4HCO_3 as precursors in a water-based system (560W for 10 minutes) [133]. The resulting GQDs exhibited blue fluorescence (λ_{em}=450 nm) under the irradiation of UV-light (λ_{ex}=365 nm) with a QY of 14% and displayed sensitivity to pH and Fe^{3+} ions. Zheng et al. produced N-GQDs by employing glucose as a carbon source and ammonia

as a nitrogen source in a water-based microwave-assisted method at room temperature and atmospheric pressure [134]. These N-GQDs, with a size of 5.3 nm, demonstrated a QY of 6.42%. This synthesis method harnessed the benefits of rapid microwave reactions along with the catalytic and doping effects of ammonia. Chan et al. synthesized N, S-C-dots by using CA as a precursor and CH_4N_2S as nitrogen and sulfur dopants through a microwave-assisted process which lasted for 6 minutes [135]. The resulting water-soluble NS-C-dots had an average size of 4.7 nm, exhibited a high QY of 28.9% and displayed pH-dependent emission properties. They also demonstrated selectivity for Fe^{3+} ions, particularly enhanced under acidic conditions at approximately pH=2. Lastly, Li et al. reported the synthesis of C-dots using $C_{10}H_{14}N_5O_8P$ and EDA via a microwave-assisted method [136]. Their average size was about 3.7 nm, and the QY was estimated as 10.4% using quinine sulfate as the reference. They suggested a mechanism which included the polymerization of precursors, followed by carbonization to form hydrophilic and AG^+ ion-sensitive C-dots. Scaling up the production of oil-soluble C-dots from cost-effective materials has been a challenge. Fang et al. successfully prepared C-dots using four different surfactants (Span 40, octadecyl sucrose, soybean lecithin, and dodecyl betaine) as precursors via a straightforward microwave-assisted method [137]. The resulting C-dots had average sizes from 1.3 nm to 2.9 nm and QYs from 0.8 % to 2.5 %. The formation mechanism involved the carbonization of hydrophilic groups, resulting in C-dots, with fatty acid chains on their surfaces, enhancing their solubility in oils. The presence of these fatty acid chains helped maintain a uniform structure and prevented further particle growth due to steric hindrance. Scaling up production, with reaction volumes reaching approximately 1 kg, was investigated, and the particles were incorporated into polymer composites, demonstrating promise for industrial-scale applications.

1.5.   Properties of C-dots

1.5.1. UV-Absorption

C-dots exhibit comparable optical characteristics despite structural differences, with variations in functionalities, synthesis methods, heteroatom doping and precursors. UV-vis spectroscopy serves as a valuable tool for gaining insights into the chemical structure of C-dots [138].

C-dots display robust absorption in the UV region, both extending into the visible and even NIR ranges [139], [140]. Generally, the absorption peak of C-dots is prominently observed in the wavelength range of 220 to 270 nm, corresponding to the core π→π* transition of aromatic C=C bonds, as it can be seen in Figure 14a [141]. Additionally, an absorption peak in the 280 to 350 nm range is attributed to electronic transitions from C–O or C=O bonds to the π* orbital (n→π* transitions) [138], [141], [142]. The absorption peak at wavelengths spanning 400 to 600 nm is linked to electron transitions of the surface functional groups of C-dots, suggesting that surface chemical moieties contribute to UV–visible region absorption [143]. Some studies have revealed that certain C-dots exhibit long-wavelength absorption ranges, originating from structures containing aromatic rings, as shown in Figure 14b [144].
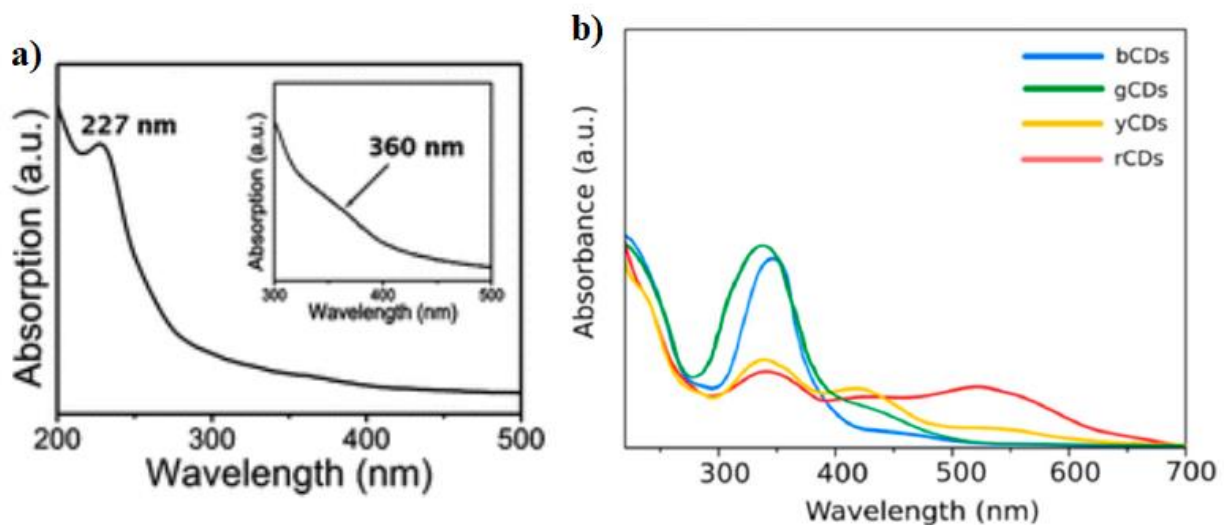
Figure 14. a) UV-vis absorption spectra of GQD aqueous solution [141], b) Absorption spectra for long wavelength emission C-dots [144].

In contrast to previously mentioned C-dots, N-CQDs exhibit a robust excitonic absorption band due to quantum-size effects. UV-vis absorption spectra of CA-based GQDs show a single absorption peak at 330 nm, corresponding to the π→π* transition attributed to aromatic sp^2, which blue-shifts to 315 nm due to nitrogen doping [145]. Reports indicate that GQDs synthesized in the absence of CH_4N_2S exhibit two UV transitions at 320 and 400 nm, while those prepared in the presence of CH_4N_2S display peaks at 335, 422, 550, and 595 nm [146]. The intensity of the peaks at 550 and 595 nm, corresponding to π→π*

and n→π* of C=S and S=O, increases with the amount of CH_4N_2S, indicating the impact of sulfur doping on absorbance.

Another characteristic of C-dots studied through UV-vis absorption spectroscopy is particle size, where absorbance bands can shift due to the QCE, similar to SQDs. For example, an increase in the size of CF-based GQDs from 1–4 nm to 7–11 nm results in a clear red shift from 270 nm to 330 nm in UV-vis absorption spectra [147]. UV-vis absorption spectra of GQDs synthesized from GO also exhibit a clear red shift, with the intensity of the absorption peak decreasing with increasing size due to size-dependent shape and edge changes [148]. However, the absorption peaks of glucose derived GQDs at 228 and 282 nm due to π→π* transition of aromatic sp^2 and n→π* transition of C=O do not show any changes, while the intensity of the peaks increases with size [149]. Therefore, fluctuations in UV-vis spectra of C-dots can be attributed to variations in the electronic structures and compositions of C-dots.

1.5.2. PL mechanism

The PL emissions of organic fluorophores, such as dyes and small organic molecules, are well-established to result from transitions of excited electrons returning to the ground state. In contrast, the PL emissions of traditional SQDs are primarily determined by quantized energy gaps arising from the QCE. However, despite nearly two decades of development, an agreement on the PL mechanism of C-dots has not been reached. This is attributed to the abundance of inexpensive carbon precursors, versatile synthesis methods, and the resulting variability and occasional contradictions in the structures, compositions, and PL properties of C-dots across different studies. Nonetheless, researchers have proposed three main mechanisms to explain the PL behaviors of C-dots: core state emissions resulting from QCE [150], [151], surface state emissions arising from surface defects [152], [153], and molecular state emissions attributed to organic fluorophores [154].

The conceptualization of core state emissions as an explanation for the PL behaviors of C-dots drew inspiration from the PL emissions observed in SQDs. When this mechanism is predominant, the PL emissions of C-dots are primarily dictated by QCE, heavily relying on the sizes of their π-π conjugated domains (Figure 15ai) [155], [156]. Specifically, with

an increase in the sizes (or the conjugated π-π domains) of C-dots, their PL emissions exhibit red shifts as the band gaps get shorter. For example, Kim et al. reported graphene-derived C-dots of varying sizes that were fabricated through the hydrothermal cutting of graphene sheets [148]. The observed size-dependent PL emissions of these C-dots demonstrated evident red shifts, signifying that their PL emissions were predominantly regulated by core states. In another study by Yang et al., C-dots derived from CA and diaminonaphthalene exhibited pronounced relation between their PL emissions and sizes, wherein the PL emissions experienced substantial red shifts as the sizes of C-dots got bigger [157]. The red shifting of the emissions was attributed to the augmented π-π domains in C-dots with increased sizes, consequently narrowing the band gap of C-dots.
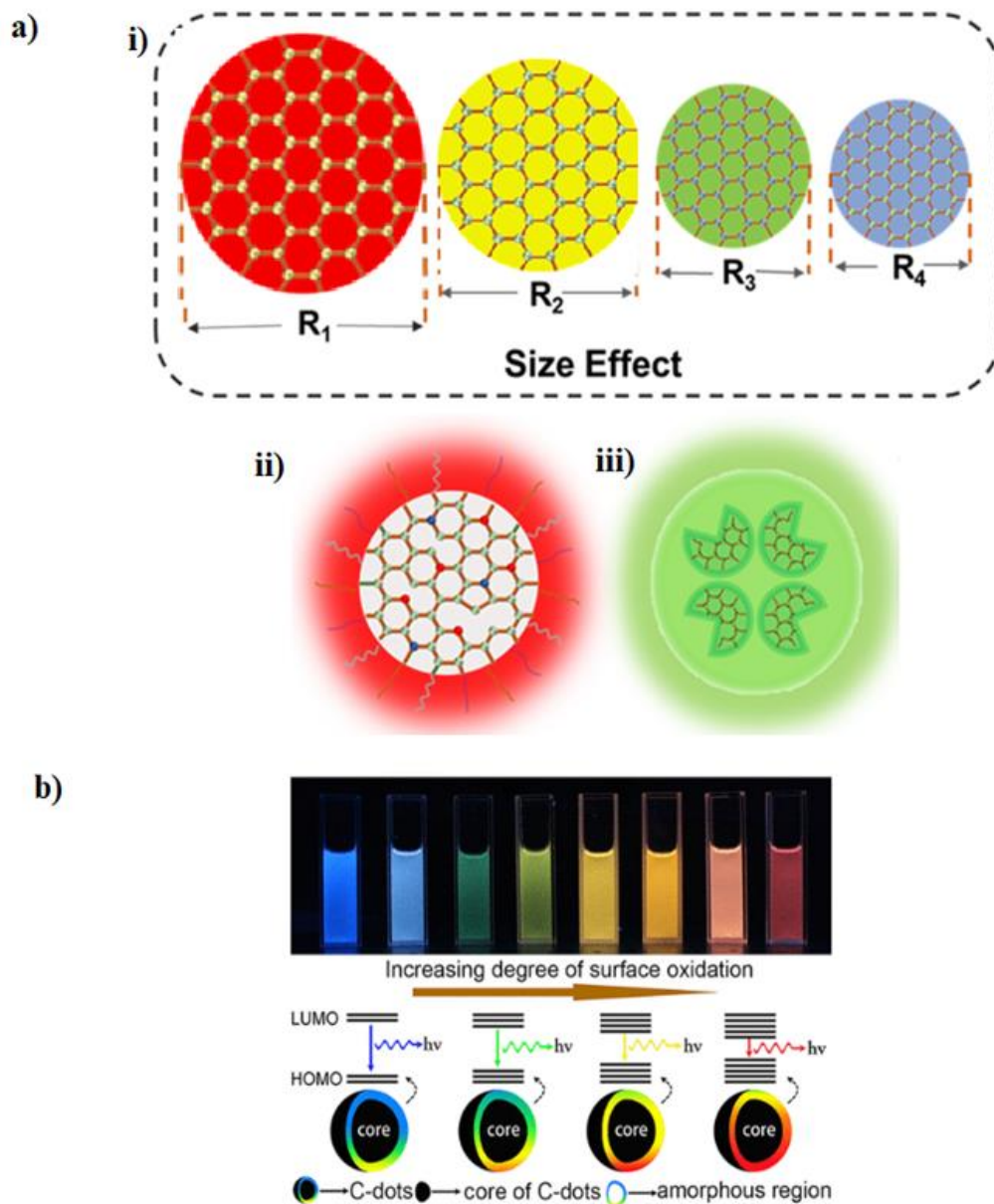
Figure 15. The conventional PL mechanisms of C-dots: (a) i-iii: core state PL, surface state PL and molecular state PL, respectively. (b) The effect of surface functional groups on the fluorescence of C-dots [158].

In the realm of flawless SQDs at the nanoscale, perfect crystals affect PL solely through QCE. Nevertheless, genuine crystals inevitably contain defects arising from imperfections like abrupt terminations of crystal structures, the incorporation of heteroatoms, and the presence of surface functional groups. These defects introduce new energy levels, giving rise to surface states that significantly impact the overall PL emissions of SQDs (Figure

15aii). Surface states are commonly believed to narrow the energy gaps between the HOMO and the LUMO, leading to a red shift in core state emissions.

Considering the numerous carbon precursors and diverse synthesis methods for C-dots, they are more susceptible to the influence of surface states than SQDs. Several studies have indicated that C-dots often exhibit multiple defects, which can result in excitation-wavelength-dependent PL behaviors and low PL QY [159], [160], [161]. For example, Ding et al. reported a series of C-dots emitting blue, green, yellow, and red lights, all with very similar sizes. This suggested that the multicolor emissions of C-dots could not be solely explained by their core state emissions [158]. Intriguingly, after observing a gradual increase in hydroxyl content on the C-dots' surfaces, as their emissions shifted from blue to red, they concluded that their multicolor emissions were ascribed to their surface state emissions, where surface states were primarily influenced by surface oxidations, and the energy gaps of the surface states decreased as the degree of surface oxidation increased (Figure 15b). Zhou et al. isolated C-dots using size exclusion chromatography, obtaining C-dots of three different sizes, in which, PL emissions were closely tied to their different surface states, rather than their sizes [152].

The concept of molecular state PL involves the incorporation of small organic fluorophores derived from the synthesis procedure into the C-dots, affecting their emissions (Figure 15iii). Krysmann et al. studied the molecular state emissions of C-dots derived from CA and EA [1]. This study revealed that the PL emission of C-dots prepared at relatively low temperatures was predominantly governed by the amide-containing molecular fluorophores, while at high temperatures, the core state took precedence as the organic fluorophores were carbonized. In another study, Yang et al. investigated the PL emissions of C-dots derived from CA and EDA, unveiling the molecular fluorophores responsible for the emissions [162], [163], [164].

1.5.3. Electrochemical behavior

C-dots exhibit distinctive electrochemical properties, making them suitable for various electrochemical applications, such as: (i) large surface area that enhances electrical conductivity through the formation of electron-hole pairs, (ii) cost-effectiveness and low toxicity [165], (iii) several surface functionalities like carboxyl, amino, and hydroxyl groups,

allowing for surface modifications to improve particle stability [166], and (iv) heteroatom doping which amplifies the electronic behavior of C-dots by enhancing intramolecular charge transfer and implementing reactive sites for electrocatalysis [167], [168]. Liu et al. observed an increase in specific capacitance with decreasing GQD size, with the smallest size exhibiting the most efficient power response at a scan rate of 5000 V/s, suggesting potential applications in high-power response microelectronics [169]. Additionally, a study by Li et al. focused on modifying husk-based activated carbon with GQDs for lithium-ion batteries, which led to improved electrochemical properties, reducing charge transfer resistance from 577.7 Ω to 123.9 Ω and enhancing electrical conductivity and cycle stability [170].

1.5.4. Toxicity

Biocompatibility and low toxicity are crucial attributes for the successful utilization of carbon nanomaterials in various biomedical applications. Assessing their biocompatibility *in vivo* remains a key aspect for advancing their applications, although the *in vitro* biocompatibility of C-dots has already been extensively studied and established by numerous research groups [171], [172].

An interesting study by Sun et al. focused on the evaluation of the toxicity of PEG_{1500N}-passivated C-dots both *in vitro* and *in vivo* [173]. *In vitro* assessments involved incubating C-dots with human breast cancer MCF-7 and human colorectal adenocarcinoma HT-29 cells. The results indicated minimal effects on cell proliferation, mortality, and viability, comparable to PEG_{1500N} (Figure 16). For *in vivo* evaluations, two groups of mice were intravenously injected with different dosages of C-dots (8 and 40 mg) per kg of body weight. A third group, serving as the non-toxic control, received exposure to a 0.9% NaCl aqueous solution. Over the course of the 4-week experiment, all mice exposed to either C-dots or the NaCl solution demonstrated 100% survival. Their food intake remained consistent, and no mice exhibited clinical symptoms such as anorexia, hair loss, vomiting, or diarrhea. The experiment indicated the well-tolerated nature of both C-dots and the control solution within the observed parameters.
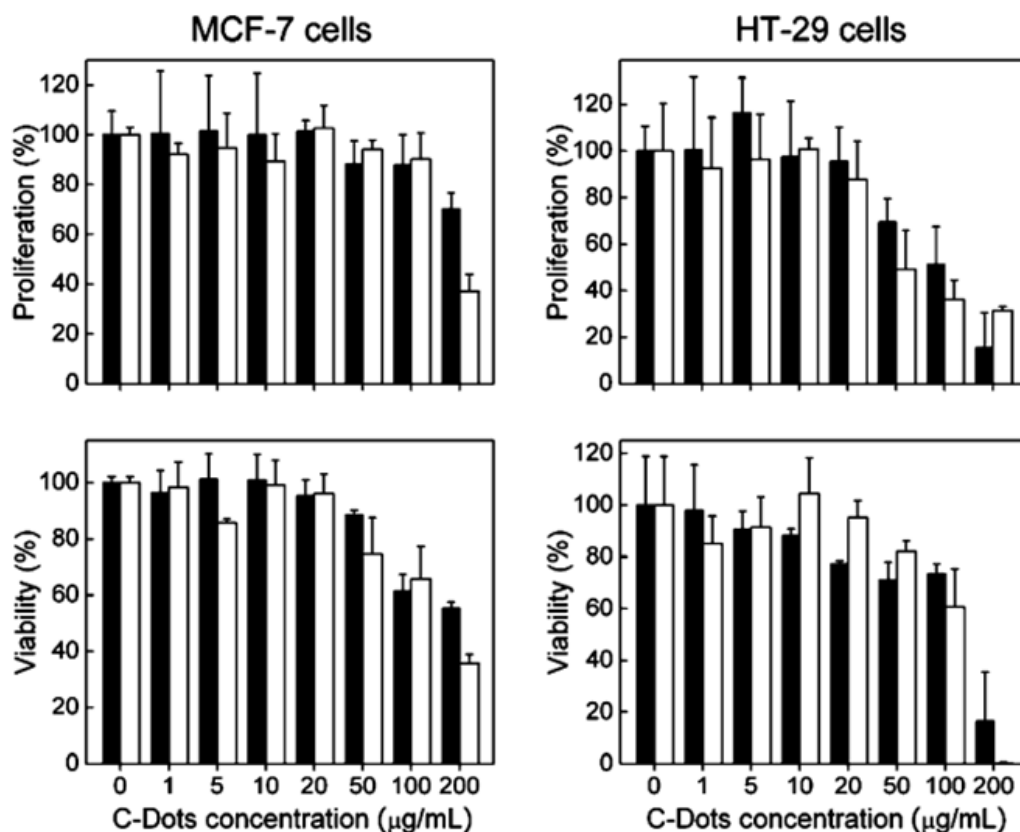
Figure 16. Results from cytotoxicity evaluations of C-Dots (black) and PEG1500N (white) in MCF-7 and HT-29 cells [173].

Furthermore, the same group explored the impact of various passivation molecules on the cytotoxicity of C-dots [174]. Different polymers, including PEG, PPEI–EI, PEI, BPEI, and PAA, were utilized for the synthesis of C-dots. The study revealed a direct connection between C-dot's toxicity and surface passivation agents. Passivation with PEI and PAA led to higher toxicity compared to PEG- and PPEI–EI- passivated C-dots, aligning with the known cytotoxicity of free PAA and PEI solutions. In a separate investigation, Huang et al. delved into the impact of injection routes on the distribution, clearance, and tumor uptake of C-dots [175]. Using PEG-functionalized NIR dye ZW800-conjugated C-dots, they explored three injection routes: intravenous (iv), subcutaneous (sc), and intramuscular (im). Biodistribution analysis revealed that, regardless of the injection route, the majority of C-dots accumulated in the kidneys after 1 hour. The signal quantification ranked injection routes as im > sc > iv. After 24 hours, no detectable signal remained in any organ, signifying efficient clearance irrespective of injection routes. Urine clearance

analysis indicated rapid and efficient removal of C-dots, with clearance rates ranked as iv > im > sc. Tumor uptake efficiency varied with injection routes, demonstrating sc > iv > im.

1.6. Applications of C-dots

C-dots, renowned for their high-efficiency fluorescent properties, offer a host of exceptional advantages and hold significant promise for a wide array of applications, spanning from sensors and bioimaging to solar cells and photocatalysis.

1.6.1. C-dots in bioimaging

Due to their remarkable water solubility, robust luminescent properties, photostability, and innate biocompatibility, C-dots have emerged as innovative nanoplatforms for applications in biological imaging. Over recent years, several investigations have highlighted the bioimaging capabilities of C-dots [176], [177], [178], [179]. To date, a growing array of cell types, encompassing human cells (such as HeLa and U87 brain cells), animal cells (including mice embryonic fibroblasts), and bacterial cells (like *E. coli* and *S. aureus*), have been effectively visualized using C-dots as bioimaging agents [180]. In a recent study, it was demonstrated that C-dots, derived through pyrolytic treatment of a binary mixture of CA and urea, exhibit low toxicity when interacting with HeLa cancer cells [181]. These C-dots were found to be internalized by the cells without causing any adverse effects on their morphology (Figure 17).
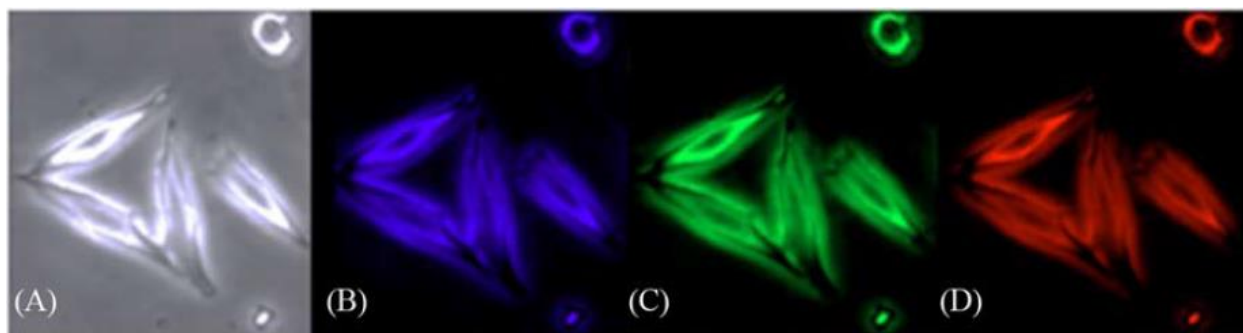
Figure 17. Fluorescence microscope images of HeLa cells incubated with C-dots under the bright field (A) and the UV (B), blue (C), green (D) excitation wavelengths [181].

Ding et al. harnessed red-emitting C-dots (R-C-dots) with an average size of 4.1 nm, for both *in vivo* and *in vitro* bioimaging applications, and conducted experiments targeting

HeLa cells to assess cell viability [182]. HeLa cells were exposed to several concentrations of R-C-dots over 48 hours, and remarkably, cell viability remained unaffected even at high R-C-dot concentrations, up to 1000 µg/mL. Moreover, bioimaging of HeLa cells was carried out using 50.0 µg/mL of R-C-dots at different time intervals and temperatures. The observations were made using a CLSM with excitation light at 535 nm and emission light at 600 nm. The resulting CLSM images of HeLa cells, incubated with R-C-dots under different time and temperature conditions (Figure 18). In another study, hyaluronic acid-conjugated C-dots were employed for both *in vivo* and *in vitro* bioimaging to facilitate targeted delivery of hyaluronic acid derivatives [183]. Hyaluronic acid is a valuable candidate for drug delivery in treating liver diseases, and bioimaging plays a crucial role in ensuring precise drug delivery to specific target sites. Furthermore, Cao et al. studied two-photon active fluorescent C-dots as bioimaging agents for breast cancer MCF-7 cells [184]. These C-dots exhibited strong luminescent properties and could be excited using two-photon excitation in the NIR region. Practical results indicated that these two-photon active C-dots outperformed conventional SQDs.
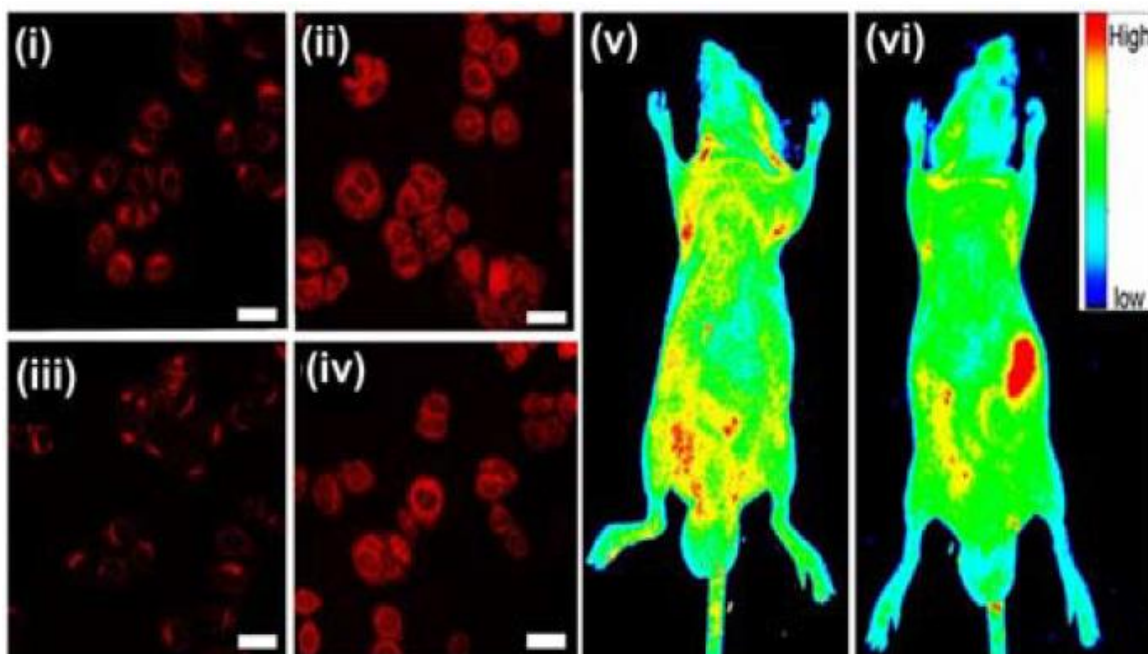
Figure 18. (i and ii) CLSM images of HeLa cells incubated with 50 µg/mL of the R-C-dots for 1, and 2 h, respectively. (iii and iv) CLSM images of HeLa cells that were incubated for 2 h at 25 ℃, and 37 ℃, respectively. PL images of a mouse (v) before and (vi) after subcutaneous injection of 50 µL of the R-C-dots aqueous solution (1 mg/mL) [182].

In comparison to other heavy metal QDs, C-dots stand out for their strong light-absorbing capabilities, which can compensate for their relatively lower fluorescence efficiency in bioimaging applications. This potential was initially demonstrated by Sun et al., who introduced a method for staining Caco-2 cells using PEG1500N-passivated C-dots, indicating the feasibility of employing C-dots as fluorescent markers for cellular imaging [185]. Subsequently, various types of cells, including HeLa cells, HepG2 cells, MCF-7 cells, pancreas progenitor cells, and human lung cancer cells, have been utilized for intracellular imaging. For instance, Zhai et al. reported that L929 cells cultured with C-dots exhibited vivid and stable blue, green, and red PL emissions when excited at wavelengths of 405 nm, 488 nm, and 543 nm, respectively (Figure 22) [186]. Furthermore, in an *in vivo* experiment, CQDs were introduced into a nude mouse at three different locations, and fluorescence images were captured using various λ_{ex}, revealing only red spots in the resulting *in vivo* images of C-dots (Figure 19) [187].
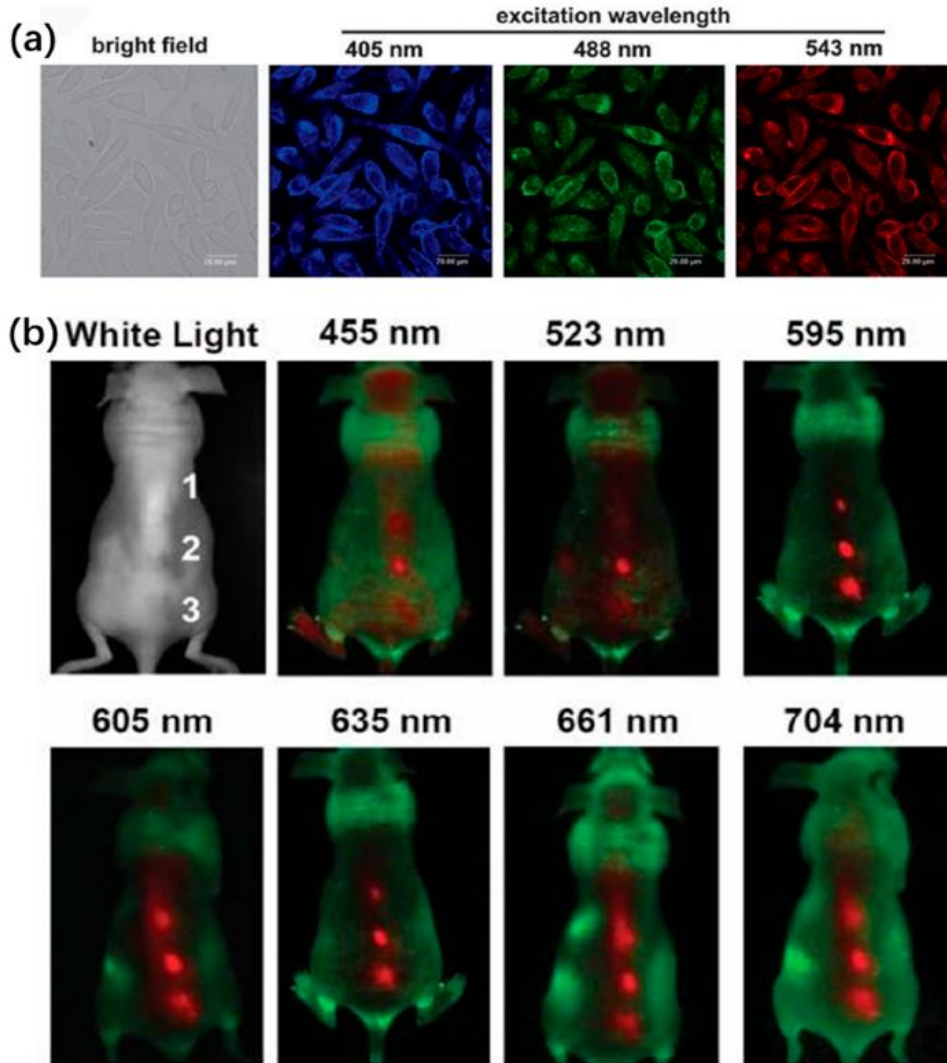
Figure 19. (a) The *in vivo* images of L929 cells which are injected with C-dots under different λ_{ex} (405 nm, 488 nm, and 543 nm) [186]. (b) *In vivo* fluorescence images of a C-dot-injected mouse. The images were taken under various λ_{ex} (455, 523, 595, 605, 635, 661, and 704 nm). Red and green represent FL signals of C-dots and the tissue autofluorescence, respectively [187].

1.6.2. C-dots in photoacoustic imaging

PAI represents an innovative approach in the realm of bioimaging techniques, capitalizing on the photoacoustic effect. This effect involves the conversion of light energy into acoustic waves, driven by the absorption of electromagnetic waves and localized thermal excitation. Recent studies have showcased the immense potential of PAI for *in vivo* bioimaging applications, focusing on areas such as tumor angiogenesis, mapping blood

oxygenation levels, quantifying MetHB concentrations, conducting functional brain imaging, and detecting skin melanoma, among others [188].

Wu et al. first demonstrated the potential of C-dots for PAI of SLN, a critical aspect of monitoring cancer progression [189]. Their hypothesis revolved around the idea that particles smaller than 10 nm, roughly the size of albumin, and possessing stable optical properties, exhibit swift lymphatic transit while also being sufficiently substantial to be retained and phagocytosed by cortical macrophages in the draining lymph nodes. Given that the C-dots they synthesized possessed both key characteristics, they emerged as ideal candidates for real-time PAI with a strong capability for SLN imaging enhancement. Their experiments unveiled a remarkable signal enhancement in the SLN, occurring within approximately 2 minutes of introducing the C-dots. On a similar note, Parvin et al. introduced a novel development by crafting dual-emissive C-dots, co-doped with phosphorus and nitrogen, enabling their application in both fluorescent imaging and PAI [190]. These synthesized C-dots exhibited robust red emission characteristics, and their photoacoustic signal intensity exhibited a linear relationship with the concentration of C-dots. Notably, this relationship was well-described by an R^2 value of 0.9921 within the concentration range of 0 to 100 µg/ml. Upon intravenous administration into mice bearing tumors, the C-dots dispersed throughout the body's organs, with a significant accumulation observed in the tumor area, attributed to the EPR effect.

Ge et al. introduced red-emissive C-dots that serve as a versatile platform for three distinct theragnostic applications [191]. These synthesized C-dots exhibit capabilities in fluorescent, photoacoustic, and thermal imaging within live mice. To evaluate their potential for PAI, they conducted experiments using an agarose gel phantom containing C-dots, revealing their impressive optical absorption at 710 nm. Importantly, this absorption displayed a linear correlation with the concentration of C-dots within the range of 0 to 200 µg/ml. In alive mice with tumors, the C-dots demonstrated a substantial accumulation within the tumor due to the EPR effect, surpassing their accumulation in blood vessels and other organs. Furthermore, Lee et al. demonstrated the utility of biodegradable C-dots, synthesized from CA, oleylamine, and octadecane, for non-invasive *in vivo* PAI [192]. In a recent study conducted by Jia et al., C-dots derived from

Hypocrella bambusae were shown to enable fluorescence imaging and PAI [193]. These C-dots, derived from *Hypocrella bambusae*, exhibited broad-spectrum optical absorption spanning from 350 to 800 nm, with a red emission peak at 610 nm (Figure 20).
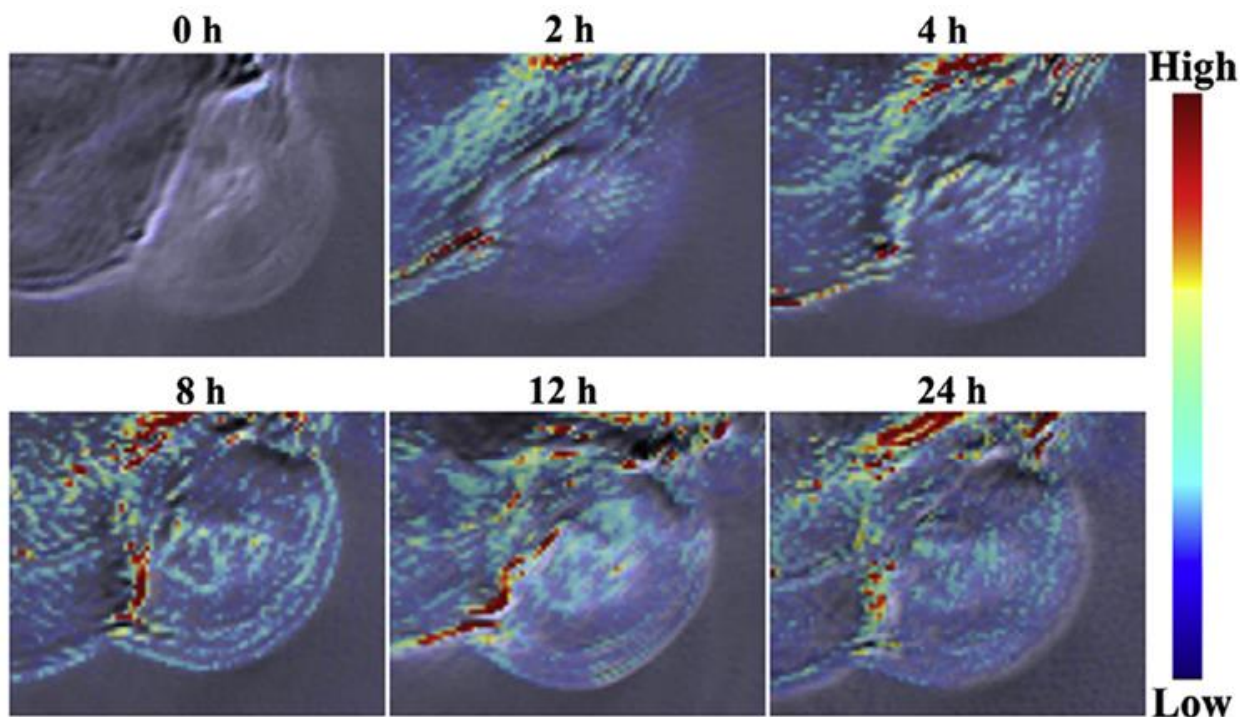
Figure 20. *In vivo* PAI of mice post-intravenous injection of HBC-dots in PBS (0h -24h) [193].

1.6.3. C-dots in photothermal therapy

PTT is an innovative treatment strategy that leverages laser light to combat diseases, notably cancer. In PTT, a NIR photoabsorber is employed to generate localized heat, effectively targeting, and eliminating specific cells, like cancer cells. This approach offers distinct advantages over traditional cancer treatments such as invasive surgery, chemotherapy, or radiotherapy. PTT boasts minimal invasiveness, high specificity, and precise temporal selectivity [194]. PTT can directly eradicate cancer cells at the primary tumor site or in nearby lymph nodes during the early stages of cancer metastasis. Furthermore, it can be synergistically employed with existing therapeutic methods to address cancer cells at metastatic sites. Over the past few years, numerous research groups have explored the therapeutic potential of PTT for cancer treatment. The effectiveness of PTT hinges significantly on the conversion of light into heat in the presence of photothermal agents, particularly nanoscale agents. To date, various

nanomaterials have been utilized as photothermal agents, including gold nanostructures, graphene, and GO. Nonetheless, due to production costs and complex synthesis procedures associated with these materials, researchers are actively seeking alternative, cost-effective photothermal agents. Interestingly, C-dots have also piqued the curiosity of researchers thanks to their unique physicochemical properties. A notable feature of C-dots is their substantial abundance of π electrons, which mimic the behavior of free electrons found in metallic nanomaterials with strong electron-electron interactions. Furthermore, the relatively low QY of C-dots hints at the significant conversion of absorbed light into heat via various non-radiative pathways. This attribute underscores the promising potential of C-dots in the realm of PTT.

For instance, Nurunnabi et al. reported CF-derived C-dots (CF-C-dots) that, when exposed to NIR laser irradiation, triggered the creation of electron clouds [195]. These electron clouds produced enough heat, exceeding 50°C, effectively eradicating approximately 70% of cancer cells through thermal ablation. Moreover, Zheng et al. developed multifunctional C-dots using a hydrophobic cyanine dye (CyOH) and PEG800 through a straightforward solvothermal process [196]. These C-dots exhibited strong absorption and NIR emission within the 600–900 nm range. With a moderate uptake rate and a high photothermal conversion efficiency of 38.7%, these C-dots demonstrated remarkable PTT efficacy. After a 30-minute incubation, with C-dots followed by 2 W/cm² laser irradiation on HepG2 and CT26 cell lines, the *in vitro* experiments showed a significant reduction in cell viability (to less than 13% for HepG2 and less than 25% for CT26 cells). Furthermore, when injected at a dose of 4 mg/kg in mice with CT26 tumors, these C-dots exhibited an impressive tumor inhibition rate of 91% (Figure 21). Li et al. synthesized C-dots which displayed strong absorbance in the visible to NIR region (470–1000 nm) and possessed a photothermal conversion efficiency of 50%, effectively killing cancer cells [197]. Combining PTT with chemotherapy has proven more effective in eradicating tumor cells than using either method alone. Wang et al. introduced a chitosan-carbon dot hybrid nanogel capable of synergistically eliminating tumors through PTT and chemotherapy [198]. The chitosan-C-dot nanogel demonstrated controlled drug release profiles in both endogenous (acidic medium) and exogenous (NIR light) conditions, effectively killing 4T1 cancer cells *in vitro*. Subsequent *in vivo* studies confirmed that the

DOX-loaded chitosan-C-dot nanogel was safe for normal tissues while significantly enhancing the destruction of 4T1 tumor tissue upon NIR laser irradiation.
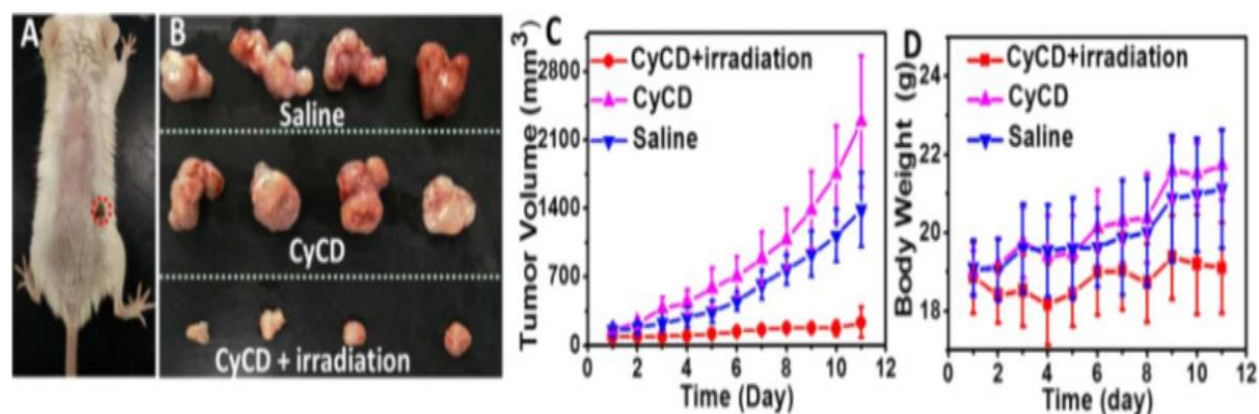
Figure 21. (A) Images of a mouse bearing a CT26 tumor are provided, with the tumor area outlined by a red line. (B) Photos of tumors on the 11th day. (C) The tumor volume and (D) body weight of the CT26 cancer-bearing mice were monitored over time, with a dosage of 4.0 mg/kg CyOH. [196]

1.6.4. C-dots in photodynamic therapy

In addition to PTT, C-dot-based PDT has drawn significant attention for its minimal invasiveness and low toxicity, particularly in targeted therapy for various debilitating conditions, including cancer [199]. PDT comprises three primary components: a photosensitizer, a light source (often a laser), and ROS. Typically, the light source excites the photosensitizer, leading to the generation of radicals or ROS, resulting in the destruction of damaged tissue. C-dots have been thoroughly employed to deliver photosensitizer agents to the afflicted tissue site, owing to their facile synthesis processes, surface functionalization capabilities, substantial drug-carrying capacity, and excellent biocompatibility.

Wu et al. developed C-dots with inherent nucleus-targeting capabilities for use in PDT [200]. They facilitated them through a one-pot hydrothermal procedure between MPD and l-cysteine. They exhibited superior nucleus-targeting abilities compared to SYTO RNAselect (which can only stain the nucleus in fixed cells), by allowing high-quality imaging in both fixed and live cells. For PDT, they conjugated PpIX with these C-dots (PpIX-C-dots), which resulted in significantly improved PDT. *In vivo* studies proved that the conjugates successfully targeted the cancerous site after intravenous injection,

causing damage to the cancer cells without harming the normal ones. In another approach, Li et al. created porphyrin-containing C-dots with remarkable PDT capabilities upon photoirradiation, that exhibited a higher tumor inhibition rate compared to TPP after being irradiated with a laser source [201]. Furthermore, He et al. synthesized C-dots using chitosan and DPP (DPP-C-dots) as precursors, which could produce singlet oxygen ($^1O_2$) with a single laser irradiation [202]. *In vitro* cytotoxicity assays on HepG2 cells revealed that DPP-C-dots were non-toxic even at concentrations as high as 200 µg/ml without laser irradiation. However, being excited with a laser of 540 nm, 100 µg/ml was sufficient to kill 50% of the cells. Likewise, during *in vivo* experiments, DPP-C-dots led to a notable decrease in tumor size when exposed to laser irradiation, in contrast to the control groups treated solely with DPP-C-dots or PBS (Figure 22).
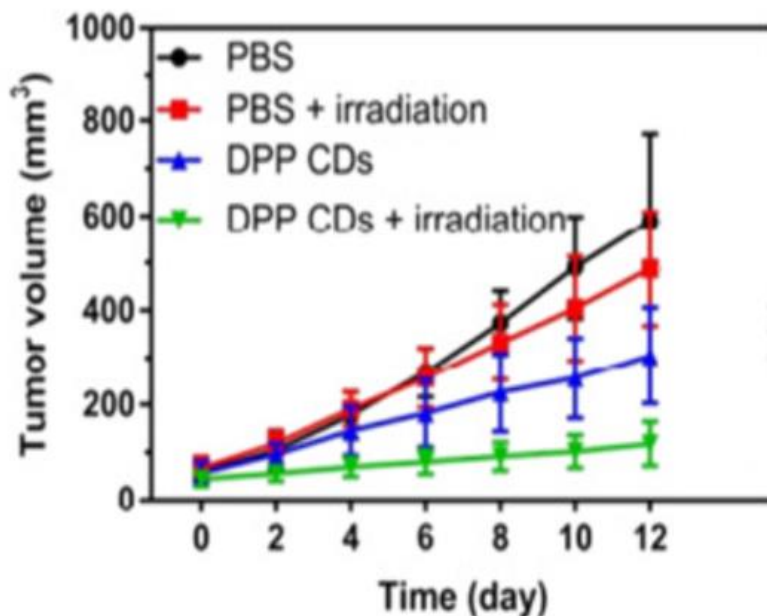
Figure 22. The progression of mouse tumor volumes over time under different medications. [202]

1.6.5. C-dots in sensing applications

The PL properties of C-dots find wide-ranging utility in the detection of various molecules, including glucose, H_2O_2 [203], dopamine [204], cholinesterase [205], etc. For instance, Shan et al. demonstrated the PL emission quenching of C-dots in response to H_2O_2 within a concentration range of 0.1 to 1.0 mM, as depicted in Figure 23a. This phenomenon was attributed to charge transfer interactions between boron and H_2O_2 [203]. In another study,

Xu et al. synthesized boron-doped C-dots (BC-dots) for detecting the Tartrazine molecule, as illustrated in Figure 23b [206]. The PL emission of BC-dots was observed to diminish with increasing Tartrazine concentrations, ranging from 0.25 µM to 32.5 µM. Song and coworkers developed C-dots from natural precursors for the purpose of sensitive Butyryl cholinesterase (BChE) detection, as shown in Figure 23c [205]. The corresponding detection limit for BChE was determined to be 0.035 mU/mL.
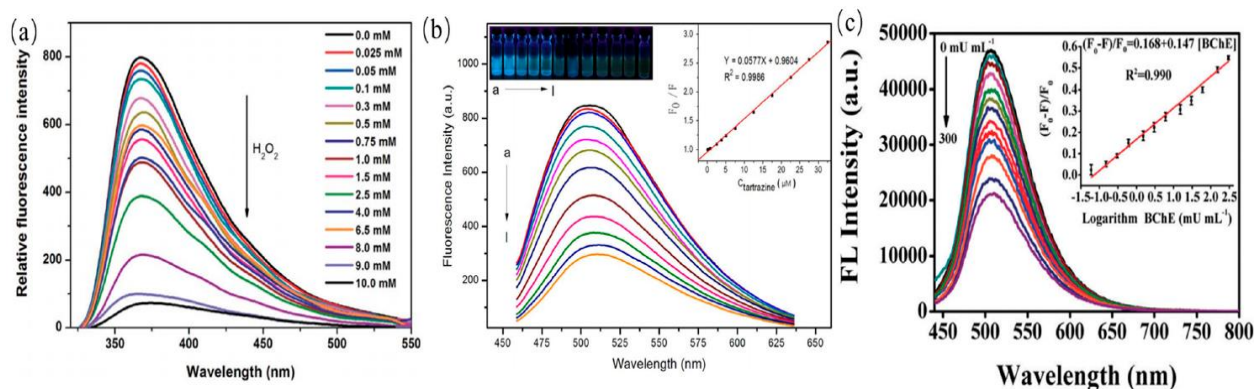
Figure 23. FL response of C-dots dispersion in the presence of various molecules: (a) H_2O_2 [203], (b) Tartrazine [206], (c) BChE [205].

In the realm of sensor applications, iron ions, specifically Fe^{3+}, are among the most frequently targeted analytes. The PL emission signal of C-dots experiences quenching when Fe^{3+} ions interact with surface functional groups like amino moieties. To illustrate, Liu et al. successfully synthesized CQDs from goose feathers, enabling the sensitive and selective detection of Fe^{3+} ions with an impressively low detection limit [207]. Similarly, Xu et al. reported their findings on the detection of Fe^{3+} ions using C-dots. Their observations revealed a gradual reduction in the PL emission intensity of C-dots upon the introduction of Fe^{3+} ions. This decrease in PL intensity indicates that Fe^{3+} ions have the capacity to quench the PL signals of C-dots, primarily due to strong coordination interactions between Fe^{3+} ions and amine-rich groups present on the surface of C-dots [208].

1.6.6. C-dots in drug delivery

Conjugates of C-dots with drugs serve as effective vehicles for enhancing drug solubility, selectively targeting cells, and delivering multiple therapeutic agents in a sustained manner. For instance, Zeng et al. developed green-emissive C-dots that were

electrostatically bonded with DOX [209]. Their findings revealed that the release of DOX was triggered specifically in the acidic environment of HepG2 liver carcinoma cells, sparing HL-7702 normal cells. In a mouse model, C-dots/DOX conjugates reduced the size of HepG2 tumors by 50% within 72 hours, compared to a 30% reduction achieved with DOX alone. In another study conducted by Sarkar et al., C-dots were synthesized from Aloe Vera leaf gel and attached to the surface of a calcium alginate film through a solution casting process [210]. This film was then loaded with the antibiotic Van. Intriguingly, the presence of C-dots substantially increased the drug loading capacity, from 38% in pure calcium alginate to 89% in the nanohybrid film, and further up to 96% with the addition of β-cyclodextrin. The antibiotic was released slowly, with 56% released over 120 hours, under pH conditions resembling the stomach environment. In a separate investigation, C-dots were derived from pasteurized milk, which is rich in phosphoproteins, fat globules, and whey proteins [211]. These C-dots were loaded with LIS, creating aggregates that functioned as multifunctional carriers. These carriers released the drug in a controlled manner while also serving as bioimaging probes for visualizing HeLa cells *in vitro*.

1.6.7. C-dots in fingerprints

For more than a century, fingerprint analysis has been a pivotal tool in criminal investigations, offering essential insights. It plays a central role not only in identifying disaster victims but also stands as the foremost method for biometric identification. The technique relies on the remarkable fact that the patterns of epidermal ridges on an individual's fingers are truly unique and distinctive.

The innovation of C-dot-based powders for visualizing latent fingerprints marked a significant development in this field. Fernandes et al. demonstrated that incorporating just 0.7 wt. % of C-dots into a SiO_2 matrix enabled the highly detailed and customizable visualization of latent fingerprints[212]. This breakthrough was observed both on glass slides and on various multicolored soft drink labels. In their study, C-dots were synthesized through a thermal process involving CA and EA, followed by dialysis in water. XPS analysis revealed a composition consisting of carbon (44.85%), hydrogen (5.75%), and nitrogen (10.85%), while the QY in water was estimated at 15% under 365 nm

excitation using anthracene as a reference. Figure 24 showcases the exceptional level of detail achieved through fluorescence using the C-dot hybrid powder. Additionally, it highlights the remarkable capability to adjust colors by employing different λ_{ex}. This eliminates the need for a range of powders to visualize fingerprints against various colored backgrounds, simplifying the process for crime scene investigators. Notably, when subjected to an Automated fingerprint identification system (AFIS) analysis, a fresh fingerprint developed using the hybrid nanopowder revealed 71 minutiae, compared to the 65 minutiae using a standard white powder under identical conditions.
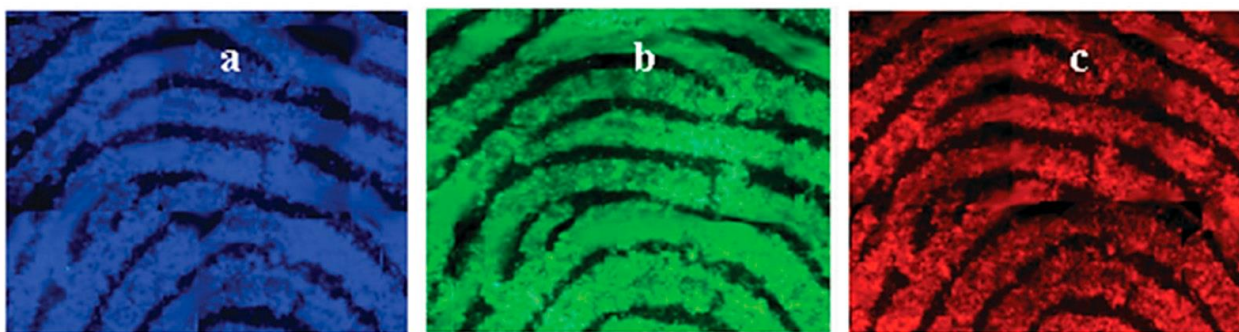
Figure 24. Fluorescence microscopy images of fingerprints deposited on a glass slide and visualized with 0.7% C-dot–SiO$_2$ hybrid nanopowder under (a) violet, (b) blue and (c) green light [212].

In another study by Fernandes et al., their focus shifted towards carbogenically-coated SiO$_2$ nanoparticles (C-SiO$_2$), which possessed an average diameter of approximately 22 nm and comprised carbon (26%), hydrogen (4%), and nitrogen (5%) [213]. The C-SiO$_2$ nanopowder displayed strong adherence to fingerprints, and provided a higher level of detail, with 73 minutiae detected, compared to a commercially available white fingerprint powder which revealed 65 minutiae under the same conditions. Notably, the C-SiO$_2$ nanopowder effectively unveiled high-quality fingerprints, even on highly fluorescent cardboard surfaces, a task that proved challenging for the commercial white fingerprint powder. Furthermore, the C-SiO$_2$ nanopowder demonstrated strong contrast when exposed to illumination within the 365–590 nm range, whereas the commercial fluorescent powder could achieve this only within a very limited range of illumination wavelengths.

1.6.8. C-dots in catalysis

C-dots stand out as promising candidates in the realm of photocatalysis, exhibiting unique fluorescence behavior and photoelectron transfer properties that are key to high-performance photocatalysts. These C-dots can be tailored by adjusting their surface functional groups and reducing their band gaps, thereby promoting efficient electron transfer during reactions. In addressing environmental pollution, advanced photocatalyst materials derived from C-dots play a central role in the degradation of dyes.

For instance, Sun et al. synthesized a composite photocatalyst comprised of N-C-dots and Bi_2O_3 for RhB degradation [214]. Their findings revealed that N-C-dots/Bi_2O_3 exhibited higher photocatalytic efficiency than C-dots/Bi_2O_3, pure Bi_2O_3, and Bi_2O_3 nanoparticles, as depicted in Figure 25a. In another study, Zhuo et al. reported a photocatalyst composed of C-dots and rutile TiO_2 for the degradation of MB. Surface photovoltage measurements demonstrated that the composite photocatalyst's efficiency was nine times greater than that of C-dots combined with anatase TiO_2. Control experiments with pure rutile TiO_2, pure anatase TiO_2, or pure C-dots as catalysts showed minimal reduction of MB, highlighting the excellent photocatalytic activity of the C-dots/rutile TiO_2 composite, as depicted in Figure 25b [215]. Furthermore, a GQDs/Cu_2O composite photocatalyst was developed by Li et al. for the photocatalytic degradation of MB [216]. This composite achieved a remarkable 90% photocatalytic degradation efficiency, indicating the significant contribution of GQDs/Cu_2O to MB degradation, as shown in Figure 25c. Control experiments using only pure GQDs or Cu_2O as photocatalysts resulted in minimal MB reduction.
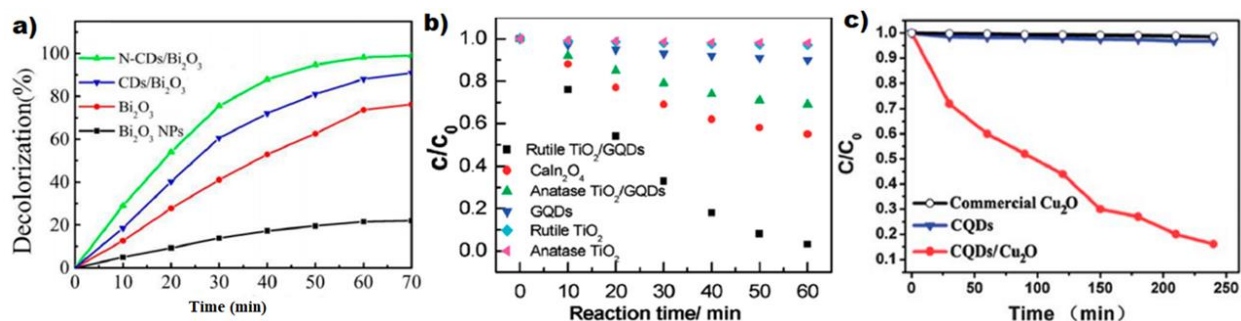
Figure 25. (a) Rate of RhB decolorization mediated by different photocatalysts under simulated sunlight irradiation [214], (b) Degradation of MB by C-dots/rutile TiO_2 composite photocatalyst [215], (c) GQDs/Cu_2O composite photocatalyst [216].

1.6.9. C-dots in LEDs

C-dots possessing luminescent properties have garnered extensive attention, particularly in the context of LEDs, where they offer the potential to replace toxic SQDs and rare earth metals [217], [218]. However, a significant challenge in utilizing C-dots in LEDs is the phenomenon known as AIQ, which can hinder their performance.

In a study by Yang et al., C-dots were synthesized with blue and yellow-green emissions in solutions at pH values of 2.1 and 1.0, respectively [219]. Interestingly, these emissions shifted to yellow and orange-red when in the solid-state. The distinct emission behaviors in solution can be attributed to variations in the conjugation degree at different pH values, influencing the carboxyl and amino groups during the carbonization process. Conversely, the altered emissions in the solid state compared to the solution arise from particle cross-linking, resulting in a reduced band gap. Subsequently, Chen et al. developed C-dots with AIE properties, wherein monomers exhibited blue emission that was quenched by AIQ [220]. This was accompanied by the appearance of yellow emission at longer wavelengths due to AIE, particularly in the solid powder form, with a high QY of 65%. Furthermore, the need for long-wavelength emissive C-dots with hydrophilic properties and high QY led to research by Lu et al., who successfully synthesized red-emitting C-dots with an impressive QY of 33.96% [221]. These particles were incorporated into PMMA and employed in red and white LEDs. In a separate study, C-dots with a maximum emission at 714 nm and a QY of 22.64% were synthesized using a solvothermal method [222]. These C-dots displayed a blue shift in emission attributed to self-oxidation in the

presence of oxygen, a characteristic utilized in preparing white-emitting diodes without the need for additional luminescent materials.

1.7. Aims and objectives

The aim of this research is to develop a new generation of PL materials that are cost-effective, scalable, and suitable for high-demand applications.

The objectives of this thesis are as follows:

- To develop and optimize post-synthesis treatments to enhance the PL properties of C-dots.
- To evaluate the toxicity and antimicrobial properties of surface-treated carbon dots for potential applications.

Gaps in current knowledge

There are several gaps in current knowledge regarding C-dots. While it is understood that factors such as particle size, surface functionalization, and structural features influence their optical behavior, the exact mechanisms behind their PL remain unclear. Additionally, existing synthesis methods often produce C-dots with inconsistent sizes and surface properties, which limits their reproducibility and scalability for broader applications. Furthermore, research on the long-term biocompatibility of C-dots, particularly in living organisms, is insufficient, posing challenges for their biomedical use in imaging and drug delivery.

What needs to be improved

There are several areas where improvements are needed in the development and application of C-dots. First, a deeper understanding of the relationship between C-dot structure and functional properties is required. Research should focus on using electrochemical treatments to precisely control their size, surface charge, and optical properties, ensuring consistent and reproducible outcomes. Additionally, comprehensive studies are necessary to evaluate the long-term stability, toxicity, and bioaccumulation

potential of C-dots in biological systems, particularly concerning their interactions with cells and tissues over extended periods.

Hypothesis

The hypothesis of this thesis is that simple post-synthesis treatments can enhance the optical properties of C-dots derived from scalable pyrolytic strategies, while maintaining their biocompatibility and introducing new functionalities.

Potential applications

The potential applications of C-dots developed in this thesis are diverse and impactful. Their enhanced PL properties make them suitable for use as stable and bright imaging agents in cellular imaging and diagnostics. Additionally, the modified C-dots exhibit significant antimicrobial activities, positioning them as ideal candidates for infection control in medical settings and for use in materials designed to prevent fungal infections and biofilm formation. The combination of optical and antimicrobial functionalities also enables these C-dots to be incorporated into advanced materials, such as smart coatings or sensors with integrated antifungal properties. Furthermore, the method developed in this thesis provides a cost-effective and scalable approach for producing C-dots, facilitating their widespread industrial application.

Chapter 2: Experimental section

2.1. Materials

Carbon-Based Nanomaterials

- **Graphene Quantum Dots**: Imidazole-modified, Aminated, and Chlorine-functionalized (ACS Material).

- **Anthracene**: 99% (Sigma-Aldrich).

Chemicals and Reagents

- **Acids**:

  - Citric acid monohydrate 99% (Alpha Aesar).

  - Nitric acid (HNO_3) (Sigma-Aldrich).

- **Salts**:

  - Sodium hypochlorite solution (NaClO) (Sigma-Aldrich).

  - Sodium chloride (NaCl) (Sigma-Aldrich).

  - Potassium chloride (KCl) (Sigma-Aldrich).

  - Calcium chloride ($CaCl_2$) (Sigma-Aldrich).

  - Potassium iodide (KI) (Sigma-Aldrich).

  - Sodium sulfate (Na_2SO_4) (Sigma-Aldrich).

  - Sodium carbonate (Na_2CO_3) (Sigma-Aldrich).

  - Sodium hydrogen carbonate ($NaHCO_3$) (Sigma-Aldrich).

  - Sodium thiosulfate ($Na_2S_2O_3$) (Sigma-Aldrich).

- **Organic Compounds**:

  - Urea (Sigma-Aldrich).

- o Ethanolamine (EA) (Alpha Aesar).

- o 2,5-Bis(5-tert-butyl-2-benzo-oxazol-2-yl) thiophene (BBOT) (Thermo Fisher Scientific).

- o Isopropyl alcohol, 70% (Sigma-Aldrich).

Biological Reagents

- **Cell Culture Media and Additives**:

  - o Dulbecco's Modified Eagle Medium (DMEM) (Thermo Fisher Scientific).

  - o Fetal Bovine Serum (FBS) (Sigma-Aldrich).

  - o L-Glutamine (Thermo Fisher Scientific).

  - o Phosphate Buffered Saline (PBS, prepared in-house).

- **Dyes and Indicators**:

  - o Trypan Blue (Sigma-Aldrich).

  - o 3-[4,5-dimethylthiazol-2-yl]-2,5-diphenyl-tetrazolium bromide (MTT) (Sigma-Aldrich).

  - o PrestoBlue (Sigma-Aldrich).

Biological Samples

- **Cells**:

  - o HeLa cells (Sigma-Aldrich).

  - o U87 cells (Sigma-Aldrich).

- **Microorganisms**:

  - o Escherichia coli (ATCC).

  - o Staphylococcus aureus (Sigma-Aldrich).

  - o Talaromyces pinophilus (T. pinophilus) ATCC 11797 (ATCC).

Analytical Tools and Supplies

- **Membranes**:

  - SnakeSkin Dialysis Tubing, 3.5 kDa MWCO, 35 mm (Thermo Fisher Scientific).

  - Benzoylated Dialysis Tubing, 1 kDa MWCO, 10 mm (Sigma-Aldrich).

- **Colloidal Silica**:

  - LUDOX HS-30, 30 wt.% (Sigma-Aldrich).

Miscellaneous

- **Cleaning Agents**:

  - Virkon (Sigma-Aldrich).

- **Nutrient Media**:

  - Nutrient broth (Breckland Scientific).

2.2. Synthesis protocols

C-dots were synthesized via the pyrolysis of citric acid (CA) and ethanolamine (EA) using a previously established method (Figure 26) [1]. In a typical procedure, 30.00 g of CA and 28.61 g of EA were mixed in a round-bottom flask and heated to 180 ℃ under reflux for 30 minutes in ambient air. The condenser was then removed, and the temperature was increased to 230 ℃ for an additional 30 minutes. The resulting material was transferred to a crucible and further pyrolyzed in an oven at 300 ℃ for 1 hour. The pyrolyzed product was treated with 400 mL of 1.5 M HNO_3 at 100 ℃ for 16 hours. Finally, the oxidized material was purified by dialysis using SnakeSkin Pleated Dialysis Tubing (3.5 kDa MWCO) and subsequently freeze-dried.
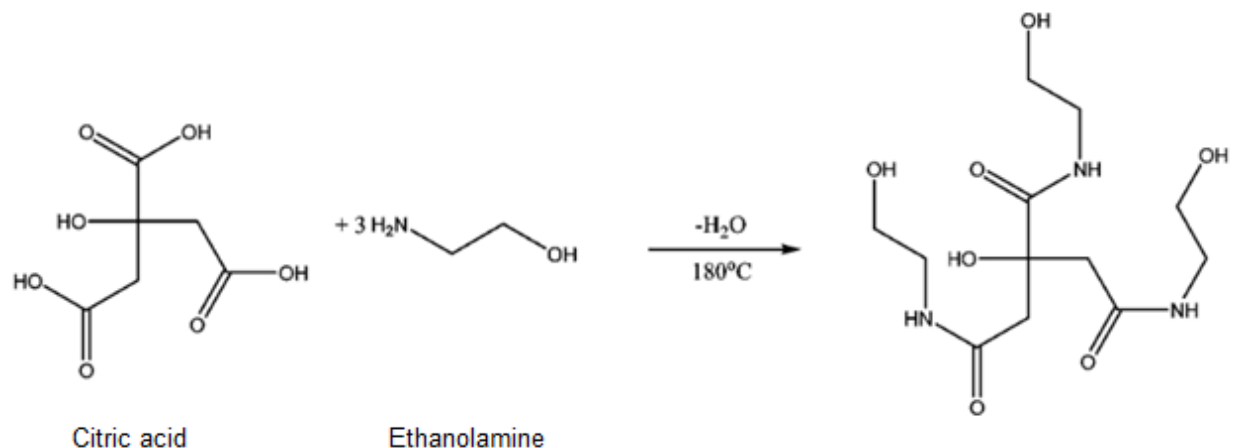
Figure 26. Reaction scheme showing the interaction between citric acid and ethanolamine) leading to the formation of organic fluorophore that is then carbonized into C-dots.

To synthesize the CU-dots for this study, we combined CA and urea (U) in two different molar ratios: 1:50 and 1:100, resulting in materials labeled as CU50D and CU100D, respectively (Figure 27). Initially, precise amounts of CA and U were weighed and placed into a porcelain crucible. These crucibles were then inserted into a furnace and heated gradually to 230°C, at a rate of 1°C/min, for a duration of 1 hour. Once the synthesis process was complete, the resulting brown solids were left to cool overnight in the furnace until reaching room temperature. Subsequently, the solid products were transferred to a mortar and ground into fine powders.

The powders obtained from the synthesis were then dissolved in water, yielding dark brown solutions. These solutions were subjected to extensive dialysis against water using Snakeskin Dialysis Tubing with a MWCO of 3.5 kDa. Dialysis was carried out for a period of 10 weeks to ensure the removal of impurities and undesirable by-products from the aqueous dispersions of CU-dots. Following dialysis, the filtered and purified aqueous solutions of carbon dots were frozen at -20°C for 24 hours. Subsequently, they underwent freeze-drying for a duration of 5 days at -50°C. Upon completion of the freeze-drying process, the as-prepared CU powders exhibited a dark brown color, indicating the successful synthesis of CU-dots.
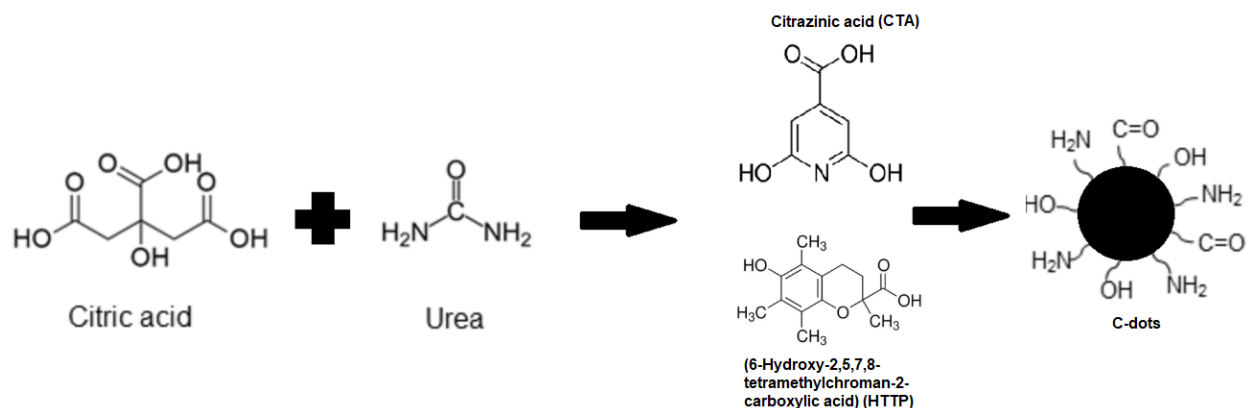
Figure 27. Schematic illustration of the preparation of C-dots from citric acid and urea.

2.3. Characterization methods

2.3.1. UV-Vis Spectroscopy

The absorption of light results in the excitation of particles, particularly electrons, by UV-Vis radiation, and their immediate de-excitation through the emission of heat or light. Typically, the excitation of bound electrons is responsible for absorption. Thus, the wavelengths of absorptions can be correlated with the types of bonds in the examined particles. Additionally, material absorption can be related to the quantitative analysis of the sample.

Light is produced by a common incandescent lamp and is analyzed by a prism across the entire visible spectrum. Subsequently, electromagnetic radiation can pass through a second monochromator and have an effect on the cell or sample. The wavelengths that traverse the sample are collected by a detector, which converts the optical signal into electrical. Concentration (c) is linked to absorption (A) through the equation $A=\varepsilon bc$, where ε is a constant and b is the optical path within the cell (Figure 28).
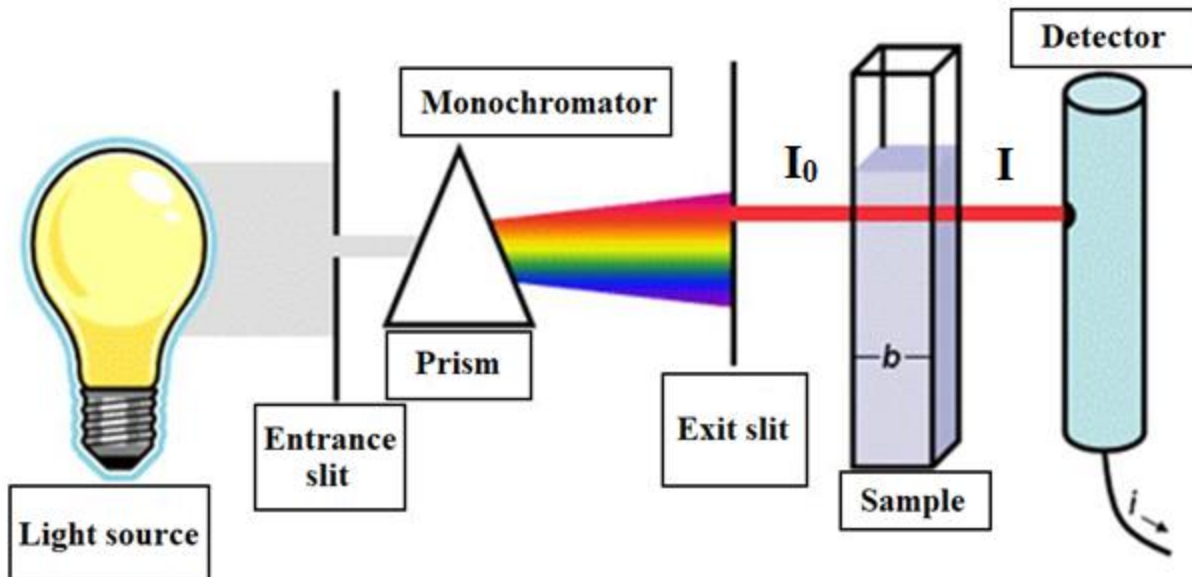
Figure 28. Visualization of the optical path inside a UV-Vis spectrophotometer.

UV-Vis spectroscopy is employed to determine the λ_{ex} and absorption spectra of C-dots. The π-electrons or n-electrons of the examined molecules absorb the energy of ultraviolet or visible light depending on the energy gap until the highest anti-bonding molecular orbitals. C-dots typically exhibit optical absorption in the ultraviolet spectrum with a tail extending into the visible spectrum. In some cases, "shoulders" may appear in the spectra due to the π-π* transitions (i.e., the transition of an electron from a bonding π orbital to an antibonding π* orbital) of double bonds between carbons (C=C) or n-π* transitions of the double bond between carbon and oxygen (C=O). There are four possible transitions, namely π-π*, n-π*, σ-σ*, and n-σ* (Figure 29).

All specimens underwent analysis utilizing a UV-3600 Shimadzu UV-Vis-NIR spectrophotometer. The signals were detected and processed using UVProb – [Kinetics] software. The testing involved the samples in a solution state contained in a quartz cuvette.
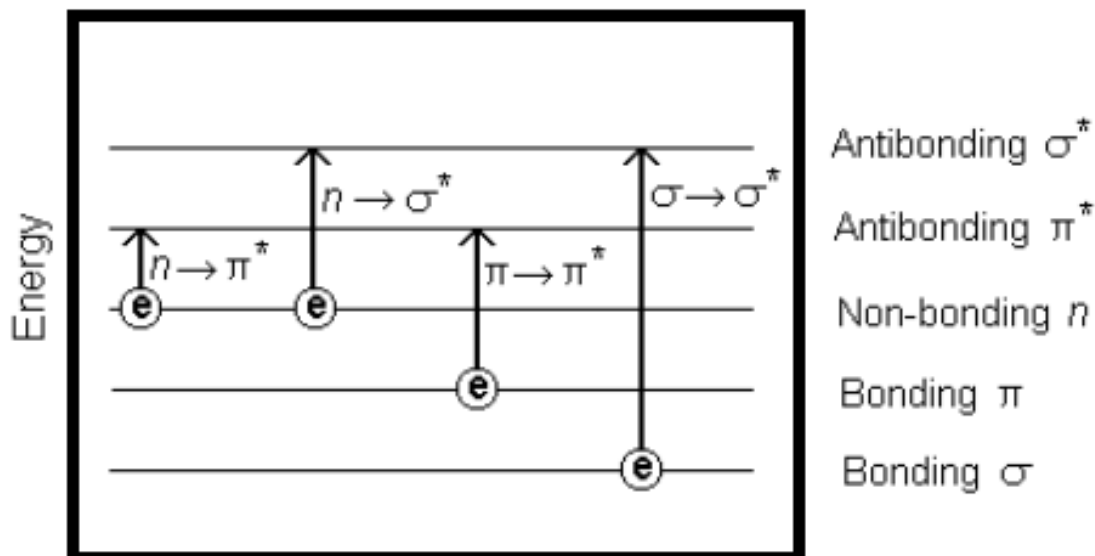
Figure 29. Schematic representation of electronic transitions between bonding and antibonding orbitals.

2.3.2. FTIR spectroscopy

FTIR spectroscopy is a powerful analytical technique employed for the identification of a wide range of materials, including organic, inorganic, and polymeric substances. This method utilizes infrared light to probe the molecular composition of samples, providing valuable insights into their chemical structure. Operating on the principle of scanning the samples with infrared radiation, FTIR spectroscopy enables the detection of alterations in the material composition through changes in the characteristic pattern of absorption bands.

In the FTIR process, infrared radiation, typically in the range of $10,000–100$ cm^{-1}, is directed onto the sample. Part of this radiation is absorbed by the sample, while the remainder passes through. The absorbed radiation undergoes a transformation within the sample, converting into vibrational or rotational energy. The resulting signal, detected by the instrument, produces a spectrum spanning from 4000 to 400 cm^{-1}. This spectrum serves as a molecular fingerprint for the analyzed samples. One of the remarkable features of FTIR spectroscopy is its capability to generate unique fingerprints for different molecules. This inherent molecular specificity arises from the distinct vibrational and rotational energy levels associated with each molecular structure. Consequently, FTIR spectroscopy stands out as an exceptional tool for chemical identification, allowing

researchers and analysts to discern the specific composition of diverse materials based on their characteristic infrared spectra [223].

All C-dot samples were subjected to analysis in a solid state. The mass of the solid samples used was only sufficient to cover the crystal (moving mirror). An Agilent Technologies Cary 630 FTIR instrument, coupled with MicroLab PC software, was employed for signal analysis.

2.3.3. FL spectroscopy

Fluorescence spectroscopy is a widely used technique to study the optical properties of materials, including C-dots. Fluorescence occurs when a molecule absorbs a photon of light and undergoes an electronic transition to an excited state. The excited state is unstable and will rapidly return to the ground state, emitting a photon of light in the process. The emitted light has a longer wavelength and lower energy than the absorbed light, and the difference in energy is lost as heat.

Upon absorption of a photon with appropriate energy, a series of photophysical processes ensue within a molecule, such as internal conversion, vibrational relaxation (loss of energy without light emission), fluorescence, intersystem crossing (transition from a singlet state to a triplet state), and phosphorescence. The variety of the molecular transitions of electrons are illustrated by the Jablonski diagram (Figure 30) [224]. In intricate detail, the electron residing in the ground molecular orbital state absorbs energy and transitions to a higher unoccupied molecular orbital, referred to as the excited state of the electron. The PL phenomena refer to the emission of light from fluorescent materials. During this process, excited electrons revert to the ground-state orbitals, emitting photons of varying intensities.
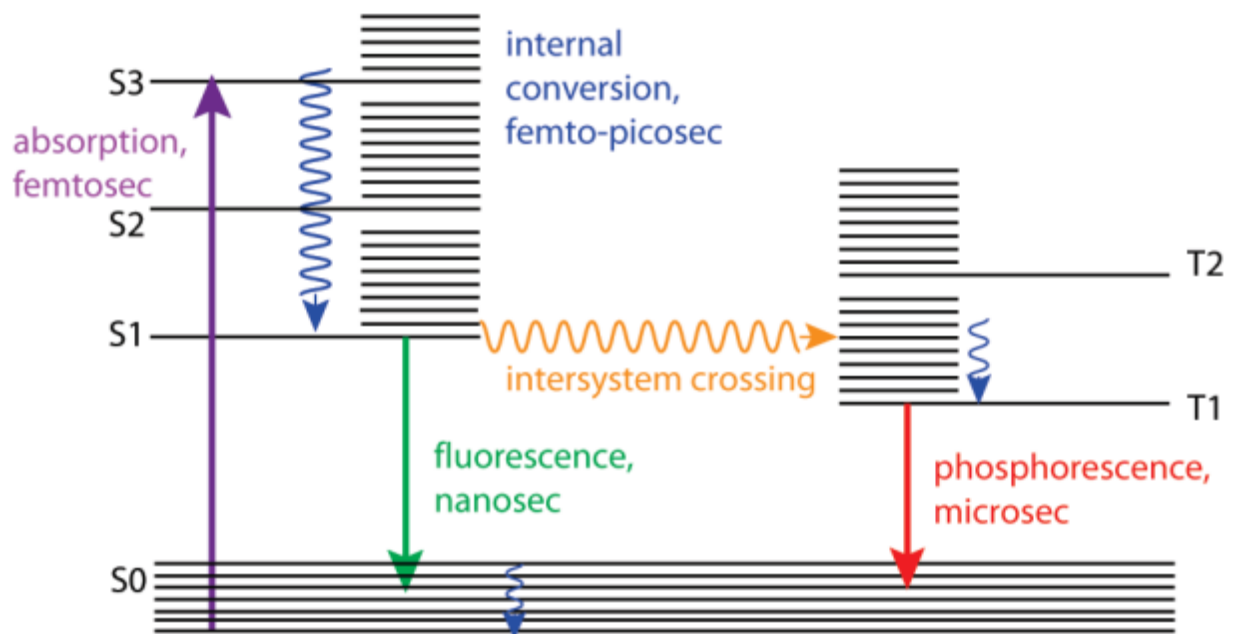
Figure 30. Jablonski diagram and a time scale of photophysical processes [224].

All specimens underwent analysis utilizing the FluoroMax-4 Spectrofluorometer from HORIBA JOBIN YVON. The signals were both detected and assessed through the FluorEssence V3.5 software, employing varied excitations ranging from 320 nm to 600 nm with increments of 20 nm. The samples were assessed in a solution form utilizing a 4 ml quartz cuvette with fully transparent walls.

2.3.4. PL lifetime

The PL lifetime serves as a complementary analysis to emission spectra, offering insights into the duration a fluorophore interacts or diffuses within its surroundings. It signifies the time the fluorophore resides in the excited state before returning to the ground state. For measuring FL, two distinct methods can be employed: time-domain and frequency-domain. The time-domain approach involves monitoring the time-dependent emission intensity of the fluorophore during excitation. Luminescent material is exposed to a pulse of light, causing fluorophores to transition to the excited state, forming an initial fluorophore population. Subsequently, this initial population decays exponentially over time due to non-radiative processes and fluorescence emission. PL lifetimes are derived from the slope of these decays, represented as the logarithm of emission intensity versus time.

The fluorescence decay post-pulse excitation is depicted in Figure 31. Decay of fluorescence intensity over time in a uniform population of excited fluorophores is described by an exponential function. A monoexponential decay indicates the presence of fluorophore populations with longer PL lifetimes, while multiexponential decay suggests the existence of various time components which have shorter lifetimes.
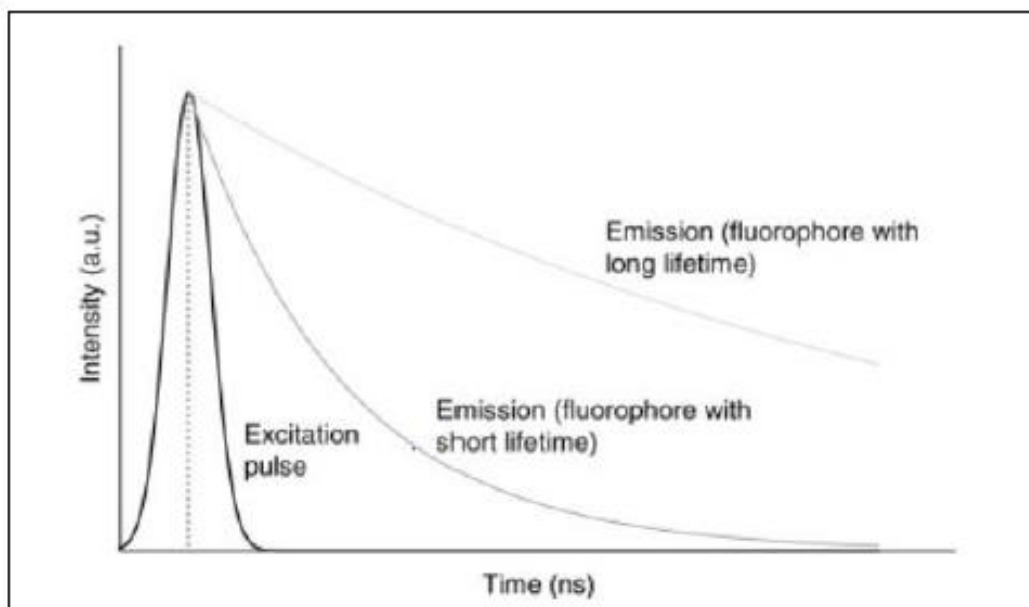
Figure 31. The potential scenarios of fluorescence decay following pulsed excitation, where the emitted fluorescence is observed in a time-resolved way [225].

Each process happens with a certain probability, characterized by decay rate constants (k). The mean lifetime, or simply lifetime, is the average length of time т for the set of molecules to decay from one state to another: т = 1/k. It can also be shown that the lifetime of a photophysical process is the time required by a population of N electronically excited molecules to be reduced by a factor of e. Correspondingly, the FL is the time required by a population of excited fluorophores to decrease exponentially to N/e via the loss of energy through fluorescence and other non-radiative processes. The equation which describes the exponential decay of the excited state population is:

$$N(t) = N_0 \cdot e^{-kt}$$

The accuracy of the computed bi-exponential deconvolution fitting was additionally assessed by comparing chi-square values (χ^2) and examining the distribution of residuals, aiming for an approximation close to 1. The amplitude-weighted τ_{avg} were determined using the following equation:

$$\tau_{avg} = \frac{\sum \alpha_i \tau_i^2}{\sum \alpha_i \tau_i}$$

Where: where τ_i is the time component of multiexponential decay fitting and α_i is the fractional weight for each lifetime component.

All specimens were examined utilizing the LifeSpec II model from EDINBURGH INSTRUMENTS. The signals were identified and assessed using the F980 software, employing two distinct laser beams at 375 nm and 450 nm. The analysis of materials was conducted on a solution placed in a 4 ml quartz cuvette with fully transparent walls.

2.3.5. Fluorescence microscopy

A fluorescence microscope is an optical microscope that uses fluorescence to study the properties of organic or inorganic substances. The term "fluorescence microscope" refers to any microscope that utilizes fluorescence to create an image, whether it is a simpler system like a fluorescence microscope or a more complex design like a confocal microscope, which uses optical sectioning for better resolution of the fluorescence image [226].

The sample is illuminated with specific wavelengths of light, which are absorbed by fluorophores, causing them to emit light of longer wavelengths (i.e., with a different color than the absorbed light) (Figure 32). The excitation light is separated from the much weaker emitted fluorescence using an emission spectral filter. Typical components of a fluorescence microscope include a light source (the most common lamps are xenon or mercury, and more advanced forms include high-power LEDs and lasers), the excitation filter, and the dichroic mirror. Filters and the dichroic beam splitter are chosen to match the excitation and emission spectral characteristics of the fluorophore used to label the sample. Multicolored images of different types of fluorophores are composed by combining multiple monochromatic images. Most fluorescence microscopes used are

epifluorescence microscopes, where both the excitation of the fluorophore and the detection of the fluorescence occur through the same path of light (i.e., through the objective lens).
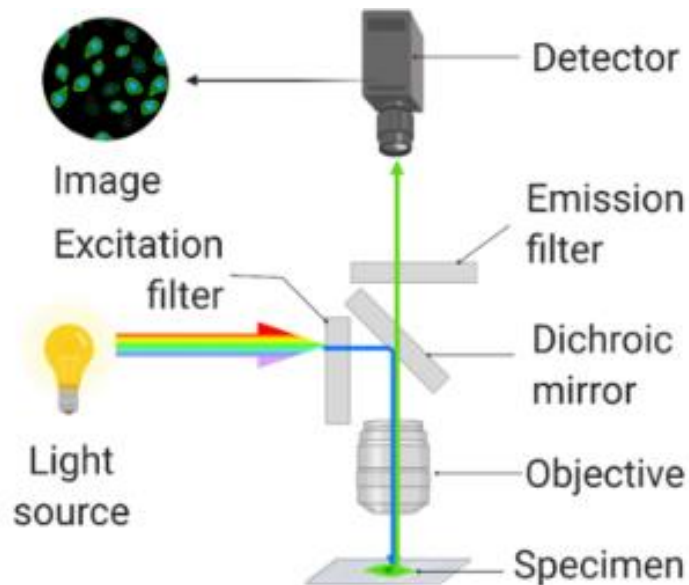
Figure 32. The basic setup of a fluorescence microscope [226].

2.3.6. Transmission Electron Microscopy

TEM is a powerful technique renowned for its ability to provide high-resolution morphological and structural insights into materials at the nanoscale [227]. Widely recognized as a cornerstone in the field of sample characterization, TEM is frequently employed due to its exceptional imaging capabilities.

The fundamental principle underpinning TEM involves the interaction of electrons with the specimen. A beam of electrons (about 100-200 kV) is transmitted through the sample, resulting in the generation of highly magnified images, often reaching up to 2 million times magnification. In Figure 33, which portrays the internal components of a TEM, the instrument features an electron source at its apex, emitting electrons that traverse a vacuum-filled column. Electromagnetic lenses within the column focus the electrons into a remarkably thin beam, which subsequently passes through the sample. During this traversal, certain electrons are scattered, while others are not. The unscattered electrons

are then collected by a detector, producing a bright-field image that portrays the components of the sample. The intricate workings of TEM allow for the visualization of nanomaterials with extraordinary detail.
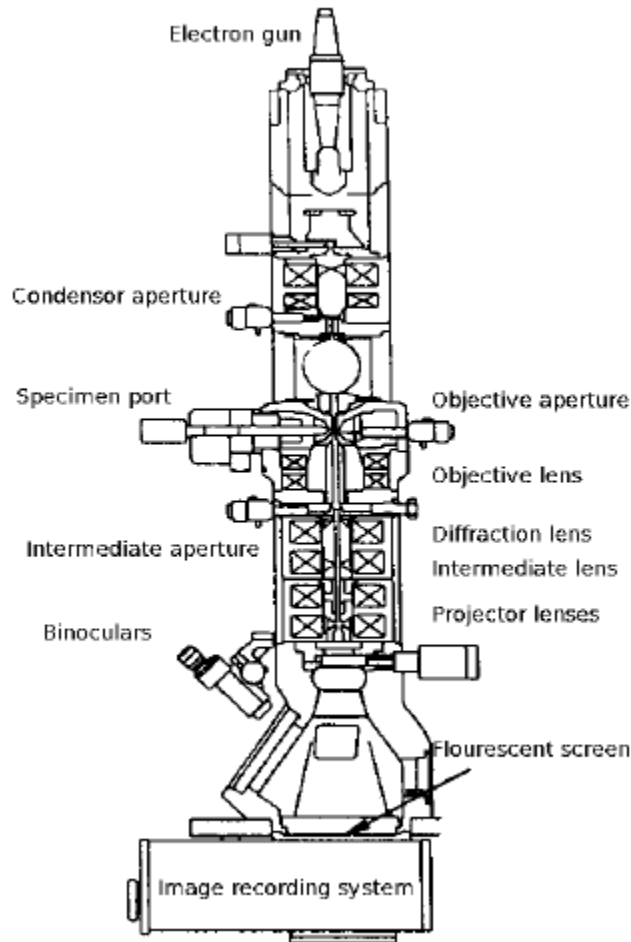
Figure 33. Schematic representation of segments of the TEM [228].

2.3.7. Zeta potential

Zeta potential plays a crucial role in governing the electrostatic interactions within particle dispersions, thus influencing the stability of colloidal systems. Understanding zeta potential is vital for optimizing the formulations of suspensions, as well as predicting their long-term stability. In aqueous media, most colloidal dispersions carry an electric charge, leading to the development of an electrical double layer (EDL) around the particles. This EDL consists of an inner region (Stern layer) where ions are tightly bound and an outer diffuse layer where ions are less strongly attached. The boundary between these layers,

known as the surface of hydrodynamic shear or slipping plane, represents the zeta potential, indicating the stability of the colloidal system (Figure 34) [229].
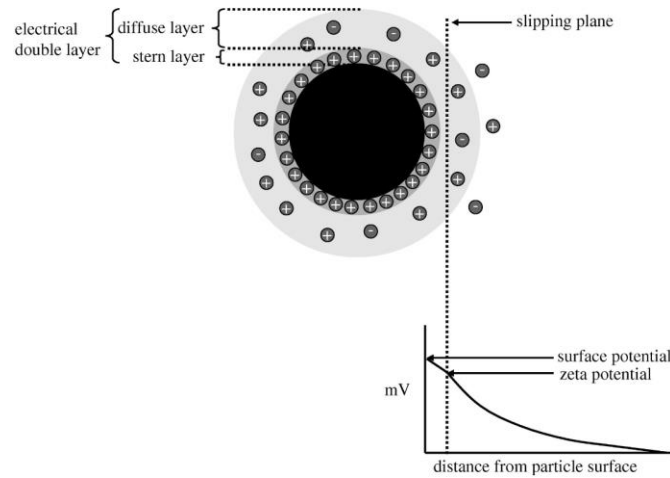
Figure 34. Illustration depicting the EDL surrounding a particle in an aqueous solution, including the location of the slipping plane. The zeta potential represents the electrical potential at the slipping plane [229].

The zeta potential of colloidal dispersions is commonly determined using micro-electrophoresis techniques. In this method, a voltage is applied across a cell containing the particle dispersion, causing charged particles to move towards oppositely charged electrodes. Their velocity is measured and expressed as electrophoretic mobility in unit field strength. Light scattering is a widely employed technique for assessing particle mobility, with Laser Doppler electrophoresis being particularly common. This method detects small frequency shifts in scattered light resulting from particle movement in an electric field. The frequency shift (Δf) is equal to:

$$\Delta f = \frac{2\,\upsilon\,\sin\frac{\theta}{2}}{\lambda}$$

where υ is the particle velocity, λ is the laser wavelength and θ is the scattering angle. The measured electrophoretic mobility (U_E) is then converted into zeta potential (ζ) using Henry's equation:

$$U_E = \frac{2\varepsilon\zeta F(\kappa a)}{3\eta}$$

where ε is the dielectric constant of the dispersant, F(κα) is the Henry function and η is the viscosity.

Zeta potential analysis was conducted using a Malvern Panalytical Zetasizer Nano-ZS equipped with a 532 nm He-Ne laser, on solutions with a concentration of 0.05 mg/mL at 25°C. To adjust the pH, small quantities of 1.0 M HCl and 1.0 M NaOH were added to the solutions. Disposable folded capillary cells from Malvern Panalytical were utilized for sample placement. All measurements were carried out in triplicate, and the averaged results were recorded.

2.3.8. Elemental analysis

Elemental analysis served as both a qualitative and quantitative method, enabling the identification of primary organic constituents, including carbon, hydrogen, nitrogen, and oxygen [230]. In this approach, an organic substance underwent oxidative decomposition, resulting in the production of carbon dioxide, water, and nitric oxide. The masses of the combustion products were then employed to compute the values for the unknown samples.

Elemental analysis was conducted utilizing the Flash 2000 CHNS-O Analyzer (Thermo Scientific, UK). Prior to the analysis, the instrument underwent calibration using an immeasurable pan (referred to as a bypass) followed by three runs of a small quantity of the standard 2,5-(Bis(5-tert-butyl-2-benzo-oxazol-2-yl) thiophene, commonly known as BBOT (Thermo Scientific, UK). The CHN analysis was carried out in aluminum pans (CE INSTRUMENTS, UK), while silver pans (CE INSTRUMENTS, UK) were employed for the analysis of O. Each sample underwent duplicate analyses.

2.3.9. Quantum yield

The QY is a crucial parameter in fluorescence spectroscopy, representing the ratio of emitted photons to absorbed photons. Paired with FL, it stands out as one of the most vital characteristics defining the behavior of a fluorophore. Assessing the QY for a specific fluorophore involves comparing it with highly fluorescent dyes, which serve as a set of reference standards with well-established QYs. Quantifying the QY suggests comparing the wavelength-integrated intensities of the examined samples with those of reference dyes, both excited by a light source at the same wavelength. Generally, a higher QY value

indicates the sample's greater capability to exhibit brighter emission. The calculation of QY for liquid dispersions of carbon-based nanomaterials involved employing the equation:

$$\Phi = \Phi_R \times (\frac{m}{m_R}) \times (\frac{\eta^2}{\eta_R^2})$$

Here, Φ_R represents the QY of the reference dye, m is the slope obtained from linear regression of the tested material, m_R is the slope obtained from linear regression of the reference dye, η^2 denotes the refractive index of water, and η_R^2 signifies the refractive index of ethanol. Anthracene (Φ=0.27) was dissolved in ethanol and utilized as a reference dye with an λ_{ex} of 365 nm. Ultrapure water was utilized to prepare aqueous solutions of the investigated nanomaterials. Absorbance measurements were conducted using a UV-3600 spectrophotometer (SHIMADZU), while integrated PL intensity was assessed using a FluoroMax-4 spectrofluorometer (HORIBA Scientific) along with quartz cuvettes featuring a 1.0 cm pathlength. The signals were detected and analyzed using FluorEssence V3.5 software. To minimize re-absorption effects, absorbance values were maintained below 0.1.

2.3.10. Cell culture procedures

2.3.10.1. Cell lines

C-dots exhibit a remarkably low level of toxicity and exceptional biocompatibility. In the current study, all synthesized samples underwent toxicity assessments through two distinct assays: MTT and PrestoBlue assay. The evaluation encompassed two different cell lines: HeLa and U87.

2.3.10.1.1. HeLa cell lines

The HeLa cells, derived from the cervical cancer of a young woman, represent a crucial and historic cell line in cancer research. They are recognized as the first continuous cancer cell line employed in *in vivo* studies. Over the years, HeLa cells have played a pivotal role in validating various physiological processes within the human body [231].

2.3.10.1.2. U87 cell lines

The U87 cells, originating from malignant glioma, specifically glioblastoma, were isolated from a male patient. These cells, crucial in neuroscience and immune oncology research, exhibit an epithelial cell morphology. Notably, U87 is recognized as one of the most aggressive cell lines among glioblastoma cells.

2.3.10.2. Aseptic techniques

All experiments, both cell and tissue culture, were conducted in a sterile environment [232]. Aseptic techniques, vital for the success of cell culture procedures, revolve around maintaining the air, floor, and working surfaces free from contamination (dust and microorganisms). Consequently, all procedures were executed within a laminar flow cabinet. The laminar flow sterile cabinet needs to be activated at least 15 minutes prior to the start of any experiment, allowing sufficient time for the machine to circulate an ample amount of sterile air and prepare the environment for sterilization. Subsequently, the interior of the laminar flow sterile cabinet should be thoroughly sprayed with isopropyl alcohol (of 70% concentration) and wiped clean. Following this process, the laminar flow sterile cabinet is deemed ready for experimentation. To uphold effective aseptic techniques, any samples or materials involved in cell culture processes within the laminar flow sterile cabinet must undergo autoclaving and be treated with an abundant application of isopropyl alcohol at 70% before getting placed in the laminar fume hood. The laminar flow sterile cabinet maintains a continuous horizontal airflow from the back to the front, ensuring a sterile environment throughout the experiment.

2.3.10.3. Media preparation

The cell and tissue culture necessitates a growth medium rich in nutrients, proteins, and antibacterial agents to ensure proper cell proliferation with the essential elements for growth. In this study, DMEM was employed, consisting of sterile-filtered DMEM, (-) L-leucine, (-) L-methionine, 4.5g/L glucose, 4.0mM L-glutamine, sodium pyruvate, and phenol red, making it a substantial energy source. DMEM exhibits some capability to mimic the composition of body plasma and blood. However, susceptibility to microbial contamination led to the addition of penicillin-streptomycin antibiotic (1%). To further

improve DMEM, FBS (10%) and L-Glutamine (1%) were introduced. With these adjustments, the medium is now prepared for use in various cell culture processes.

2.3.10.4. Cell viability calculations

Assessing the cell viability is crucial for determining the viable cell count in a flask. It provides essential information for subculturing cells and calculating the necessary cell suspension for various tests. Two methods are commonly employed for cell counting: 1) Utilizing a haemocytometer and coverslip, and 2) Employing a cell counter machine.

2.3.10.4.1. Haemocytometer

The haemocytometer and coverslip must undergo cleaning with alcohol and thorough drying before use. The coverslip is moistened with PBS and affixed well onto the haematocytometer chambers. In a sterile Eppendorf tube, 100 µL of the cell suspension is combined with 400 µL of Trypan Blue to stain the cells, and the mixture is gently mixed. Using a pipette, 10 µL of the Trypan Blue-treated cell suspension is carefully placed on one of the haemocytometer chambers, allowing capillary action to evenly load the entire chamber. The process is repeated for the other chamber. Cell counting is performed using a light microscope with a 10X objective.

The haemocytometer features a square with nine grids, each composed of 16 squares with a side length of 1 mm, and the capacity of each grid is 10^{-4} mL of cell suspension (Figure 35). Living cells are counted individually in every block of grids (red line). Cells are considered only if they are inside the grid or lie on the red square's right or bottom sides. The number of viable cells is determined by averaging the cell counts from all 4 blocks. This average is then multiplied by 10^4 to calculate the number of cells in 1 mL of the cell suspension. To correct for the 1:5 dilution (100 µL of cell suspension and 400 µL Trypan Blue), the number is multiplied by 5, providing the total number of living cells in 1 mL of the cell suspension (e.g. Average number of cells per block * dilution factor * 10^4).
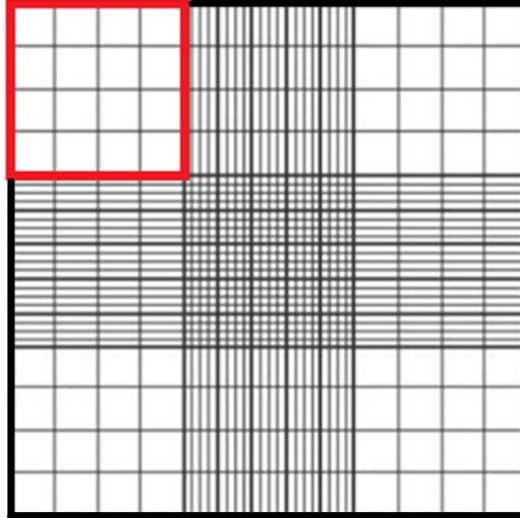
Figure 35. The grids within a single chamber on the haemocytometer.

2.3.10.4.2. Cell counter

The cell countess method involves using an automated counter along with a disposable slide designed for the cell countess, which has two chambers. In a sterile Eppendorf tube, 100 µL of the cell suspension were mixed with 400 µL of Trypan Blue to stain and gently blend the cells. Using a pipette, 10 µL of the Trypan Blue-treated cell suspension were transferred into one of the chambers on the slide. Subsequently, the slide was inserted into a designated slot in the cell countess, and the cells were automatically counted. The cell countess is capable of tallying both living and dead cells, providing a viability percentage.

2.3.10.5. Cell thawing

The cells were stored in 1.5 mL cryogenic vials and preserved by freezing at -70 °C using liquid nitrogen freezers. When needed, the cells underwent a thawing process, where the cryogenic vial was placed in a warm water bath (37 °C) for one minute. Within the laminar flow sterile cabinet, the cells were transferred to a universal tube with 10 mL of media, followed by centrifugation at 800 rpm for 5 minutes. The supernatant was discarded, and the pellet (containing the cells) was resuspended in 10 mL of media. A second round of centrifugation aimed to remove DMSO. After resuspending the pellet in 10 mL of media for the second time, a cell suspension was obtained, and which was now ready for cell-viability counting.

2.3.10.6.   Cell growing and splitting

To replicate the conditions of the human body, cells are cultured in the lab environment. After counting the cells in a suspension, 10^4 cells are transferred into a T-75 flask and topped up to 7 mL with media. The flask is then placed in an incubator set to 5% CO_2 and 37 °C, providing an environment similar to that of blood. Initially, the cells move freely in the medium, but over time, they adhere to the surface of the flask and begin to grow. Cell growth is monitored every 24 hours under a microscope. After 24 hours, the cells reach 20% confluency, and they are left to grow for another 24 hours (Figure 36). Upon rechecking, the confluency increases to 70%, and after another 24 hours, it reaches 85%, indicating readiness for splitting. Splitting is necessary to prevent overcrowding, which can lead to cell death.
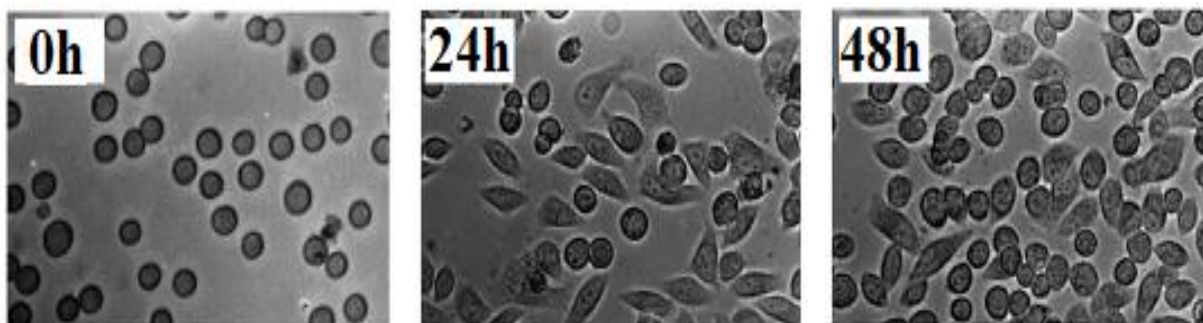
Figure 36. Images obtained with a microscope (20x magnification) to observe the attachment of HeLa cells to the substrate over a period of 48 hours [233].

When cell confluency reaches 85% or higher, it's advisable to perform cell splitting, known as trypsinization. All necessary materials, equipment, and the T-75 flask were placed inside the cabinet using aseptic techniques. The culture medium was then removed from the flask using a sterile pipette and disposed of in a waste container containing Virkon, a disinfectant used to eliminate pathogens [234]. Next, 3 mL of trypsin-EDTA solution were added to the T-75 flask. Trypsin-EDTA, a serine protease enzyme, effectively breaks down the peptide bonds that attach the cells to the flask walls and separates them from each other. The flask was gently shaken for a few seconds to ensure that the trypsin-EDTA solution reached all areas of the flask. Following this, the trypsin-EDTA-treated cells were placed in an incubator with 5% CO_2 at 37 °C for 3 minutes. It's crucial to monitor the incubation time carefully to avoid damaging the cell membranes. After incubation, the

flask was removed from the incubator, and 6 mL of fresh media were added to the flask inside the laminar flow sterile cabinet to neutralize the effect of trypsin.

2.3.10.7.   Cell preservation

Freezing cells is a crucial step to preserve them when they are not actively in use. To freeze cells, they should be in suspension form, achieved by centrifuging the cell suspension at 900 rpm for 5 minutes. After discarding the supernatant into a waste container containing Virkon, the cell pellet is resuspended in 1 mL of freezing media (which consisted of 90% DMEM culture media and 10% DMSO) and transferred to a 1.5 mL cryogenic vial. These vials are then stored in an -80 °C freezer for future use.

2.3.10.8.   Cell viability assays

2.3.10.8.1.   Plating cells

In this study, the toxicity of the synthesized materials was evaluated using the MTT and PrestoBlue assays with HeLa and U87 cell lines cultured in a 96-well plate. The experimental setup necessitated precise control over cell growth in the limited space of each well, and uniform cell populations were crucial for obtaining reliable results.

To plate the cells, they were first prepared in a cell suspension with media, and cell counting was conducted before the plating. Each well was intended to contain 50 µL of cell suspension, with a concentration of $0.5*10^5$ cells/mL. Once the viable cell count/mL of the cell suspension was determined, the volume of media required for dilution was calculated. For a 96-well plate, each well required 50 µL of cell suspension, totaling 4.8 mL for the entire plate (Figure 37).
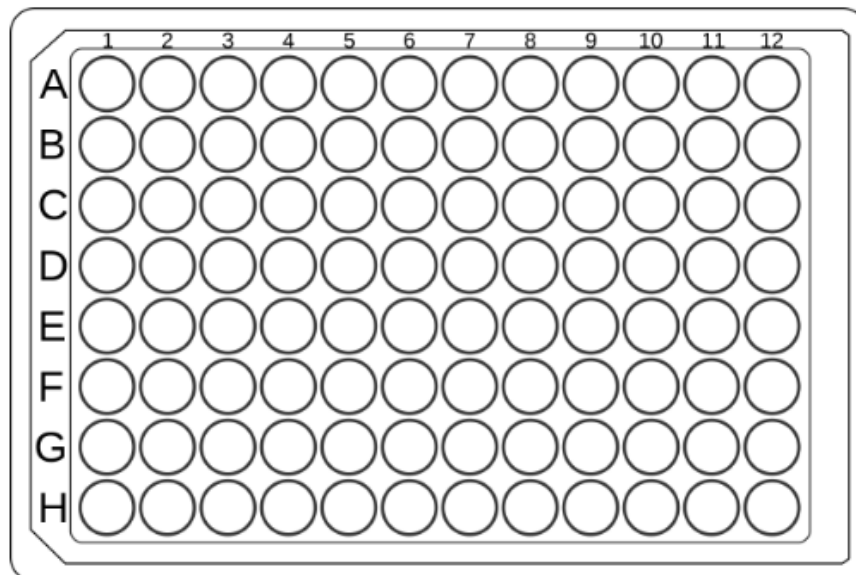
Figure 37. Layout of a 96-well plate.

2.3.10.8.1.1. MTT assay

The compound MTT serves as a reagent employed in a colorimetric assay for assessing cell viability [235]. The MTT assay procedure commences with the plating of cells into a 96-well plate. 50 µL of cell suspension containing $0.5*10^5$ cells/mL was added to each well, except for the first column, where only 50 µL of media was added (blank sample). Subsequently, the 96-well plate was placed in an incubator with 5% CO_2 at 37 °C for 24 hours to allow the cells to adhere to the well surface and recover from the trypsinization process. Following this, 10 different concentrations of the synthesized samples were prepared. The concentrations for each sample were: 10, 20, 30, ..., up to 100 µg/mL, with each sample tested three times. Both a positive control, consisting of the cell suspension without the addition of samples, and a negative control, consisting of media without cells, were utilized. Next, the 96-well plate underwent incubation in an environment with 5% CO_2 at 37 °C for another 24 hours. Following this, 10 µL of the MTT reagent was put into each well, enclosing those with sample-treated cells, the positive control, and the negative control, in a darkened environment. Subsequently, the plate was incubated once more in an environment with 5% CO_2 at 37 °C for 2-4 hours. During this incubation period, living cells initiated the reduction of the tetrazolium salt, resulting in the formation of formazan crystals, while non-viable cells did not participate in this process. As a result, the suspensions in the wells changed into a purple color, varying in intensity. The formazan

product accumulates both inside the cells, manifesting as an insoluble precipitate, in the culture medium, as well as around cell surfaces. Before recording absorbance readings, it is imperative to solubilize the formazan product using an acidified solubilizing solution. This solubilization process additionally induces a color change in phenol red to yellow, minimizing interference with absorbance readings. Consequently, 150 µL of lysis buffer, serving as the solubilizing solution, was put into all 96 wells, and incubated for a duration of 3 hours. Finally, the 96-well plate was inserted into the plate reader to assess the absorbance of the living cells, utilizing a filter with a wavelength range of 550-600 nm. In this project, the TECAN Labtech.com infinite F200PRO plate reader and Omega – Data Analysis software were employed to visualize the collected data.

2.3.10.8.1.2. PrestoBlue assay

PrestoBlue is a reagent based on resazurin which is used to assess cell viability through a fluorescence-based assay [235]. In this quick cell-mediated cytotoxicity test, PrestoBlue undergoes a change from its initial state to its reduced form, resorufin, during the aerobic respiration of metabolically active cells. The reduction of PrestoBlue leads to a red colour, indicating viable cells, as only metabolically active cells can convert PrestoBlue to its red form.

One notable advantage of PrestoBlue is its rapid signal detection within 10 minutes, which is notably shorter compared to other cell viability assays requiring up to 4 hours of incubation. The PrestoBlue assay involves plating cells in a manner similar to the MTT assay. After incubating the 96-well plate in a CO_2 incubator at 37 °C for 24 hours, samples are added following the same procedure as in the MTT assay. The 96-well plate is then further incubated for 24 hours.

Subsequently, 10 µL of PrestoBlue reagent is added to each well, including those with samples-treated cells, positive controls (+ve control), and negative controls (-ve control). The 96-well plate is incubated in a CO_2 incubator at 37 °C for 10 minutes, during which PrestoBlue is reduced by viable cells, resulting in a colour change from blue to pink, with varying intensities depending on the number of viable cells.

Finally, the 96-well plate is subjected to a plate reader, and the absorption of living cells is measured using a filter with a wavelength range of 535-560 nm. The same plate reader

and software used for the MTT assay are employed for data analysis in this project. This streamlined process allows for a rapid and efficient assessment of cell viability in various samples.

2.3.11. Antifungal testing

The process of culturing *Talaromyces pinophilus (T. pinophilus)* ATCC 11797 begins with its acquisition from the American Type Culture Collection (ATCC) and subsequent maintenance on potato dextrose agar plates, stored within a refrigerated environment maintained between 3 to 5°C.

The preparation phase involves: 10 mL of sterile distilled water is introduced into a 50 mL sterile falcon tube. A plate of *T. pinophilus* is carefully transferred into the tube, where it is subjected to a thorough grinding process to liberate the spores. The resulting mixture is then meticulously filtered through sterile filter floss to remove any residual debris. Following filtration, the spore-containing suspension undergoes centrifugation at 4000 rpm for 5 minutes, leading to the separation of spores from the supernatant. This supernatant is discarded, while the concentrated spores are resuspended in another 10 mL of sterile distilled water. This suspension is subjected to a second round of centrifugation to further purify the spores, with the supernatant once again being discarded. The purified spores are then resuspended in a nutrient salt solution, meticulously prepared by dissolving specific quantities of ammonium sulfate, dipotassium phosphate, monopotassium phosphate, magnesium sulfate, sodium chloride, ferrous sulfate, zinc sulfate, and manganous sulfate in 1 liter of distilled water. Additionally, for the preparation of nutrient salt agar, 15 grams of agar powder are incorporated into the solution before autoclaving to ensure sterility.

Moving on to the antifungal testing phase, C-dot solutions are prepared from a stock solution with a concentration of 0.1 mg/mL. These solutions undergo successive dilutions in sterile distilled water, with each dilution being a 1 in 2 dilution, resulting in a range of concentrations from 0.1 mg/mL to 0.0008 mg/mL. Sterile samples, cut to approximately 10 mm x 10 mm in size, are soaked in either water (serving as the control) or C-dot solutions for a period of 30 minutes. Following soaking, the samples are removed and

allowed to dry completely. Subsequently, 100 µL of the fungal spore suspension are evenly spread onto nutrient salt agar plates, onto which the control or test squares are placed. Each test plate consists of duplicate sets of squares, each treated with different dilutions of C-dot solutions, ranging from 0.1 mg/mL to 0.0008 mg/mL. These plates are then incubated at a temperature of 25°C over a period of 28 days, with regular observations conducted at 7-day intervals to monitor any inhibition of fungal growth.

Chapter 3: Electrochemical modulation of C-dot structure and properties

3.1. Introduction

In recent years, various electrochemical methods have been devised to regulate the size, modify the surface, analyse surface structures, and thereby uncover the PL properties of C-dots [236], [237]. C-dots, recognized as one of the most promising nano-emitters, are known for their excitation wavelength-dependent emission and exceptional resistance to photobleaching, offering performance comparable to traditional heavy-metal-based quantum dots [238], [239], [240], [241], [242]. However, the precise mechanism behind the PL behavior of C-dots remains unclear, making the creation of customized C-dots an ongoing challenge. C-dots with well-defined properties can be produced through the thermal processing of renewable materials such as fruits [99] and grass [96], as well as molecular precursors like urea [181], ethanolamine [243] and citric acid [244]. Pyrolysis-based synthesis yields C-dots in various forms, including aqueous solutions, solid states, or embedded within polymer matrices [245].

Due to their unique properties, C-dots have been widely studied for use in various fields, including bioimaging [246], antimicrobial coatings [247], energy conversion [248], and electrocatalysis [166]. When employed in areas such as electrocatalysis, electrochemical sensing, photovoltaics, batteries, and LEDs, C-dots are subjected to different electrochemical potentials. Their electrogeneration can occur through a top-down approach, involving the exfoliation of carbon-based materials like graphene, graphite, carbon nanotubes [249], or charcoal [250], or a bottom-up approach, using electrooxidation or electropolymerization of small molecules such as alcohols [251] and acetonitrile [252]. Ongoing advancements aim to achieve precise control over the size and photoluminescent behavior of C-dots to unlock further applications.

In a previous study, researchers have highlighted the significant impact of cyclic voltammetry on the structure and PL characteristics of pyrolytically synthesized C-dots, providing an important basis for further exploration [253]. They demonstrated that cyclic voltammetry could induce extensive structural rearrangements in C-dots prepared from ethanolamine and citric acid at 230°C. These changes included the formation of

oxygenated defects, such as C–O and C=O groups, and a reduction in C=C bonds, leading to a notable suppression of PL intensity. This process, revealed through XPS and FTIR analyses, also caused shifts in fluorescence emission wavelengths, with a blue shift attributed to surface fluorophores and a red shift associated with carbogenic cores.

Building on this previous research, this chapter explores an electrochemical etching process driven by cyclic voltammetry to induce substantial changes in the structural and optical properties of C-dots. The method promotes extensive surface oxidation and cleavage of carbon-carbon bonds, leading to a progressive reduction in nanoparticle size. Notably, this technique results in a QY enhancement of up to 640%, offering an innovative approach for precise control of size and PL emission. This study provides the first conclusive evidence of this highly efficient restructuring mechanism, unlocking new opportunities for the advanced optimization of C-dots. This chapter, by extending the insights gained from cyclic voltammetry-induced structural changes, demonstrates how electrochemical strategies can be harnessed to tailor C-dot properties for innovative applications in nanotechnology.

3.2. Results and discussion

Synthesis of C-dots

C-dots were prepared through the pyrolysis of a mixture of citric acid (CA) and ethanolamine (EA), following a previously reported method [1]. In a standard procedure, 30.00 g of CA and 28.61 g of EA were combined in a round-bottom flask and heated to 180 ℃ for 30 minutes under reflux in ambient air. Afterward, the condenser was removed, and the temperature was raised to 230 ℃ for an additional 30 minutes. The resulting product was transferred to a crucible and subjected to further pyrolysis in an oven at 300 ℃ for 1 hour. The pyrolyzed material was then treated with 400 mL of 1.5 M HNO_3 at 100 ℃ for 16 hours. Finally, the oxidized product was purified through dialysis using SnakeSkin Pleated Dialysis Tubing (with a molecular weight cut-off of 3500 Da) and subsequently freeze-dried.

Electrochemical Treatment

Chronoamperometry experiments were conducted at room temperature using a Gamry Interface 1000 potentiostat with a three-electrode setup. This setup included an Ag/AgCl electrode as the reference, and two platinum electrodes serving as the working and counter electrodes. C-dots were dispersed in a 0.15 M KCl solution, with the applied voltage ranging from 0.5 to 3.0 V in 0.5 V increments. Each treatment lasted 60 seconds across all tests.

Chemical Treatment

For chemical treatment, 10 mL of a 0.04 mg/mL aqueous C-dot dispersion was stirred into separate beakers containing 10 mL of NaClO solutions at concentrations of 0.1, 0.5, 1.0, 1.5, and 2.0 mM. The mixtures were allowed to react at room temperature for 48 hours before measuring their PL spectra.

3.2.1. Structural properties

3.2.1.1. TEM analysis

TEM analysis demonstrates that untreated C-dots exhibit an average diameter of approximately 12 nm (Figure 38a). Following exposure to an electrochemical field (2.0 V for 60 seconds), the nanoparticles maintain their spherical morphology but undergo a dramatic reduction in size, with an average diameter decreasing to around 3 nm (Figure 38b). This substantial size contraction corresponds to the extensive surface oxidation and carbon framework degradation observed during treatment. To further investigate, the chronoamperometry protocol was applied consecutively five times (2.0 V, 60 seconds per cycle). The resulting dispersion exhibited negligible PL and TEM analysis revealed no detectable structural features, strongly suggesting the complete decomposition of the nanoparticles.
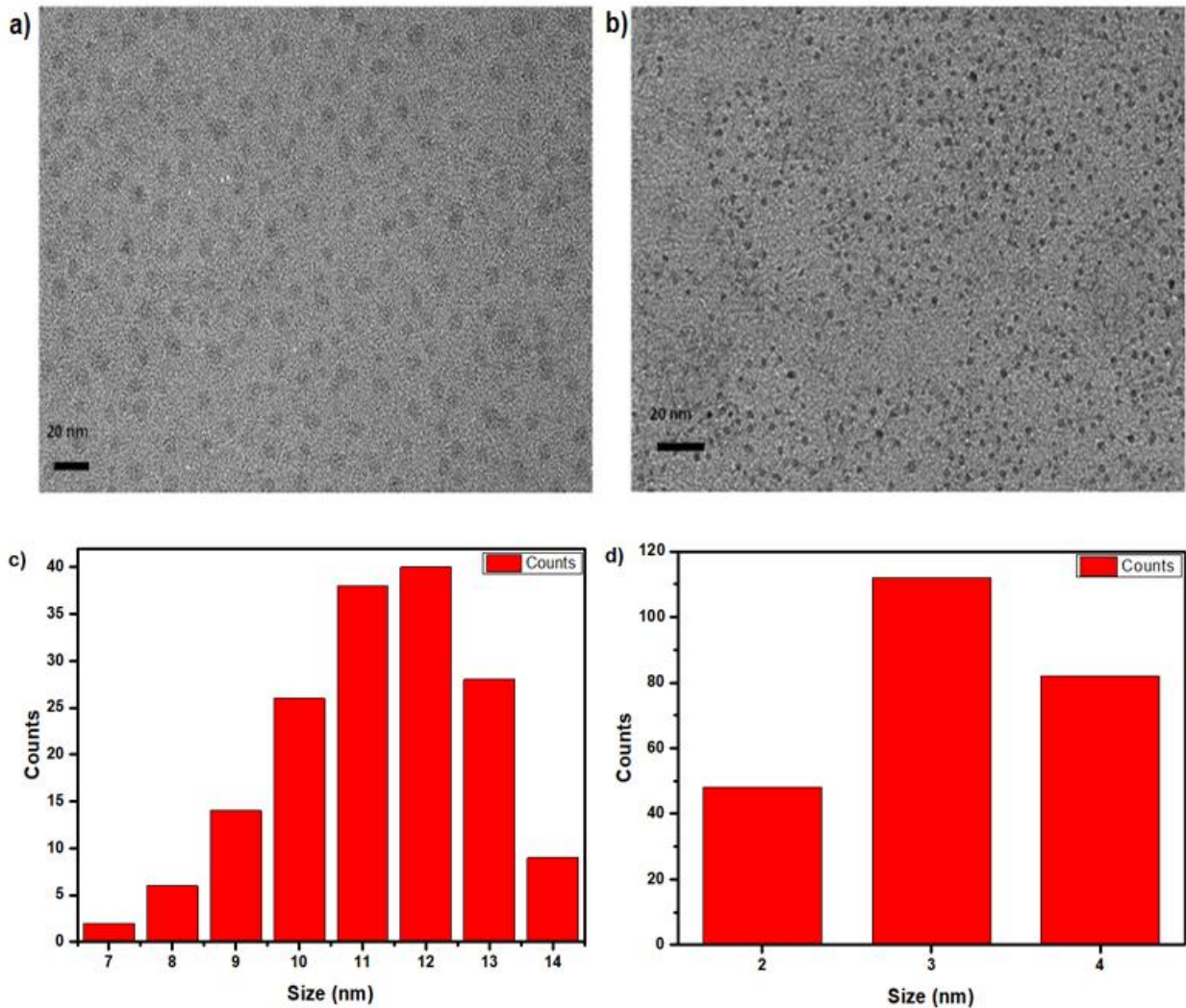
Figure 38. TEM images of C-dots (a) before and (b) after exposure to an electrochemical field (2.0 V for 60 s) and their respective size distribution charts (c-d).

3.2.1.2. FTIR analysis

The FTIR spectrum of untreated C-dots (black line, Figure 39) displays distinct peaks at 935 and 850 cm^{-1}, corresponding to the bending vibrations of the C=C–H bonds in sp^2 carbon. However, these peaks are absent in the spectra of the treated samples (red line, Figure 37). Additionally, peaks associated with functional groups such as C–N, C=O, and C=O/C=N, observed at 1185, 1653, and 1691 cm^{-1} respectively, are noticeably diminished in the electrochemically etched C-dots.
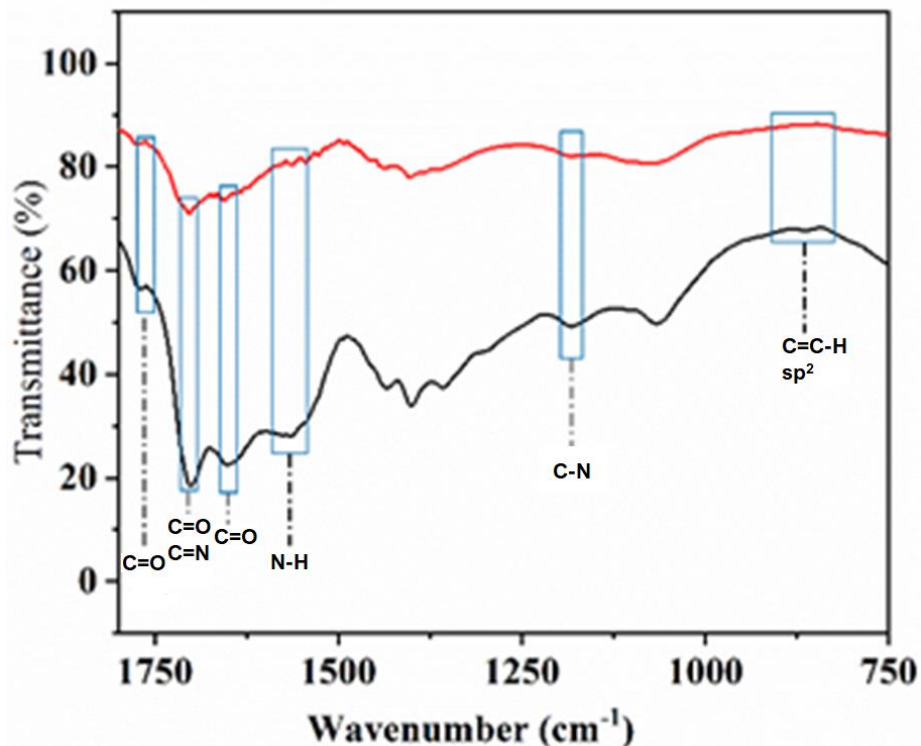
Figure 39. FTIR spectra of C-dots before (black line) and after (red line) the chronoamperometry treatment at 2.0 V for 60 s.

3.2.1.3. XPS analysis

XPS analysis shows that the C1s spectrum of untreated C-dots (Figure 40a) is primarily composed of 60.6% sp³ carbon, 19.1% sp² carbon (accompanied by a minor π–π* satellite peak), 17.8% C=O, and 2.4% C–O. After chronoamperometry treatment (2.0 V for 60 seconds), the XPS spectrum (Figure 40b) reveals significant changes, with sp³ carbon reduced to 42.4%, sp² carbon to 4.9%, and C=O to 13.1%, while the proportion of C–O increases substantially to 39.6%. These findings, summarized in Table 1, in combination with FTIR data, strongly indicate that the application of an electric field induces extensive surface oxidation and significant disruption of carbon-carbon bonds.
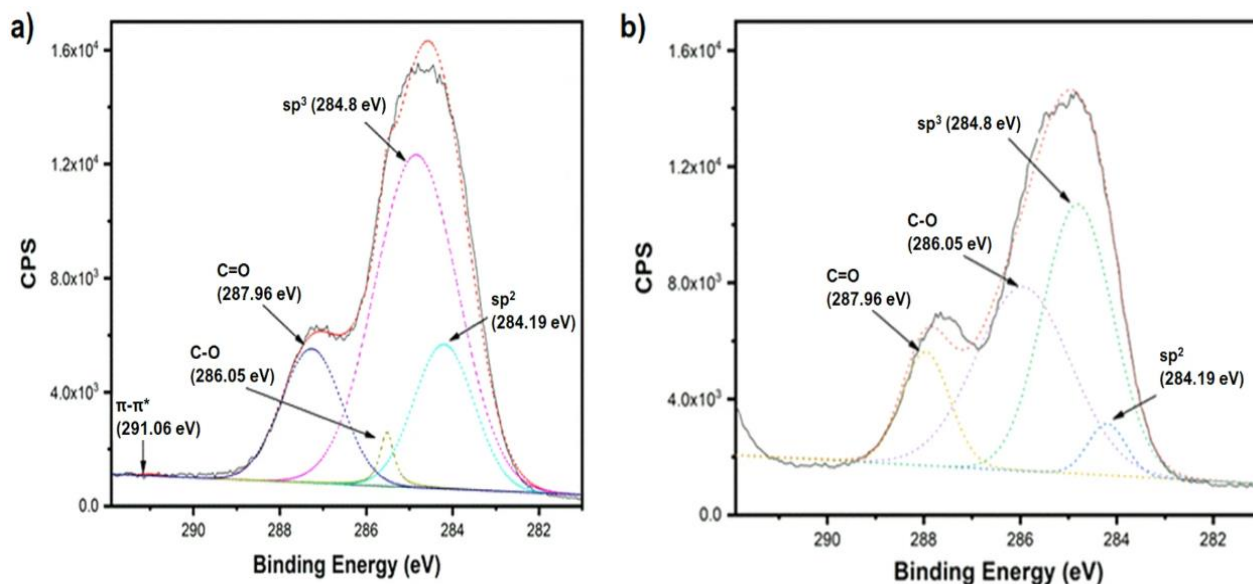
Figure 40. C1s XPS spectra of C-dots before (a) and after (b) chronoamperometry treatment at 2.0 V for 60 s. Solid lines refer to the recorded data, while the dashed lines refer to the fitted curves.

Table 1. Analysis of the C1s XPS spectrum of untreated C-dots (up) and C-dots that have been subjected to chronoamperometry treatment a 2.0 V for 60 s (down).

Chemical Bind	Combined energy peak position (eV)	Peak area %
Untreated C-dots		
sp^2	284.19	19.1
sp^3	284.80	60.6
C–O	286.05	2.4
C=O	287.96	17.8
π–π*	291.05	0.1
C-dots after treatment at 2.0 V for 60 s		
sp^2	284.20	4.9
sp^3	284.81	42.4
C–O	285.94	39.6
C=O	287.97	13.1

3.2.2. Optical properties

3.2.2.1. UV-Vis spectroscopy

The UV-vis absorbance of the samples treated at 0.5 V and 1.0 V is nearly identical to that of the untreated dispersion. However, as the applied voltage increases to 1.5, 2.0,

2.5, and 3.0 V, a gradual decline in absorbance is observed (Figure 41a). Images comparing the untreated dispersion with C-dot dispersions subjected to chronoamperometry at voltages between 0.5 and 3.0 V, taken under daylight and UV light, are presented in Figure 41b. Notably, the dispersions treated at 1.5 and 2.0 V demonstrate the strongest fluorescence.
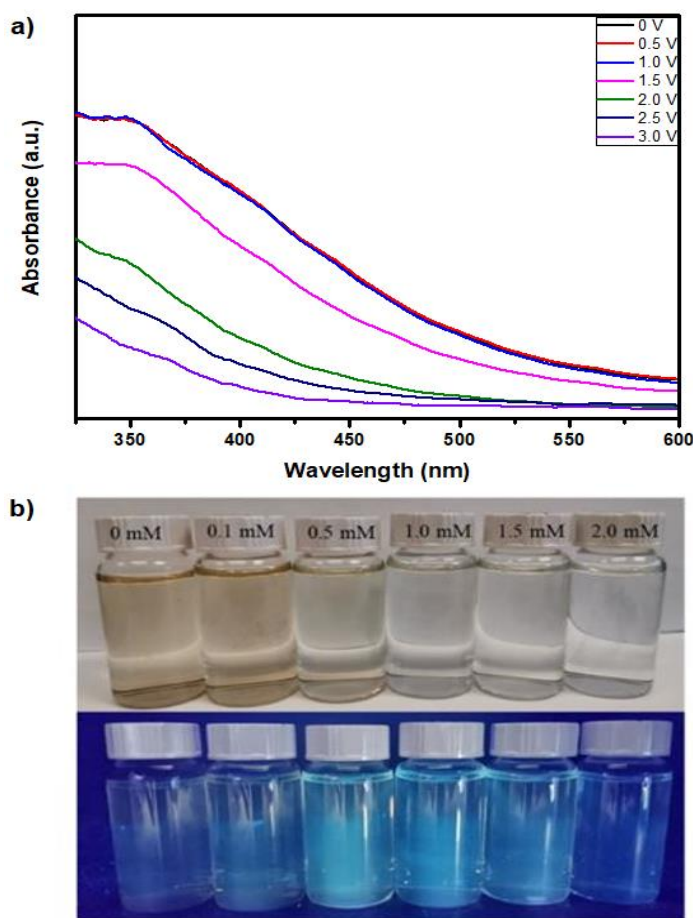
Figure 41. (a) UV–Vis absorbance spectra and (b) photos of 0.02 mg/ml C-dots dispersions in 0.15 M KCl that have been subjected to chronoamperometry treatments for 60 s at applied voltages from 0.5 to 3.0 V compared to the untreated sample under (top) daylight and (bottom) UV-radiation (λ_{ex} = 365 nm).

3.2.2.2. PL spectroscopy

The PL spectra of C-dot aqueous dispersions (Figure 42) exhibit a distinctive λ_{ex} dependent emission pattern ranging from 380 to 500 nm, where the λ_{em} shifts to longer wavelengths as λ_{ex} increases. This type of emission behaviour is attributed to electronic bandgap transitions within conjugated π-domains, surface defect states, edge effects,

and crosslink-enhanced emissions. In contrast, molecular chromophores are generally linked to λ_{ex}-independent emission contributions [1], [254], [255].
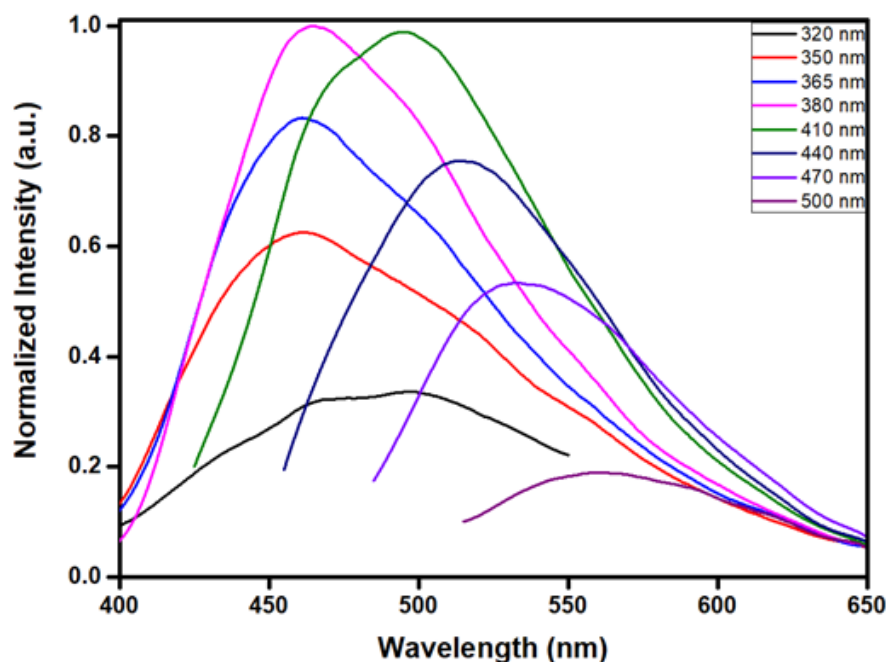
Figure 42. Normalized PL spectra of 0.01 mg/mL aqueous C-dot dispersions relative to the maximum intensity (Imax) at λex = 380 nm. The excitation wavelength (λex) was adjusted between 320 and 500 nm.

The PL spectra (λ_{ex} = 410 nm) of 0.02 mg/mL C-dot dispersions in 0.15 M Na_2CO_3 aqueous electrolyte remain largely unchanged after chronoamperometry treatments with applied voltages up to 3V (Figure 43a). Similar trends were observed for $NaHCO_3$ and Na_2SO_4 electrolytes. However, when KCl is used as the electrolyte (Figure 43b), significant changes in the PL properties are evident, and equilibrium is reached 48 hours after the electric field is removed.
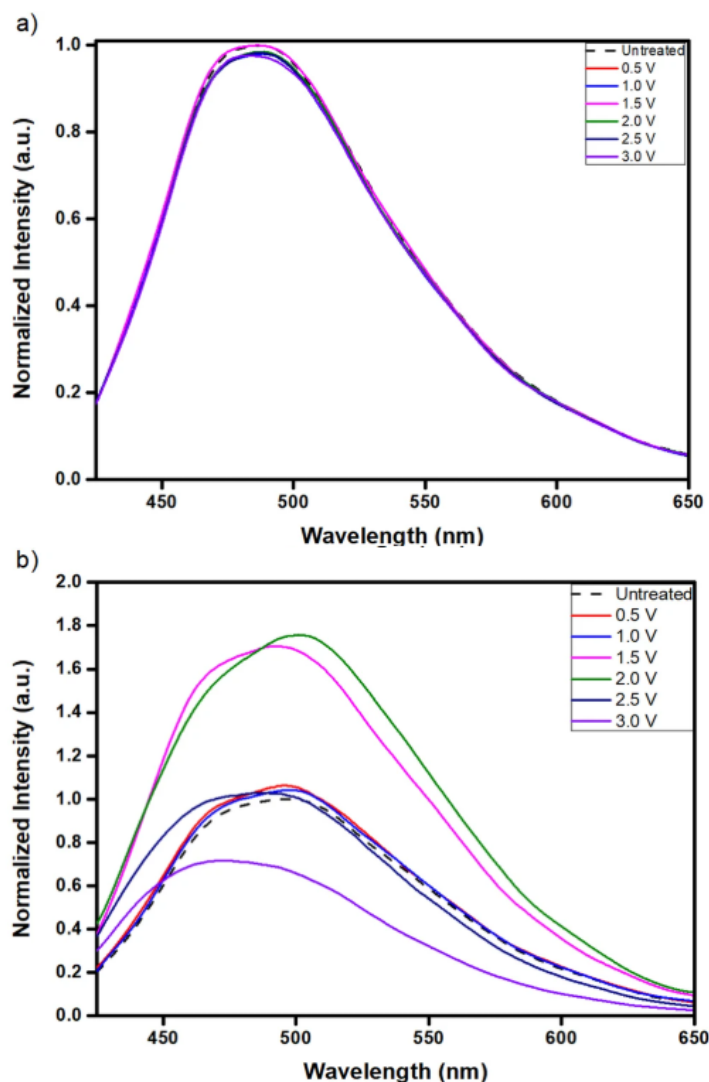
Figure 43. Normalized (against Imax of the untreated dispersion) PL spectra (λex = 410 nm) of 0.02 mg/ml C-dots dispersed in 0.15 M aqueous solutions of (a) Na_2CO_3 and (b) KCl that have been subjected to chronoamperometry treatment for 60 s at applied voltage from 0.5 to 3.0 V.

As depicted in Figure 44, the maximum emission intensity (I_{max}) of C-dots subjected to electrochemical treatment increases with KCl concentration up to 0.1 M, remains stable between 0.1 M and 0.2 M, and then decreases sharply as the concentration is further increased (all subsequent experiments utilized 0.15 M KCl). Figure 45a demonstrates that while I_{max} undergoes minimal changes at applied voltages of 0.5 and 1.0 V (λex = 410 nm), a notable rise occurs at 1.5 V, followed by a further increase at 2.0 V. Beyond this point, at 2.5 and 3.0 V, I_{max} declines sharply. Comparable behavior is observed for excitation wavelengths of 350, 380, and 470 nm. Notably, the treatment at 2.0 V results in a redshift,

consistent with surface oxidation effects [256], although the overall trend in Figure 45b shows a blue shift, which may be attributed to changes in the size of the carbogenic cores.
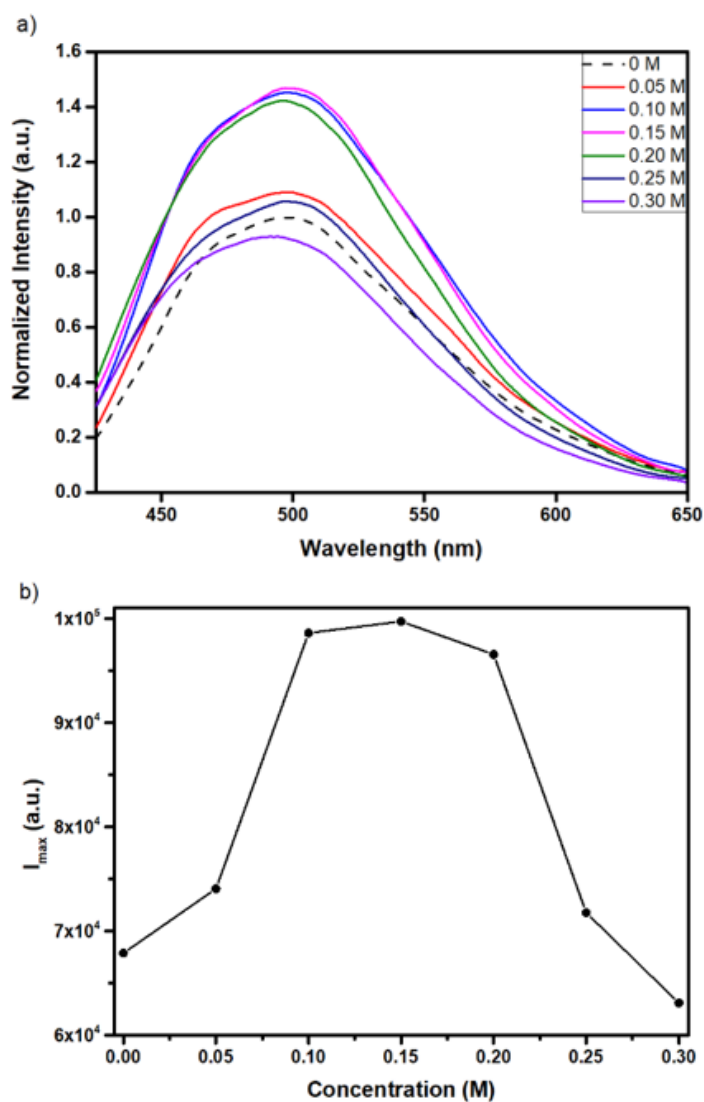
Figure 44. 0.02 mg/ml C-dots dispersions subjected to chronoamperometry treatments for 60 s at 2.0 V in the presence of 0.05, 0.10, 0.15, 0.20, 0.25, 0.30 M KCl. (a) PL spectra (λex = 410 nm) and (b) Imax as a function of KCl concentration.
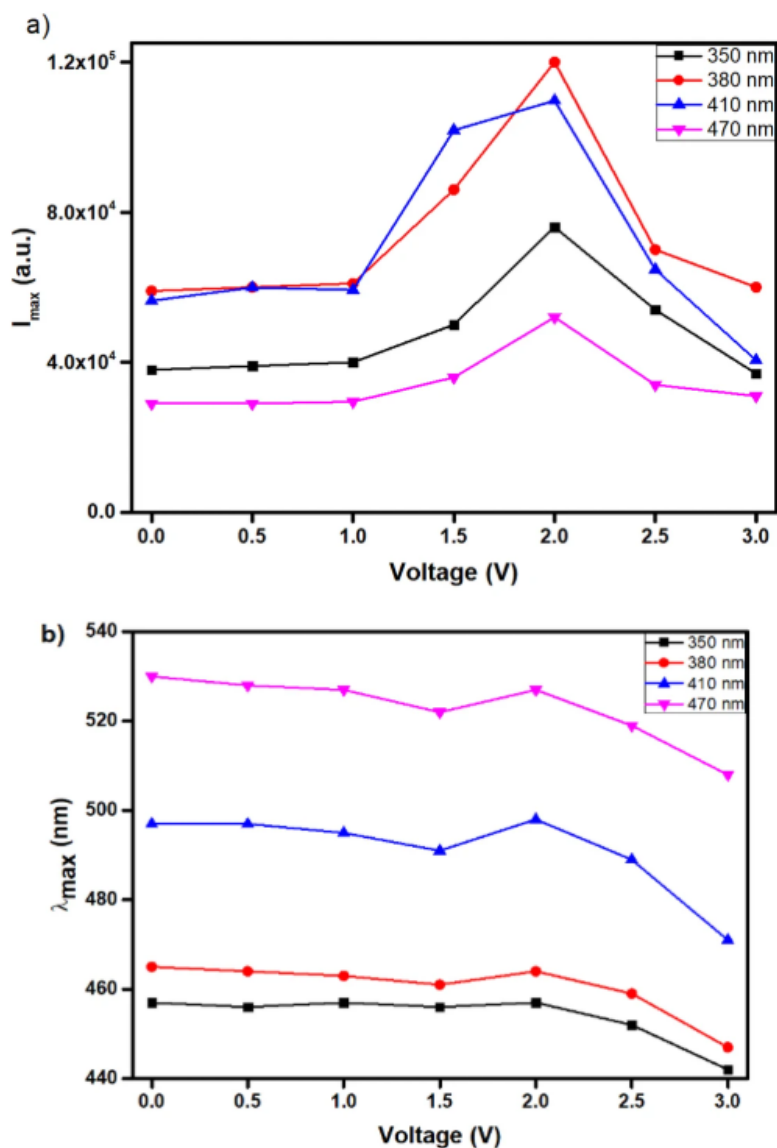
Figure 45. 0.02 mg/ml C-dots dispersion in 0.15 M KCl subjected to chronoamperometry treatments for 60 s within applied voltage from 0.5 to 3.0 V compared to the untreated dispersion. (a) Imax at λex = 350,380,410, 470 nm, (b) λmax as a function of the applied voltage.

3.2.2.3. QY

As shown in Figure 46, the QY (λ_{ex} = 365 nm) of the untreated C-dot dispersions is 1.2%, determined relative to anthracene (Φ = 0.27, λ_{ex} = 365 nm). The QY increases progressively upon electrochemical treatment, reaching 1.3%, 2.7%, and peaking at 7.8% for samples treated at 1.0, 1.5, and 2.0 V, respectively. At higher applied voltages of 2.5 and 3.0 V, the QY decreases slightly to 2.9% and 1.4%, respectively, highlighting an

optimal enhancement at intermediate voltages (up to 640%) before further structural modifications reduce the fluorescence efficiency (Table 2).
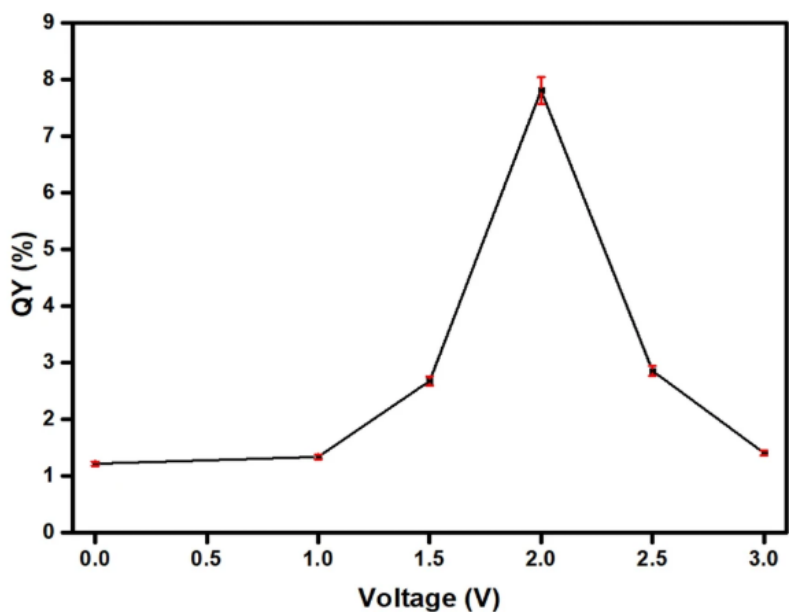
Figure 46. QY (%) of C-dots subjected to chronoamperometry treatments for 60 s within applied voltage from 0.5 to 3.0 V compared to the untreated ones.

Table 2. QY values of 0.02 mg/ml C-dots dispersion in 0.15 M KCl subjected to chronoamperometry treatments for 60 s within applied voltage from 0.5 to 3.0 V compared to the untreated dispersion, using anthracene as a reference (λex=365 nm).

Material	QY %
C-dots	1.2
C-dots (+ 1.0 V)	1.3
C-dots (+ 1.5 V)	2.7
C-dots (+ 2.0 V)	7.8
C-dots (+ 2.5 V)	2.9
C-dots (+ 3.0 V)	1.4

The significant alterations in the PL characteristics of the C-dots are intrinsically linked to the electrochemical generation of hypochlorite ions (ClO^-) [257], a well-documented phenomenon widely utilized in water purification processes [258]. Using iodometric titration with sodium thiosulfate, it was determined that the KCl solution subjected to a 3 V treatment for 60 seconds contained 3.5 mM hypochlorite ions. To investigate this effect further, Figure 47a presents the PL spectra of C-dots measured 48 hours after dispersion in NaClO solutions with varying concentrations. As shown in Figure 47b, I_{max} steadily increases with NaClO concentration up to 1 mM, followed by a sharp decline with higher concentrations. Concurrently, λ_{max} at I_{max} shifts from 493 nm in water to 498 nm, 485 nm, and 469 nm for NaClO concentrations of 0.5 mM, 1.5 mM, and 2.0 mM, respectively, as depicted in Figure 47c. It is important to note that the data in Figure 47 is unrelated to any electrochemical process and is solely attributed to the oxidative effects of NaClO. The progressive discoloration of C-dot dispersions with increasing NaClO concentrations (Figure 47d) suggests significant structural transformations induced by the oxidizing agent. Notably, C-dots pre-oxidized with NaClO exhibit minimal changes in PL properties when subsequently exposed to chronoamperometry treatments (Figure 47f).
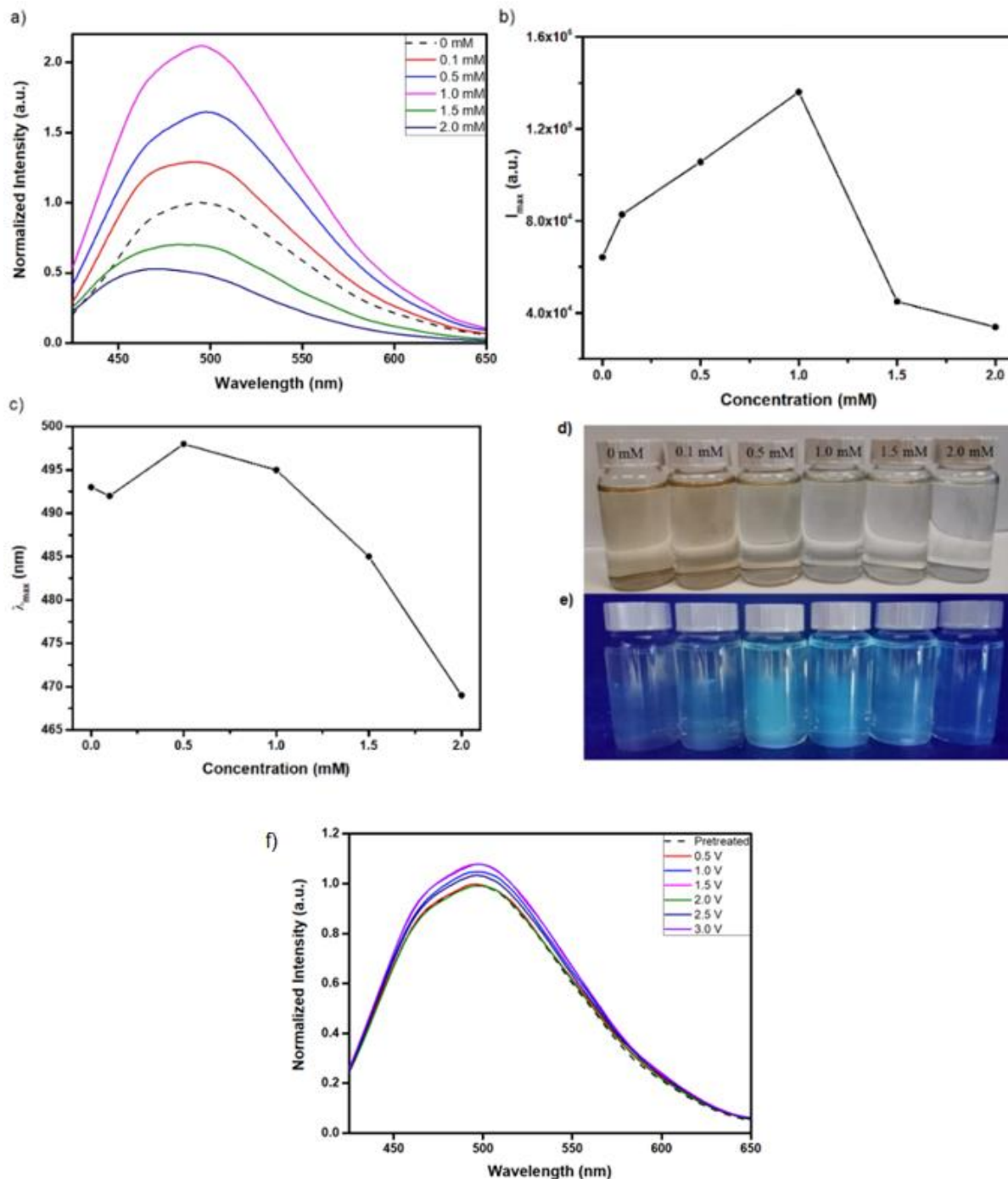
Figure 47. 0.02 mg/ml C-dots dispersed in aqueous solution of NaClO with salt concentrations 0.1, 0.5, 1.0, 1.5 and 2.0 mM, compared to the untreated sample. (a) PL spectra (λex = 410 nm), (b) the corresponding maximum PL intensity (Imax) and (c) λmax as a function of the electrolyte concentration, photos of C-dots dispersions under (d) daylight and (e) UV radiation, and (f) PL spectra (λex = 410 nm) of 0.02 mg/ml C-dots pretreated with 1mM NaClO solution for 48 h and then subjected to chronoamperometry treatments for 60s. All data have been collected 48 h after the dispersion of C-dots in the aqueous solution of NaClO.

It has been suggested that the potent, non-specific oxidizing agent hypochlorite can promote the cleavage of carbon-carbon double bonds (C=C) [259] and imine groups (C=N) [260], while also targeting ether bonds and hydroxyl groups. For instance, the degradation of GO by hypochlorite under UV light has been shown to result in the production of graphene dots [260]. This process involves the attack of epoxy and alkoxy groups on the basal plane of GO by NaClO, leading to the breakdown of skeletal carbon bonds and the oxidation of peripheral groups into COOH [261]. Similarly, electrochemical exfoliation of graphite rods in an aqueous KCl solution under applied voltages ranging from 9 to 30 V produces C-dots with diameters around 2 nm [262]. Based on the findings presented in this study, it appears plausible to associate such previously reported phenomena with the generation of hypochlorite ions during electrochemical processes.

3.3. Conclusion

This chapter provides significant insights into the previously unexamined electrochemical restructuring mechanisms of C-dots. Using a combination of structural and optical analyses, this study demonstrates that the application of electrochemical treatments induces profound transformations in the physicochemical properties of C-dots, characterized by nanoscale restructuring, extensive surface oxidation, and notable alterations in optical behavior.

The results reveal that untreated C-dots have an average diameter of approximately 12 nm, which is drastically reduced to ~3 nm following a 60-second electrochemical etching process at 2.0 V. TEM confirms the retention of spherical morphology despite this size reduction. Successive cycles of chronoamperometry, however, lead to complete decomposition of the nanoparticles, as evidenced by the absence of structural features in TEM images and the loss of PL. FTIR spectroscopy corroborates these findings, showing the disappearance of characteristic sp^2 carbon bending vibrations and a substantial reduction in functional groups, such as C=N and C=O, indicative of extensive surface oxidation and carbon framework degradation. These findings are further substantiated by XPS, which reveals a significant decrease in sp^2 carbon content, coupled with an increase in oxygen-containing functional groups.

The optical properties of C-dots exhibit a pronounced dependency on the applied electrochemical conditions. UV-Vis spectroscopy highlights a decline in absorbance with increasing voltage, particularly above 1.5 V, while PL measurements reveal an excitation-dependent emission pattern attributed to transitions within conjugated π-domains, surface defects, and crosslink-enhanced emission. Notably, the I_{max} increases markedly at intermediate voltages (1.5–2.0 V) and subsequently decreases at higher voltages (2.5–3.0 V). This behavior aligns with QY data, which shows a peak enhancement at 2.0 V, with QY reaching 7.8% compared to 1.2% in untreated samples—an improvement of over 640%. However, further increases in voltage lead to reduced fluorescence efficiency, likely due to structural disruption.

Electrogenerated ClO^-, identified as key contributors to the observed changes, are shown to facilitate the oxidative degradation of the carbon framework. Iodometric titration confirms the generation of 3.5 mM ClO^- in KCl electrolyte after treatment at 3 V for 60 seconds. Subsequent experiments using NaClO solutions demonstrate similar trends in PL behavior, with I_{max} peaking at 1 mM NaClO before declining at higher concentrations. Concurrent redshifts and blueshifts in emission maxima reflect complex structural dynamics involving oxidation-induced surface modifications and size variations of the carbogenic cores. These findings draw parallels with reported mechanisms of hypochlorite-mediated degradation of graphene oxide and electrochemical exfoliation of graphite rods, supporting the hypothesis that hypochlorite ions play a pivotal role in restructuring the C-dots.

Chapter 4: Synthesis and functionalization of citric acid/urea-based carbon dots via hypochlorite treatment

4.1. Introduction

A wide variety of C-dots with different sizes and degrees of graphitization can be synthesized using cost-effective methods, primarily through the pyrolytic decomposition of precursor materials such as biomass waste and natural sources [263], [264]. C-dots can also be produced in situ within polymer matrices and powder mixtures [245], [265], using techniques that align with standard industrial processes. Additionally, C-dots exhibit a broad range of tuneable PL emissions, which can be attributed to factors such as bandgap transitions in the conjugated π-domains of the carbon cores, surface defects that act as exciton capture centers, embedded organic fluorophores, and emissions enhanced by crosslinking [266], [267]. Although C-dots generally emit the strongest PL in the blue/green regions of the spectrum, systems exhibiting extensive conjugation of sp^2 domains, heteroatom doping, or solvatochromism can display intense red/NIR emission signals [268].

Surface modification and passivation techniques post-synthesis (often involving amines, ethylenediamine, polyethyleneimine, polyethylene glycol, or thiourea) have been investigated to adjust the PL properties of C-dots, including QY, λ_{em}, and τ [266], [269]. For instance, Sun et al. showed that C-dots produced by laser ablation of a carbon target initially lack fluorescence. However, after acid treatment and the addition of non-emissive passivation agents like diamine-terminated poly(ethylene glycol) oligomers or poly(propionylethyleneimine-co-ethyleneimine), they become highly fluorescent [43]. Additionally, another study found that C-dots derived from biomass, when treated with ethanolamine, exhibit hydrophilic properties, while treatment with oleylamine allows them to disperse easily in toluene [96].

The goal of this study is to develop scalable, low-cost methods for producing highly luminescent C-dots. This chapter explores a simple post-synthesis treatment for C-dots

derived from CA and urea, utilizing sodium hypochlorite (NaClO), a strong oxidizing agent known for its ability to degrade stable carbon structures. The treatment induces surface oxidation, etching, and significant structural rearrangements of the C-dots, resulting in a 6-fold enhancement of their PL properties. In addition, the modified C-dots retain low cytotoxicity against HeLa and U87 cell lines. Furthermore, various polymeric materials, including polyurethane sponge, polyvinylidene fluoride membrane, and polyester fabric, impregnated with modified C-dots, exhibit advanced antifungal activity against *Talaromyces pinophilus*, while untreated materials fail to show any antifungal effect. This approach highlights the potential of NaClO-treated C-dots in both enhancing PL properties and providing added functionality, such as antifungal performance, without compromising their non-toxic nature.

4.2. Results and discussion

Synthesis of C-dots (CU-dots)

C-dots were synthesized following a protocol previously established in our laboratory [1]. Briefly, CA and urea were mixed at a molar ratio of CA to urea ($f_{CA/urea}$) of 1:50 and 1:100. These two ratios were selected, among others (1:25 and 1:3), as they had already demonstrated better performance in terms of their optical properties. The mixture was placed in a crucible and heated at 230 °C for 1 hour. The resulting product was ground into a fine powder, dissolved in water, and purified through dialysis using Snakeskin Dialysis Tubing with a molecular weight cut-off (MWCO) of 3.5 kDa for 4 weeks, during which the water was replaced daily. The purified product was then freeze-dried and stored in a desiccator.

Treatment of CU-dots with NaClO

To prepare oxidized CU-dots, varying volumes of 0.1 M aqueous sodium hypochlorite solution were added to 20 mL of 0.1 mg/mL aqueous dispersions of C-dots under continuous stirring, as detailed in Table 1. The mixtures were left at room temperature for 24 hours prior to PL measurements. For all subsequent analyses, the CU-dots were

purified through dialysis against water for 4 weeks using Snakeskin Dialysis Tubing with a MWCO of 1 kDa, followed by freeze-drying.

Table 3. . Sample description of CU-dots with respect to the amounts of C-dots and NaClO used for their preparation.

Volume (in mL) of 0.1 mg/mL dispersion of C-dots	Volume (in mL) of 0.1 M solution of NaClO	NaClO concentration (mM)
20	0.5	2.5
20	1.0	5
20	1.5	7.5
20	2.0	10
20	2.5	12.5
20	3.0	15
20	4.0	20
20	2.0*	400

*Concentration 4.4 M

4.2.1. Structural properties

4.2.1.1. TEM analysis

The TEM images of CU100D nanoparticles reveal their spherical morphology with average diameters 4.3 nm (Figure 48a) (Standard deviation=2.94). Their graphitic structure is further confirmed by High-Resolution TEM, which showed that the CU100D lattice spacing was around 0.24 nm (Figure 52c). Previous research has indicated that the size of C-dots synthesized from CA and urea mixtures typically ranges from 5 to 40 nm [270], [271], [272], [273]. TEM images of CU100D reveal that following treatment with 7.5 mM NaClO, their average diameter decreases to approximately 2.9 nm while retaining their spherical shape (Figure 52b) (Standard deviation=18.94). This considerable reduction in the size of CU-dots induced by NaClO aligns with the extensive oxidation

and breakdown of the carbon framework [274]. The observed shrinkage suggests a significant alteration in the structural integrity of the nanoparticles, indicating the efficacy of NaClO in inducing tailor-made surface modifications.
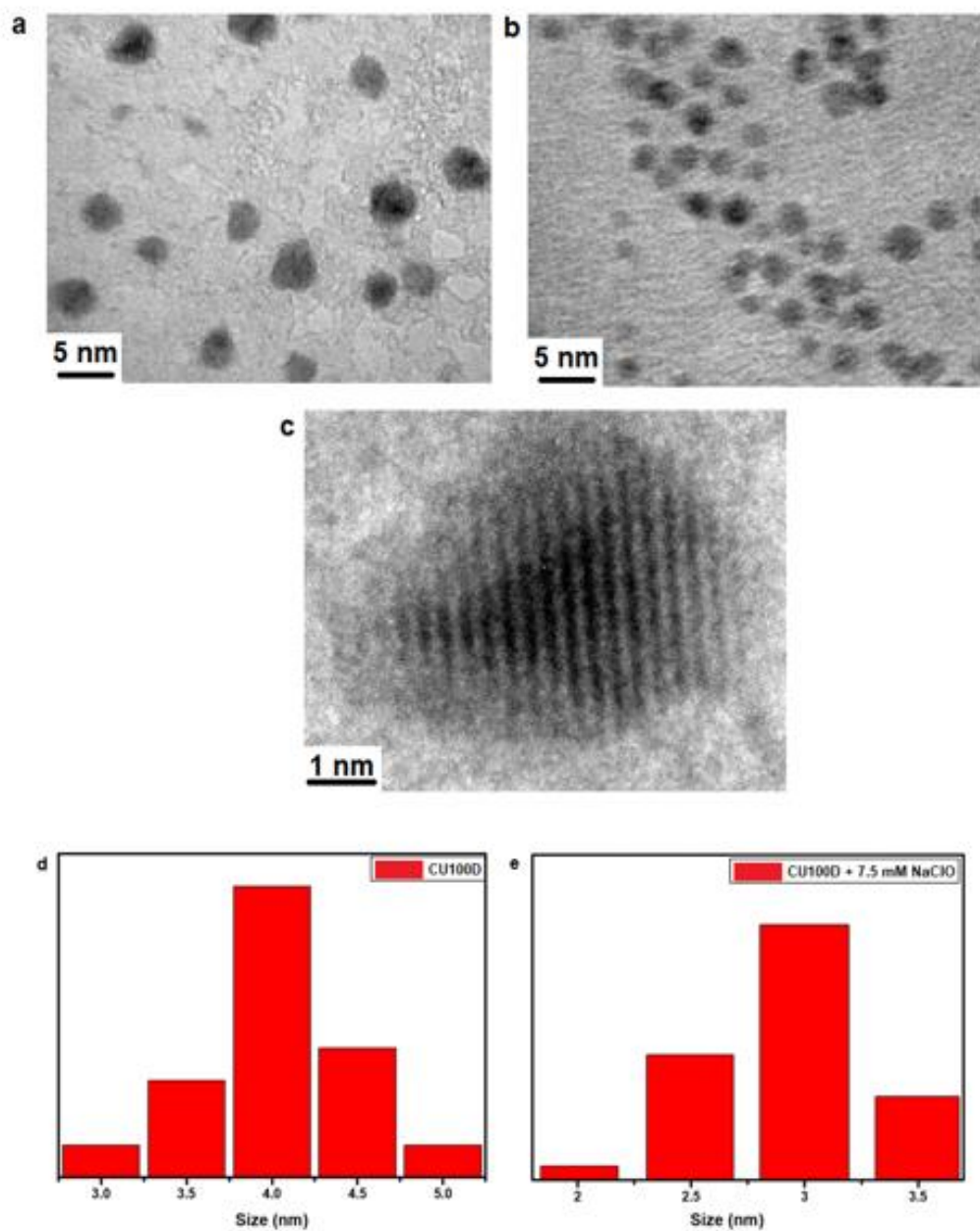
Figure 48. TEM images of (a) CU100D , (b) CU100D after 7.5 mM NaClO treatment, and (c) HRTEM image of CU100D. Size distribution histograms (n=50) of (d) CU100D and (e) CU100D after 7.5 mM NaClO treatment

The reduction in size of CU-dots following treatment with NaClO is evident from the images in Figure 49. Initially, when placed in a Snakeskin Dialysis Tubing membrane with a MWCO of 3.5 kDa, CU100D particles are larger than the pores of the membrane, thus remaining inside the tubing during dialysis (Figure 49a). However, upon oxidation with NaClO, the size of CU100D decreases to a level smaller than the pore size, allowing them to escape from the tubing into the surrounding beaker (Figure 49b). By replacing the Snakeskin Dialysis Tubing with benzoylated Dialysis Tubing with a 1 kDa MWCO, NaClO-treated CU-dots can be effectively retained within the membrane, while any remnants of the oxidative process can pass through the pores (Figure 49c). This method enables the purification of samples from unwanted sodium compounds.
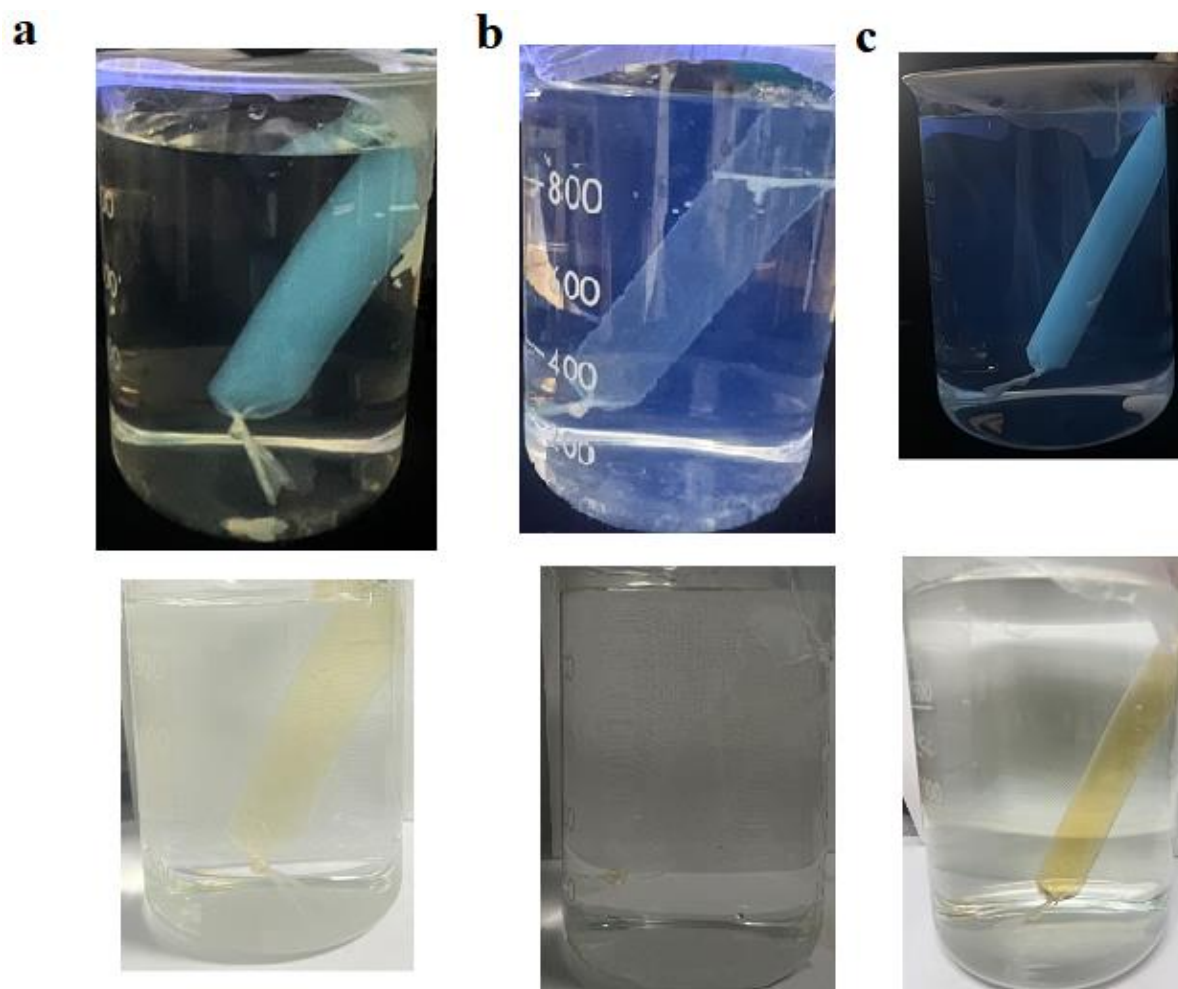
Figure 49. Photos of CU100D during dialysis under (top) UV lamp (λ_{ex}=365 nm) and (bottom) daylight. (a) CU100D in a 3.5 kDa MWCO membrane, CU100D after 7.5 mM NaClO treatment in (b) 3.5 kDa and (c) 1 kDa MWCO membranes.

4.2.1.2. Elemental analysis

Elemental analysis showed a marked increase in oxygen content in CU100D after NaClO treatment, rising from 25.6% in untreated CU100D to 38.2% in CU100D (+7.5mM NaClO) and 49.5% in CU100D (+20mM NaClO) (Table 4). This substantial increase highlights the introduction of oxygen-containing functional groups as a result of the oxidative process. Meanwhile, the carbon content remained relatively consistent, ranging between 38% and 43% across all samples. In contrast, the nitrogen content exhibited a significant decline, decreasing from 32.4% in untreated CU100D to 17.6% and 11.9% in CU100D (+7.5mM NaClO) and CU100D (+20mM NaClO), respectively. This reduction is likely due to NaClO's ability to react with nitrogen-containing compounds, converting them into volatile products such as chloramines and nitrogen trichloride [275].

Moreover, the treatment's effect was visually apparent: initially colorless dispersions of NaClO-treated C-dots became white and turbid upon the addition of $CaCl_2$. This behavior indicates the presence of carbonate ions formed via CO_2 generation, likely a decomposition product of the oxidative process. This observation is consistent with findings from previous studies [18], further validating this oxidative mechanism.

Table 4. Elemental analysis results of CU100D, pre- and post- treatment with NaClO (up to 20mM).

Material	C %	H %	N %	O %
CU100D	38.6	3.4	32.4	25.6
CU100D + 7.5mM NaClO	43.1	1.1	17.6	38.2
CU100D + 20mM NaClO	37.9	0.7	11.9	49.5

4.2.1.3. XPS analysis

The C1s XPS spectrum of CU100D (Figure 50) reveals distinct chemical environments, with the carbon atoms distributed as follows: 18.5% sp^2 hybridized carbon, 19.7% sp^3 hybridized carbon, 36.1% attributed to C=O or C=N groups, 15.8% associated with C-O or C-N bonds, and 9.8% corresponding to O-C=O functionalities. After treatment with 7.5 mM of NaClO, the C1s XPS spectrum indicates notable changes in these distributions,

with 15.6% sp^2 carbon, 34.1% sp^3 carbon, 33.3% C=O or C=N groups, 15.8% C-O or C-N bonds, and only 1.2% O-C=O groups.

These shifts suggest a reduction in conjugated sp^2 carbon content and carboxylate groups (O-C=O), alongside a significant increase in sp^3 hybridization, which is indicative of structural rearrangements and increased oxidation of the C-dot surfaces. The enhanced presence of C-O and C=N groups supports the incorporation of oxygen- and nitrogen-containing functional groups during the oxidative treatment (Figures 51 and 52). Additional data from C1s, O1s, and N1s XPS analyses, presented in Tables 5, 6 and 7, respectively, further confirm these chemical modifications, providing a detailed overview of the surface chemistry changes induced by NaClO treatment.
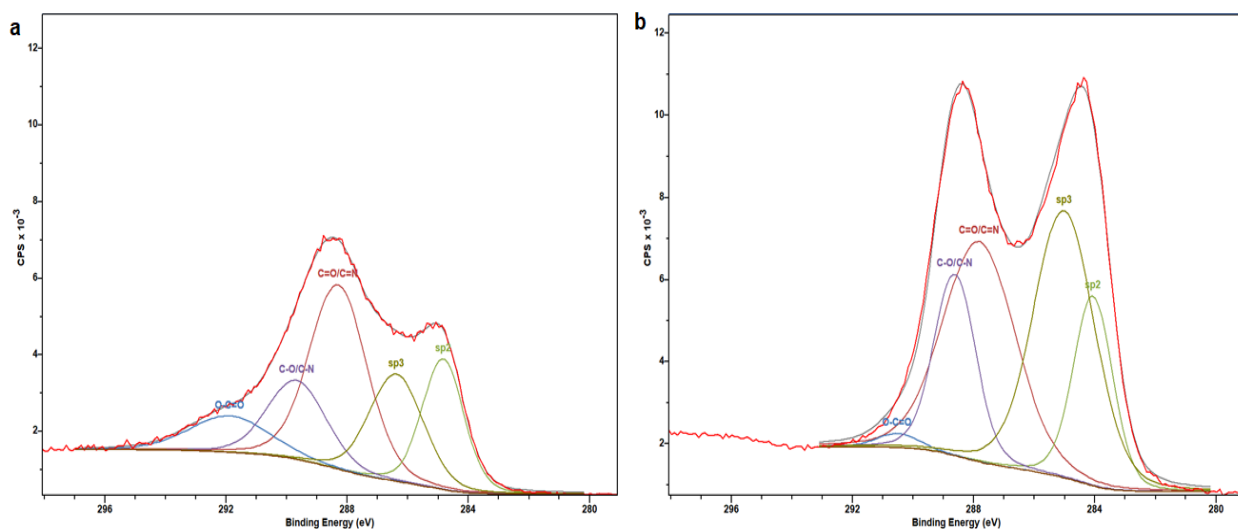
Figure 50. Deconvolution of C1s XPS spectra of: (a) CU100D-dots and (b) CU100D + 7.5mM NaClO.

Table 5. Data derived from the deconvolution of C1s XPS spectrum of CU100D and CU100D + 7.5mM NaClO.

Sample	sp^2 %	sp^3 %	C=O/C=N %	O-C=O %	C-O/C-N %
CU100D	18.54	19.71	36.11	9.82	15.83
CU100D + 7.5mM NaClO	15.64	34.05	33.30	1.22	15.79
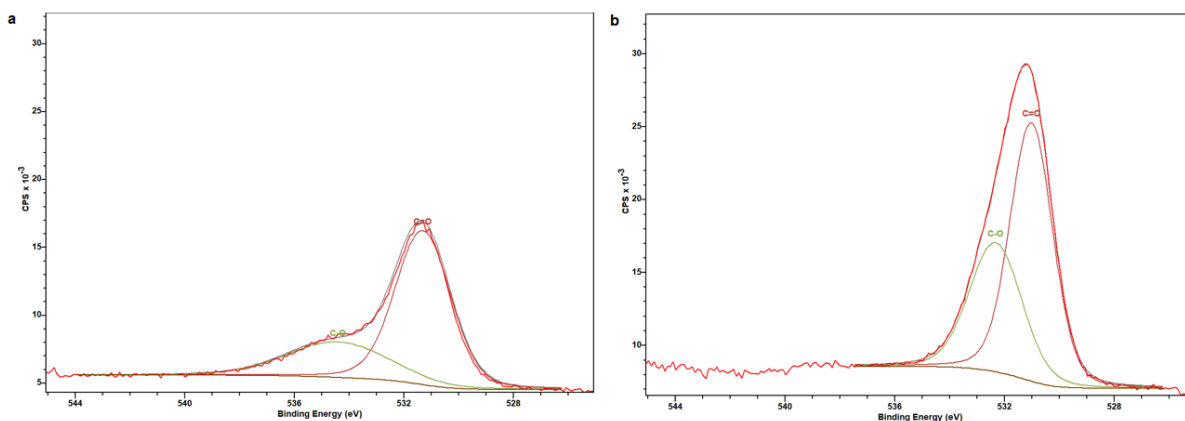
Figure 51. Deconvolution of O1s XPS spectra of: (a) CU100D-dots and (b) CU100D + 7.5mM NaClO.

Table 6. Data derived from the deconvolution of O1s XPS spectrum of CU100D and CU100D + 7.5mM NaClO.

Sample	C=O %	C-O %
CU100D	70.16	29.84
CU100D + 7.5mM NaClO	61.92	38.08
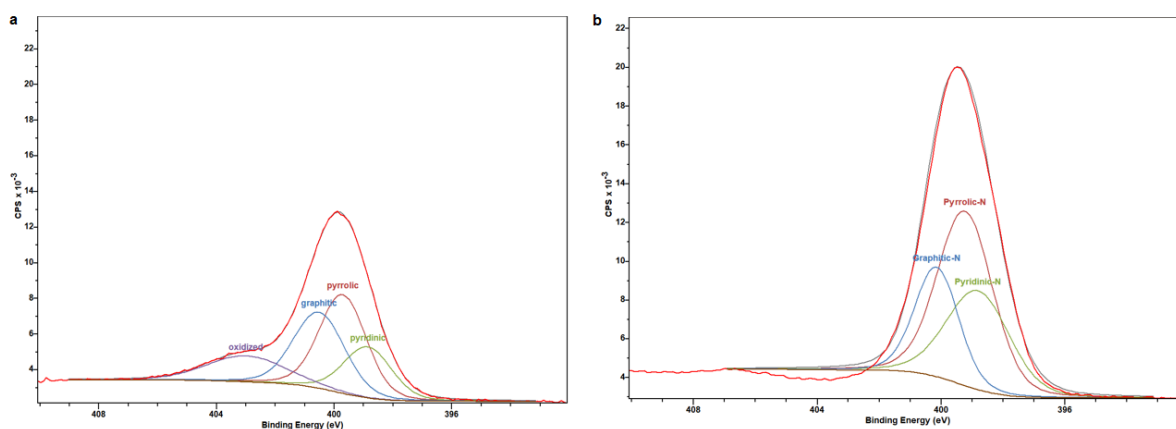
Figure 52. Deconvolution of N1s XPS spectra of: (a) CU100D-dots and (b) CU100D + 7.5mM NaClO.

Table 7. Data derived from the deconvolution of N1s XPS spectrum of CU100D and CU100D + 7.5mM NaClO.

Sample	Pyrrolic-N %	Pyridinic-N%	Graphitic-N %	Oxidized-N %
CU100D	35.44	18.90	29.80	15.87
CU100D + 7.5mM NaClO	46.60	30.15	23.25	-

4.2.1.4.   FTIR analysis

The FTIR spectra of both CU50D and CU100D samples, even following interaction with NaClO (up to 20mM), reveal distinct peaks indicative of various molecular vibrations (Figure 53). These include the bending of O-H at 550 cm^{-1}, stretching of C-O-C at 851 cm^{-1}, anti-symmetrical stretching of C-O at 967 cm^{-1}, stretching of C-N at 1175 cm^{-1}, bending of CH$_2$ groups at 1463 cm^{-1}, stretching of bonds involving C=C, C=O, and C=N in the range of 1554 cm^{-1} to 1723 cm^{-1}, and stretching of C-H bonds at 2869 cm^{-1} [276], [277]. Furthermore, broad bands spanning from 3026 cm^{-1} to 3294 cm^{-1} are attributed to the presence of hydrophilic amine (N–H) and hydroxyl (O–H) functional groups. The peaks around 1600 cm^{-1} are related to benzene skeleton vibrations [278], while the ones of N-H and O-H groups enhance water solubility and serve as reaction sites for NaClO [279]. Changes in absorption bands between 800 to 1600 cm^{-1} suggest an interaction between CU-dots and NaClO. NaClO tends to oxidize single-bond structures like C–H and C-O, forming double-bond C=C or C=O. Crosslinking between NaClO and CU-dots may produce ester functional groups, as indicated by a peak at 1560 cm^{-1}. The appearance of a peak at 820 cm^{-1} suggests a nucleophilic substitution reaction of aromatic compounds, possibly due to newly formed oxygen atoms released during hypochlorite decomposition [280]. Overall, the FTIR spectra of NaClO-treated CU50D and CU100D show no significant shifts in peak positions compared to untreated C-dots. However, the peaks exhibit higher intensity, suggesting an increased abundance of functional surface groups.

Collectively, the data presented below highlight the significant oxidation effects of NaClO on the surface of CU-dots, leading to substantial structural rearrangements. This behavior is comparable to the UV-assisted degradation of GO by NaClO, as previously reported, which involves cleavage of the carbon skeleton and attacks on epoxy and alkoxy groups, resulting in the formation of peripheral -COOH groups [261]. Due to its strong oxidizing properties, NaClO is capable of breaking C=C double bonds and C=N imine groups, as well as targeting hydroxyl groups and ether bonds [259], [260]. These reactions ultimately degrade structures such as SWCNTs, multi-walled carbon nanotubes, nanohorns, and graphene oxide [281], [282], [283]. This behavior is notably different from oxidants like

KIO_4, $KMnO_4$, and $K_2Cr_2O_7$, which can oxidize surface hydroxyl groups on C-dots but do not induce structural breakdown [256].
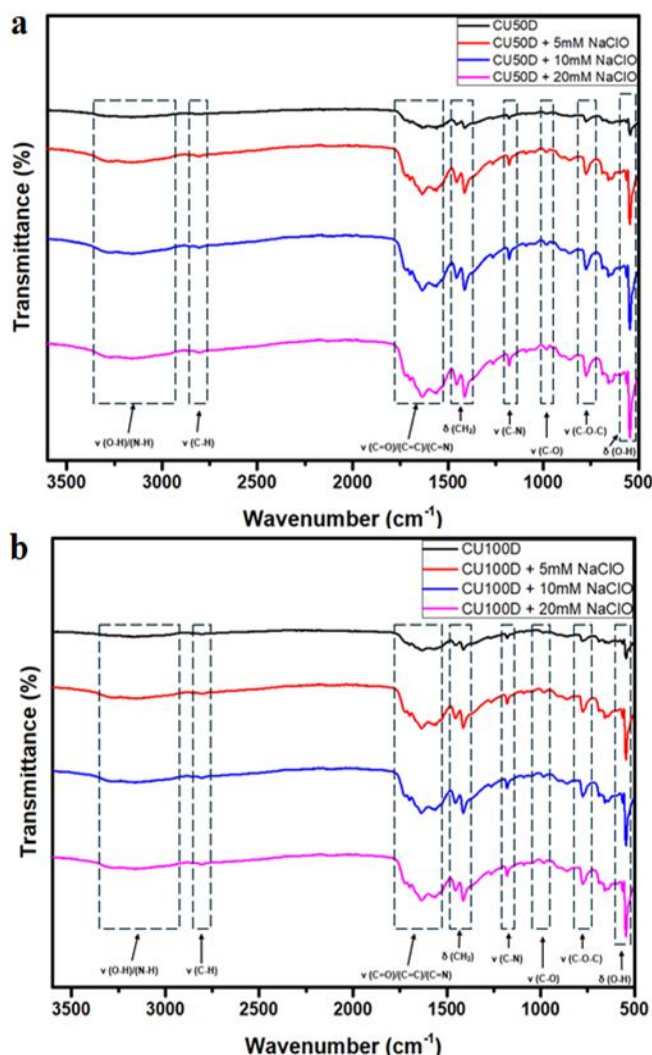
Figure 53. FTIR spectra of (a) CU50D and (b) CU100D pre- and post- treatment with NaClO (up to 20mM).

4.2.1.5. Zeta potential

To evaluate the surface charge and colloidal stability of CU-dots, we conducted zeta potential (ζ) analysis (Figure 54). The ζ values of CU100D aqueous dispersions (black squares) exhibit positive values at acidic conditions (ranging from ζ=2.9 mV at pH=1 to ζ=2.7 mV at pH=2) and negative values at higher pH (ranging from ζ = −11.7 mV at pH = 4 to ζ = −38.1 mV at pH = 12). This shift towards lower ζ values at higher pH is attributed to the deprotonation of carboxylic and hydroxyl groups on the CU-dots' surface [284].

Upon exposure to 7.5 mM NaClO (red circles), the ζ values of CU100D dispersions also transition from positive to negative as pH increases (from ζ=2.4 mV at pH=1 to ζ=-72.3 mV at pH=12). The more negative ζ values at pH=4 and above indicate an increased abundance of negatively charged (–COOH) and (–OH) functional groups, attributable to the oxidative action of NaClO. This treatment with NaClO leads to a reduction in the number of amine groups on the CU100D surface, contributing to the cumulative negative surface charge [285].
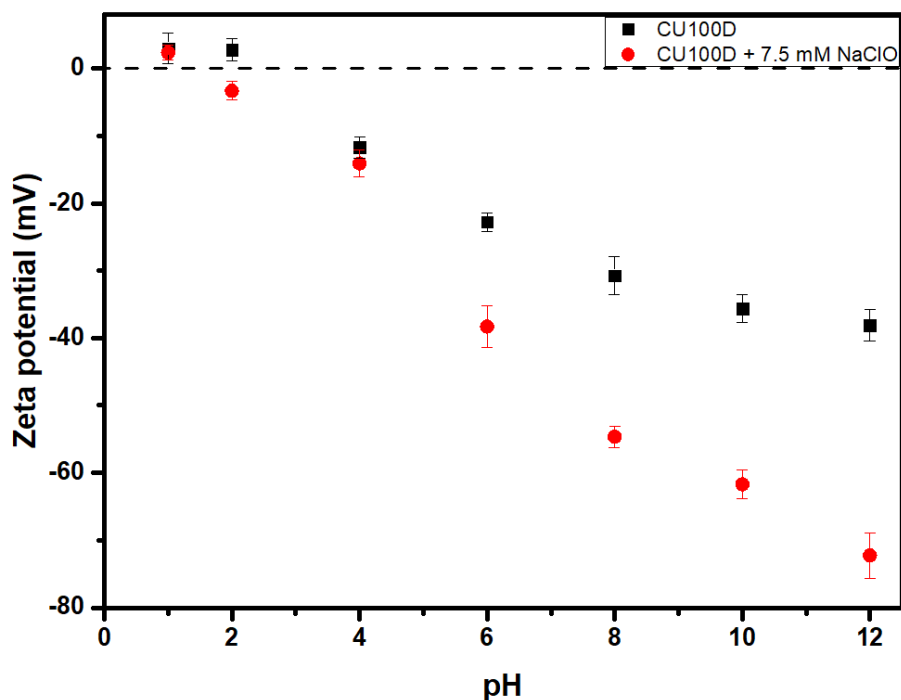
Figure 54. Zeta potential of 0.05 mg/ml aqueous dispersions of CU100D before (black) and after (red) treatment with 7.5 mM NaClO.

4.2.2. Optical properties

4.2.2.1.   UV-Vis spectroscopy

The UV-Vis spectra of CU50D and CU100D (Figure 55) display absorption bands located at approximately 275 nm and 415 nm, which are associated with the π-π* transitions of the pyridone ring of the fluorophore HPPT. Additionally, there is a less prominent absorption band around 335 nm, indicative of the n-π* transitions of citrazinic acid aggregates [286]. Following the interaction with CU50D and CU100D, the distinctive

absorption peak of NaClO at 292 nm is no longer evident, indicating its full consumption in the process. This observation suggests that the NaClO undergoes a reaction upon contact with CU50D and CU100D, leading to the disappearance of its characteristic absorbance peak at 292 nm (Figure 56). The presence of HTTP fluorophore contributes to the green-blue color of the aqueous dispersions of CU50D and CU100D under UV irradiation (λ_{ex}=365 nm). Upon the addition of NaClO, the samples undergo a gradual transition, acquiring a unique blue colour that stabilizes after a 24-hour period. Interestingly, their initial dark brown appearance (under daylight) diminishes over the same duration, eventually yielding an almost clear solution (upon interaction with 10mM NaClO) (Figure 57). This observation aligns with earlier studies that highlighted the ability of NaClO to degrade organic dyes [287], [288].
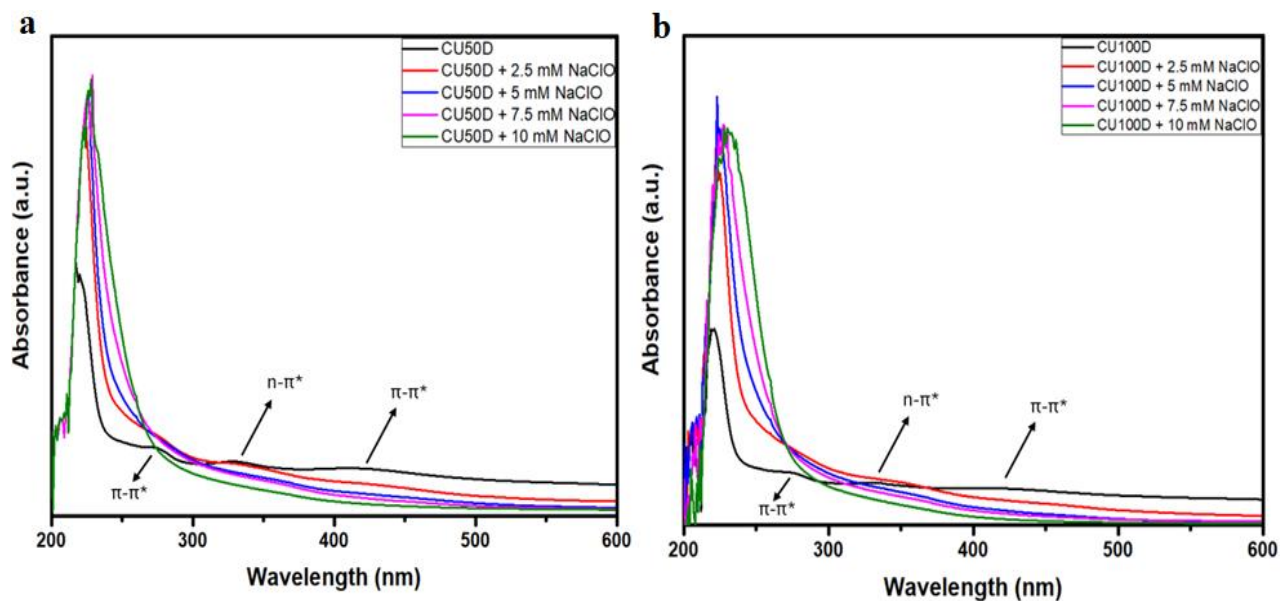
Figure 55. UV-Vis spectrum of aqueous dispersions of CU50D and CU100D before and after treatment with NaClO (up to 10 mM). The concentration of the solutions was 0.1 mg/ml.
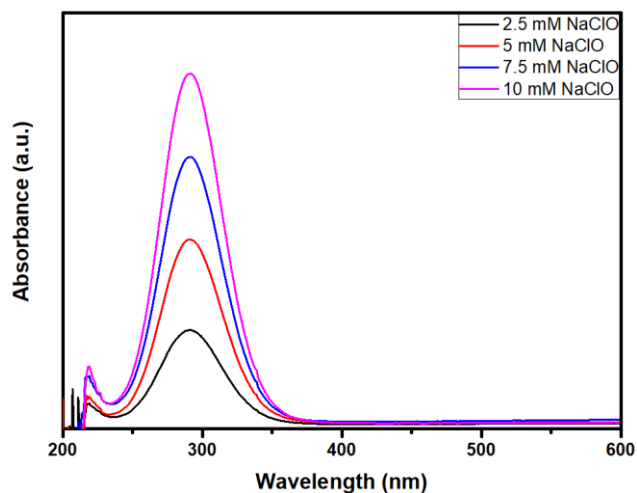
Figure 56. UV-Vis spectrum of aqueous dispersions of NaClO (up to 10 mM).
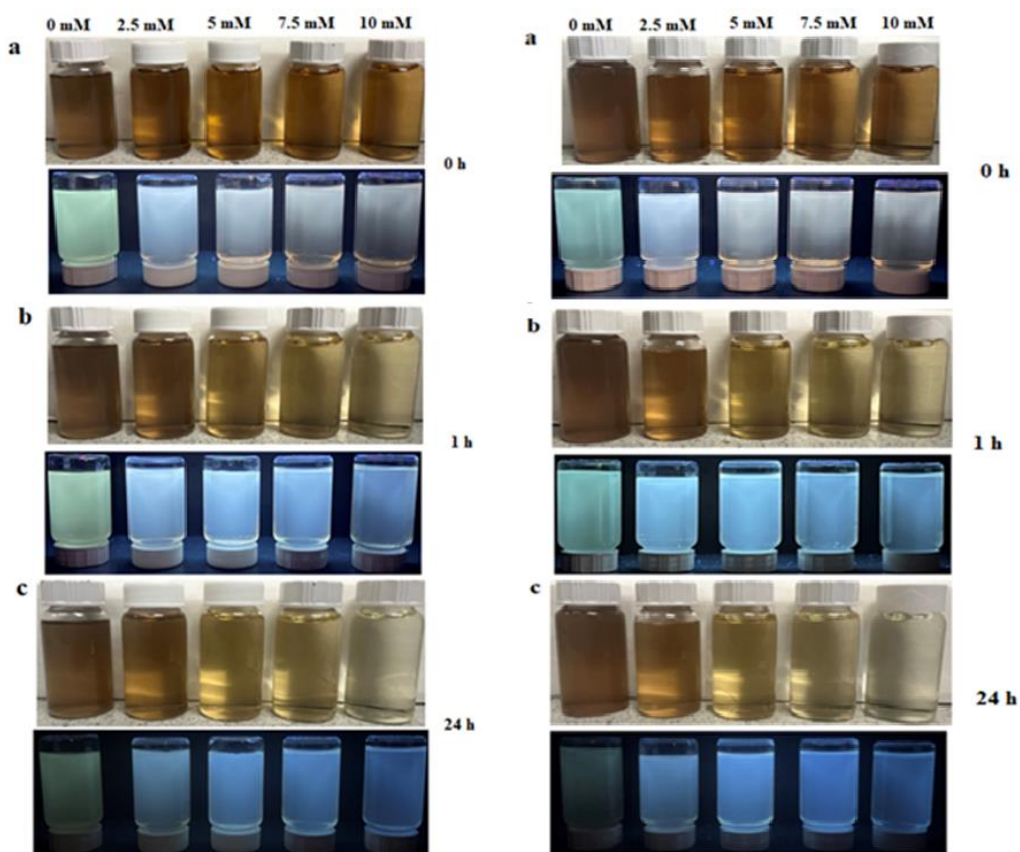
Figure 57. Photos of aqueous dispersions of (left) CU50D and (right) CU100D (a) 0 h, (b) 1 h, and (c) 24 h upon the addition of NaClO (0-10 mM) under daylight (up) and UV light (down). The concentration of the solutions was 0.1 mg/ml.

4.2.2.2. PL spectroscopy

The PL spectra of CU50D (Figure 58a) exhibit distinctive luminescent behaviour dependent on the λ_{ex}, spanning from 300 nm to 620 nm. Emission peaks are observed across a wide range from 390 nm (blue region) to 630 nm (red region). These spectra reveal contributions from both the HPPT fluorophore (λ_{em}= 520 nm) and citrazinic acid (λ_{em}= 390 nm), indicating the presence of multiple emitting species within the CU50D sample [286]. Upon exposure to NaClO, the intensity of the citrazinic acid peak at 390 nm gradually diminishes, disappearing entirely when NaClO concentration exceeds 5 mM (Figures 58b-e). The maximum PL emission for CU50D, occurring at 520 nm (λ_{ex}=420 nm), undergoes a blue shift upon NaClO addition, with emission peaks shifting to λ_{em}= 465 nm (λ_{ex}=420 nm) (Figures 58b-e). Similarly, the PL spectra of CU100D (Figure 59a) exhibit excitation wavelength-dependent luminescence behaviour, spanning from 300 nm to 620 nm, with emission peaks ranging from 390 nm to 630 nm. Contributions from both the HPPT fluorophore and citrazinic acid are observed at λ_{em}= 520 nm and λ_{em}= 390 nm, respectively. Upon addition of NaClO, the citrazinic acid peak gradually diminishes, disappearing when NaClO concentration gets over 5 mM (Figures 59b-e). The maximum PL emission for CU100D, located at 520 nm (λ_{ex}=420 nm), also experiences a blue shift to λ_{em}= 465 nm (λ_{ex}=420 nm) upon NaClO addition (Figures 59b-e). At high NaClO concentrations (4.4 M), the PL intensity decreases significantly, by up to 3 orders of magnitude compared to 20 mM NaClO, indicating the depletion of CU-dots due to oxidative processes (Figure 59f). Significantly, the pH of the CU100D solution exhibited no change following the introduction of NaClO, thereby indicating that the structural changes of HTTP (most likely decomposition) are irreversible in a way that doesn't depend on the pH of the solution.

The emission mechanism of CU50D and CU100D likely arises from multiple factors, reflecting their complex nature. Firstly, the isolated sp^2 carbon cores with sp^3 domains may contribute to the PL emission, indicating the existence of surface defects or crosslink-enhanced emission facilitated by various molecular fluorophores [286], [289]. Additionally, surface functional groups such as amino, carboxyl, and hydroxyl groups play a crucial role, communicating through the distorted sp^2 carbon framework [280].

123

Furthermore, the observed blue shift can be attributed to surface state alterations induced by the oxidation of surface hydroxyl groups with ClO- [290].
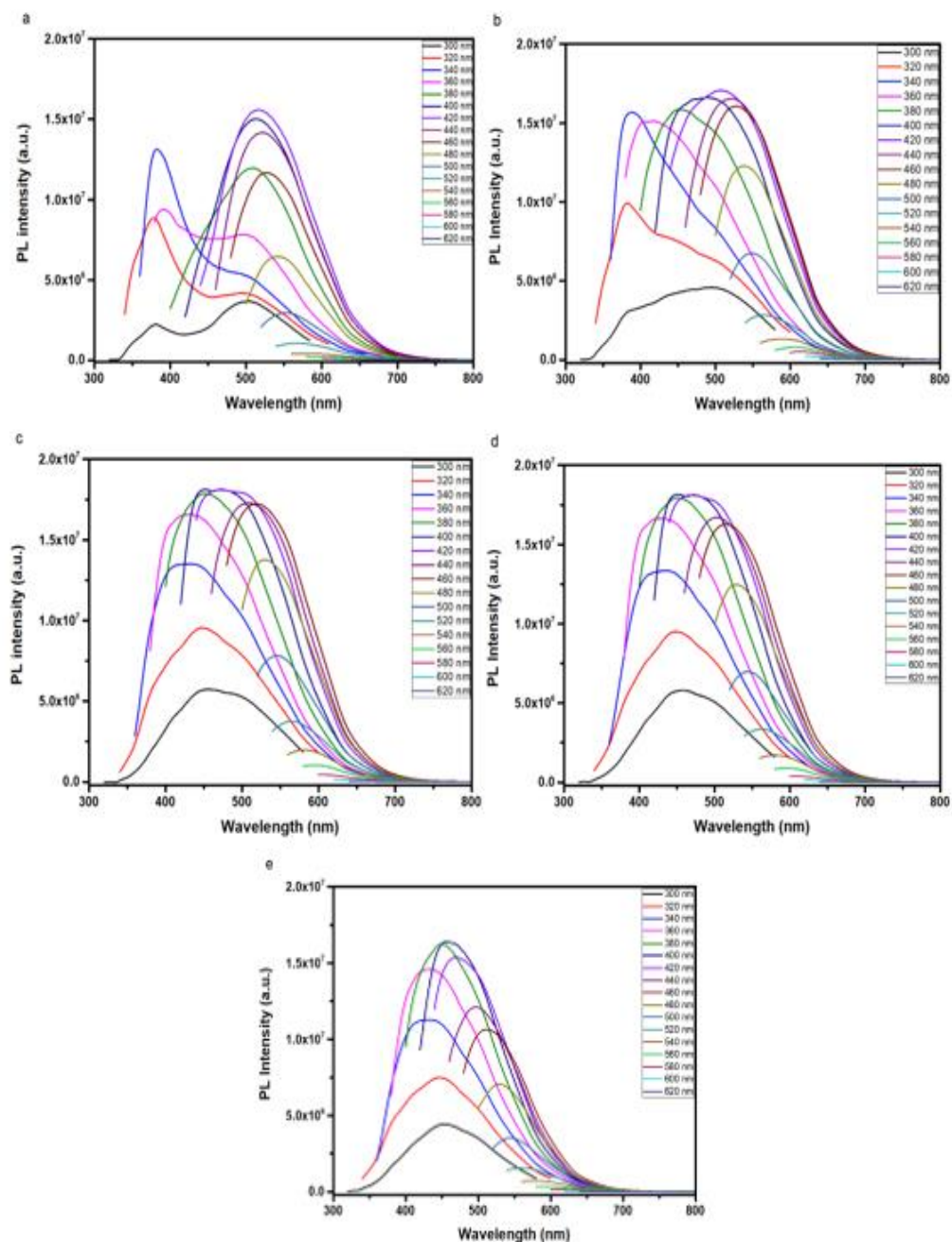
Figure 58. PL spectra of 0.1 mg/ml aqueous dispersions of (a) CU50D plus (b) 2.5 mM, (c) 5 mM, (d) 10 mM and (e) 20 mM NaClO with an increment of 20 nm.
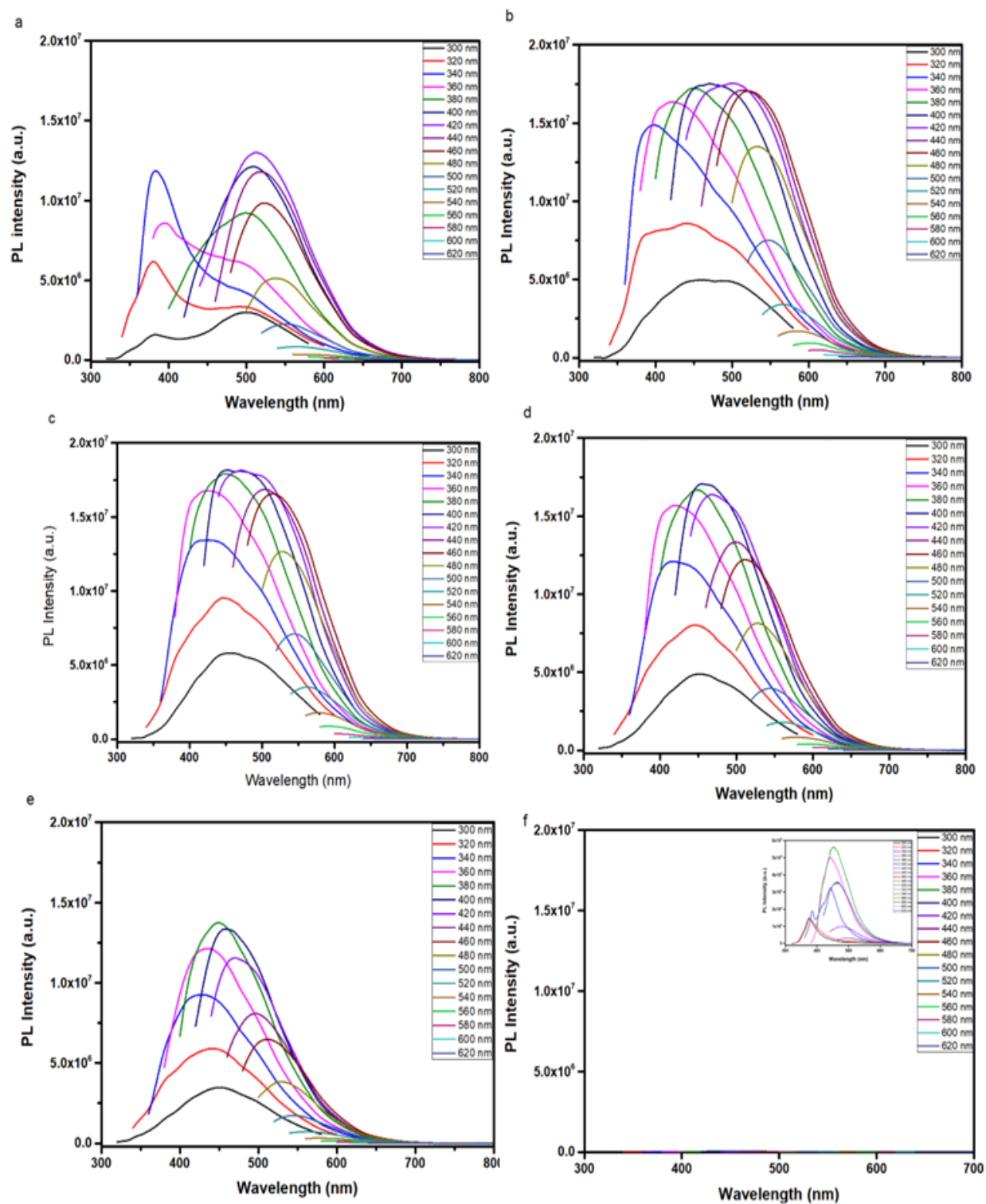
Figure 59. PL spectra of 0.1 mg/ml aqueous dispersions of (a) CU100D plus (b) 2.5 mM, (c) 5 mM, (d) 10 mM, (e) 20 mM and (f) 4.4 M NaClO with an increment of 20 nm; (inset in image f shows the same spectrum at a different scale).

4.2.2.3. QY

Moreover, the quantum yield values of CU-dots, both before and after exposure to varying concentrations of NaClO (up to 10 mM), were determined relative to anthracene (Φ=0.27, λ_{ex}= 365 nm) (Table 8). Interestingly, CU50D and CU100D exhibited a PL QY of approximately 6.5 %, which gradually increased upon addition of NaClO, peaking at 26.8 % and 29.4 %, respectively, at 7.5 mM NaClO. Even at higher concentrations, the QY of CU-dots remained relatively high, although there was a slight decrease observed. The impact of NaClO on the QY of CU-dots demonstrates a notable enhancement, with QY values increasing by up to 350 % (Figure 60). These findings align with previous studies where oxidative treatments significantly boosted QY in various types of C-dots. For instance, sucrose-derived C-dots achieved a six-fold increase in QY after 24 hours of catalytic surface oxidation with N-methyl morpholine N-oxide [291]. Similarly, glucose-derived C-dots subjected to aerial oxidation in the presence of $MgSO_4$ for six months showed a QY increase from 0.61% to 4.26% [292]. Together, these results underscore the pivotal role of oxidative processes in tailoring and improving the optical properties of C-dots, with NaClO proving to be particularly effective in achieving such enhancements.

Table 8. QY values of aqueous solutions (0.1 mg/ml) of CU-dots before and after treatment with NaClO (up to 10 mM), using anthracene as a reference.

Material	QY %
CU50D	6.7
CU50D + 2.5 mM NaClO	11.9
CU50D + 5 mM NaClO	14.3
CU50D + 7.5 mM NaClO	26.8
CU50D + 10 mM NaClO	21.4
CU100D	6.5
CU100D + 2.5 mM NaClO	12.9
CU100D + 5 mM NaClO	17.3
CU100D + 7.5 mM NaClO	29.4
CU100D + 10 mM NaClO	21.2
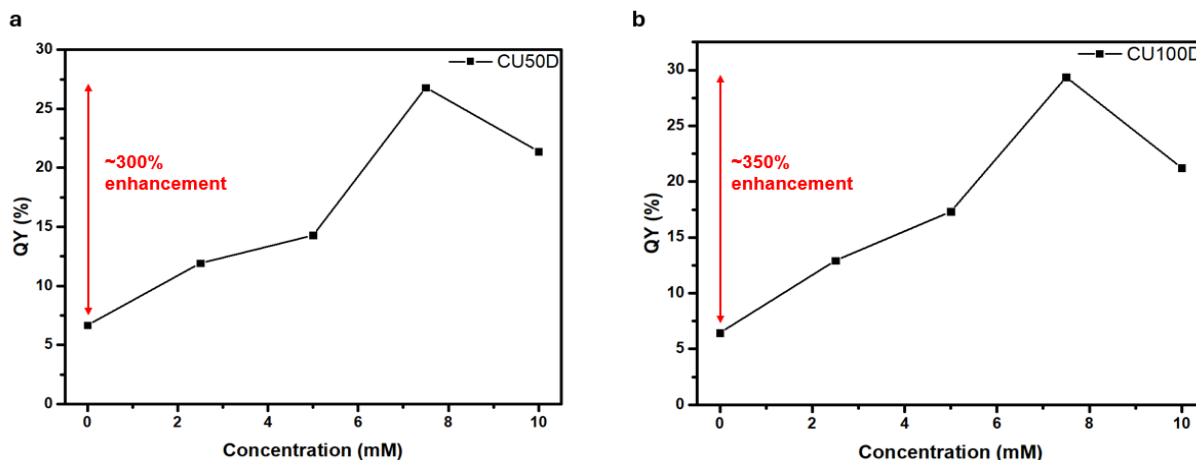
Figure 60. QY (%) of (a) CU50D and (b) CU100D as a function of the concentration of added NaClO

4.2.2.4.   PL lifetime

The fluorescence lifetime decays of CU50D and CU100D before and after treatment with NaClO (up to 20 mM) were investigated using time-resolved PL measurements at two excitation wavelengths: 375 nm and 450 nm (Figures 61 and 62). The obtained τ_{avg} for both samples decreased from 2.9 ns to around 1.8 ns, with the addition of NaClO, after them been excited with a 375 nm laser (Table 9). Similarly, the τ_{avg} of CU50D and CU100D upon excitation with a 450 nm laser decreased from 7.0 ns and 7.2 ns to 3.8 ns and 3.7 ns, respectively as the concentration of NaClO increased (Table 10). Both samples showed τ_{avg} in accordance with previous studies [293]. The reduction in τ_{avg} is attributed to the oxidation of surface functional groups on the CU-dots by ClO⁻, leading to a decrease in the presence of amino groups on their surface [294].
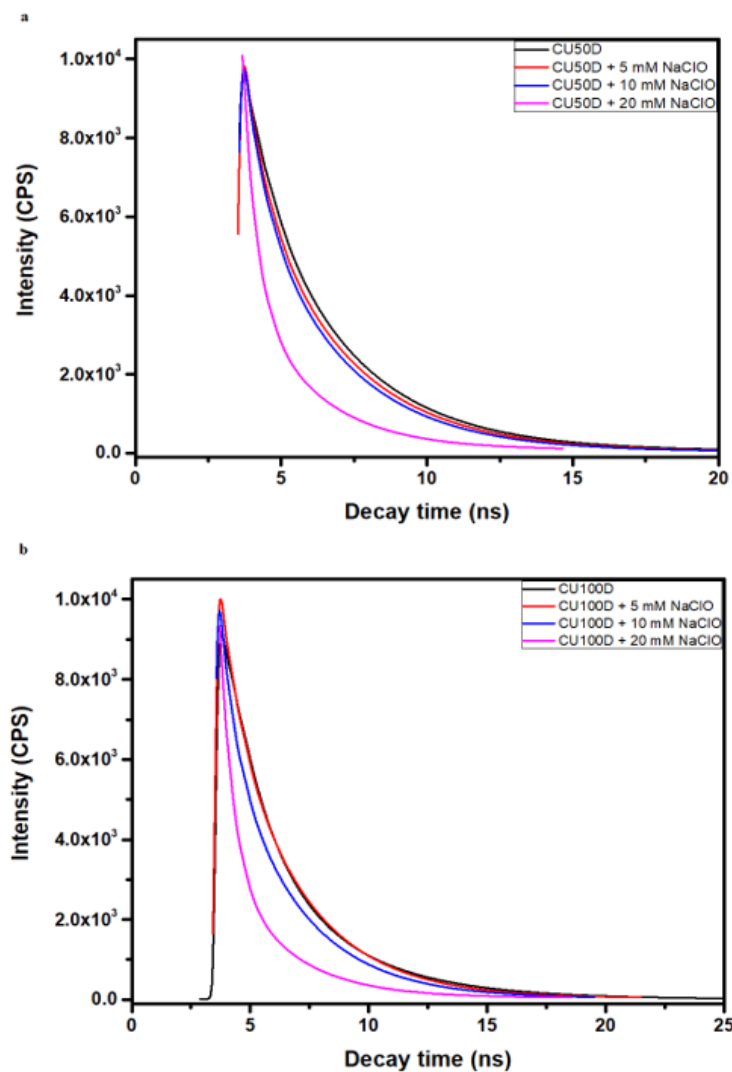
Figure 61. Liquid-state PL lifetime decays of aqueous dispersions of CU50D and CU100D before and after treatment with NaClO (up to 20 mM) at λ_{ex}= 375 nm. The concentration of the solutions was 0.1 mg/ml.

Table 9. Average lifetime values of aqueous dispersions of CU50D and CU100D before and after treatment with NaClO (up to 20 mM) at λ_{ex}= 375 nm.

λ_{ex} = 375 nm	CU50D	CU100D
-	2.9 ns	2.9 ns
+ 5 mM NaClO	2.8 ns	2.8 ns
+ 10 mM NaClO	2.7 ns	2.7 ns
+ 20 mM NaClO	1.7 ns	1.9 ns
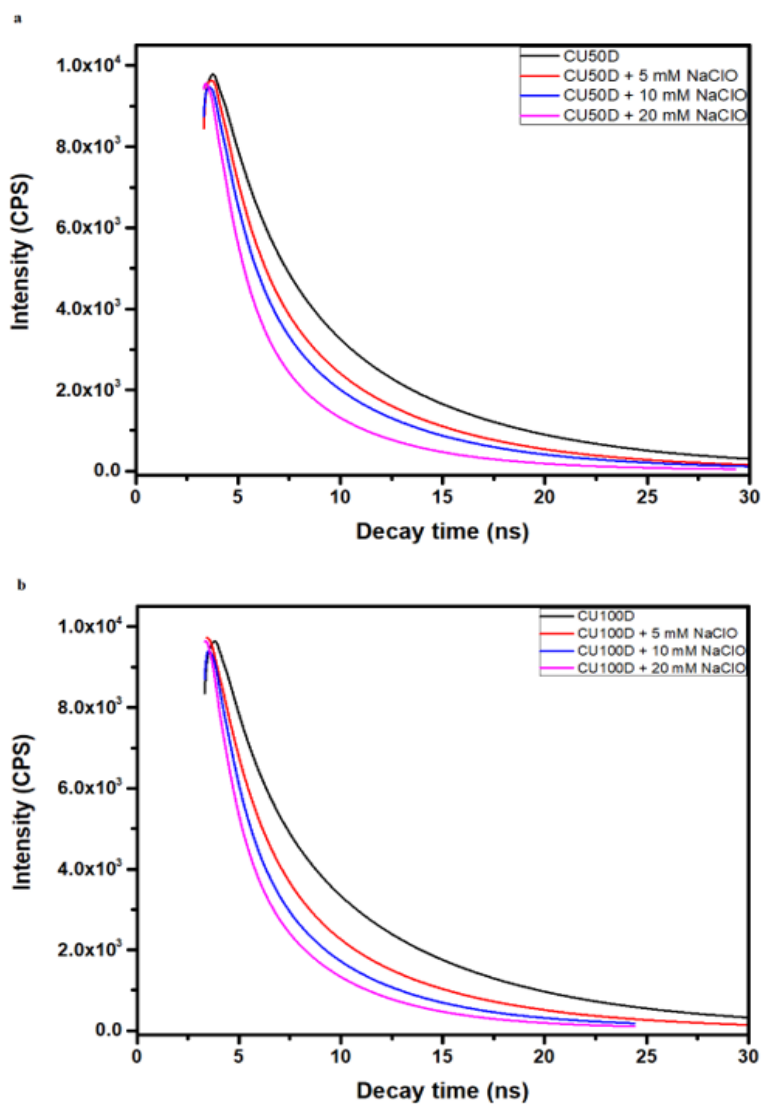
Figure 62. Liquid-state PL lifetime decays of aqueous dispersions of CU50D and CU100D before and after treatment with NaClO (up to 20 mM) at λex= 450 nm. The concentration of the solutions was 0.1 mg/ml.

Table 10. Average lifetime values of aqueous dispersions of CU50D and CU100D before and after treatment with NaClO (up to 20 mM) at λex= 450 nm.

λ_{ex} = 450 nm	CU50D	CU100D
-	7.0 ns	7.2 ns
+ 5 mM NaClO	5.6 ns	5.7 ns
+ 10 mM NaClO	5.0 ns	4.3 ns
+ 20 mM NaClO	3.8 ns	3.7 ns

4.2.3. Biological analysis

In this chapter, a series of biological analyses were conducted to evaluate the suitability of CU-dots for biomedical applications. CU100D exhibit significant antimicrobial properties against *E. coli* and *S. aureus*, causing reduction in the colonies 79% and 97.20%, respectively. Two toxicity assays, namely the MTT assay and the PrestoBlue assay, were performed to assess the cytotoxicity of the samples. The MTT assay measures cell viability based on mitochondrial activity by reducing MTT to formazan, while the PrestoBlue assay evaluates cell viability through the reduction of resazurin to resorufin, a process that is faster and more sensitive.

Sodium hypochlorite is a widely used disinfectant with powerful oxidative properties. It has been extensively studied in biomedical applications, particularly in the context of its cytotoxic effects on human cells. In low concentrations, NaClO is often used for disinfection, while higher concentrations are employed for bleaching and antimicrobial purposes. However, its strong oxidative nature raises concerns regarding potential toxicity to surrounding tissues, especially when applied in vivo or in cell culture models. Several studies have investigated the cytotoxic effects of NaClO on various human cell types, including human fibroblasts, mesenchymal stem cells, and dental pulp cells. The concentration of NaClO plays a pivotal role in determining its cytotoxicity, with higher concentrations generally inducing more severe cell damage. For instance, research by Hidalgo et al. demonstrated that NaClO concentrations as low as 0.05% caused significant reductions in cell viability in human dermal fibroblasts, leading to ATP depletion and mitochondrial dysfunction [295]. These effects were even more pronounced at higher concentrations, which resulted in complete cell death. Similarly, Coaguila-Llerena et al. assessed the cytotoxicity of NaClO on human mesenchymal stem cells and found that concentrations as low as 0.025% NaClO resulted in significant cell death, emphasizing the need for caution in its clinical use [296]. This study highlights the dose-dependent nature of NaClO's cytotoxicity, as concentrations at or above 0.1% NaClO can severely compromise cellular function.

4.2.3.1. MTT assays

4.2.3.1.1.   HeLa cell lines

The cytocompatibility of CU100D nanoparticles and CU100D nanoparticles treated with 7.5 mM NaClO was evaluated using the MTT assay on HeLa cells across a concentration range of 0 to 100 µg/ml (Figure 63). The analysis showed that the average cell viability for CU100D was 88.60%, while CU100D + 7.5 mM NaClO exhibited a slightly higher mean viability of 89.58%. Both conditions demonstrated relatively low variability, with standard deviations of 4.90% and 5.79%, respectively, indicating reproducible results. Importantly, both formulations maintained high cytocompatibility across the tested concentrations, though a slight decrease in cell viability was noted at higher nanoparticle concentrations (over 50 µg/ml). Paired t-tests were conducted to compare cell viability between CU100D and CU100D + 7.5 mM NaClO at each concentration. While some variations in cell viability were observed, the statistical analysis yielded no significant differences, with all p-values exceeding the standard threshold of 0.05. These findings indicate that the addition of 7.5 mM NaClO does not negatively impact the cytocompatibility of CU100D nanoparticles. The absence of significant differences supports the conclusion that both formulations exhibit similar biocompatibility profiles and are well-suited for potential biomedical applications.
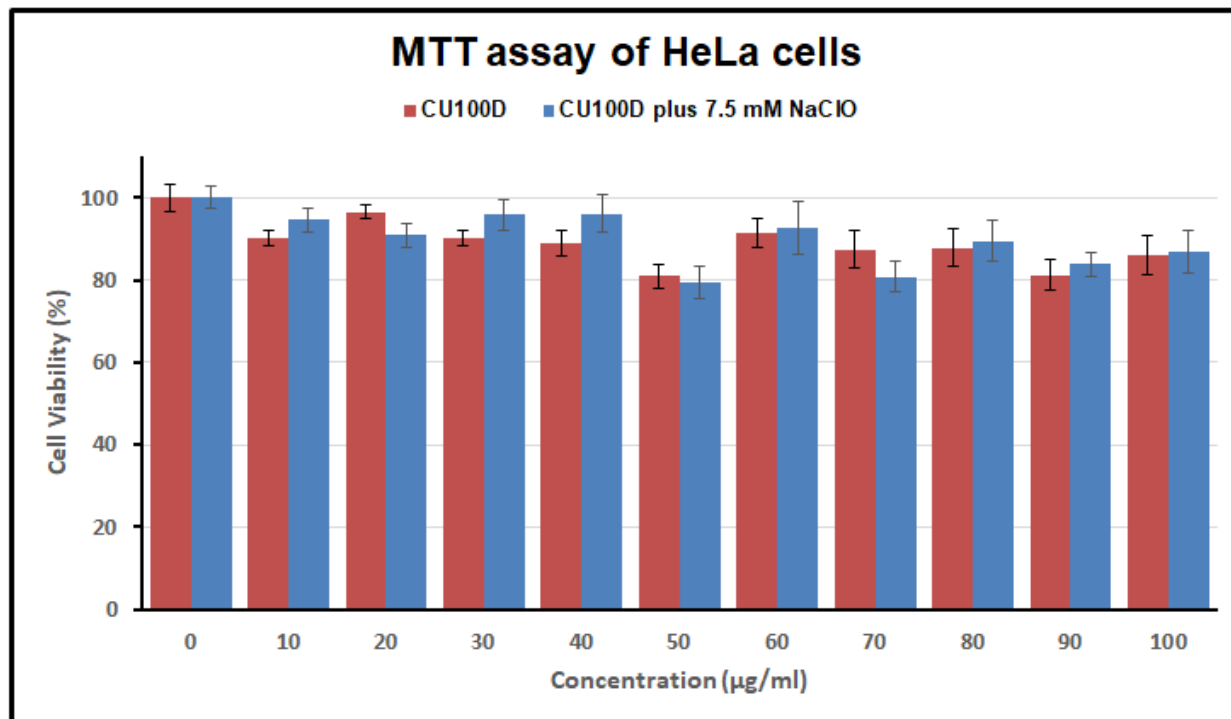
Figure 63. MTT assay of HeLa cells following incubation with CU100D and CU100D (after been subjected to 7.5 mM NaClO treatment) for 24h. Results are presented as the mean value ± standard deviation of triplicate experiments, with cell viability expressed as a percentage relative to untreated controls.

4.2.3.1.2.   U87 cell lines

The cytocompatibility of CU100D nanoparticles, before and after treatment with 7.5 mM NaClO, was assessed using the MTT assay on U87 cells over a concentration range of 0 to 100 µg/mL (Figure 64). The CU100D nanoparticles showed an average cell viability of 91.82%, with a standard deviation of 5.06%, while the combination with NaClO resulted in an average viability of 92.46% and a slightly lower standard deviation of 3.76%. Both groups consistently demonstrated high cell viability (≥83%) across all tested concentrations, indicating good biocompatibility. Additionally, the low variability across samples highlights the reproducibility and reliability of the experimental findings. To further examine these trends, paired t-tests were conducted to compare the cell viability between CU100D and CU100D + 7.5 mM NaClO at each concentration. Although minor differences were detected, none of these reached statistical significance ($p > 0.05$). This outcome suggests that the addition of NaClO does not negatively impact the cytocompatibility of CU100D nanoparticles.
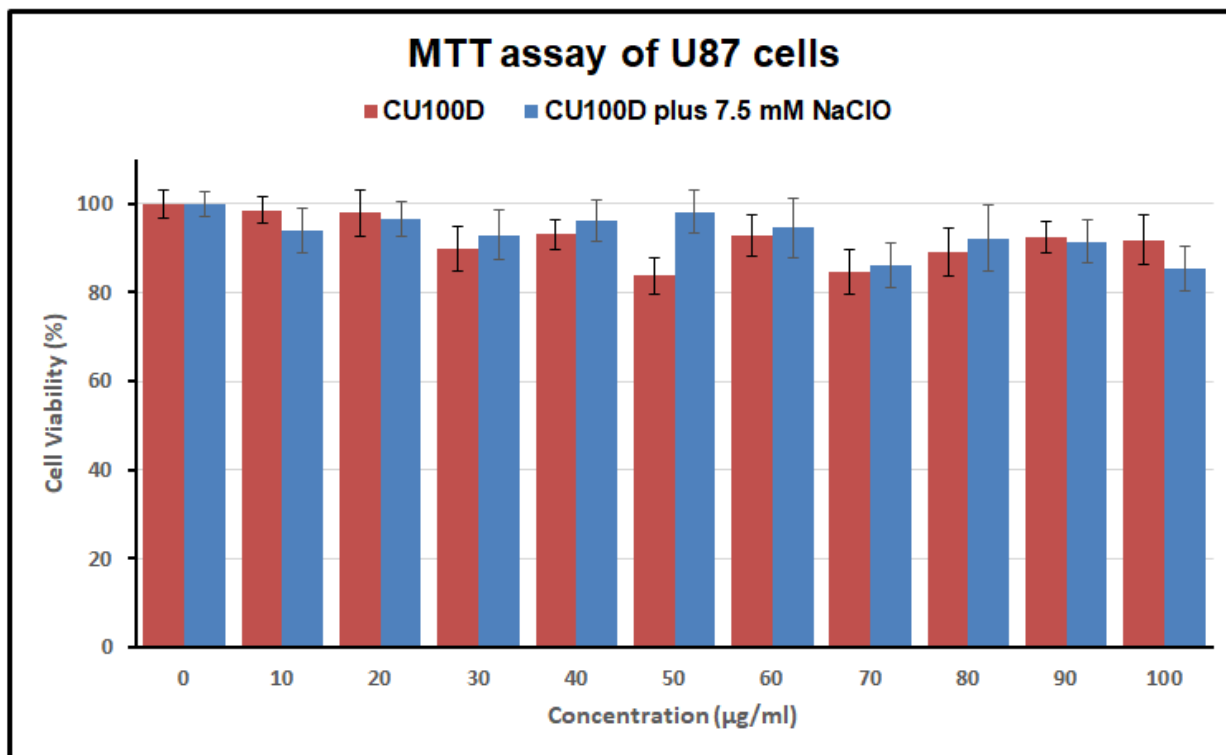
Figure 64. MTT assay of U87 cells following incubation with CU100D and CU100D (after been subjected to 7.5 mM NaClO treatment) for 24h. Results are presented as the mean value ± standard deviation of triplicate experiments, with cell viability expressed as a percentage relative to untreated controls.

4.2.3.2. Prestoblue assays

4.2.3.2.1. HeLa cell lines

The analysis of cell viability data of both CU100D and CU100D + 7.5 mM NaClO, revealed the following findings: The mean cell viability for CU100D was 92.60%, with a standard deviation of 3.52%, while for CU100D + NaClO, the mean was 90.23%, and the standard deviation was 5.30% (Figure 65). Although the viability in the CU100D group was slightly higher, the larger variability in the CU100D + NaClO group suggests that the oxidative stress induced by NaClO might lead to more heterogeneous cellular responses. A paired t-test comparing the two conditions yielded a t-statistic of 1.45 and a p-value of 0.177,

indicating no statistically significant difference in cell viability between the two treatments at the concentrations tested. These results suggest that the addition of NaClO to CU100D did not significantly affect cell viability. The larger standard deviation in the CU100D + NaClO group highlights the potential complexity of cellular responses to oxidative stress.
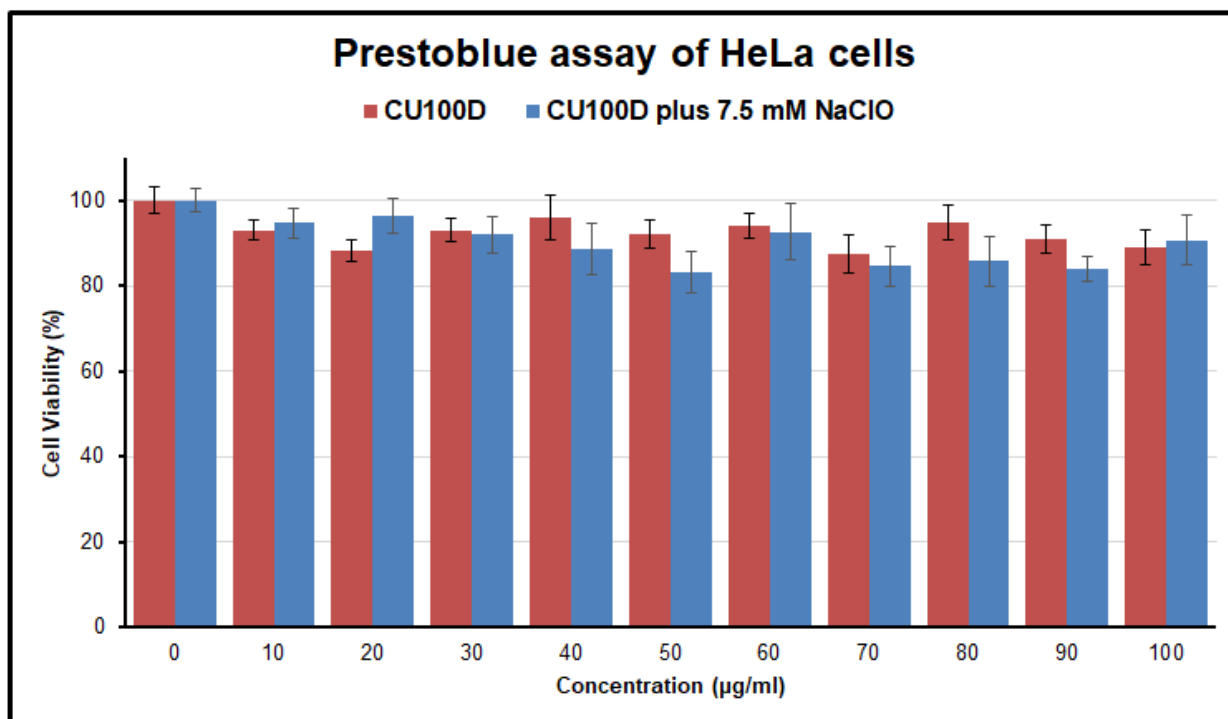
Figure 65. Prestoblue assay of HeLa cells following incubation with CU100D and CU100D (after been subjected to 7.5 mM NaClO treatment) for 24h. Results are presented as the mean value ± standard deviation of triplicate experiments, with cell viability expressed as a percentage relative to untreated controls.

4.2.3.2.2.   U87 cell lines

The cytocompatibility of CU100D nanoparticles and CU100D nanoparticles exposed to 7.5 mM NaClO was assessed using U87 cells across a concentration range of 0 to 100 µg/mL via a PrestoBlue assay, which measures metabolic activity as an indicator of cell viability (Figure X). The results showed an average cell viability of 93.67% for CU100D and a slightly higher value of 94.11% for CU100D + 7.5 mM NaClO. Both groups exhibited low variability, with standard deviations of 3.74% and 4.00%, respectively, indicating consistent and reproducible results. A line graph of cell viability trends revealed that both

groups maintained high viability (≥85%) across all concentrations, following similar patterns. Statistical analysis using paired t-tests showed no significant differences between the two groups at any concentration ($p > 0.05$), confirming that the addition of 7.5 mM NaClO does not adversely affect the cytocompatibility of CU100D nanoparticles. These findings highlight the excellent biocompatibility of CU100D nanoparticles and their modified counterparts with 7.5 mM NaClO, supporting their potential use in biomedical applications such as drug delivery and imaging. The slight increase in viability observed with NaClO-treated CU100D may suggest a stabilizing effect, though the differences remain minimal.
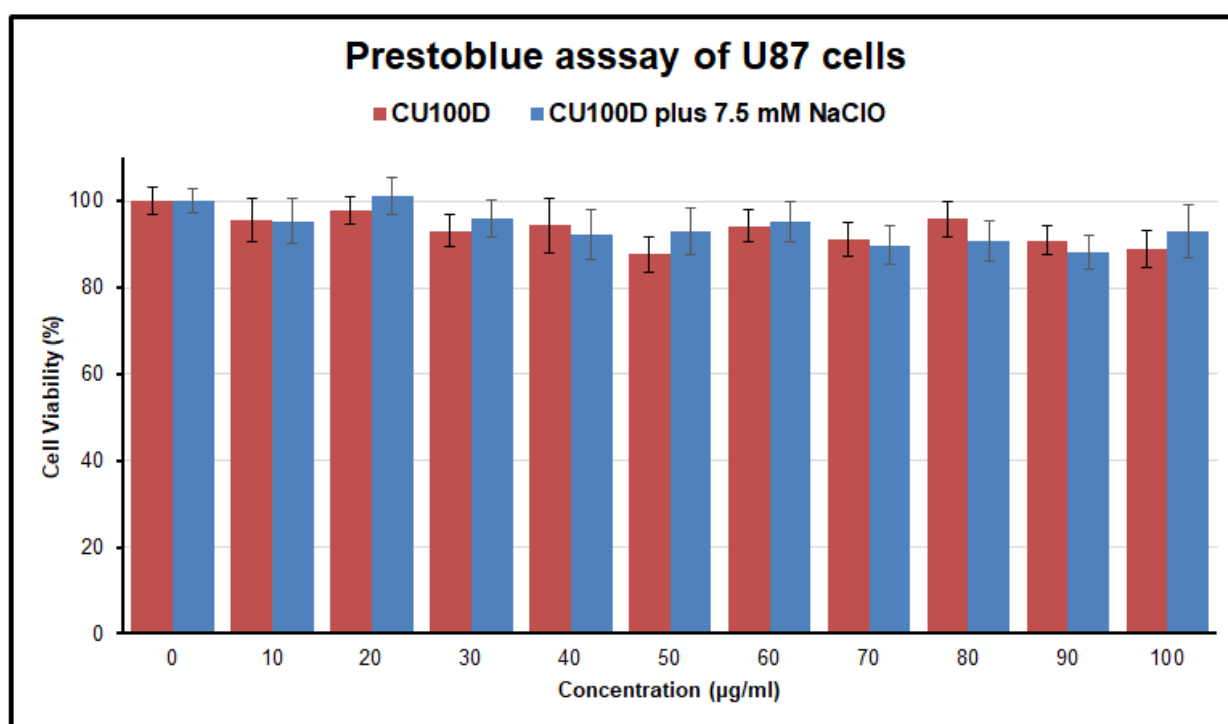
Figure 66. Prestoblue assay of U87 cells following incubation with CU100D and CU100D (after been subjected to 7.5 mM NaClO treatment) for 24h. Results are presented as the mean value ± standard deviation of triplicate experiments, with cell viability expressed as a percentage relative to untreated controls.

4.2.4.   Antifungal testing

Antifungal activity of CU100D was assessed against *T. phinophilus*. CU100D solutions were initially prepared at a concentration of 0.1 mg/mL from a stock solution and

subsequently diluted in sterile distilled water using a 1:2 serial dilution method, yielding concentrations ranging from 0.1 mg/mL to 0.0008 mg/ml. Sterile samples measuring approximately 10 mm x 10 mm were immersed in either water (control) or CU100D solutions for 30 minutes, then allowed to dry completely. After drying, 100 µL of fungal spore suspension was evenly spread over nutrient salt agar plates. The control and test samples were placed on the plates. Each test plate contained four concentrations: 0.1 – 0.0125 mg/mL for the 'high' concentration plates, and 0.0063 – 0.0008 mg/mL for the 'low' concentration plates, with duplicates for each concentration. Plates were incubated at 25°C for 28 days, and fungal growth was observed at 7-day intervals. The results indicated that CU100D exhibited antifungal activity at all concentrations, as shown in Figure 67.

These findings are in line with recent studies reporting the antifungal efficacy of carbon-based nanoparticles. For instance, nitrogen-doped carbon quantum dots have been shown to exhibit significant antifungal activity against *Mucor indicus*, a common pathogen responsible for bone infections, with both *in vitro* and *in vivo* tests demonstrating their strong fungicidal effects [297]. In another study, the fungicidal effects of carbon dots synthesized from citric acid and urea (CDs-CO_2H/NH_2) revealed that these carbon dots were effective against *C. albicans*, with the positive charge of the carbon dots enhancing their interaction with the negatively charged microbial cell walls, leading to effective internalization and disruption of fungal cells [298]. Furthermore, the antifungal activity of citric acid/urea-based carbon dots was not only dose-dependent but also exhibited notable inhibition of biofilm formation, a critical factor in the virulence of fungal infections. This effect was observed at concentrations as low as 125 µg/ml, which underscores the potential of CU100D as a viable antifungal agent.

In a follow-up experiment, polyester fabric was treated with CU100D after exposure to 7.5 mM NaClO. The results showed that NaClO-treated CU100D exhibited a stronger antifungal effect compared to untreated C-dots, as demonstrated by the formation of larger zones of inhibition and distinct swirling diffusion patterns across the agar plates Figures 68a-b). When NaClO-treated CU100D were impregnated onto PVDF membranes, the corresponding agar plates exhibited a noticeably lighter yellow color than

the control, suggesting reduced fungal growth. A similar trend was observed for polyurethane sponges impregnated with both untreated and treated CU100D (Figure 68c). The enhanced antifungal activity of NaClO-treated CU100D can be attributed to their ability to interact with fungal ergosterol and induce the production of reactive oxygen species (ROS), which causes DNA damage and protein denaturation [298]. Furthermore, the presence of hydrogen-donating groups, such as carbonyl and hydroxyl groups, on the treated C-dots likely contributes to increased ROS production, which may explain the superior antifungal effects observed in this experiment [299].
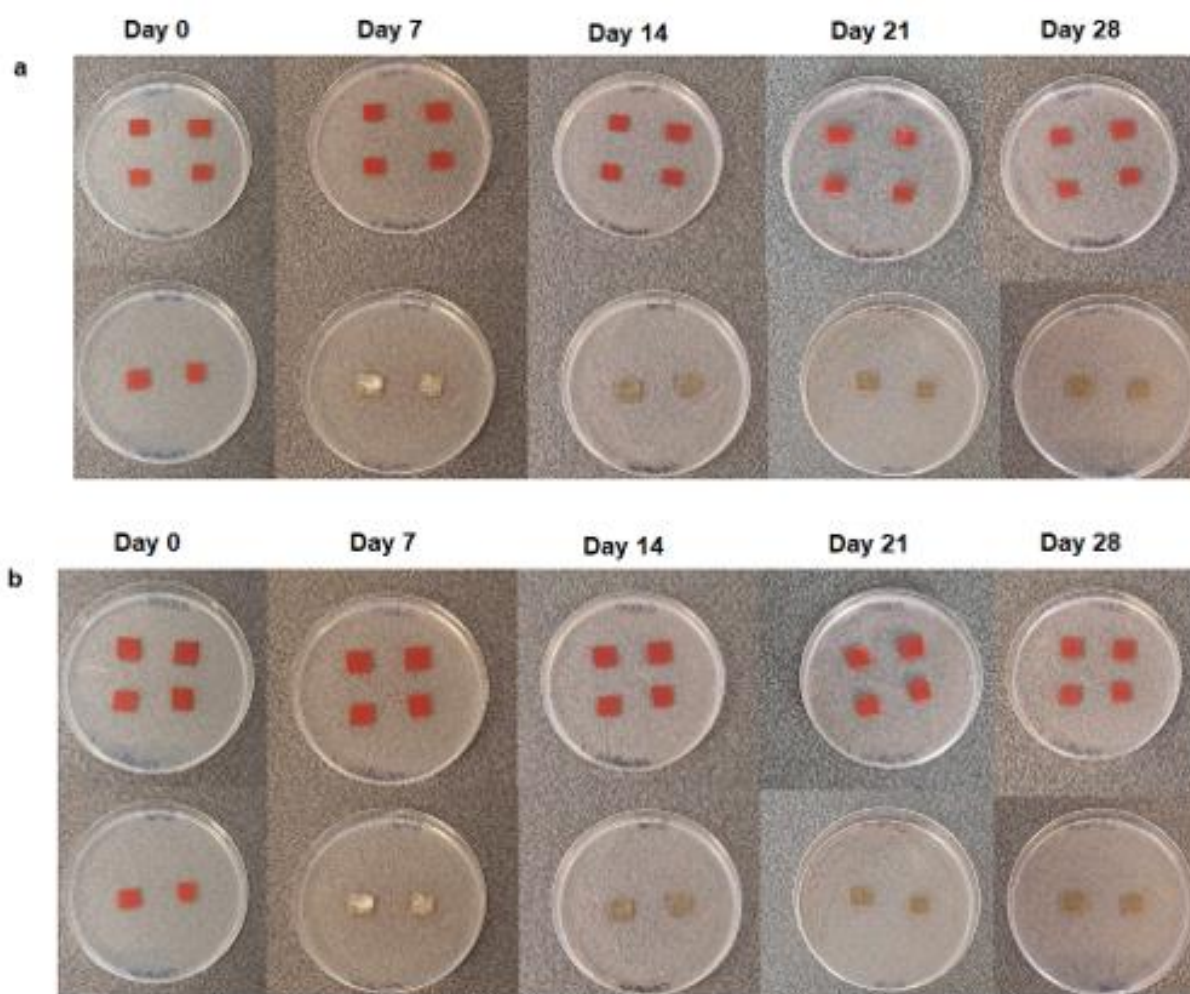
Figure 67. Antifungal testing of CU100D against *T. Phinophilus*. (a) Low (0.0063 – 0.0008 mg/ml) and (b) high (0.1 – 0.0125 mg/ml) concentrations of CU100D on red paper are depicted at the top images. Samples at the bottom of the image acted as the control.
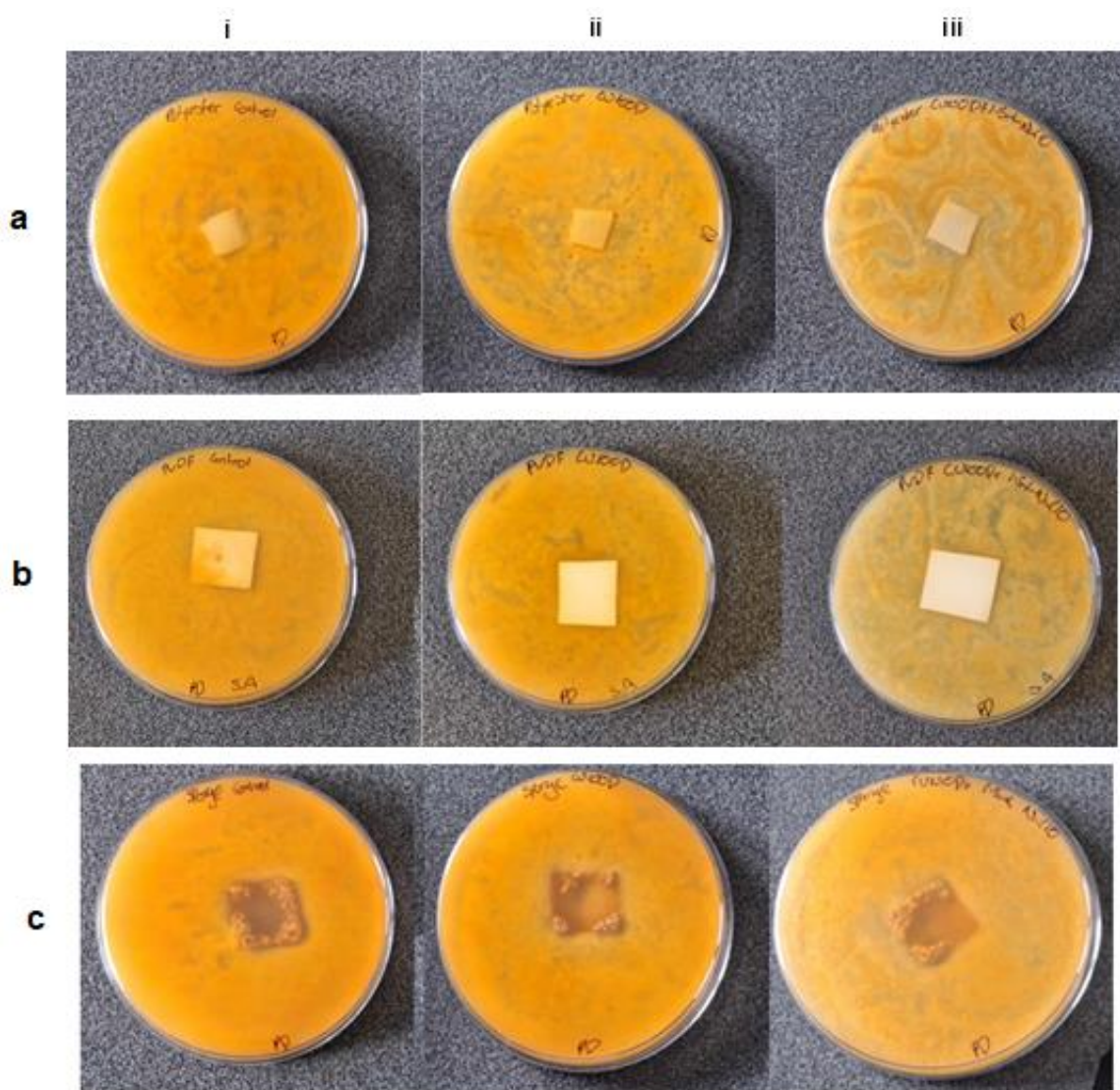
Figure 68. Photos of the Petri dishes containing *T. Pinophilus* cultures in the presence of polyester fabric (a), PVDF membrane (b) and polyurethane sponge impregnated with i) water (control), ii) CU100D, iii) CU100D after exposure to 7.5 mM NaClO.

4.3. Conclusion

This study demonstrates that NaClO treatment is a promising method for enhancing the optical properties of CU100D. The application of NaClO induces surface oxidation, leading to structural rearrangements that result in significant improvements in the PL characteristics of the CU100D. Specifically, NaClO treatment enhances the PL emission

by up to six-fold, while also maintaining the cytocompatibility of the CU100D, as evidenced by low cytotoxicity towards both HeLa and U87 cell lines.

The morphological and structural analysis reveals that NaClO treatment causes a reduction in the size of the CU100D, with an average diameter decreasing from 4.3 nm to 2.9 nm. This size reduction is attributed to the oxidation and etching effects of NaClO on the C-dot surface. Elemental analysis further confirms the increase in oxygen content and a reduction in nitrogen content following NaClO treatment, which corresponds to the formation of new oxygen-containing surface functional groups. These changes are associated with the enhancement of the C-dots' fluorescence properties, as evidenced by the observed blue shift in the PL emission spectrum. The modification of the CU100D with NaClO also alters their surface charge, with a more negative zeta potential observed after treatment. This suggests improved colloidal stability and a higher degree of functionalization, likely due to the increased presence of carboxyl and hydroxyl groups on the surface. The shift in surface chemistry plays a key role in the enhanced optical properties of the CU100D, contributing to an increase in their QY, which is enhanced by up to 350% compared to untreated ones.

The biological analysis of CU100D nanoparticles revealed their potential for various biomedical applications, demonstrating notable antimicrobial and cytocompatible properties. The antimicrobial activity was particularly evident in the significant reduction of colony counts of *E. coli* and *S. aureus* by 79% and 97.2%, respectively, suggesting that CU100D nanoparticles can be effective in controlling bacterial infections. Cytocompatibility was assessed using MTT and PrestoBlue assays on HeLa and U87 cell lines, with results showing high cell viability (over 88% for HeLa and 91% for U87 cells) across a concentration range of up to 100 µg/ml. The addition of 7.5 mM NaClO, an oxidative agent, did not negatively impact the cell viability in either cell line, suggesting that the CU100D nanoparticles maintain their antifungal ability and biocompatibility under oxidative stress. This indicates that CU100D nanoparticles are not only non-toxic but also stable in environments that may otherwise induce toxicity, such as in disinfection or sterilization processes, thereby supporting their potential for biomedical applications. Furthermore, the antifungal activity of CU100D nanoparticles was evaluated against *T.*

phinophilus, with the results indicating significant inhibition of fungal growth across all tested concentrations. The nanoparticles exhibited effective antifungal activity at concentrations as low as 0.0125 mg/mL, likely due to the positive charge on the nanoparticles enhancing their interaction with the negatively charged fungal cell walls, leading to effective internalization and disruption of fungal cells. This activity was dose-dependent and showed potential for biofilm inhibition, a crucial factor in the virulence of fungal infections.

In addition to their cytocompatibility, CU100D nanoparticles also demonstrated promising antifungal properties. The antifungal efficacy of CU100D was evident against *T. phinophilus,* showing activity at all concentrations tested, with the findings supporting previous studies on the antifungal capabilities of carbon-based nanoparticles. The observed dose-dependent activity and inhibition of biofilm formation further enhance the potential of CU100D as an effective antifungal agent. Moreover, treatment with NaClO significantly enhanced the antifungal activity of CU100D, as demonstrated by larger zones of inhibition and reduced fungal growth on various substrates, including polyester fabric, PVDF membranes, and polyurethane sponges. This enhanced activity can be attributed to the increased production of ROS, induced by NaClO treatment, which contributes to fungal cell damage. The results underscore the dual functionality of CU100D nanoparticles, not only as a biocompatible material but also as a potent antifungal agent, with potential applications in infection control and medical treatments.

Chapter 5:   Commercially available graphene quantum dots

5.1. Introduction

Graphene quantum dots (GQDs) represent a fascinating class of carbon-based nanomaterials that have garnered significant attention due to their unique combination of quantum confinement effects, edge effects, and versatile chemical functionalization. These zero-dimensional (0D) materials, derived from graphene or its derivatives, are typically composed of sp^2-hybridized carbon atoms arranged in a hexagonal lattice. These features allow GQDs to exhibit strong, stable fluorescence and tunable emission wavelengths. The size of GQDs plays a pivotal role in determining their optical and electronic behavior. GQDs with smaller sizes exhibit quantum confinement effects more prominently, leading to higher energy band gaps and blue-shifted PL. Larger GQDs, on the other hand, tend to exhibit red-shifted emission due to reduced confinement. Studies, such as that by Liu et al., have demonstrated that precise control of GQD dimensions can fine-tune their optical properties, enabling their use in specific applications ranging from fluorescence imaging to photovoltaics [300]. Structurally, GQDs possess a combination of graphitic sp^2 domains interspersed with functional groups, defects, and oxygen-containing groups. These structural features significantly influence their chemical reactivity and interaction with external molecules. Functional groups on the edges and surfaces of GQDs enhance their solubility and enable diverse chemical modifications.

The versatility of GQDs stems largely from their ability to undergo functionalization. Functional groups not only enhance the intrinsic properties of GQDs but also open new avenues for targeted applications. Among the most extensively studied modifications are amine-, chlorine-, and imidazole-functionalized GQDs, each of which imparts distinct characteristics to the material. Amine-functionalization of GQDs involves the introduction of amine groups ($-NH_2$) onto their surface, achieved through either covalent bonding or non-covalent interactions. This modification significantly enhances the solubility of GQDs in aqueous media, improves their biocompatibility, and enables their binding to biomolecules, making them highly suitable for a range of biomedical applications. In a study by Kumar et al, the excitation-dependent PL in amino-functionalized GQDs, ranging from 5 to 7 nm in size, reveals dual cyan emission originating from $\pi^*-\pi$ and $n-\pi$ transitions [301]. This behavior is attributed to the formation of interband states resulting

from p orbital hybridization at C–N edge sites. Interestingly, larger flakes (20–30 nm) show minimal changes in their PL profiles, emphasizing the critical role of edge functionality in modulating the optical properties of GQDs. Moreover, an eco-friendly synthesis method has been developed for producing size-controllable amine-functionalized GQDs using a combination of graphene oxide, ammonia, and hydrogen peroxide [302]. The process enables fine separation, yielding single- or double-layer GQDs, with hydrogen peroxide facilitating the cleavage of graphene oxide and ammonia effectively passivating the surface. These amine-functionalized GQDs demonstrate low cytotoxicity, excellent biocompatibility, and strong multiwavelength imaging properties. Remarkably, they also exhibit novel antimycoplasma effects, positioning them as promising, cost-effective agents for diverse biomedical applications. The production or elimination of ROS is crucial in antioxidant, photodynamic, and antibacterial applications. Chlorine-doped GQDs (Cl-GQDs) with tunable Cl doping show enhanced anti- and pro-oxidant properties [303]. The scavenging performance and free radical-producing efficiency of Cl-GQDs were seven and three times higher, respectively, than undoped GQDs. Cl-GQDs also exhibit improved singlet oxygen generation, making them promising for antibacterial applications. Imidazole-functionalized GQDs show enhanced chemical stability, optical properties, and interaction with various substrates. Gao et al. explored the use of imidazole-functionalized GQDs in tailoring the interface of FAPbI$_3$ planar perovskite solar cells [304]. The study showed that these modified GQDs significantly improved the charge extraction efficiency, reduced interfacial energy losses, and stabilized the perovskite layer under operational conditions.

5.2. Structural and optical properties

5.2.1. TEM analysis

The TEM images of GQDs-Imid nanoparticles reveal their spherical morphology with average diameters 6 nm (Figure 69a). Their graphene structure is further confirmed by High-Resolution TEM, which showed that the GQDs-Imid lattice spacing was around 0.22 nm (Figure 69b).
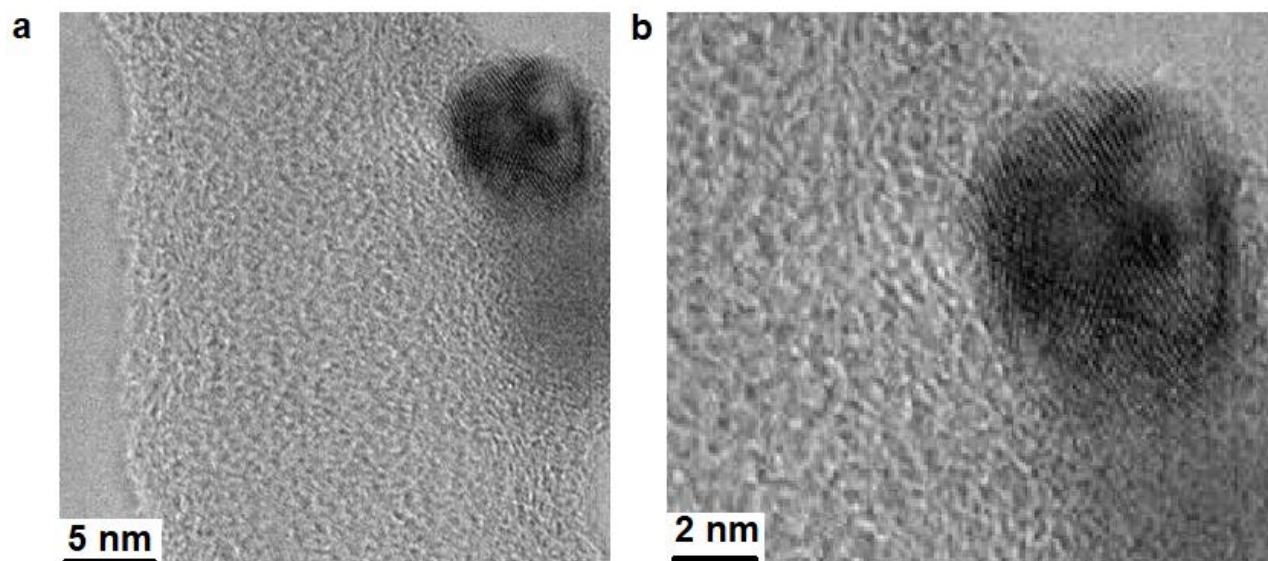
Figure 69. (a) TEM image and (b) HRTEM image of GQDs-Imid.

5.2.2. UV-Vis Spectroscopy

The absorption spectra of the functionalized GQD samples are depicted in Figure 70. All samples showed a common absorption peak located at 210 nm attributed to the π−π* transition of the aromatic sp^2 domain. In addition, GQDs-Amin and GQDs-Chlor displayed an extra absorption peak at 287 nm, corresponding to the n−π* transition of C-N bonds on the surface of GQDs [305].
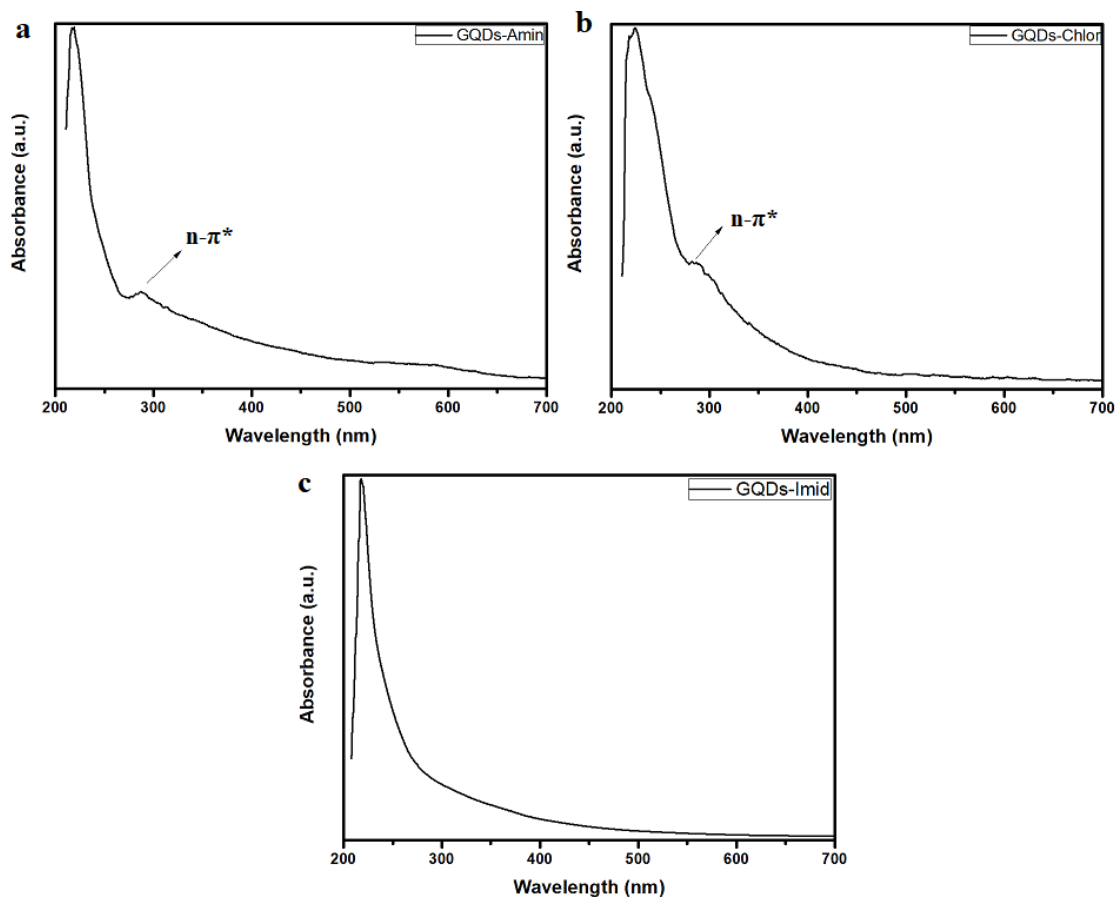
Figure 70. UV-Vis spectra of (a) GQDs-Amin, (b) GQDs-Chlor and (c) GQDs-Imid.

5.2.3. PL spectroscopy

The PL spectra of the functionalized GQD samples are depicted in Figure 71. For GQDs-Amin, the excitation at 400 nm, resulted in the maximum emission peak at 420 nm. The fluorescence intensity varied with the excitation wavelength, as illustrated in Figure 71a. Excitation between 300 and 400 nm led to an increase in emission, but a decline was observed thereafter, from 420 to 620 nm. Likewise, GQDs-Chlor exhibited excitation-wavelength dependent emission behaviour, with λ_{ex} ranging from 300 nm to 620 nm. The highest peak in PL emission occurred at approximately 458 nm when the sample was excited at 360 nm (Figure 71b), consistent with previous findings [306]. In contrast, GQDs-Imid displayed a maximum emission peak at 450 nm when excited at 380 nm (Figure 71c). The PL emission also varied with changes in λ_{ex}, as indicated in the manufacturer's technical specifications.

144
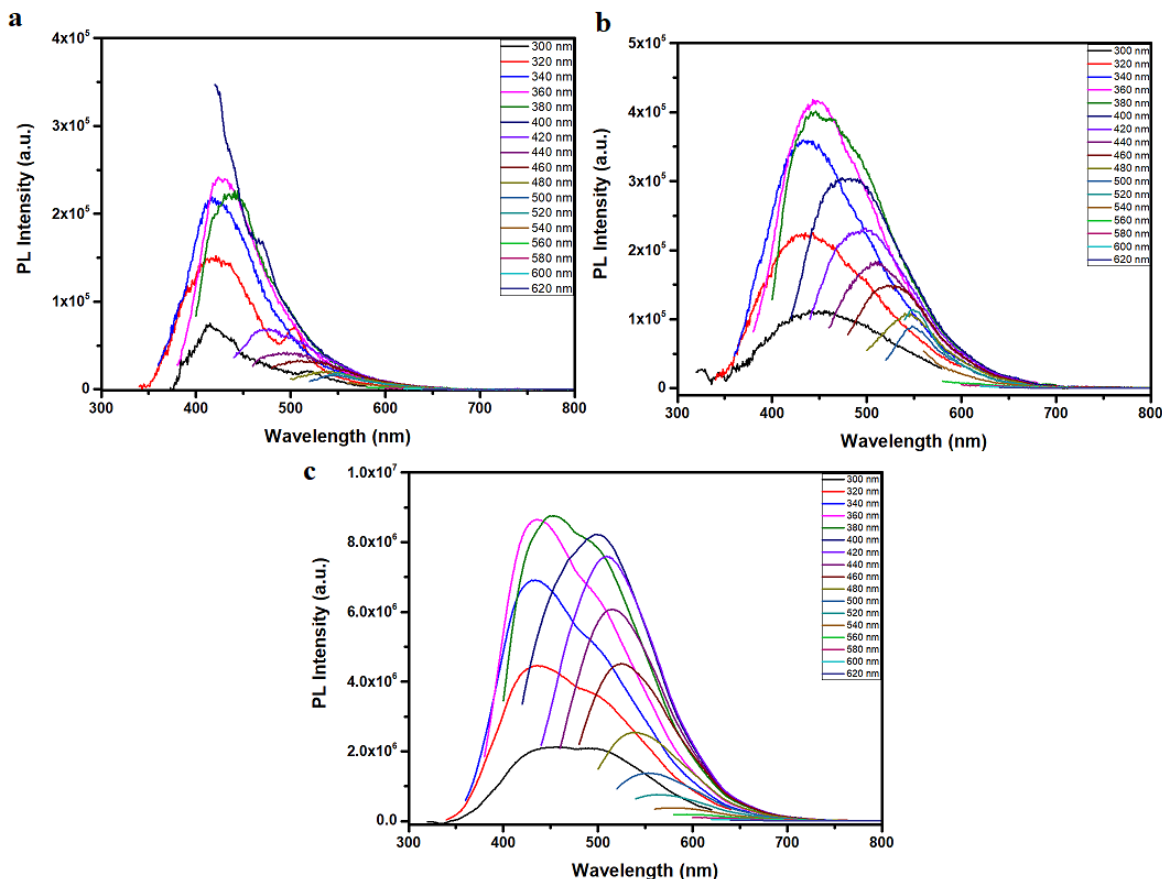
Figure 71. PL spectra of aqueous solutions (0.1 mg/ml) of (a) GQDs-Amin, (b) GQDs-Chlor and (c) GQDs-Imid.

5.2.4. QY

Furthermore, the quantum yield values of functionalized GQDs, were determined relative to anthracene (Φ=0.27, λ_{ex}= 365 nm). GQDs-Amin and GQDs-Chlor yielded similar values (0.3% and 0.6%, respectively), while GQDs-Imid had a QY of 9.1% (Table 11). All samples confirmed the manufacturer's technical specifications.

Table 11. QY values and average PL lifetimes of aqueous solutions (0.1 mg/ml) of GQDs-Amin, GQDs-Chlor and GQDs-Imid, using anthracene as a reference.

Material	QY %	Average PL lifetimes (ns)
GQDs-Amin	0.3	4.13
GQDs-Chlor	0.6	2.73
GQDs-Imid	9.1	3.52

5.2.5. PL Lifetime

Additionally, the PL lifetimes of the functionalized GQDs were measured (λ_{ex}=375 nm), with average decay times of 4.13 ns, 2.73 ns and 3.52 ns for GQDs-Amin, GQDs-Chlor, and GQDs-Imid, respectively (Figure 72).
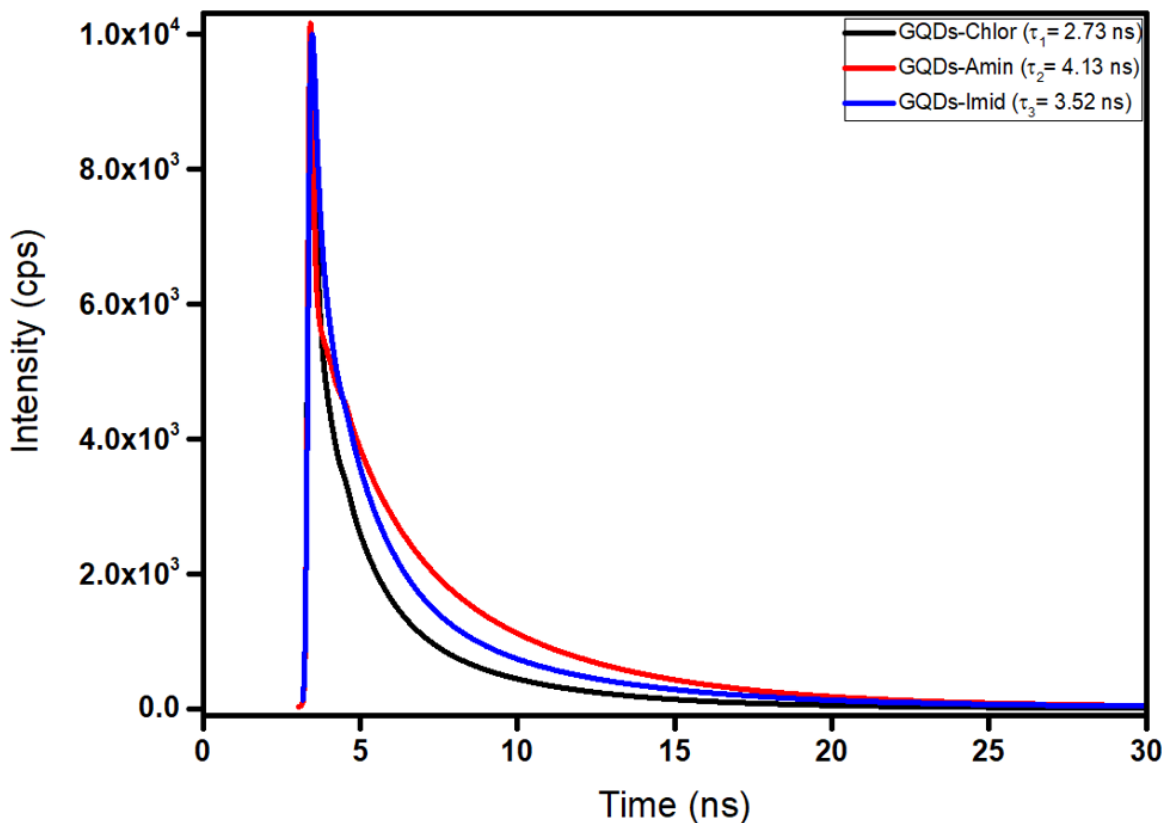
Figure 72. Liquid-state PL lifetime decays of aqueous dispersions of GQDs-Amin, GQDs-Chlor and GQDs-Imid at λ_{ex}= 375 nm. The concentration of the solutions was 0.1 mg/ml.

5.3.   Biological analysis

In this chapter, a series of biological analyses were conducted to evaluate the suitability of functionalized GQDs for biomedical applications. GQDs-Imid exhibit significant antimicrobial properties against *E. coli* and *S. aureus*, causing reduction in the colonies 91.40% and 77.80%, respectively. Furthermore, two toxicity assays, namely the MTT assay and the PrestoBlue assay, were performed to assess the cytotoxicity of the samples. The MTT assay determines cell viability by assessing mitochondrial function,

which involves converting MTT to formazan, whereas the PrestoBlue assay gauges cell viability by transforming resazurin into resorufin, a quicker and more sensitive process.

5.3.1. MTT assays

5.3.1.1.   HeLa cell lines

The cytocompatibility of three different nanoparticle samples (GQDS-Imid, GQDS-Amin, and GQDS-Chlor) was evaluated using the MTT assay on HeLa cells across a concentration range of 0 to 100 µg/ml (Figure 73). The analysis showed that the average cell viability for GQDS-Imid was 70.57%, GQDS-Amin exhibited a higher average viability of 85.32%, and GQDS-Chlor showed an intermediate value of 73.75%. The standard deviations for these samples were 11.23%, 8.67%, and 11.27%, respectively, indicating a moderate level of variability in the results across the concentrations tested. While all three formulations demonstrated a general trend of decreasing cell viability at higher concentrations, GQDS-Amin exhibited notably higher cell viability compared to both GQDS-Imid and GQDS-Chlor, suggesting better cytocompatibility. The variability in cell viability was relatively low for GQDS-Amin and GQDS-Chlor, while GQDS-Imid showed higher variability, especially at the higher concentrations. Paired t-tests were conducted to compare cell viability between the samples at each concentration. The results of the statistical analysis revealed significant differences in cell viability between GQDS-Imid and GQDS-Amin, with a p-value of 1.70×10^{-5}, indicating that GQDS-Imid resulted in significantly lower cell viability compared to GQDS-Amin. There was no significant difference between GQDS-Imid and GQDS-Chlor (p = 0.0688), though a trend toward lower cell viability in GQDS-Imid was observed. Similarly, GQDS-Amin exhibited significantly higher cell viability compared to GQDS-Chlor (p = 7.16×10^{-5}), further confirming the superior cytocompatibility of GQDS-Amin.
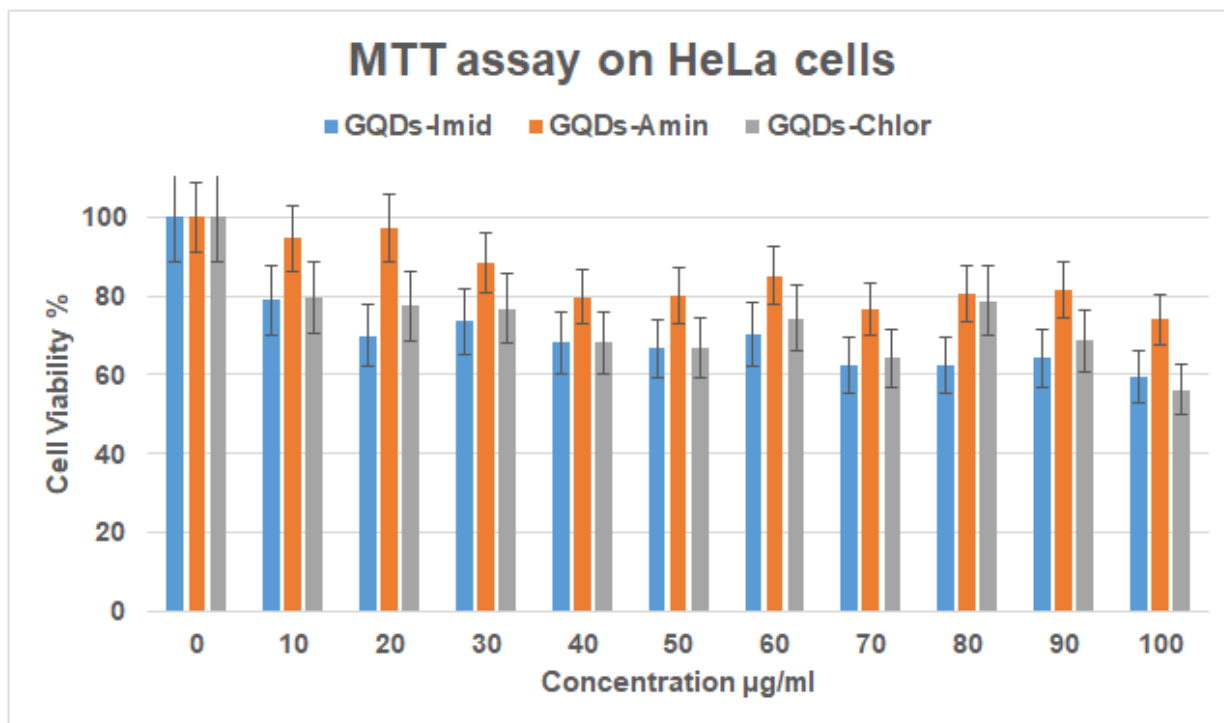
Figure 73. MTT assay of HeLa cells following incubation with GQDS-Imid, GQDS-Amin, and GQDS-Chlor for 24h. Results are presented as the mean value ± standard deviation of triplicate experiments, with cell viability expressed as a percentage relative to untreated control.

5.3.1.2.   U87 cell lines

The cytocompatibility of three nanoparticle formulations (GQDS-Imid, GQDS-Amin, and GQDS-Chlor) was assessed on U87 cells using the MTT assay across concentrations ranging from 0 to 100 µg/ml (Figure 74). The results revealed that GQDS-Imid had an average cell viability of 84.47%, GQDS-Amin showed a higher average viability of 91.15%, and GQDS-Chlor displayed an intermediate value of 81.51%. The standard deviations were 11.76%, 6.59%, and 10.27%, respectively, reflecting some variability in cell viability at different concentrations. Across all tested concentrations, GQDS-Amin consistently demonstrated the highest cell viability, indicating better overall cytocompatibility. In contrast, GQDS-Imid exhibited a wider range of variability, especially at the higher concentrations, while GQDS-Chlor showed more stable results, albeit lower cell viability than GQDS-Amin. Paired t-tests were used to compare the cell viability between the samples at each concentration. Significant differences were observed

between GQDS-Imid and GQDS-Amin, with a p-value of 1.70×10^{-5}, indicating that GQDS-Imid resulted in significantly lower cell viability compared to GQDS-Amin. The difference between GQDS-Imid and GQDS-Chlor was not statistically significant (p = 0.0897), though GQDS-Imid tended to show lower viability than GQDS-Chlor. GQDS-Amin demonstrated significantly higher cell viability than GQDS-Chlor (p = 3.62×10^{-5}), further emphasizing its superior cytocompatibility.
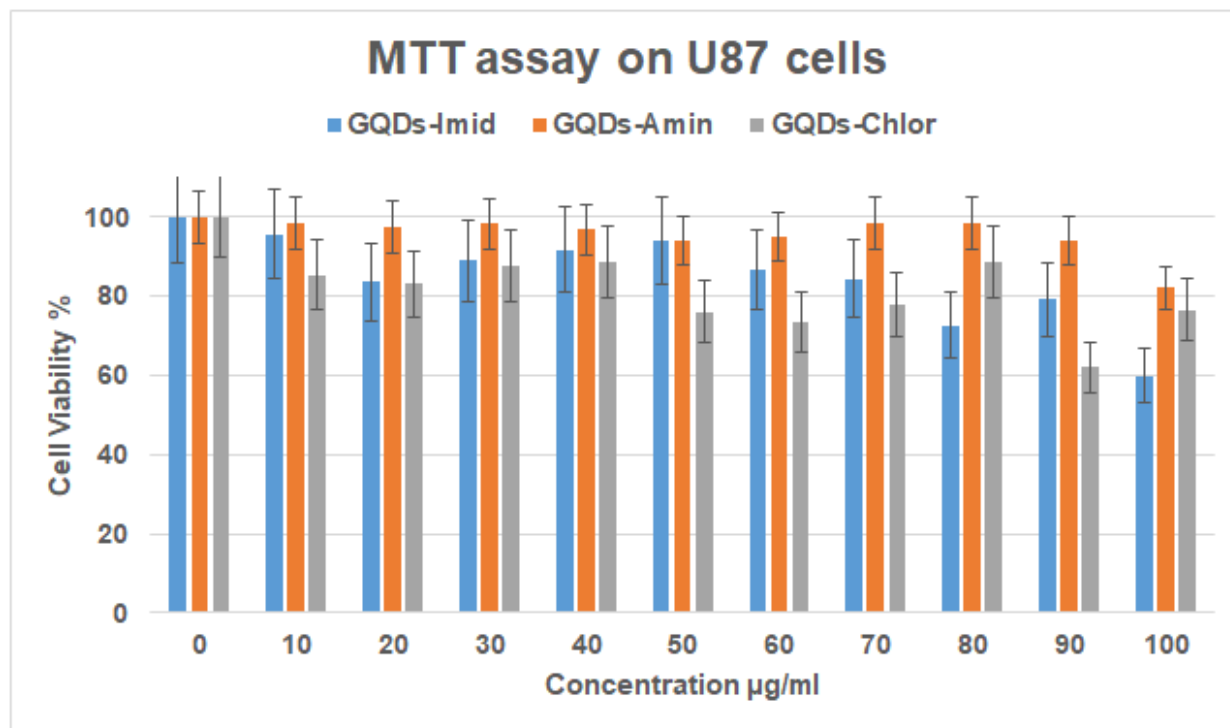
Figure 74. MTT assay of U87 cells following incubation with GQDS-Imid, GQDS-Amin, and GQDS-Chlor for 24h. Results are presented as the mean value ± standard deviation of triplicate experiments, with cell viability expressed as a percentage relative to untreated control.

5.3.2. Prestoblue assays

5.3.2.1.   HeLa cell lines

The cytocompatibility of three nanoparticle formulations—GQDS-Imid, GQDS-Amin, and GQDS-Chlor—was assessed on HeLa cells using the PrestoBlue assay across concentrations ranging from 0 to 100 µg/ml (Figure 75). The results indicated that GQDS-Imid had an average cell viability of 75.97%, GQDS-Amin showed a higher average

149

viability of 82.24%, and GQDS-Chlor had an average viability of 72.76%. The standard deviations were 11.09%, 4.60%, and 12.58%, respectively, suggesting variability in the results across different concentrations. While all formulations exhibited a decline in cell viability at increasing concentrations, GQDS-Amin consistently demonstrated the best performance in terms of maintaining cell viability. GQDS-Imid showed a wider range of variability, especially at higher concentrations, while GQDS-Chlor had stable but comparatively lower viability. To further assess the differences between the formulations, paired t-tests were performed. Significant differences were found between GQDS-Imid and GQDS-Amin, with a p-value of 3.16×10^{-6}, indicating that GQDS-Imid led to significantly lower cell viability than GQDS-Amin. No significant difference was observed between GQDS-Imid and GQDS-Chlor (p = 0.1305), although GQDS-Imid showed a tendency for lower viability compared to GQDS-Chlor. On the other hand, GQDS-Amin displayed significantly higher viability than GQDS-Chlor (p = 4.57×10^{-5}), further supporting its better cytocompatibility.
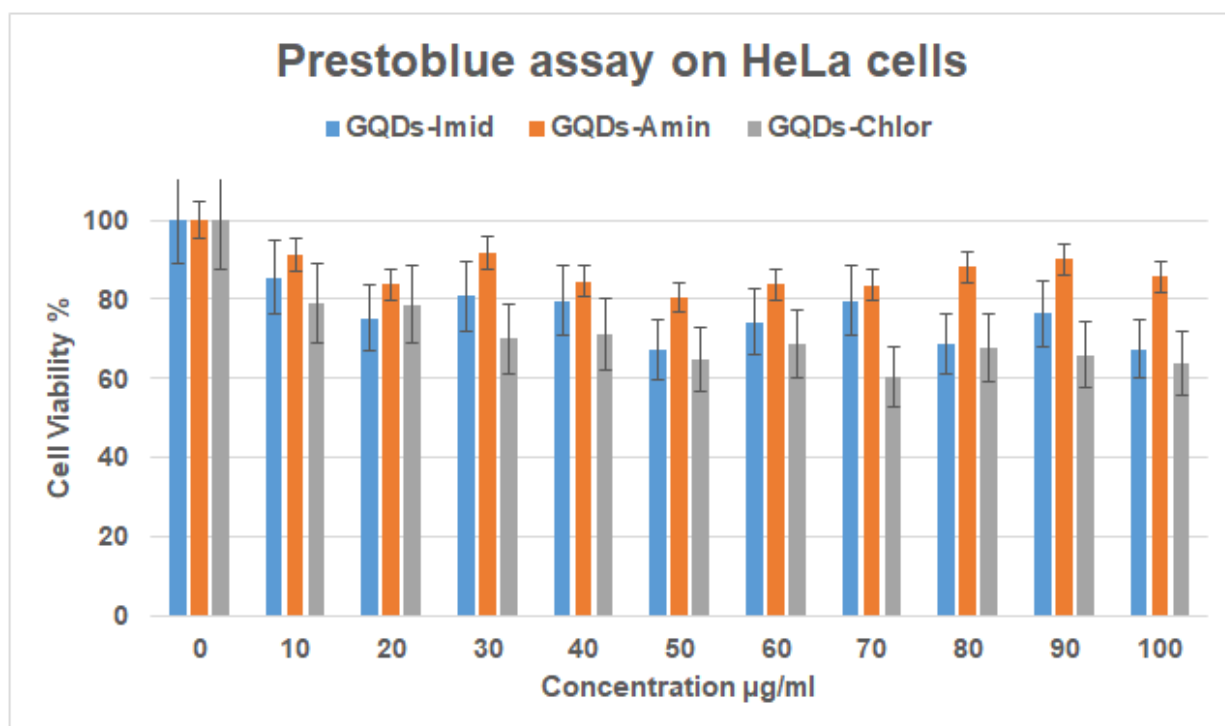
Figure 75. Prestoblue assay of HeLa cells following incubation with GQDS-Imid, GQDS-Amin, and GQDS-Chlor for 24h. Results are presented as the mean value ± standard deviation of triplicate experiments, with cell viability expressed as a percentage relative to untreated control.

The cytocompatibility of three nanoparticle formulations—GQDS-Imid, GQDS-Amin, and GQDS-Chlor—was examined on U87 cells through the PrestoBlue assay, spanning concentrations from 0 to 100 µg/ml (Figure 76). The data showed that GQDS-Imid resulted in an average cell viability of 73.67%, GQDS-Amin achieved a higher average of 86.52%, and GQDS-Chlor had an average viability of 77.72%. The standard deviations were 12.77%, 7.29%, and 14.68%, respectively, indicating some variability in cell viability across different concentrations for each formulation. Overall, GQDS-Amin maintained the highest cell viability, demonstrating superior cytocompatibility. GQDS-Imid showed more variability in its results, particularly at higher concentrations, while GQDS-Chlor had stable viability, but lower values compared to GQDS-Amin. A significant difference was found between GQDS-Imid and GQDS-Amin, with a p-value of 2.41×10^{-6}, suggesting that GQDS-Imid caused lower cell viability compared to GQDS-Amin. No significant difference was found between GQDS-Imid and GQDS-Chlor (p = 0.2865), although GQDS-Imid generally showed lower cell viability. Furthermore, GQDS-Amin exhibited a significantly higher cell viability than GQDS-Chlor (p = 3.38×10^{-5}), reinforcing its enhanced cytocompatibility.
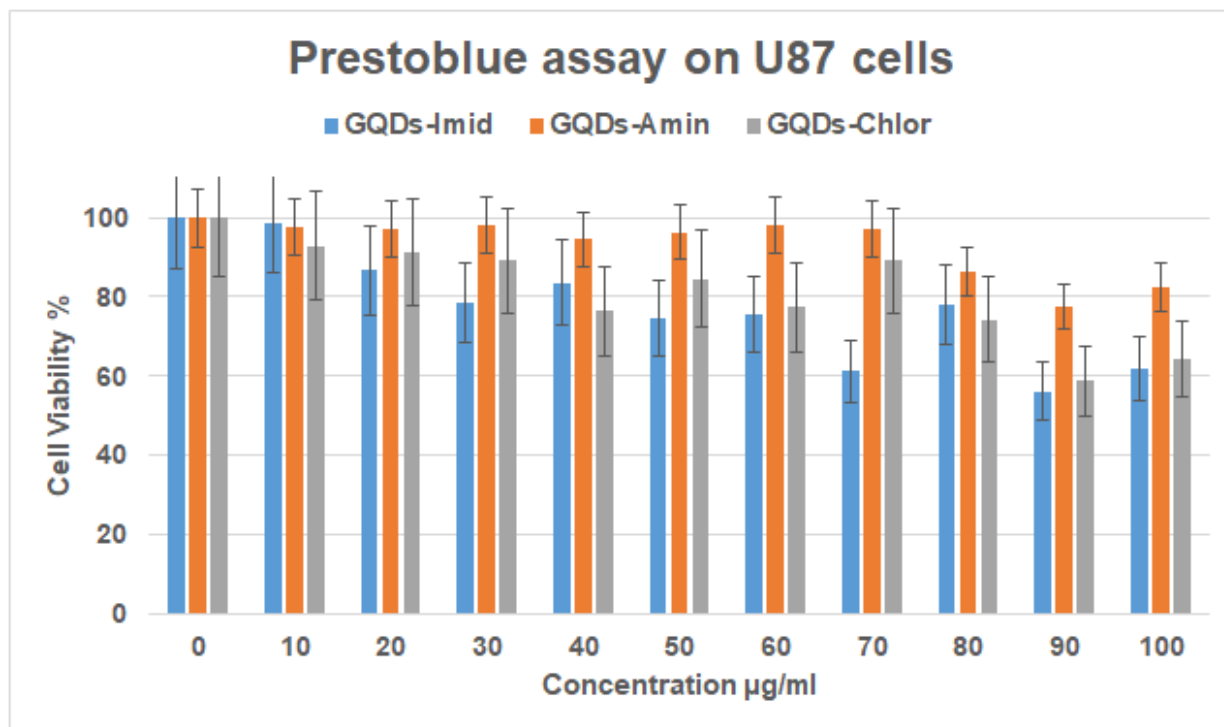
Figure 76. Prestoblue assay of U87 cells following incubation with GQDS-Imid, GQDS-Amin, and GQDS-Chlor for 24h. Results are presented as the mean value ± standard deviation of triplicate experiments, with cell viability expressed as a percentage relative to untreated control.

5.4. Conclusion

This chapter has provided a comprehensive investigation into the structural, optical, and biological properties of functionalized GQDs (GQDS-Imid, GQDS-Amin, and GQDS-Chlor), shedding light on their potential for various biomedical applications.

From a structural standpoint, TEM confirmed that GQDs-Imid nanoparticles exhibited a spherical morphology with an average diameter of 6 nm. High-resolution TEM further validated their graphene lattice structure, with a lattice spacing of approximately 0.22 nm. These results align with the general understanding of graphene-based nanomaterials and demonstrate the structural integrity of the functionalized GQDs. In addition, UV-Vis spectroscopy revealed common absorption characteristics across all functionalized GQD samples, with a primary peak at 210 nm attributed to the π–π* transitions within the aromatic sp^2 domain. The presence of additional absorption peaks in GQDs-Amin and GQDs-Chlor at 287 nm further indicates the modification of the surface chemistry,

particularly through the introduction of C-N bonds. These findings highlight the successful incorporation of functional groups, which are known to influence the optical and electronic properties of GQDs. The PL emission spectra showed clear excitation-dependent fluorescence behavior, with GQDs-Amin, GQDs-Chlor, and GQDs-Imid exhibiting distinct emission profiles. Specifically, GQDs-Amin exhibited a maximum emission at 420 nm when excited at 400 nm, while GQDs-Chlor and GQDs-Imid displayed peaks at 458 nm and 450 nm, respectively. These results suggest that the surface modifications influence the electronic structure of the GQDs, altering their fluorescence properties. Notably, GQDs-Imid demonstrated the highest QY (Φ = 9.1%). The PL lifetime measurements provided further insight into the dynamics of fluorescence emission. GQDs-Amin exhibited an average decay time of 4.13 ns, which was higher than that of GQDs-Chlor (2.73 ns) and GQDs-Imid (3.52 ns). These variations in PL lifetimes can be attributed to differences in the surface functionality. Longer PL lifetimes, as observed in GQDs-Amin, are often associated with more stable fluorescence, which is a desirable characteristic for long-term imaging applications. Conversely, the shorter PL lifetimes of GQDs-Imid and GQDs-Chlor may make them more suitable for applications requiring fast optical responses, such as sensing and detection.

The functionalized GQDs demonstrated varied levels of cytocompatibility, with GQDs-Amin consistently showing the highest cell viability across both MTT and PrestoBlue assays. These assays, which assess mitochondrial function and cell viability, revealed that GQDs-Amin exhibited average viability of 85.32% in HeLa cells and 91.15% in U87 cells, making them the most biocompatible among the tested formulations. The lower cytotoxicity of GQDs-Amin can be attributed to the amine functionalization, which enhances solubility in aqueous media and facilitates better interaction with cellular components, potentially reducing toxicity. In contrast, GQDs-Imid exhibited lower cell viability (70.57% for HeLa cells and 84.47% for U87 cells), with higher variability observed at higher concentrations. The statistical analysis using paired t-tests further confirmed that the difference in cell viability between GQDs-Imid and GQDs-Amin was statistically significant, reinforcing the superior cytocompatibility of GQDs-Amin. While GQDs-Chlor displayed intermediate cytocompatibility, their stability and cell viability were lower than those of GQDs-Amin, as evidenced by both assays. These findings suggest that the

choice of surface functionalization plays a critical role in determining the biocompatibility of GQDs, which is a key factor for their use in medical applications. The antimicrobial properties of GQDs-Imid were particularly noteworthy, showing significant reductions in the colonies of E. coli and S. aureus (91.40% and 77.80%, respectively). These results suggest that GQDs-Imid may have potential applications in antibacterial therapies, particularly in settings where antimicrobial resistance is a concern. The enhanced antimicrobial properties of GQDs-Imid can be attributed to the imidazole functionalization, which may facilitate interactions with bacterial membranes, leading to disruption and inactivation of microbial cells. This makes GQDs-Imid a promising candidate for novel antimicrobial agents that can be incorporated into coatings, wound dressings, or drug delivery systems.

Conclusions

This thesis has delved into the synthesis, structural transformation, and multifunctional applications of C-dots and functionalized GQDs. Through systematic investigations, it has elucidated the underlying mechanisms driving their optical and biological behaviors, offering significant advancements in understanding and enhancing their functional properties.

The first chapter in this thesis focused on the electrochemical restructuring of C-dots, revealing profound transformations in their physicochemical properties. The application of electrochemical etching resulted in a drastic reduction in the size of untreated C-dots from an average diameter of 12 nm to approximately 3 nm while preserving their spherical morphology. The restructuring process induced extensive surface oxidation and structural modifications, leading to pronounced alterations in optical behavior. These findings were substantiated through a combination of TEM, FTIR spectroscopy, and XPS analyses, which confirmed the loss of sp² carbon content and the emergence of oxygen-containing functional groups, such as carboxyl and hydroxyl moieties. Optical studies demonstrated an optimal enhancement in PL and QY at intermediate voltages, with QY peaking at 7.8%, a remarkable improvement compared to untreated samples. However, excessive electrochemical treatment led to nanoparticle degradation, evidenced by the disappearance of structural features in TEM images and the loss of PL, underscoring the delicate balance required in optimizing synthesis parameters.

The second chapter explored the NaClO treatment of citric acid and urea-based C-dots (CU100D) as a strategy to enhance their optical and biological properties. NaClO treatment resulted in substantial morphological and structural changes, reducing the particle size from 4.3 nm to 2.9 nm. This size reduction was accompanied by significant surface oxidation, with the introduction of new oxygen-containing functional groups, such as carbonyl and hydroxyl groups. These modifications improved the PL emission by up to six-fold and enhanced colloidal stability, as evidenced by a more negative zeta potential. The QY increased by up to 350%, indicating remarkable improvements in the optical properties of the CU100D nanoparticles. Biological assessments demonstrated their cytocompatibility in HeLa and U87 cell lines, with cell viability exceeding 88% across

a concentration range of up to 100 µg/ml. These results highlighted the stability and biocompatibility of CU100D even under oxidative conditions. Moreover, CU100D nanoparticles exhibited significant antimicrobial and antifungal activities. The reduction in colony counts of *E. coli* and *S. aureus* by 79% and 97.2%, respectively, underscores their potential in combating bacterial infections. Additionally, CU100D nanoparticles inhibited fungal growth and biofilm formation against *T. phinophilus*, showing efficacy at concentrations as low as 0.0125 mg/ml. These enhancements in antimicrobial and antifungal properties were attributed to oxidative surface modifications and the increased production of ROS, further confirming the multifunctionality of CU100D nanoparticles.

The final chapter investigated the structural, optical, and biological properties of functionalized GQDs, specifically GQDs-Imid, GQDs-Amin, and GQDs-Chlor. Structural analysis confirmed the preservation of graphene lattice integrity, with TEM revealing an average diameter of 6 nm. UV-Vis spectroscopy identified characteristic absorption peaks, including π–π^* transitions at 210 nm and additional peaks in GQDs-Amin and GQDs-Chlor at 287 nm, indicative of C-N bond formation. Surface modifications significantly influenced the optical properties, with GQDs-Imid exhibiting the highest QY (9.1%) and distinct excitation-dependent PL behaviors observed across all samples. PL lifetime measurements provided further insights into fluorescence dynamics, with GQDs-Amin demonstrating the longest decay times, suggesting stable fluorescence suitable for imaging applications. In contrast, the shorter lifetimes of GQDs-Imid and GQDs-Chlor suggest their potential utility in rapid sensing and detection applications. Biocompatibility assessments revealed that GQDs-Amin consistently exhibited the highest cell viability, attributed to the solubility and interaction benefits conferred by amine functionalization. While GQDs-Imid showed slightly lower cytocompatibility, they exhibited superior antimicrobial properties, reducing *E. coli* and *S. aureus* colonies by 91.4% and 77.8%, respectively. The antimicrobial activity was likely facilitated by imidazole functionalization, which enhanced interactions with bacterial membranes, leading to effective microbial cell disruption. These findings emphasize the critical role of surface functionalization in tailoring the properties of GQDs for specific biomedical applications.

The outcome of this thesis indicates that CU100D nanoparticles, both untreated and treated with NaClO, offer superior performance compared to commercial GQDs in multiple key areas, including optical properties and cytocompatibility. In terms of optical properties, NaClO-treated CU100D nanoparticles exhibited a significant increase in PL and QY, with a remarkable QY of 29.4%, a substantial improvement compared to 7.8% for untreated CU100D and 9.1% for commercial GQDs. This enhancement makes NaClO-treated CU100D more suitable for applications requiring high fluorescence intensity, such as bioimaging and sensing, where higher QY correlates with better signal intensity and performance. Regarding cytocompatibility, NaClO-treated CU100D demonstrated impressive biocompatibility, with cell viability exceeding 88% in both HeLa and U87 cell lines, even at concentrations as high as 100 µg/ml. This is notably higher than untreated CU100D (72% viability) and commercial GQDs (80% viability) at similar concentrations. The superior biocompatibility of NaClO-treated CU100D underscores its potential for safe use in biomedical applications, particularly in drug delivery and therapeutic areas where cytotoxicity is a concern. Finally, when assessing antimicrobial properties, NaClO-treated CU100D nanoparticles exhibited significant reductions in *E. coli* and *S. aureus* colony counts (79% and 97.2%, respectively), as well as antifungal activity against *T. phinophilus*, outperforming commercial GQDs in terms of antimicrobial efficacy. While commercial GQDs reduced *E. coli* by 91.4% and *S. aureus* by 77.8%, NaClO-treated CU100D exhibited superior performance, particularly against *S. aureus*. This antimicrobial potential, enhanced by oxidative surface modifications, positions NaClO-treated CU100D as a more effective candidate for combating bacterial infections compared to commercial GQDs.

In summary, CU100D nanoparticles, especially when treated with NaClO, offer enhanced optical properties, greater cytocompatibility, and more potent antimicrobial activity than commercial GQDs, making them a promising alternative for diverse biomedical and environmental applications.

Future work

This thesis has demonstrated the potential of CU100D in enhancing optical and biological properties. However, several areas warrant further exploration:

Optimization of electrochemical etching: Future studies should refine the electrochemical etching conditions to improve reproducibility, optimize particle size reduction, and ensure structural stability, exploring various voltage and electrolyte combinations.

Long-term biocompatibility: Further in vivo studies are needed to evaluate the long-term biocompatibility, biodistribution, and potential toxicity of CU100D nanoparticles, particularly for medical applications.

Additional surface functionalization: Future research could explore other surface functionalization to improve properties such as drug delivery, targeted therapy, and cellular uptake, enhancing their biomedical potential.

Scalable synthesis methods: Developing scalable, cost-effective synthesis methods is crucial for industrial applications. Exploring continuous flow reactors or microfluidic systems could enable large-scale production of C-dots.

Environmental applications: The antimicrobial and antifungal properties of CU100D could be further investigated for environmental uses, such as in coatings or water treatment applications.

Multifunctional nanoparticles: Future work could focus on developing composite nanoparticle systems that combine C-dots with other materials, offering enhanced functionalities for a broader range of applications.

In conclusion, continued research in these areas will expand the practical applications of CU100D in both biomedical and environmental fields.

Attachments

List of publications during the PhD:

- M. S. Beg, E. N. Gibbons, S. Gavalas, M. A. Holden, M. Krysmann, and A. Kelarakis, "Antimicrobial coatings based on amine-terminated graphene oxide and Nafion with remarkable thermal resistance," Nanoscale Adv, 2024, doi: 10.1039/D3NA01154B.

- E. Gibbons, M. Krysmann, S. Gavalas, K. Heslop, and A. Kelarakis, "Nafion-Based Layer-by-Layer Coatings with Antimicrobial Activity," in IOCN 2023, Basel Switzerland: MDPI, May 2023, p. 10. doi: 10.3390/IOCN2023-14471.

- Q. Yang et al., "Resculpting carbon dots via electrochemical etching," Sci Rep, vol. 13, no. 1, p. 3710, Mar. 2023, doi: 10.1038/s41598-023-30547-6.

- J. D. Stachowska, S. Gavalas, and A. Kelarakis, "Current trends in carbon dots applications," in Carbon Dots in Agricultural Systems, Elsevier, 2022, pp. 21–37. doi: 10.1016/B978-0-323-90260-1.00008-5.

- S. Gavalas and A. Kelarakis, "Towards Red Emissive Systems Based on Carbon Dots," Nanomaterials, vol. 11, no. 8, p. 2089, Aug. 2021, doi: 10.3390/nano11082089.

- Gavalas, S.; Beg, M.S.; Gibbons, E.N.; Kelarakis, A. Enhancing the Fluorescence and Antimicrobial Performance of Carbon Dots via Hypochlorite Treatment. Nanomaterials 2025, 15, 184. https://doi.org/10.3390/nano15030184

References

[1]   M. J. Krysmann, A. Kelarakis, P. Dallas, and E. P. Giannelis, "Formation mechanism of carbogenic nanoparticles with dual photoluminescence emission," *J Am Chem Soc*, vol. 134, no. 2, pp. 747–750, Jan. 2012, doi: 10.1021/ja204661r.

[2]   S. Mourdikoudis, R. M. Pallares, and N. T. K. Thanh, "Characterization techniques for nanoparticles: comparison and complementarity upon studying nanoparticle properties," *Nanoscale*, vol. 10, no. 27, pp. 12871–12934, 2018, doi: 10.1039/C8NR02278J.

[3]   J. Du *et al.*, "Folic acid functionalized gadolinium-doped carbon dots as fluorescence / magnetic resonance imaging contrast agent for targeted imaging of liver cancer," *Colloids Surf B Biointerfaces*, p. 113721, Dec. 2023, doi: 10.1016/j.colsurfb.2023.113721.

[4]   H. Ding, F. Du, P. Liu, Z. Chen, and J. Shen, "DNA-carbon dots function as fluorescent vehicles for drug delivery," *ACS Appl Mater Interfaces*, vol. 7, no. 12, pp. 6889–6897, Apr. 2015, doi: 10.1021/acsami.5b00628.

[5]   R. K. Shukla, A. Badiye, K. Vajpayee, and N. Kapoor, "Genotoxic Potential of Nanoparticles: Structural and Functional Modifications in DNA," *Front Genet*, vol. 12, Sep. 2021, doi: 10.3389/fgene.2021.728250.

[6]   H. W. Kroto, J. R. Heath, S. C. O'Brien, R. F. Curl, and R. E. Smalley, "C60: Buckminsterfullerene," *Nature*, vol. 318, no. 6042, pp. 162–163, Nov. 1985, doi: 10.1038/318162a0.

[7]   R. V. Honeychuck, "Science of Fullerenes and Carbon Nanotubes By M. S. Dresselhaus (MIT), G. Dresselhaus (MIT), and P. C. Eklund (University of Kentucky). Academic Press: San Diego. 1996, xviii + 965 pp. ISBN 0-12-221820-5.," *J Am Chem Soc*, vol. 118, no. 37, pp. 8987–8987, Jan. 1996, doi: 10.1021/ja965593l.

[8]   S. Iijima, "Helical microtubules of graphitic carbon," *Nature*, vol. 354, no. 6348, pp. 56–58, Nov. 1991, doi: 10.1038/354056a0.

[9]   R. H. Baughman, A. A. Zakhidov, and W. A. de Heer, "Carbon Nanotubes--the Route Toward Applications," *Science (1979)*, vol. 297, no. 5582, pp. 787–792, Aug. 2002, doi: 10.1126/science.1060928.

[10]   K. S. Novoselov *et al.*, "Electric Field Effect in Atomically Thin Carbon Films," *Science (1979)*, vol. 306, no. 5696, pp. 666–669, Oct. 2004, doi: 10.1126/science.1102896.

[11]   S. Y. Lim, W. Shen, and Z. Gao, "Carbon quantum dots and their applications," *Chem Soc Rev*, vol. 44, no. 1, pp. 362–381, Jan. 2015, doi: 10.1039/C4CS00269E.

[12]   H. L. Kagdada, A. K. Bhojani, and D. K. Singh, "An Overview of Nanomaterials: History, Fundamentals, and Applications," in *Nanomaterials*, Singapore: Springer Nature Singapore, 2023, pp. 1–26. doi: 10.1007/978-981-19-7963-7_1.

[13]   A. Cayuela, M. L. Soriano, C. Carrillo-Carrión, and M. Valcárcel, "Semiconductor and carbon-based fluorescent nanodots: the need for consistency," *Chemical Communications*, vol. 52, no. 7, pp. 1311–1326, 2016, doi: 10.1039/C5CC07754K.

[14]   Y.-P. Sun *et al.*, "Quantum-Sized Carbon Dots for Bright and Colorful Photoluminescence," *J Am Chem Soc*, vol. 128, no. 24, pp. 7756–7757, Jun. 2006, doi: 10.1021/ja062677d.

[15]   A. Sciortino *et al.*, "Different natures of surface electronic transitions of carbon nanoparticles," *Physical Chemistry Chemical Physics*, vol. 19, no. 34, pp. 22670–22677, 2017, doi: 10.1039/C7CP04548D.

[16]   A. Cayuela, M. L. Soriano, M. C. Carrión, and M. Valcárcel, "Functionalized carbon dots as sensors for gold nanoparticles in spiked samples: Formation of nanohybrids," *Anal Chim Acta*, vol. 820, pp. 133–138, Apr. 2014, doi: 10.1016/j.aca.2014.02.010.

[17]   S. Qu, X. Wang, Q. Lu, X. Liu, and L. Wang, "A Biocompatible Fluorescent Ink Based on Water-Soluble Luminescent Carbon Nanodots," *Angewandte Chemie International Edition*, vol. 51, no. 49, pp. 12215–12218, Dec. 2012, doi: 10.1002/anie.201206791.

[18]   S. Hu, J. Liu, J. Yang, Y. Wang, and S. Cao, "Laser synthesis and size tailor of carbon quantum dots," *Journal of Nanoparticle Research*, vol. 13, no. 12, pp. 7247–7252, Dec. 2011, doi: 10.1007/s11051-011-0638-y.

[19]   F. Arcudi, L. Đorđević, and M. Prato, "Synthesis, Separation, and Characterization of Small and Highly Fluorescent Nitrogen-Doped Carbon NanoDots," *Angewandte Chemie*, vol. 128, no. 6, pp. 2147–2152, Feb. 2016, doi: 10.1002/ange.201510158.

[20]   A. Das, V. Gude, D. Roy, T. Chatterjee, C. K. De, and P. K. Mandal, "On the Molecular Origin of Photoluminescence of Nonblinking Carbon Dot," *Journal of Physical Chemistry C*, vol. 121, no. 17, pp. 9634–9641, May 2017, doi: 10.1021/acs.jpcc.7b02433.

[21]   A. Cayuela, M. Laura Soriano, and M. Valcárcel, "Strong luminescence of Carbon Dots induced by acetone passivation: Efficient sensor for a rapid analysis of two different pollutants," *Anal Chim Acta*, vol. 804, pp. 246–251, Dec. 2013, doi: 10.1016/j.aca.2013.10.031.

[22]   A. Cayuela, M. L. Soriano, and M. Valcárcel, "Reusable sensor based on functionalized carbon dots for the detection of silver nanoparticles in cosmetics via inner filter effect," *Anal Chim Acta*, vol. 872, pp. 70–76, May 2015, doi: 10.1016/j.aca.2015.02.052.

[23]   H. Ding, P. Zhang, T. Y. Wang, J. L. Kong, and H. M. Xiong, "Nitrogen-doped carbon dots derived from polyvinyl pyrrolidone and their multicolor cell imaging," *Nanotechnology*, vol. 25, no. 20, May 2014, doi: 10.1088/0957-4484/25/20/205604.

[24]   V. Nguyen, J. Si, L. Yan, and X. Hou, "Direct demonstration of photoluminescence originated from surface functional groups in carbon nanodots," *Carbon N Y*, vol. 108, pp. 268–273, Nov. 2016, doi: 10.1016/j.carbon.2016.07.019.

[25]   L. Sciortino *et al.*, "Tailoring the Emission Color of Carbon Dots through Nitrogen-Induced Changes of Their Crystalline Structure," *Journal of Physical Chemistry C*, vol. 122, no. 34, pp. 19897–19903, Aug. 2018, doi: 10.1021/acs.jpcc.8b04514.

[26]   W. Chen, C. Hu, Y. Yang, J. Cui, and Y. Liu, "Rapid Synthesis of Carbon Dots by Hydrothermal Treatment of Lignin," *Materials*, vol. 9, no. 3, p. 184, Mar. 2016, doi: 10.3390/ma9030184.

[27] D. B. Shinde and V. K. Pillai, "Electrochemical preparation of luminescent graphene quantum dots from multiwalled carbon nanotubes," *Chemistry - A European Journal*, vol. 18, no. 39, pp. 12522–12528, Sep. 2012, doi: 10.1002/chem.201201043.

[28] N. Fuyuno *et al.*, "Drastic Change in Photoluminescence Properties of Graphene Quantum Dots by Chromatographic Separation," *Adv Opt Mater*, vol. 2, no. 10, pp. 983–989, Oct. 2014, doi: 10.1002/adom.201400200.

[29] D. Pan, J. Zhang, Z. Li, and M. Wu, "Hydrothermal route for cutting graphene sheets into blue-luminescent graphene quantum dots," *Advanced Materials*, vol. 22, no. 6, pp. 734–738, Feb. 2010, doi: 10.1002/adma.200902825.

[30] A. Cayuela, M. L. Soriano, and M. Valcárcel, "Photoluminescent carbon dot sensor for carboxylated multiwalled carbon nanotube detection in river water," *Sens Actuators B Chem*, no. PartA, pp. 596–601, Feb. 2015, doi: 10.1016/j.snb.2014.10.102.

[31] A. B. Bourlinos, A. Stassinopoulos, D. Anglos, R. Zboril, M. Karakassides, and E. P. Giannelis, "Surface Functionalized Carbogenic Quantum Dots," *Small*, vol. 4, no. 4, pp. 455–458, Mar. 2008, doi: 10.1002/smll.200700578.

[32] S. Liu *et al.*, "Hydrothermal treatment of grass: A low-cost, green route to nitrogen-doped, carbon-rich, photoluminescent polymer nanodots as an effective fluorescent sensing platform for label-free detection of Cu(II) ions," *Advanced Materials*, vol. 24, no. 15, pp. 2037–2041, Apr. 2012, doi: 10.1002/adma.201200164.

[33] S. Sahu, B. Behera, T. K. Maiti, and S. Mohapatra, "Simple one-step synthesis of highly luminescent carbon dots from orange juice: Application as excellent bio-imaging agents," *Chemical Communications*, vol. 48, no. 70, pp. 8835–8837, Aug. 2012, doi: 10.1039/c2cc33796g.

[34] G. Tong *et al.*, "Amorphous carbon dots with high two-photon fluorescence for cellular imaging passivated by hyperbranched poly(amino amine)," *J Mater Chem B*, vol. 3, no. 4, pp. 700–706, Jan. 2015, doi: 10.1039/c4tb01643b.

[35] J. T. Margraf, V. Strauss, D. M. Guldi, and T. Clark, "The Electronic Structure of Amorphous Carbon Nanodots," *J Phys Chem B*, vol. 119, no. 24, pp. 7258–7265, Jun. 2015, doi: 10.1021/jp510620j.

[36] H. Peng and J. Travas-Sejdic, "Simple aqueous solution route to luminescent carbogenic dots from carbohydrates," *Chemistry of Materials*, vol. 21, no. 23, pp. 5563–5565, Dec. 2009, doi: 10.1021/cm901593y.

[37] A. Sharma, T. Gadly, S. Neogy, S. K. Ghosh, and M. Kumbhakar, "Molecular Origin and Self-Assembly of Fluorescent Carbon Nanodots in Polar Solvents," *Journal of Physical Chemistry Letters*, vol. 8, no. 5, pp. 1044–1052, Mar. 2017, doi: 10.1021/acs.jpclett.7b00170.

[38] W. Zhang *et al.*, "Supramolecular interactions via hydrogen bonding contributing to citric-acid derived carbon dots with high quantum yield and sensitive photoluminescence," *RSC Adv*, vol. 7, no. 33, pp. 20345–20353, 2017, doi: 10.1039/c7ra02160g.

[39] H. Li, Z. Kang, Y. Liu, and S.-T. Lee, "Carbon nanodots: synthesis, properties and applications," *J Mater Chem*, vol. 22, no. 46, p. 24230, 2012, doi: 10.1039/c2jm34690g.

[40] M. Hashida, H. Mishima, S. Tokita, and S. Sakabe, "Non-thermal ablation of expanded polytetrafluoroethylene with an intense femtosecond-pulse laser," *Opt Express*, vol. 17, no. 15, p. 13116, Jul. 2009, doi: 10.1364/OE.17.013116.

[41] Y. Suda, T. Nishimura, T. Ono, M. Akazawa, Y. Sakai, and N. Homma, "Deposition of fine carbon particles using pulsed ArF laser ablation assisted by inductively coupled plasma," *Thin Solid Films*, vol. 374, no. 2, pp. 287–290, Oct. 2000, doi: 10.1016/S0040-6090(00)01167-6.

[42] X. Li, H. Wang, Y. Shimizu, A. Pyatenko, K. Kawaguchi, and N. Koshizaki, "Preparation of carbon quantum dots with tunable photoluminescence by rapid laser passivation in ordinary organic solvents," *Chem. Commun.*, vol. 47, no. 3, pp. 932–934, 2011, doi: 10.1039/C0CC03552A.

[43] Y.-P. Sun *et al.*, "Quantum-Sized Carbon Dots for Bright and Colorful Photoluminescence," *J Am Chem Soc*, vol. 128, no. 24, pp. 7756–7757, Jun. 2006, doi: 10.1021/ja062677d.

[44] S.-L. Hu, K.-Y. Niu, J. Sun, J. Yang, N.-Q. Zhao, and X.-W. Du, "One-step synthesis of fluorescent carbon nanoparticles by laser irradiation," *J. Mater. Chem.*, vol. 19, no. 4, pp. 484–488, 2009, doi: 10.1039/B812943F.

[45] S. H. Kang *et al.*, "Ultrafast Method for Selective Design of Graphene Quantum Dots with Highly Efficient Blue Emission," *Sci Rep*, vol. 6, no. 1, p. 38423, Dec. 2016, doi: 10.1038/srep38423.

[46] H. Liu, T. Ye, and C. Mao, "Fluorescent Carbon Nanoparticles Derived from Candle Soot," *Angewandte Chemie International Edition*, vol. 46, no. 34, pp. 6473–6475, Aug. 2007, doi: 10.1002/anie.200701271.

[47] J. Peng *et al.*, "Graphene Quantum Dots Derived from Carbon Fibers," *Nano Lett*, vol. 12, no. 2, pp. 844–849, Feb. 2012, doi: 10.1021/nl2038979.

[48] P. Zhao *et al.*, "Facile One-Pot Conversion of Petroleum Asphaltene to High Quality Green Fluorescent Graphene Quantum Dots and Their Application in Cell Imaging," *Particle & Particle Systems Characterization*, vol. 33, no. 9, pp. 635–644, Sep. 2016, doi: 10.1002/ppsc.201600070.

[49] D. B. Gunjal *et al.*, "Nitrogen doped waste tea residue derived carbon dots for selective quantification of tetracycline in urine and pharmaceutical samples and yeast cell imaging application," *Opt Mater (Amst)*, vol. 98, p. 109484, Dec. 2019, doi: 10.1016/j.optmat.2019.109484.

[50] H. Sun, H. Ji, E. Ju, Y. Guan, J. Ren, and X. Qu, "Synthesis of Fluorinated and Nonfluorinated Graphene Quantum Dots through a New Top-Down Strategy for Long-Time Cellular Imaging," *Chemistry - A European Journal*, vol. 21, no. 9, pp. 3791–3797, Feb. 2015, doi: 10.1002/chem.201406345.

[51] H. Soni and P. S. Pamidimukkala, "Green synthesis of N, S co-doped carbon quantum dots from triflic acid treated palm shell waste and their application in nitrophenol sensing," *Mater Res Bull*, vol. 108, pp. 250–254, Dec. 2018, doi: 10.1016/j.materresbull.2018.08.033.

[52] M. L. Desai, S. Jha, H. Basu, R. K. Singhal, T.-J. Park, and S. K. Kailasa, "Acid Oxidation of Muskmelon Fruit for the Fabrication of Carbon Dots with Specific Emission Colors for Recognition of Hg [2+] Ions and Cell Imaging," *ACS Omega*, vol. 4, no. 21, pp. 19332–19340, Nov. 2019, doi: 10.1021/acsomega.9b02730.

[53] S. K. Kailasa *et al.*, "Tuning of carbon dots emission color for sensing of Fe3+ ion and bioimaging applications," *Materials Science and Engineering: C*, vol. 98, pp. 834–842, May 2019, doi: 10.1016/j.msec.2019.01.002.

[54] R. V. Nair, R. T. Thomas, V. Sankar, H. Muhammad, M. Dong, and S. Pillai, "Rapid, Acid-Free Synthesis of High-Quality Graphene Quantum Dots for Aggregation Induced Sensing of Metal Ions and Bioimaging," *ACS Omega*, vol. 2, no. 11, pp. 8051–8061, Nov. 2017, doi: 10.1021/acsomega.7b01262.

[55] C. Zhu *et al.*, "A new mild, clean and highly efficient method for the preparation of graphene quantum dots without by-products," *J Mater Chem B*, vol. 3, no. 34, pp. 6871–6876, 2015, doi: 10.1039/C5TB01093D.

[56] J. Lu, J. Yang, J. Wang, A. Lim, S. Wang, and K. P. Loh, "One-Pot Synthesis of Fluorescent Carbon Nanoribbons, Nanoparticles, and Graphene by the Exfoliation of Graphite in Ionic Liquids," *ACS Nano*, vol. 3, no. 8, pp. 2367–2375, Aug. 2009, doi: 10.1021/nn900546b.

[57] M. Liu, Y. Xu, F. Niu, J. J. Gooding, and J. Liu, "Carbon quantum dots directly generated from electrochemical oxidation of graphite electrodes in alkaline alcohols and the applications for specific ferric ion detection and cell imaging," *Analyst*, vol. 141, no. 9, pp. 2657–2664, 2016, doi: 10.1039/C5AN02231B.

[58] Y. Hou, Q. Lu, J. Deng, H. Li, and Y. Zhang, "One-pot electrochemical synthesis of functionalized fluorescent carbon dots and their selective sensing for mercury ion," *Anal Chim Acta*, vol. 866, pp. 69–74, Mar. 2015, doi: 10.1016/j.aca.2015.01.039.

[59] S. Ahirwar, S. Mallick, and D. Bahadur, "Electrochemical Method To Prepare Graphene Quantum Dots and Graphene Oxide Quantum Dots," *ACS Omega*, vol. 2, no. 11, pp. 8343–8353, Nov. 2017, doi: 10.1021/acsomega.7b01539.

[60] H. Huang *et al.*, "Electrochemical Cutting in Weak Aqueous Electrolytes: The Strategy for Efficient and Controllable Preparation of Graphene Quantum Dots," *Langmuir*, vol. 34, no. 1, pp. 250–258, Jan. 2018, doi: 10.1021/acs.langmuir.7b03425.

[61] J. B. Joffrion, W. Clower, and C. G. Wilson, "Tunable excitation-independent emissions from graphene quantum dots through microplasma-assisted electrochemical synthesis," *Nano-Structures & Nano-Objects*, vol. 19, p. 100341, Jul. 2019, doi: 10.1016/j.nanoso.2019.100341.

[62] M. He, X. Guo, J. Huang, H. Shen, Q. Zeng, and L. Wang, "Mass production of tunable multicolor graphene quantum dots from an energy resource of coke by a one-step electrochemical exfoliation," *Carbon N Y*, vol. 140, pp. 508–520, Dec. 2018, doi: 10.1016/j.carbon.2018.08.067.

[63]   S. Y. Park *et al.*, "Photoluminescent Green Carbon Nanodots from Food-Waste-Derived Sources: Large-Scale Synthesis, Properties, and Biomedical Applications," *ACS Appl Mater Interfaces*, vol. 6, no. 5, pp. 3365–3370, Mar. 2014, doi: 10.1021/am500159p.

[64]   S. Zhuo, M. Shao, and S.-T. Lee, "Upconversion and Downconversion Fluorescent Graphene Quantum Dots: Ultrasonic Preparation and Photocatalysis," *ACS Nano*, vol. 6, no. 2, pp. 1059–1064, Feb. 2012, doi: 10.1021/nn2040395.

[65]   S. H. Song *et al.*, "Highly Efficient Light-Emitting Diode of Graphene Quantum Dots Fabricated from Graphite Intercalation Compounds," *Adv Opt Mater*, vol. 2, no. 11, pp. 1016–1023, Nov. 2014, doi: 10.1002/adom.201400184.

[66]   H. Dang, L.-K. Huang, Y. Zhang, C.-F. Wang, and S. Chen, "Large-Scale Ultrasonic Fabrication of White Fluorescent Carbon Dots," *Ind Eng Chem Res*, vol. 55, no. 18, pp. 5335–5341, May 2016, doi: 10.1021/acs.iecr.6b00894.

[67]   H. Huang *et al.*, "A one-step ultrasonic irradiation assisted strategy for the preparation of polymer-functionalized carbon quantum dots and their biological imaging," *J Colloid Interface Sci*, vol. 532, pp. 767–773, Dec. 2018, doi: 10.1016/j.jcis.2018.07.099.

[68]   Y. Zhang, M. Park, H. Y. Kim, B. Ding, and S.-J. Park, "A facile ultrasonic-assisted fabrication of nitrogen-doped carbon dots/BiOBr up-conversion nanocomposites for visible light photocatalytic enhancements," *Sci Rep*, vol. 7, no. 1, p. 45086, Mar. 2017, doi: 10.1038/srep45086.

[69]   L. Fan *et al.*, "Direct Synthesis of Graphene Quantum Dots by Chemical Vapor Deposition," *Particle & Particle Systems Characterization*, vol. 30, no. 9, pp. 764–769, Sep. 2013, doi: 10.1002/ppsc.201300125.

[70]   X. Ding, "Direct synthesis of graphene quantum dots on hexagonal boron nitride substrate," *J. Mater. Chem. C*, vol. 2, no. 19, pp. 3717–3722, 2014, doi: 10.1039/C4TC00298A.

[71]   S. Kumar, S. T. Aziz, O. Girshevitz, and G. D. Nessim, "One-Step Synthesis of N-Doped Graphene Quantum Dots from Chitosan as a Sole Precursor Using Chemical Vapor Deposition," *The Journal of Physical Chemistry C*, vol. 122, no. 4, pp. 2343–2349, Feb. 2018, doi: 10.1021/acs.jpcc.7b05494.

[72]   K. Huang, W. Lu, X. Yu, C. Jin, and D. Yang, "Highly Pure and Luminescent Graphene Quantum Dots on Silicon Directly Grown by Chemical Vapor Deposition," *Particle & Particle Systems Characterization*, vol. 33, no. 1, pp. 8–14, Jan. 2016, doi: 10.1002/ppsc.201500132.

[73]   R. Wang, K.-Q. Lu, Z.-R. Tang, and Y.-J. Xu, "Recent progress in carbon quantum dots: synthesis, properties and applications in photocatalysis," *J Mater Chem A Mater*, vol. 5, no. 8, pp. 3717–3734, 2017, doi: 10.1039/C6TA08660H.

[74]   A. Sharma and J. Das, "Small molecules derived carbon dots: synthesis and applications in sensing, catalysis, imaging, and biomedicine," *J Nanobiotechnology*, vol. 17, no. 1, p. 92, Dec. 2019, doi: 10.1186/s12951-019-0525-8.

[75]   J. P. Naik, P. Sutradhar, and M. Saha, "Molecular scale rapid synthesis of graphene quantum dots (GQDs)," *J Nanostructure Chem*, vol. 7, no. 1, pp. 85–89, Mar. 2017, doi: 10.1007/s40097-017-0222-9.

[76]   L. Qiao, T. Sun, X. Zheng, M. Zheng, and Z. Xie, "Exploring the optimal ratio of d-glucose/l-aspartic acid for targeting carbon dots toward brain tumor cells," *Materials Science and Engineering: C*, vol. 85, pp. 1–6, Apr. 2018, doi: 10.1016/j.msec.2017.12.011.

[77]   X. Wu, F. Tian, W. Wang, J. Chen, M. Wu, and J. X. Zhao, "Fabrication of highly fluorescent graphene quantum dots using l-glutamic acid for in vitro/in vivo imaging and sensing," *J Mater Chem C Mater*, vol. 1, no. 31, p. 4676, 2013, doi: 10.1039/c3tc30820k.

[78]   H. Kalita, J. Mohapatra, L. Pradhan, A. Mitra, D. Bahadur, and M. Aslam, "Efficient synthesis of rice based graphene quantum dots and their fluorescent properties," *RSC Adv*, vol. 6, no. 28, pp. 23518–23524, 2016, doi: 10.1039/C5RA25706A.

[79]   Y. Dong *et al.*, "Blue luminescent graphene quantum dots and graphene oxide prepared by tuning the carbonization degree of citric acid," *Carbon N Y*, vol. 50, no. 12, pp. 4738–4743, Oct. 2012, doi: 10.1016/j.carbon.2012.06.002.

[80]   J. P. Naik, P. Sutradhar, and M. Saha, "Molecular scale rapid synthesis of graphene quantum dots (GQDs)," *J Nanostructure Chem*, vol. 7, no. 1, pp. 85–89, Mar. 2017, doi: 10.1007/s40097-017-0222-9.

[81]   C. Ma, C. Yin, Y. Fan, X. Yang, and X. Zhou, "Highly efficient synthesis of N-doped carbon dots with excellent stability through pyrolysis method," *J Mater Sci*, vol. 54, no. 13, pp. 9372–9384, Jul. 2019, doi: 10.1007/s10853-019-03585-7.

[82]   Y. Li *et al.*, "Large-scale direct pyrolysis synthesis of excitation-independent carbon dots and analysis of ferric (III) ion sensing mechanism," *Appl Surf Sci*, vol. 538, p. 148151, Feb. 2021, doi: 10.1016/j.apsusc.2020.148151.

[83]   X. Liu, X. Jin, H. Deng, Z. Sha, and X. Zhou, "Formation of nitrogen-doped blue- and green-emitting fluorescent carbon dots via a one-step solid-phase pyrolysis," *Journal of Nanoparticle Research*, vol. 23, no. 2, p. 45, Feb. 2021, doi: 10.1007/s11051-021-05162-z.

[84]   J. Qin, L. Zhang, and R. Yang, "Powder carbonization to synthesize novel carbon dots derived from uric acid for the detection of Ag(I) and glutathione," *Spectrochim Acta A Mol Biomol Spectrosc*, vol. 207, pp. 54–60, Jan. 2019, doi: 10.1016/j.saa.2018.08.066.

[85]   X. Wei *et al.*, "Green Synthesis of Fluorescent Carbon Dots from Gynostemma for Bioimaging and Antioxidant in Zebrafish," *ACS Appl Mater Interfaces*, vol. 11, no. 10, pp. 9832–9840, Mar. 2019, doi: 10.1021/acsami.9b00074.

[86]   Y. Guo, Z. Wang, H. Shao, and X. Jiang, "Hydrothermal synthesis of highly fluorescent carbon nanoparticles from sodium citrate and their use for the detection of mercury ions," *Carbon N Y*, vol. 52, pp. 583–589, Feb. 2013, doi: 10.1016/j.carbon.2012.10.028.

[87]   Z.-C. Yang *et al.*, "Intrinsically fluorescent carbon dots with tunable emission derived from hydrothermal treatment of glucose in the presence of monopotassium phosphate," *Chemical Communications*, vol. 47, no. 42, p. 11615, 2011, doi: 10.1039/c1cc14860e.

[88]   S. Sahu, B. Behera, T. K. Maiti, and S. Mohapatra, "Simple one-step synthesis of highly luminescent carbon dots from orange juice: application as excellent bio-imaging agents," *Chemical Communications*, vol. 48, no. 70, p. 8835, 2012, doi: 10.1039/c2cc33796g.

[89]   R. Bandi, B. R. Gangapuram, R. Dadigala, R. Eslavath, S. S. Singh, and V. Guttena, "Facile and green synthesis of fluorescent carbon dots from onion waste and their potential applications as sensor and multicolour imaging agents," *RSC Adv*, vol. 6, no. 34, pp. 28633–28639, 2016, doi: 10.1039/C6RA01669C.

[90]   A. Sachdev and P. Gopinath, "Green synthesis of multifunctional carbon dots from coriander leaves and their potential application as antioxidants, sensors and bioimaging agents," *Analyst*, vol. 140, no. 12, pp. 4260–4269, 2015, doi: 10.1039/C5AN00454C.

[91]   S. Zhao *et al.*, "Green Synthesis of Bifunctional Fluorescent Carbon Dots from Garlic for Cellular Imaging and Free Radical Scavenging," *ACS Appl Mater Interfaces*, vol. 7, no. 31, pp. 17054–17060, Aug. 2015, doi: 10.1021/acsami.5b03228.

[92]   N. Wang, Y. Wang, T. Guo, T. Yang, M. Chen, and J. Wang, "Green preparation of carbon dots with papaya as carbon source for effective fluorescent sensing of Iron (III) and Escherichia coli," *Biosens Bioelectron*, vol. 85, pp. 68–75, Nov. 2016, doi: 10.1016/j.bios.2016.04.089.

[93]   B. S. B. Kasibabu, S. L. D'souza, S. Jha, R. K. Singhal, H. Basu, and S. K. Kailasa, "One-step synthesis of fluorescent carbon dots for imaging bacterial and fungal cells," *Analytical Methods*, vol. 7, no. 6, pp. 2373–2378, 2015, doi: 10.1039/C4AY02737J.

[94]   J. Zhang, Y. Yuan, G. Liang, and S. Yu, "Scale-Up Synthesis of Fragrant Nitrogen-Doped Carbon Dots from Bee Pollens for Bioimaging and Catalysis," *Advanced Science*, vol. 2, no. 4, Apr. 2015, doi: 10.1002/advs.201500002.

[95]   J. Xu, Y. Zhou, S. Liu, M. Dong, and C. Huang, "Low-cost synthesis of carbon nanodots from natural products used as a fluorescent probe for the detection of ferrum(iii) ions in lake water," *Analytical Methods*, vol. 6, no. 7, p. 2086, 2014, doi: 10.1039/c3ay41715h.

[96]   M. J. Krysmann, A. Kelarakis, and E. P. Giannelis, "Photoluminescent carbogenic nanoparticles directly derived from crude biomass," *Green Chemistry*, vol. 14, no. 11, pp. 3141–3145, 2012, doi: 10.1039/c2gc35907c.

[97]   V. N. Mehta, S. Jha, and S. K. Kailasa, "One-pot green synthesis of carbon dots by using Saccharum officinarum juice for fluorescent imaging of bacteria (Escherichia coli) and yeast (Saccharomyces cerevisiae) cells," *Materials Science and Engineering: C*, vol. 38, pp. 20–27, May 2014, doi: 10.1016/j.msec.2014.01.038.

[98]   W. Lu *et al.*, "Economical, Green Synthesis of Fluorescent Carbon Nanoparticles and Their Use as Probes for Sensitive and Selective Detection of Mercury(II) Ions," *Anal Chem*, vol. 84, no. 12, pp. 5351–5357, Jun. 2012, doi: 10.1021/ac3007939.

[99]   S. Sahu, B. Behera, T. K. Maiti, and S. Mohapatra, "Simple one-step synthesis of highly luminescent carbon dots from orange juice: application as excellent bio-imaging agents," *Chemical Communications*, vol. 48, no. 70, p. 8835, 2012, doi: 10.1039/c2cc33796g.

[100]   H. Huang *et al.*, "One-pot green synthesis of nitrogen-doped carbon nanoparticles as fluorescent probes for mercury ions," *RSC Adv*, vol. 3, no. 44, p. 21691, 2013, doi: 10.1039/c3ra43452d.

[101]   Y. Liu, Y. Zhao, and Y. Zhang, "One-step green synthesized fluorescent carbon nanodots from bamboo leaves for copper(II) ion detection," *Sens Actuators B Chem*, vol. 196, pp. 647–652, Jun. 2014, doi: 10.1016/j.snb.2014.02.053.

[102]   J. Li, L. Zhang, P. Li, Y. Zhang, and C. Dong, "One step hydrothermal synthesis of carbon nanodots to realize the fluorescence detection of picric acid in real samples," *Sens Actuators B Chem*, vol. 258, pp. 580–588, Apr. 2018, doi: 10.1016/j.snb.2017.11.096.

[103]   R. Atchudan *et al.*, "Tunable fluorescent carbon dots from biowaste as fluorescence ink and imaging human normal and cancer cells," *Environ Res*, vol. 204, p. 112365, Mar. 2022, doi: 10.1016/j.envres.2021.112365.

[104]   L. Wang *et al.*, "Facile synthesis of fluorescent graphene quantum dots from coffee grounds for bioimaging and sensing," *Chemical Engineering Journal*, vol. 300, pp. 75–82, Sep. 2016, doi: 10.1016/j.cej.2016.04.123.

[105]   W. Zhang, L. Jia, X. Guo, R. Yang, Y. Zhang, and Z. Zhao, "Green synthesis of up- and down-conversion photoluminescent carbon dots from coffee beans for Fe^{3+} detection and cell imaging," *Analyst*, vol. 144, no. 24, pp. 7421–7431, 2019, doi: 10.1039/C9AN01953G.

[106]   Y. Guo and W. Zhao, "Hydrothermal synthesis of highly fluorescent nitrogen-doped carbon quantum dots with good biocompatibility and the application for sensing ellagic acid," *Spectrochim Acta A Mol Biomol Spectrosc*, vol. 240, p. 118580, Oct. 2020, doi: 10.1016/j.saa.2020.118580.

[107]   J.-Y. Li *et al.*, "One-Pot Hydrothermal Synthesis of Carbon Dots with Efficient Up- and Down-Converted Photoluminescence for the Sensitive Detection of Morin in a Dual-Readout Assay," *Langmuir*, vol. 33, no. 4, pp. 1043–1050, Jan. 2017, doi: 10.1021/acs.langmuir.6b04225.

[108]   H. Ding, X.-X. Zhou, Z.-H. Zhang, Y.-P. Zhao, J.-S. Wei, and H.-M. Xiong, "Large scale synthesis of full-color emissive carbon dots from a single carbon source by a solvent-free method," *Nano Res*, vol. 15, no. 4, pp. 3548–3555, Apr. 2022, doi: 10.1007/s12274-021-3891-0.

[109]   K. Qu, J. Wang, J. Ren, and X. Qu, "Carbon Dots Prepared by Hydrothermal Treatment of Dopamine as an Effective Fluorescent Sensing Platform for the Label-Free Detection of Iron(III) Ions and Dopamine," *Chemistry - A European Journal*, vol. 19, no. 22, pp. 7243–7249, May 2013, doi: 10.1002/chem.201300042.

[110]   D. Pan, J. Zhang, Z. Li, and M. Wu, "Hydrothermal Route for Cutting Graphene Sheets into Blue-Luminescent Graphene Quantum Dots," *Advanced Materials*, vol. 22, no. 6, pp. 734–738, Feb. 2010, doi: 10.1002/adma.200902825.

[111] W. Chen, C. Hu, Y. Yang, J. Cui, and Y. Liu, "Rapid Synthesis of Carbon Dots by Hydrothermal Treatment of Lignin," *Materials*, vol. 9, no. 3, p. 184, Mar. 2016, doi: 10.3390/ma9030184.

[112] A. Halder *et al.*, "One-Pot Green Synthesis of Biocompatible Graphene Quantum Dots and Their Cell Uptake Studies," *ACS Appl Bio Mater*, vol. 1, no. 2, pp. 452–461, Aug. 2018, doi: 10.1021/acsabm.8b00170.

[113] Y. Deng, J. Qian, and Y. Zhou, "Solvothermal Synthesis and Inkjet Printing of Carbon Quantum Dots," *ChemistrySelect*, vol. 5, no. 47, pp. 14930–14934, Dec. 2020, doi: 10.1002/slct.202003487.

[114] W. Li *et al.*, "Simple and Green Synthesis of Nitrogen-Doped Photoluminescent Carbonaceous Nanospheres for Bioimaging," *Angewandte Chemie International Edition*, vol. 52, no. 31, pp. 8151–8155, Jul. 2013, doi: 10.1002/anie.201303927.

[115] X. Yang, Y. Zhuo, S. Zhu, Y. Luo, Y. Feng, and Y. Dou, "Novel and green synthesis of high-fluorescent carbon dots originated from honey for sensing and imaging," *Biosens Bioelectron*, vol. 60, pp. 292–298, Oct. 2014, doi: 10.1016/j.bios.2014.04.046.

[116] A. L. Himaja, P. S. Karthik, B. Sreedhar, and S. P. Singh, "Synthesis of Carbon Dots from Kitchen Waste: Conversion of Waste to Value Added Product," *J Fluoresc*, vol. 24, no. 6, pp. 1767–1773, Nov. 2014, doi: 10.1007/s10895-014-1465-1.

[117] Y. Shin *et al.*, "Acid-free and oxone oxidant-assisted solvothermal synthesis of graphene quantum dots using various natural carbon materials as resources," *Nanoscale*, vol. 7, no. 13, pp. 5633–5637, 2015, doi: 10.1039/C5NR00814J.

[118] R. Tian *et al.*, "Solvothermal method to prepare graphene quantum dots by hydrogen peroxide," *Opt Mater (Amst)*, vol. 60, pp. 204–208, Oct. 2016, doi: 10.1016/j.optmat.2016.07.032.

[119] Z. Qian, J. Ma, X. Shan, H. Feng, L. Shao, and J. Chen, "Highly Luminescent N-Doped Carbon Quantum Dots as an Effective Multifunctional Fluorescence Sensing Platform," *Chemistry - A European Journal*, vol. 20, no. 8, pp. 2254–2263, Feb. 2014, doi: 10.1002/chem.201304374.

[120] M. Sun *et al.*, "Efficient full-color emitting carbon-dot-based composite phosphors by chemical dispersion," *Nanoscale*, vol. 12, no. 29, pp. 15823–15831, 2020, doi: 10.1039/D0NR02021D.

[121] C.-L. Shen *et al.*, "In-situ embedding of carbon dots in a trisodium citrate crystal matrix for tunable solid-state fluorescence," *Carbon N Y*, vol. 136, pp. 359–368, Sep. 2018, doi: 10.1016/j.carbon.2018.05.015.

[122] X. Miao *et al.*, "Synthesis of Carbon Dots with Multiple Color Emission by Controlled Graphitization and Surface Functionalization," *Advanced Materials*, vol. 30, no. 1, Jan. 2018, doi: 10.1002/adma.201704740.

[123] Zhao *et al.*, "Synthesis of Multicolor Carbon Dots Based on Solvent Control and Its Application in the Detection of Crystal Violet," *Nanomaterials*, vol. 9, no. 11, p. 1556, Nov. 2019, doi: 10.3390/nano9111556.

[124] D. Zhang *et al.*, "One-Step Green Solvothermal Synthesis of Full-Color Carbon Quantum Dots Based on a Doping Strategy," *J Phys Chem Lett*, vol. 12, no. 37, pp. 8939–8946, Sep. 2021, doi: 10.1021/acs.jpclett.1c02475.

[125] S. Zhu *et al.*, "Strongly green-photoluminescent graphene quantum dots for bioimaging applications," *Chemical Communications*, vol. 47, no. 24, p. 6858, 2011, doi: 10.1039/c1cc11122a.

[126] S. Mitra, S. Chandra, S. H. Pathan, N. Sikdar, P. Pramanik, and A. Goswami, "Room temperature and solvothermal green synthesis of self passivated carbon quantum dots," *RSC Adv*, vol. 3, no. 10, p. 3189, 2013, doi: 10.1039/c2ra23085b.

[127] C. Zhao *et al.*, "Synthesis of graphene quantum dots and their applications in drug delivery," *J Nanobiotechnology*, vol. 18, no. 1, p. 142, Dec. 2020, doi: 10.1186/s12951-020-00698-z.

[128] L.-L. Li *et al.*, "A Facile Microwave Avenue to Electrochemiluminescent Two-Color Graphene Quantum Dots," *Adv Funct Mater*, vol. 22, no. 14, pp. 2971–2979, Jul. 2012, doi: 10.1002/adfm.201200166.

[129] Q. Wang, X. Liu, L. Zhang, and Y. Lv, "Microwave-assisted synthesis of carbon nanodots through an eggshell membrane and their fluorescent application," *Analyst*, vol. 137, no. 22, p. 5392, 2012, doi: 10.1039/c2an36059d.

[130] M. K. Kumawat, M. Thakur, R. B. Gurung, and R. Srivastava, "Graphene Quantum Dots from *Mangifera indica* : Application in Near-Infrared Bioimaging and Intracellular Nanothermometry," *ACS Sustain Chem Eng*, vol. 5, no. 2, pp. 1382–1391, Feb. 2017, doi: 10.1021/acssuschemeng.6b01893.

[131] N. R. Pires, C. M. W. Santos, R. R. Sousa, R. C. M. de Paula, P. L. R. Cunha, and J. P. A. Feitosa, "Novel and Fast Microwave-Assisted Synthesis of Carbon Quantum Dots from Raw Cashew Gum," *J Braz Chem Soc*, 2015, doi: 10.5935/0103-5053.20150094.

[132] Q. Ren, L. Ga, and J. Ai, "Rapid Synthesis of Highly Fluorescent Nitrogen-Doped Graphene Quantum Dots for Effective Detection of Ferric Ions and as Fluorescent Ink," *ACS Omega*, vol. 4, no. 14, pp. 15842–15848, Oct. 2019, doi: 10.1021/acsomega.9b01612.

[133] C. Zhang, Y. Cui, L. Song, X. Liu, and Z. Hu, "Microwave assisted one-pot synthesis of graphene quantum dots as highly sensitive fluorescent probes for detection of iron ions and pH value," *Talanta*, vol. 150, pp. 54–60, Apr. 2016, doi: 10.1016/j.talanta.2015.12.015.

[134] B. Zheng *et al.*, "Ultrafast ammonia-driven, microwave-assisted synthesis of nitrogen-doped graphene quantum dots and their optical properties," *Nanophotonics*, vol. 6, no. 1, pp. 259–267, Jan. 2017, doi: 10.1515/nanoph-2016-0102.

[135] K. K. Chan, C. Yang, Y.-H. Chien, N. Panwar, and K.-T. Yong, "A facile synthesis of label-free carbon dots with unique selectivity-tunable characteristics for ferric ion detection and cellular imaging applications," *New Journal of Chemistry*, vol. 43, no. 12, pp. 4734–4744, 2019, doi: 10.1039/C8NJ06306K.

[136] Q. Li *et al.*, "Rapid microwave-assisted green synthesis of guanine-derived carbon dots for highly selective detection of Ag+ in aqueous solution," *Spectrochim Acta A Mol Biomol Spectrosc*, vol. 248, p. 119208, Mar. 2021, doi: 10.1016/j.saa.2020.119208.

[137] L. Fang, M. Wu, C. Huang, Z. Liu, J. Liang, and H. Zhang, "Industrializable synthesis of narrow-dispersed carbon dots achieved by microwave-assisted selective carbonization of surfactants and their applications as fluorescent nano-additives," *J Mater Chem A Mater*, vol. 8, no. 40, pp. 21317–21326, 2020, doi: 10.1039/D0TA07252D.

[138] S. Das, L. Ngashangva, and P. Goswami, "Carbon Dots: An Emerging Smart Material for Analytical Applications," *Micromachines (Basel)*, vol. 12, no. 1, p. 84, Jan. 2021, doi: 10.3390/mi12010084.

[139] E. Liu *et al.*, "Enhanced Near-Infrared Emission from Carbon Dots by Surface Deprotonation," *J Phys Chem Lett*, vol. 12, no. 1, pp. 604–611, Jan. 2021, doi: 10.1021/acs.jpclett.0c03383.

[140] D. Li *et al.*, "Near-Infrared Excitation/Emission and Multiphoton-Induced Fluorescence of Carbon Dots," *Advanced Materials*, vol. 30, no. 13, Mar. 2018, doi: 10.1002/adma.201705913.

[141] M. Zhang *et al.*, "Facile synthesis of water-soluble, highly fluorescent graphene quantum dots as a robust biological label for stem cells," *J Mater Chem*, vol. 22, no. 15, p. 7461, 2012, doi: 10.1039/c2jm16835a.

[142] G. Rajender, U. Goswami, and P. K. Giri, "Solvent dependent synthesis of edge-controlled graphene quantum dots with high photoluminescence quantum yield and their application in confocal imaging of cancer cells," *J Colloid Interface Sci*, vol. 541, pp. 387–398, Apr. 2019, doi: 10.1016/j.jcis.2019.01.099.

[143] M. Liu, "Optical Properties of Carbon Dots: A Review," *Nanoarchitectonics*, vol. 1, no. 1, pp. 1–12, Jan. 2020, doi: 10.37256/nat.112020124.1-12.

[144] K. Holá *et al.*, "Graphitic Nitrogen Triggers Red Fluorescence in Carbon Dots," *ACS Nano*, vol. 11, no. 12, pp. 12402–12410, Dec. 2017, doi: 10.1021/acsnano.7b06399.

[145] T. Van Tam, N. B. Trung, H. R. Kim, J. S. Chung, and W. M. Choi, "One-pot synthesis of N-doped graphene quantum dots as a fluorescent sensing platform for Fe3+ ions detection," *Sens Actuators B Chem*, vol. 202, pp. 568–573, Oct. 2014, doi: 10.1016/j.snb.2014.05.045.

[146] D. Qu *et al.*, "Highly luminescent S, N co-doped graphene quantum dots with broad visible absorption bands for visible light photocatalysts," *Nanoscale*, vol. 5, no. 24, p. 12272, 2013, doi: 10.1039/c3nr04402e.

[147] J. Peng *et al.*, "Graphene Quantum Dots Derived from Carbon Fibers," *Nano Lett*, vol. 12, no. 2, pp. 844–849, Feb. 2012, doi: 10.1021/nl2038979.

[148] S. Kim *et al.*, "Anomalous Behaviors of Visible Luminescence from Graphene Quantum Dots: Interplay between Size and Shape," *ACS Nano*, vol. 6, no. 9, pp. 8203–8208, Sep. 2012, doi: 10.1021/nn302878r.

[149] L. Tang, R. Ji, X. Li, K. S. Teng, and S. P. Lau, "Size-Dependent Structural and Optical Characteristics of Glucose-Derived Graphene Quantum Dots," *Particle & Particle Systems Characterization*, vol. 30, no. 6, pp. 523–531, Jun. 2013, doi: 10.1002/ppsc.201200131.

[150] M. Sun *et al.*, "Realization of the Photostable Intrinsic Core Emission from Carbon Dots through Surface Deoxidation by Ultraviolet Irradiation," *J Phys Chem Lett*, vol. 10, no. 11, pp. 3094–3100, Jun. 2019, doi: 10.1021/acs.jpclett.9b00842.

[151] K. Hola *et al.*, "Photoluminescence effects of graphitic core size and surface functional groups in carbon dots: COO− induced red-shift emission," *Carbon N Y*, vol. 70, pp. 279–286, Apr. 2014, doi: 10.1016/j.carbon.2014.01.008.

[152] Y. Zhou *et al.*, "Size-dependent photocatalytic activity of carbon dots with surface-state determined photoluminescence," *Appl Catal B*, vol. 248, pp. 157–166, Jul. 2019, doi: 10.1016/j.apcatb.2019.02.019.

[153] L. Han *et al.*, "Facile synthesis of multicolor photoluminescent polymer carbon dots with surface-state energy gap-controlled emission," *J. Mater. Chem. C*, vol. 5, no. 41, pp. 10785–10793, 2017, doi: 10.1039/C7TC03314A.

[154] Y. Xiong, J. Schneider, E. V. Ushakova, and A. L. Rogach, "Influence of molecular fluorophores on the research field of chemically synthesized carbon dots," *Nano Today*, vol. 23, pp. 124–139, Dec. 2018, doi: 10.1016/j.nantod.2018.10.010.

[155] J. Liu *et al.*, "Deep Red Emissive Carbonized Polymer Dots with Unprecedented Narrow Full Width at Half Maximum," *Advanced Materials*, vol. 32, no. 17, Apr. 2020, doi: 10.1002/adma.201906641.

[156] M. A. Sk, A. Ananthanarayanan, L. Huang, K. H. Lim, and P. Chen, "Revealing the tunable photoluminescence properties of graphene quantum dots," *J. Mater. Chem. C*, vol. 2, no. 34, pp. 6954–6960, 2014, doi: 10.1039/C4TC01191K.

[157] F. Yuan *et al.*, "Bright Multicolor Bandgap Fluorescent Carbon Quantum Dots for Electroluminescent Light-Emitting Diodes," *Advanced Materials*, vol. 29, no. 3, Jan. 2017, doi: 10.1002/adma.201604436.

[158] H. Ding, S. B. Yu, J. S. Wei, and H. M. Xiong, "Full-color light-emitting carbon dots with a surface-state-controlled luminescence mechanism," *ACS Nano*, vol. 10, no. 1, pp. 484–491, Jan. 2016, doi: 10.1021/acsnano.5b05406.

[159] P. M. Gharat, J. M. Chethodil, A. P. Srivastava, P. K. Praseetha, H. Pal, and S. D. Choudhury, "An insight into the molecular and surface state photoluminescence of carbon dots revealed through solvent-induced modulations in their excitation wavelength dependent emission properties," *Photochemical & Photobiological Sciences*, vol. 18, no. 1, pp. 110–119, Jan. 2019, doi: 10.1039/c8pp00373d.

[160] D. Shen *et al.*, "Tuning the fluorescence performance of carbon dots with a reduction pathway," *Nanoscale*, vol. 11, no. 13, pp. 5998–6003, 2019, doi: 10.1039/C8NR09587F.

[161] X. Meng, Q. Chang, C. Xue, J. Yang, and S. Hu, "Full-colour carbon dots: from energy-efficient synthesis to concentration-dependent photoluminescence properties," *Chemical Communications*, vol. 53, no. 21, pp. 3074–3077, 2017, doi: 10.1039/C7CC00461C.

[162] S. Zhu, X. Zhao, Y. Song, S. Lu, and B. Yang, "Beyond bottom-up carbon nanodots: Citric-acid derived organic molecules," *Nano Today*, vol. 11, no. 2, pp. 128–132, Apr. 2016, doi: 10.1016/j.nantod.2015.09.002.

[163] Y. Song *et al.*, "Investigation from chemical structure to photoluminescent mechanism: a type of carbon dots from the pyrolysis of citric acid and an amine," *J Mater Chem C Mater*, vol. 3, no. 23, pp. 5976–5984, 2015, doi: 10.1039/C5TC00813A.

[164] S. Zhu *et al.*, "Highly Photoluminescent Carbon Dots for Multicolor Patterning, Sensors, and Bioimaging," *Angewandte Chemie International Edition*, vol. 52, no. 14, pp. 3953–3957, Apr. 2013, doi: 10.1002/anie.201300519.

[165] B. D. Mansuriya and Z. Altintas, "Graphene Quantum Dot-Based Electrochemical Immunosensors for Biomedical Applications," *Materials*, vol. 13, no. 1, p. 96, Dec. 2019, doi: 10.3390/ma13010096.

[166] L. Tian, Z. Li, P. Wang, X. Zhai, X. Wang, and T. Li, "Carbon quantum dots for advanced electrocatalysis," *Journal of Energy Chemistry*, vol. 55, pp. 279–294, Apr. 2021, doi: 10.1016/j.jechem.2020.06.057.

[167] S. Miao, K. Liang, J. Zhu, B. Yang, D. Zhao, and B. Kong, "Hetero-atom-doped carbon dots: Doping strategies, properties and applications," *Nano Today*, vol. 33, p. 100879, Aug. 2020, doi: 10.1016/j.nantod.2020.100879.

[168] Q. Xu *et al.*, "Heteroatom-doped carbon dots: synthesis, characterization, properties, photoluminescence mechanism and biological applications," *J Mater Chem B*, vol. 4, no. 45, pp. 7204–7219, 2016, doi: 10.1039/C6TB02131J.

[169] Y. Liu, R. Wang, J. Lang, and X. Yan, "Insight into the formation mechanism of graphene quantum dots and the size effect on their electrochemical behaviors," *Physical Chemistry Chemical Physics*, vol. 17, no. 21, pp. 14028–14035, 2015, doi: 10.1039/C5CP00646E.

[170] Y. Li, F. Wu, X. Jin, H. Xu, X. Liu, and G. Shi, "Preparation and electrochemical properties of graphene quantum dots/biomass activated carbon electrodes," *Inorg Chem Commun*, vol. 112, p. 107718, Feb. 2020, doi: 10.1016/j.inoche.2019.107718.

[171] W. Shang *et al.*, "The uptake mechanism and biocompatibility of graphene quantum dots with human neural stem cells," *Nanoscale*, vol. 6, no. 11, pp. 5799–5806, 2014, doi: 10.1039/C3NR06433F.

[172] S. Zhu *et al.*, "The crosslink enhanced emission (CEE) in non-conjugated polymer dots: from the photoluminescence mechanism to the cellular uptake mechanism and internalization," *Chem. Commun.*, vol. 50, no. 89, pp. 13845–13848, 2014, doi: 10.1039/C4CC05806B.

[173] S.-T. Yang *et al.*, "Carbon Dots as Nontoxic and High-Performance Fluorescence Imaging Agents," *The Journal of Physical Chemistry C*, vol. 113, no. 42, pp. 18110–18114, Oct. 2009, doi: 10.1021/jp9085969.

[174] Y. Wang *et al.*, "Carbon dots of different composition and surface functionalization: cytotoxicity issues relevant to fluorescence cell imaging," *Exp Biol Med*, vol. 236, no. 11, pp. 1231–1238, Nov. 2011, doi: 10.1258/ebm.2011.011132.

[175] X. Huang *et al.*, "Effect of Injection Routes on the Biodistribution, Clearance, and Tumor Uptake of Carbon Dots," *ACS Nano*, vol. 7, no. 7, pp. 5684–5693, Jul. 2013, doi: 10.1021/nn401911k.

[176] C. Dias *et al.*, "Biocompatibility and bioimaging potential of fruit-based carbon dots," *Nanomaterials*, vol. 9, no. 2, Feb. 2019, doi: 10.3390/nano9020199.

[177] Y. Wang *et al.*, "Carbon dots of different composition and surface functionalization: Cytotoxicity issues relevant to fluorescence cell imaging," *Exp Biol Med*, vol. 236, no. 11, pp. 1231–1238, Nov. 2011, doi: 10.1258/ebm.2011.011132.

[178] W. Wang, Y. Li, L. Cheng, Z. Cao, and W. Liu, "Water-soluble and phosphorus-containing carbon dots with strong green fluorescence for cell labeling," *J Mater Chem B*, vol. 2, no. 1, pp. 46–48, Jan. 2014, doi: 10.1039/c3tb21370f.

[179] Y. Zhuo, H. Miao, D. Zhong, S. Zhu, and X. Yang, "One-step synthesis of high quantum-yield and excitation-independent emission carbon dots for cell imaging," *Mater Lett*, vol. 139, pp. 197–200, Jan. 2015, doi: 10.1016/j.matlet.2014.10.048.

[180] Y. Choi, X. T. Zheng, and Y. N. Tan, "Bioinspired carbon dots (biodots): emerging fluorophores with tailored multiple functionalities for biomedical, agricultural and environmental applications," *Mol Syst Des Eng*, vol. 5, no. 1, pp. 67–90, 2020, doi: 10.1039/C9ME00086K.

[181] J. D. Stachowska *et al.*, "A rich gallery of carbon dots based photoluminescent suspensions and powders derived by citric acid/urea," *Sci Rep*, vol. 11, no. 1, p. 10554, May 2021, doi: 10.1038/s41598-021-89984-w.

[182] H. Ding, J.-S. Wei, N. Zhong, Q.-Y. Gao, and H.-M. Xiong, "Highly Efficient Red-Emitting Carbon Dots with Gram-Scale Yield for Bioimaging," *Langmuir*, vol. 33, no. 44, pp. 12635–12642, Nov. 2017, doi: 10.1021/acs.langmuir.7b02385.

[183] E. J. Goh *et al.*, "Bioimaging of Hyaluronic Acid Derivatives Using Nanosized Carbon Dots," *Biomacromolecules*, vol. 13, no. 8, pp. 2554–2561, Aug. 2012, doi: 10.1021/bm300796q.

[184] L. Cao *et al.*, "Carbon dots for multiphoton bioimaging," *J Am Chem Soc*, vol. 129, no. 37, pp. 11318–11319, Sep. 2007, doi: 10.1021/ja073527l.

[185] Y.-P. Sun *et al.*, "Quantum-Sized Carbon Dots for Bright and Colorful Photoluminescence," *J Am Chem Soc*, vol. 128, no. 24, pp. 7756–7757, Jun. 2006, doi: 10.1021/ja062677d.

[186] X. Zhai *et al.*, "Highly luminescent carbon nanodots by microwave-assisted pyrolysis," *Chemical Communications*, vol. 48, no. 64, p. 7955, 2012, doi: 10.1039/c2cc33869f.

[187]   H. Tao *et al.*, "In vivo NIR fluorescence imaging, biodistribution, and toxicology of photoluminescent carbon dots produced from carbon nanotubes and graphite," *Small*, vol. 8, no. 2, pp. 281–290, 2012, doi: 10.1002/smll.201101706.

[188]   M. Xu and L. V. Wang, "Photoacoustic imaging in biomedicine," *Review of Scientific Instruments*, vol. 77, no. 4, Apr. 2006, doi: 10.1063/1.2195024.

[189]   L. Wu *et al.*, "A green synthesis of carbon nanoparticles from honey and their use in real-time photoacoustic imaging," *Nano Res*, vol. 6, no. 5, pp. 312–325, May 2013, doi: 10.1007/s12274-013-0308-8.

[190]   N. Parvin and T. K. Mandal, "Dually emissive P,N-co-doped carbon dots for fluorescent and photoacoustic tissue imaging in living mice," *Microchimica Acta*, vol. 184, no. 4, pp. 1117–1125, Apr. 2017, doi: 10.1007/s00604-017-2108-4.

[191]   J. Ge *et al.*, "Red-Emissive Carbon Dots for Fluorescent, Photoacoustic, and Thermal Theranostics in Living Mice," *Advanced Materials*, vol. 27, no. 28, pp. 4169–4177, Jul. 2015, doi: 10.1002/adma.201500323.

[192]   C. Lee *et al.*, "Biodegradable Nitrogen-Doped Carbon Nanodots for Non-Invasive Photoacoustic Imaging and Photothermal Therapy," *Theranostics*, vol. 6, no. 12, pp. 2196–2208, 2016, doi: 10.7150/thno.16923.

[193]   Q. Jia *et al.*, "Synthesis of carbon dots from Hypocrella bambusae for bimodel fluorescence/photoacoustic imaging-guided synergistic photodynamic/photothermal therapy of cancer," *J Colloid Interface Sci*, vol. 526, pp. 302–311, Sep. 2018, doi: 10.1016/j.jcis.2018.05.005.

[194]   L. Zou *et al.*, "Current Approaches of Photothermal Therapy in Treating Cancer Metastasis with Nanotherapeutics," *Theranostics*, vol. 6, no. 6, pp. 762–772, 2016, doi: 10.7150/thno.14988.

[195]   M. Nurunnabi, Z. Khatun, G. R. Reeck, D. Y. Lee, and Y. Lee, "Photoluminescent Graphene Nanoparticles for Cancer Phototherapy and Imaging," *ACS Appl Mater Interfaces*, vol. 6, no. 15, pp. 12413–12421, Aug. 2014, doi: 10.1021/am504071z.

[196]   M. Zheng, Y. Li, S. Liu, W. Wang, Z. Xie, and X. Jing, "One-Pot To Synthesize Multifunctional Carbon Dots for Near Infrared Fluorescence Imaging and Photothermal Cancer Therapy," *ACS Appl Mater Interfaces*, vol. 8, no. 36, pp. 23533–23541, Sep. 2016, doi: 10.1021/acsami.6b07453.

[197]   D. Li *et al.*, "Supra-(carbon nanodots) with a strong visible to near-infrared absorption band and efficient photothermal conversion," *Light Sci Appl*, vol. 5, no. 7, pp. e16120–e16120, Mar. 2016, doi: 10.1038/lsa.2016.120.

[198]   H. Wang, S. Mukherjee, J. Yi, P. Banerjee, Q. Chen, and S. Zhou, "Biocompatible Chitosan–Carbon Dot Hybrid Nanogels for NIR-Imaging-Guided Synergistic Photothermal–Chemo Therapy," *ACS Appl Mater Interfaces*, vol. 9, no. 22, pp. 18639–18649, Jun. 2017, doi: 10.1021/acsami.7b06062.

[199]   J. Chen *et al.*, "New Technology for Deep Light Distribution in Tissue for Phototherapy," *The Cancer Journal*, vol. 8, no. 2, pp. 154–163, Mar. 2002, doi: 10.1097/00130404-200203000-00009.

[200] X.-W. Hua, Y.-W. Bao, and F.-G. Wu, "Fluorescent Carbon Quantum Dots with Intrinsic Nucleolus-Targeting Capability for Nucleolus Imaging and Enhanced Cytosolic and Nuclear Drug Delivery," *ACS Appl Mater Interfaces*, vol. 10, no. 13, pp. 10664–10677, Apr. 2018, doi: 10.1021/acsami.7b19549.

[201] Y. Li *et al.*, "Porphyrin-Based Carbon Dots for Photodynamic Therapy of Hepatoma," *Adv Healthc Mater*, vol. 6, no. 1, Jan. 2017, doi: 10.1002/adhm.201600924.

[202] H. He *et al.*, "Diketopyrrolopyrrole-based carbon dots for photodynamic therapy," *Nanoscale*, vol. 10, no. 23, pp. 10991–10998, 2018, doi: 10.1039/C8NR02643B.

[203] X. Shan, L. Chai, J. Ma, Z. Qian, J. Chen, and H. Feng, "B-doped carbon quantum dots as a sensitive fluorescence probe for hydrogen peroxide and glucose detection," *Analyst*, vol. 139, no. 10, pp. 2322–2325, 2014, doi: 10.1039/C3AN02222F.

[204] Y. Jiang, B. Wang, F. Meng, Y. Cheng, and C. Zhu, "Microwave-assisted preparation of N-doped carbon dots as a biosensor for electrochemical dopamine detection," *J Colloid Interface Sci*, vol. 452, pp. 199–202, Aug. 2015, doi: 10.1016/j.jcis.2015.04.016.

[205] Y. Song *et al.*, "Highly photoluminescent carbon dots derived from linseed and their applications in cellular imaging and sensing," *J Mater Chem B*, vol. 6, no. 19, pp. 3181–3187, 2018, doi: 10.1039/C8TB00116B.

[206] H. Xu, X. Yang, G. Li, C. Zhao, and X. Liao, "Green Synthesis of Fluorescent Carbon Dots for Selective Detection of Tartrazine in Food Samples," *J Agric Food Chem*, vol. 63, no. 30, pp. 6707–6714, Aug. 2015, doi: 10.1021/acs.jafc.5b02319.

[207] R. Liu *et al.*, "A facile microwave-hydrothermal approach towards highly photoluminescent carbon dots from goose feathers," *RSC Adv*, vol. 5, no. 6, pp. 4428–4433, 2015, doi: 10.1039/C4RA12077A.

[208] Q. Xu *et al.*, "Preparation of highly photoluminescent sulfur-doped carbon dots for Fe(iii) detection," *J Mater Chem A Mater*, vol. 3, no. 2, pp. 542–546, 2015, doi: 10.1039/c4ta05483k.

[209] Q. Zeng *et al.*, "Carbon dots as a trackable drug delivery carrier for localized cancer therapy in vivo," *J Mater Chem B*, vol. 4, no. 30, pp. 5119–5126, 2016, doi: 10.1039/C6TB01259K.

[210] N. Sarkar, G. Sahoo, R. Das, G. Prusty, and S. K. Swain, "Carbon quantum dot tailored calcium alginate hydrogel for pH responsive controlled delivery of vancomycin," *European Journal of Pharmaceutical Sciences*, vol. 109, pp. 359–371, Nov. 2017, doi: 10.1016/j.ejps.2017.08.015.

[211] V. N. Mehta, S. S. Chettiar, J. R. Bhamore, S. K. Kailasa, and R. M. Patel, "Green Synthetic Approach for Synthesis of Fluorescent Carbon Dots for Lisinopril Drug Delivery System and their Confirmations in the Cells," *J Fluoresc*, vol. 27, no. 1, pp. 111–124, Jan. 2017, doi: 10.1007/s10895-016-1939-4.

[212] D. Fernandes, M. J. Krysmann, and A. Kelarakis, "Carbon dot based nanopowders and their application for fingerprint recovery," *Chemical Communications*, vol. 51, no. 23, pp. 4902–4905, 2015, doi: 10.1039/c5cc00468c.

[213] D. Fernandes, M. J. Krysmann, and A. Kelarakis, "Carbogenically coated silica nanoparticles and their forensic applications," *Chemical Communications*, vol. 52, no. 53, pp. 8294–8296, 2016, doi: 10.1039/c6cc02556k.

[214] Y. Sun *et al.*, "An ordered and porous N-doped carbon dot-sensitized Bi_2O_3 inverse opal with enhanced photoelectrochemical performance and photocatalytic activity," *Nanoscale*, vol. 7, no. 33, pp. 13974–13980, 2015, doi: 10.1039/C5NR03402G.

[215] S. Zhuo, M. Shao, and S.-T. Lee, "Upconversion and Downconversion Fluorescent Graphene Quantum Dots: Ultrasonic Preparation and Photocatalysis," *ACS Nano*, vol. 6, no. 2, pp. 1059–1064, Feb. 2012, doi: 10.1021/nn2040395.

[216] H. Li *et al.*, "Carbon quantum dots/Cu2O composites with protruding nanostructures and their highly efficient (near) infrared photocatalytic behavior," *J Mater Chem*, vol. 22, no. 34, p. 17470, 2012, doi: 10.1039/c2jm32827e.

[217] H. Song, X. Liu, B. Wang, Z. Tang, and S. Lu, "High production-yield solid-state carbon dots with tunable photoluminescence for white/multi-color light-emitting diodes," *Sci Bull (Beijing)*, vol. 64, no. 23, pp. 1788–1794, Dec. 2019, doi: 10.1016/j.scib.2019.10.006.

[218] H.-J. Wang, W.-Y. Hou, Y.-W. Hao, W.-S. Jiang, H.-L. Chen, and Q.-Q. Zhang, "Novel yellow solid-state fluorescent-emitting carbon dots with high quantum yield for white light-emitting diodes," *Spectrochim Acta A Mol Biomol Spectrosc*, vol. 250, p. 119340, Apr. 2021, doi: 10.1016/j.saa.2020.119340.

[219] T. Feng *et al.*, "Color-Tunable Carbon Dots Possessing Solid-State Emission for Full-Color Light-Emitting Diodes Applications," *ACS Photonics*, vol. 5, no. 2, pp. 502–510, Feb. 2018, doi: 10.1021/acsphotonics.7b01010.

[220] Y. Zhang *et al.*, "Solid-State Fluorescent Carbon Dots with Aggregation-Induced Yellow Emission for White Light-Emitting Diodes with High Luminous Efficiencies," *ACS Appl Mater Interfaces*, vol. 11, no. 27, pp. 24395–24403, Jul. 2019, doi: 10.1021/acsami.9b04600.

[221] B. Wang, J. Li, Z. Tang, B. Yang, and S. Lu, "Near-infrared emissive carbon dots with 33.96% emission in aqueous solution for cellular sensing and light-emitting diodes," *Sci Bull (Beijing)*, vol. 64, no. 17, pp. 1285–1292, Sep. 2019, doi: 10.1016/j.scib.2019.07.021.

[222] X. Yang *et al.*, "Red-emitting, self-oxidizing carbon dots for the preparation of white LEDs with super-high color rendering index," *Sci China Chem*, vol. 64, no. 9, pp. 1547–1553, Sep. 2021, doi: 10.1007/s11426-021-1033-6.

[223] M. Taha, M. Hassan, S. Essa, and Y. Tartor, "Use of Fourier transform infrared spectroscopy (FTIR) spectroscopy for rapid and accurate identification of Yeasts isolated from human and animals," *Int J Vet Sci Med*, vol. 1, no. 1, pp. 15–20, Jun. 2013, doi: 10.1016/j.ijvsm.2013.03.001.

[224] M. Y. Berezin and S. Achilefu, "Fluorescence Lifetime Measurements and Biological Imaging," *Chem Rev*, vol. 110, no. 5, pp. 2641–2684, May 2010, doi: 10.1021/cr900343z.

[225]   A. Jain, C. Blum, and V. Subramaniam, "Fluorescence Lifetime Spectroscopy and Imaging of Visible Fluorescent Proteins," in *Advances in Biomedical Engineering*, Elsevier, 2009, pp. 147–176. doi: 10.1016/B978-0-444-53075-2.00004-6.

[226]   X. Wang and Y. Lai, "Three basic types of fluorescence microscopy and recent improvement," *E3S Web of Conferences*, vol. 290, p. 01031, Jul. 2021, doi: 10.1051/e3sconf/202129001031.

[227]   D. B. Williams and C. B. Carter, "The Transmission Electron Microscope," in *Transmission Electron Microscopy*, Boston, MA: Springer US, 1996, pp. 3–17. doi: 10.1007/978-1-4757-2519-3_1.

[228]   C. Y. Tang and Z. Yang, "Transmission Electron Microscopy (TEM)," in *Membrane Characterization*, Elsevier, 2017, pp. 145–159. doi: 10.1016/B978-0-444-63776-5.00008-5.

[229]   M. Kaszuba, J. Corbett, F. M. Watson, and A. Jones, "High-concentration zeta potential measurements using light-scattering techniques," *Philosophical Transactions of the Royal Society A: Mathematical, Physical and Engineering Sciences*, vol. 368, no. 1927, pp. 4439–4451, Sep. 2010, doi: 10.1098/rsta.2010.0175.

[230]   V. P. Fadeeva, V. D. Tikhova, and O. N. Nikulicheva, "Elemental analysis of organic compounds with the use of automated CHNS analyzers," *Journal of Analytical Chemistry*, vol. 63, no. 11, pp. 1094–1106, Nov. 2008, doi: 10.1134/S1061934808110142.

[231]   J. R. Masters, "HeLa cells 50 years on: the good, the bad and the ugly," *Nat Rev Cancer*, vol. 2, no. 4, pp. 315–319, Apr. 2002, doi: 10.1038/nrc775.

[232]   O. L. Gamborg and G. C. Phillips, "Sterile Techniques," in *Plant Cell, Tissue and Organ Culture*, Berlin, Heidelberg: Springer Berlin Heidelberg, 1995, pp. 35–42. doi: 10.1007/978-3-642-79048-5_3.

[233]   S. Deng, X. Yu, and P. Wang, "An irregular-shaped homogeneous refractive index model for interpretation of the surface plasmon resonance response from living cell attachment," *Analytical Methods*, vol. 8, no. 16, pp. 3301–3306, 2016, doi: 10.1039/C6AY00524A.

[234]   J. C. Bartlett, R. J. Radcliffe, P. Convey, K. A. Hughes, and S. A. L. Hayward, "The effectiveness of Virkon® S disinfectant against an invasive insect and implications for Antarctic biosecurity practices," *Antarct Sci*, vol. 33, no. 1, pp. 1–9, Feb. 2021, doi: 10.1017/S0954102020000413.

[235]   M. Boncler, M. Różalski, U. Krajewska, A. Podsędek, and C. Watala, "Comparison of PrestoBlue and MTT assays of cellular viability in the assessment of anti-proliferative effects of plant extracts on human endothelial cells," *J Pharmacol Toxicol Methods*, vol. 69, no. 1, pp. 9–16, Jan. 2014, doi: 10.1016/j.vascn.2013.09.003.

[236]   Y.-M. Long, Q.-L. Zhao, Z.-L. Zhang, Z.-Q. Tian, and D.-W. Pang, "Electrochemical methods--important means for fabrication of fluorescent nanoparticles.," *Analyst*, vol. 137, no. 4, pp. 805–15, Feb. 2012, doi: 10.1039/c2an15740c.

[237]   B.-P. Qi, L. Bao, Z.-L. Zhang, and D.-W. Pang, "Electrochemical Methods to Study Photoluminescent Carbon Nanodots: Preparation, Photoluminescence Mechanism and Sensing," *ACS Appl Mater Interfaces*, vol. 8, no. 42, pp. 28372–28382, Oct. 2016, doi: 10.1021/acsami.5b11551.

[238] S. Y. Lim, W. Shen, and Z. Gao, "Carbon quantum dots and their applications," *Chem Soc Rev*, vol. 44, no. 1, pp. 362–381, 2015, doi: 10.1039/C4CS00269E.

[239] F. Yuan, S. Li, Z. Fan, X. Meng, L. Fan, and S. Yang, "Shining carbon dots: Synthesis and biomedical and optoelectronic applications," *Nano Today*, vol. 11, no. 5, pp. 565–586, Oct. 2016, doi: 10.1016/j.nantod.2016.08.006.

[240] M. L. Liu, B. Bin Chen, C. M. Li, and C. Z. Huang, "Carbon dots: synthesis, formation mechanism, fluorescence origin and sensing applications," *Green Chemistry*, vol. 21, no. 3, pp. 449–471, 2019, doi: 10.1039/C8GC02736F.

[241] C.-L. Shen, Q. Lou, K.-K. Liu, L. Dong, and C.-X. Shan, "Chemiluminescent carbon dots: Synthesis, properties, and applications," *Nano Today*, vol. 35, p. 100954, Dec. 2020, doi: 10.1016/j.nantod.2020.100954.

[242] Y. Liu, H. Huang, W. Cao, B. Mao, Y. Liu, and Z. Kang, "Advances in carbon dots: from the perspective of traditional quantum dots," *Mater Chem Front*, vol. 4, no. 6, pp. 1586–1613, 2020, doi: 10.1039/D0QM00090F.

[243] X. Dong *et al.*, "Fast one-step synthesis of N-doped carbon dots by pyrolyzing ethanolamine," *J Mater Chem C Mater*, vol. 2, no. 36, pp. 7477–7481, Sep. 2014, doi: 10.1039/c4tc01139b.

[244] S. Chahal, N. Yousefi, and N. Tufenkji, "Green Synthesis of High Quantum Yield Carbon Dots from Phenylalanine and Citric Acid: Role of Stoichiometry and Nitrogen Doping," *ACS Sustain Chem Eng*, vol. 8, no. 14, pp. 5566–5575, Apr. 2020, doi: 10.1021/acssuschemeng.9b07463.

[245] D. Fernandes, K. A. Heslop, A. Kelarakis, M. J. Krysmann, and L. Estevez, "In situ generation of carbon dots within a polymer matrix," *Polymer (Guildf)*, vol. 188, Feb. 2020, doi: 10.1016/j.polymer.2020.122159.

[246] H. Li *et al.*, "Recent advances in carbon dots for bioimaging applications," *Nanoscale Horiz*, vol. 5, no. 2, pp. 218–234, 2020, doi: 10.1039/C9NH00476A.

[247] X. Dong, W. Liang, M. J. Meziani, Y.-P. Sun, and L. Yang, "Carbon Dots as Potent Antimicrobial Agents," *Theranostics*, vol. 10, no. 2, pp. 671–686, 2020, doi: 10.7150/thno.39863.

[248] C. Hu, M. Li, J. Qiu, and Y.-P. Sun, "Design and fabrication of carbon dots for energy conversion and storage," *Chem Soc Rev*, vol. 48, no. 8, pp. 2315–2337, 2019, doi: 10.1039/C8CS00750K.

[249] J. Zhou *et al.*, "An Electrochemical Avenue to Blue Luminescent Nanocrystals from Multiwalled Carbon Nanotubes (MWCNTs)," *J Am Chem Soc*, vol. 129, no. 4, pp. 744–745, Jan. 2007, doi: 10.1021/ja0669070.

[250] N. R. Nirala, G. Khandelwal, B. Kumar, Vinita, R. Prakash, and V. Kumar, "One step electro-oxidative preparation of graphene quantum dots from wood charcoal as a peroxidase mimetic," *Talanta*, vol. 173, pp. 36–43, Oct. 2017, doi: 10.1016/j.talanta.2017.05.061.

[251] J. Deng *et al.*, "Electrochemical Synthesis of Carbon Nanodots Directly from Alcohols," *Chemistry – A European Journal*, vol. 20, no. 17, pp. 4993–4999, Apr. 2014, doi: 10.1002/chem.201304869.

[252] F. Niu, Y. Xu, M. Liu, J. Sun, P. Guo, and J. Liu, "Bottom-up electrochemical preparation of solid-state carbon nanodots directly from nitriles/ionic liquids using carbon-free electrodes and the applications in specific ferric ion detection and cell imaging," *Nanoscale*, vol. 8, no. 10, pp. 5470–5477, 2016, doi: 10.1039/C6NR00023A.

[253] Y. Tian *et al.*, "Dramatic photoluminescence quenching in carbon dots induced by cyclic voltammetry," *Chemical Communications*, vol. 54, no. 65, pp. 9067–9070, 2018, doi: 10.1039/C8CC03617A.

[254] S. Zhu, Y. Song, X. Zhao, J. Shao, J. Zhang, and B. Yang, "The photoluminescence mechanism in carbon dots (graphene quantum dots, carbon nanodots, and polymer dots): current state and future perspective," *Nano Res*, vol. 8, no. 2, pp. 355–381, Feb. 2015, doi: 10.1007/s12274-014-0644-3.

[255] A. Kelarakis, "Graphene quantum dots: In the crossroad of graphene, quantum dots and carbogenic nanoparticles," *Curr Opin Colloid Interface Sci*, vol. 20, no. 5–6, pp. 354–361, Oct. 2015, doi: 10.1016/j.cocis.2015.11.001.

[256] H. Zheng, Q. Wang, Y. Long, H. Zhang, X. Huang, and R. Zhu, "Enhancing the luminescence of carbon dots with a reduction pathway," *Chemical Communications*, vol. 47, no. 38, pp. 10650–10652, Oct. 2011, doi: 10.1039/c1cc14741b.

[257] A. T. Kuhn and R. B. Lartey, "Electrolytic Generation 'In-Situ' of Sodium Hypochlorite," *Chemie Ingenieur Technik*, vol. 47, no. 4, pp. 129–135, Feb. 1975, doi: 10.1002/cite.330470404.

[258] C.-H. Yang, C.-C. Lee, and T.-C. Wen, "Hypochlorite generation on Ru–Pt binary oxide for treatment of dye wastewater," *J Appl Electrochem*, vol. 30, no. 9, pp. 1043–1051, 2000, doi: 10.1023/A:1004038503410.

[259] J. Skarzewski and R. Siedlecka, "SYNTHETIC OXIDATIONS WITH HYPOCHLORITES. A REVIEW," *Org Prep Proced Int*, vol. 24, no. 6, pp. 623–647, Dec. 1992, doi: 10.1080/00304949209356237.

[260] D. Zhang, "Highly selective and sensitive colorimetric probes for hypochlorite anion based on azo derivatives," *Spectrochim Acta A Mol Biomol Spectrosc*, vol. 77, no. 2, pp. 397–401, Oct. 2010, doi: 10.1016/j.saa.2010.05.028.

[261] X. Zhou, S. Guo, P. Zhong, Y. Xie, Z. Li, and X. Ma, "Large scale production of graphene quantum dots through the reaction of graphene oxide with sodium hypochlorite," *RSC Adv*, vol. 6, no. 60, pp. 54644–54648, 2016, doi: 10.1039/C6RA06012A.

[262] X. Li *et al.*, "Rapid and large-scale production of carbon dots by salt-assisted electrochemical exfoliation of graphite rods," *Journal of Electroanalytical Chemistry*, vol. 851, p. 113390, Oct. 2019, doi: 10.1016/j.jelechem.2019.113390.

[263] G. Gedda, S. A. Sankaranarayanan, C. L. Putta, K. K. Gudimella, A. K. Rengan, and W. M. Girma, "Green synthesis of multi-functional carbon dots from medicinal plant leaves for antimicrobial, antioxidant, and bioimaging applications," *Sci Rep*, vol. 13, no. 1, p. 6371, Apr. 2023, doi: 10.1038/s41598-023-33652-8.

[264] H. Salimi Shahraki, A. Ahmad, and R. Bushra, "Green carbon dots with multifaceted applications– Waste to wealth strategy," *FlatChem*, vol. 31, p. 100310, Jan. 2022, doi: 10.1016/j.flatc.2021.100310.

[265] F. Lian, C. Wang, Q. Wu, M. Yang, Z. Wang, and C. Zhang, "*In situ* synthesis of stretchable and highly stable multi-color carbon-dots/polyurethane composite films for light-emitting devices," *RSC Adv*, vol. 10, no. 3, pp. 1281–1286, 2020, doi: 10.1039/C9RA06729A.

[266] F. Yan, Z. Sun, H. Zhang, X. Sun, Y. Jiang, and Z. Bai, "The fluorescence mechanism of carbon dots, and methods for tuning their emission color: a review," *Microchimica Acta*, vol. 186, no. 8, p. 583, Aug. 2019, doi: 10.1007/s00604-019-3688-y.

[267] M. Alafeef, I. Srivastava, T. Aditya, and D. Pan, "Carbon Dots: From Synthesis to Unraveling the Fluorescence Mechanism," *Small*, vol. 20, no. 4, Jan. 2024, doi: 10.1002/smll.202303937.

[268] S. Gavalas and A. Kelarakis, "Towards Red Emissive Systems Based on Carbon Dots," *Nanomaterials*, vol. 11, no. 8, p. 2089, Aug. 2021, doi: 10.3390/nano11082089.

[269] H. Wang *et al.*, "Surface Modification Functionalized Carbon Dots," *Chemistry – A European Journal*, vol. 29, no. 65, Nov. 2023, doi: 10.1002/chem.202302383.

[270] T. Ogi, K. Aishima, F. A. Permatasari, F. Iskandar, E. Tanabe, and K. Okuyama, "Kinetics of nitrogen-doped carbon dot formation via hydrothermal synthesis," *New Journal of Chemistry*, vol. 40, no. 6, pp. 5555–5561, 2016, doi: 10.1039/C6NJ00009F.

[271] S. Qu *et al.*, "Toward Efficient Orange Emissive Carbon Nanodots through Conjugated sp^2-Domain Controlling and Surface Charges Engineering," *Advanced Materials*, vol. 28, no. 18, pp. 3516–3521, May 2016, doi: 10.1002/adma.201504891.

[272] F. A. Permatasari, H. Fukazawa, T. Ogi, F. Iskandar, and K. Okuyama, "Design of Pyrrolic-N-Rich Carbon Dots with Absorption in the First Near-Infrared Window for Photothermal Therapy," *ACS Appl Nano Mater*, vol. 1, no. 5, pp. 2368–2375, May 2018, doi: 10.1021/acsanm.8b00497.

[273] S. Gu *et al.*, "Fluorescence of functionalized graphene quantum dots prepared from infrared-assisted pyrolysis of citric acid and urea," *J Lumin*, vol. 217, p. 116774, Jan. 2020, doi: 10.1016/j.jlumin.2019.116774.

[274] Q. Yang *et al.*, "Resculpting carbon dots via electrochemical etching," *Sci Rep*, vol. 13, no. 1, p. 3710, Mar. 2023, doi: 10.1038/s41598-023-30547-6.

[275] C. L. Hawkins and M. J. Davies, "Hypochlorite-Induced Damage to Nucleosides: Formation of Chloramines and Nitrogen-Centered Radicals," *Chem Res Toxicol*, vol. 14, no. 8, pp. 1071–1081, Aug. 2001, doi: 10.1021/tx010071r.

[276] T. Wang *et al.*, "Carbon dots with molecular fluorescence and their application as a 'turn-off' fluorescent probe for ferricyanide detection," *Sci Rep*, vol. 9, no. 1, p. 10723, Jul. 2019, doi: 10.1038/s41598-019-47168-7.

[277] S. R. M. Santiago, Y. A. Wong, T.-N. Lin, C.-H. Chang, C.-T. Yuan, and J.-L. Shen, "Effect of nitrogen doping on the photoluminescence intensity of graphene quantum dots," *Opt Lett*, vol. 42, no. 18, p. 3642, Sep. 2017, doi: 10.1364/OL.42.003642.

[278] Y. Dong *et al.*, "Blue luminescent graphene quantum dots and graphene oxide prepared by tuning the carbonization degree of citric acid," *Carbon N Y*, vol. 50, no. 12, pp. 4738–4743, Oct. 2012, doi: 10.1016/j.carbon.2012.06.002.

[279] A. Sharma, V. Panwar, V. Chopra, J. Thomas, S. Kaushik, and D. Ghosh, "Interaction of Carbon Dots with Endothelial Cells: Implications for Biomedical Applications," *ACS Appl Nano Mater*, vol. 2, no. 9, pp. 5483–5491, Sep. 2019, doi: 10.1021/acsanm.9b01080.

[280] X. Pang, L. Li, P. Wang, Y. Zhang, W. Dong, and Q. Mei, "Adenine-derived carbon dots for the chemosensing of hypochlorite based on fluorescence enhancement," *Microchemical Journal*, vol. 168, p. 106400, Sep. 2021, doi: 10.1016/j.microc.2021.106400.

[281] M. Zhang *et al.*, "A Simple Method for Removal of Carbon Nanotubes from Wastewater Using Hypochlorite," *Sci Rep*, vol. 9, no. 1, p. 1284, Feb. 2019, doi: 10.1038/s41598-018-38307-7.

[282] L. Newman *et al.*, "Hypochlorite degrades 2D graphene oxide sheets faster than 1D oxidised carbon nanotubes and nanohorns," *NPJ 2D Mater Appl*, vol. 1, no. 1, p. 39, Dec. 2017, doi: 10.1038/s41699-017-0041-3.

[283] M. Zhang, M. Yang, H. Nakajima, M. Yudasaka, S. Iijima, and T. Okazaki, "Diameter-Dependent Degradation of 11 Types of Carbon Nanotubes: Safety Implications," *ACS Appl Nano Mater*, vol. 2, no. 7, pp. 4293–4301, Jul. 2019, doi: 10.1021/acsanm.9b00757.

[284] M. S. Beg, E. N. Gibbons, S. Gavalas, M. A. Holden, M. Krysmann, and A. Kelarakis, "Antimicrobial coatings based on amine-terminated graphene oxide and Nafion with remarkable thermal resistance," *Nanoscale Adv*, 2024, doi: 10.1039/D3NA01154B.

[285] Zulfajri, Dayalan, Li, Chang, Chang, and Huang, "Nitrogen-Doped Carbon Dots from Averrhoa carambola Fruit Extract as a Fluorescent Probe for Methyl Orange," *Sensors*, vol. 19, no. 22, p. 5008, Nov. 2019, doi: 10.3390/s19225008.

[286] W. Kasprzyk, T. Świergosz, S. Bednarz, K. Walas, N. V. Bashmakova, and D. Bogdał, "Luminescence phenomena of carbon dots derived from citric acid and urea – a molecular insight," *Nanoscale*, vol. 10, no. 29, pp. 13889–13894, 2018, doi: 10.1039/C8NR03602K.

[287] J. Oakes, "Principles of colour loss. Part 1: Mechanisms of oxidation of model azo dyes by detergent bleaches," *Review of Progress in Coloration and Related Topics*, vol. 32, no. 1, pp. 63–79, Jun. 2002, doi: 10.1111/j.1478-4408.2002.tb00251.x.

[288] H. Kanazawa and T. Onami, "Mechanism of the degradation of Orange G by sodium hypochlorite," *Coloration Technology*, vol. 117, no. 6, pp. 323–327, Nov. 2001, doi: 10.1111/j.1478-4408.2001.tb00083.x.

[289] Y. Xiong, J. Schneider, C. J. Reckmeier, H. Huang, P. Kasák, and A. L. Rogach, "Carbonization conditions influence the emission characteristics and the stability against photobleaching of

nitrogen doped carbon dots," *Nanoscale*, vol. 9, no. 32, pp. 11730–11738, 2017, doi: 10.1039/C7NR03648E.

[290] B. Yin *et al.*, "Green synthesis of carbon dots with down- and up-conversion fluorescent properties for sensitive detection of hypochlorite with a dual-readout assay," *Analyst*, vol. 138, no. 21, p. 6551, 2013, doi: 10.1039/c3an01003a.

[291] S. K. Misra *et al.*, "Carbon dots with induced surface oxidation permits imaging at single-particle level for intracellular studies," *Nanoscale*, vol. 10, no. 39, pp. 18510–18519, 2018, doi: 10.1039/C8NR04065F.

[292] P. Zhang *et al.*, "The Enhanced Photoluminescence Properties of Carbon Dots Derived from Glucose: The Effect of Natural Oxidation," *Nanomaterials*, vol. 14, no. 11, p. 970, Jun. 2024, doi: 10.3390/nano14110970.

[293] V. Strauss, H. Wang, S. Delacroix, M. Ledendecker, and P. Wessig, "Carbon nanodots revised: the thermal citric acid/urea reaction," *Chem Sci*, vol. 11, no. 31, pp. 8256–8266, 2020, doi: 10.1039/D0SC01605E.

[294] H. Wang *et al.*, "Fluorescently tuned nitrogen-doped carbon dots from carbon source with different content of carboxyl groups," *APL Mater*, vol. 3, no. 8, Aug. 2015, doi: 10.1063/1.4928028.

[295] E. Hidalgo, R. Bartolome, and C. Dominguez, "Cytotoxicity mechanisms of sodium hypochlorite in cultured human dermal fibroblasts and its bactericidal effectiveness," *Chem Biol Interact*, vol. 139, no. 3, pp. 265–282, Mar. 2002, doi: 10.1016/S0009-2797(02)00003-0.

[296] H. Coaguila-Llerena, L. Raphael da Silva, and G. Faria, "Research methods assessing sodium hypochlorite cytotoxicity: A scoping review," *Heliyon*, vol. 10, no. 1, p. e23060, Jan. 2024, doi: 10.1016/j.heliyon.2023.e23060.

[297] A. Belal *et al.*, "Nitrogen-doped carbon quantum dots as a novel treatment for black fungal bone infections (Mucormycosis): *in vitro* and *in vivo* study," *Artif Cells Nanomed Biotechnol*, vol. 52, no. 1, pp. 131–144, Dec. 2024, doi: 10.1080/21691401.2024.2318212.

[298] E. Sturabotti, A. Camilli, F. Leonelli, and F. Vetica, "Carbon Dots as Bioactive Antifungal Nanomaterials," *ChemMedChem*, vol. 19, no. 23, Dec. 2024, doi: 10.1002/cmdc.202400463.

[299] S. Zhao, L. Huang, Y. Xie, B. Wang, F. Wang, and M. Lan, "Green synthesis of multifunctional carbon dots for anti-cancer and anti-fungal applications," *Chin J Chem Eng*, vol. 37, pp. 97–104, Sep. 2021, doi: 10.1016/j.cjche.2021.03.008.

[300] Y. Cui *et al.*, "A Review of Advances in Graphene Quantum Dots: From Preparation and Modification Methods to Application," *C (Basel)*, vol. 10, no. 1, p. 7, Jan. 2024, doi: 10.3390/c10010007.

[301] G. Sandeep Kumar *et al.*, "Amino-functionalized graphene quantum dots: origin of tunable heterogeneous photoluminescence," *Nanoscale*, vol. 6, no. 6, p. 3384, 2014, doi: 10.1039/c3nr05376h.

[302] F. Jiang *et al.*, "Eco-friendly synthesis of size-controllable amine-functionalized graphene quantum dots with antimycoplasma properties," *Nanoscale*, vol. 5, no. 3, p. 1137, 2013, doi: 10.1039/c2nr33191h.

[303] L. Wang *et al.*, "Chlorine-Doped Graphene Quantum Dots with Enhanced Anti- and Pro-Oxidant Properties," *ACS Appl Mater Interfaces*, vol. 11, no. 24, pp. 21822–21829, Jun. 2019, doi: 10.1021/acsami.9b03194.

[304] Z. Gao *et al.*, "Tailoring the Interface in FAPbI$_3$ Planar Perovskite Solar Cells by Imidazole-Graphene-Quantum-Dots," *Adv Funct Mater*, vol. 31, no. 27, Jul. 2021, doi: 10.1002/adfm.202101438.

[305] V. A. Chhabra, R. Kaur, N. Kumar, A. Deep, C. Rajesh, and K.-H. Kim, "Synthesis and spectroscopic studies of functionalized graphene quantum dots with diverse fluorescence characteristics," *RSC Adv*, vol. 8, no. 21, pp. 11446–11454, 2018, doi: 10.1039/C8RA01148F.

[306] J. Zhao *et al.*, "Fabrication and properties of a high-performance chlorine doped graphene quantum dot based photovoltaic detector," *RSC Adv*, vol. 5, no. 37, pp. 29222–29229, 2015, doi: 10.1039/C5RA02358K.